IASJ
المجلات الاكاديمية العراقية

KJPS
AL-Kitab Journal For Pure Sciences

AL-Kitab Journal For Pure Sciences

Volume : 9 (2025)

Issue: 2

ISSN: 2617-1260 (print)

ISSN: 2617-8141 (online)

DOI: http://10.32441/kjps

Deposit number at the Notional House of Books and Archives, Iraq, 2271 in 2017

Al-Kitab Journal for Pure Science

KJPS

ISSN: 2617-1260 (print), 2617-8141(online)
DOI: http://10.32441/kjps
https://isnra.net/index.php/kjps

An Academic Semi-Annual Journal

Volume: 09 Issue: 02 Dec. 2025

Iraqi Academic Scientific Journals IASJ: https://iasj.rdd.edu.iq/journals/journal/issue/
Journal Website: https://isnra.net/index.php/kjps
E-mail: kjps@uoalkitab.edu.iq

Editorial Board for Al-Kitab Journal for Pure Sciences

Aims and Scope

The Al-Kitab Journal for Pure Sciences aims to provide an international forum for the publication and dissemination of original work that contributes to the understanding of the principal and related disciplines of science. Al-Kitab Journal for Pure Sciences publishes two peer-reviewed issues per year, an online and print journal, which publishes innovative research papers, literature reviews, and technical notes on the fields of Biology, Computer Sciences, Chemistry, Physics, and Mathematics.

Authors Guidelines

Rules and Instructions for Publication in Al-Kitab Journal for Pure Sciences

First: General requirements

1. The paper is submitted to the Editorial Secretariat directly in four copies with CD-ROM or E-mail of the magazine in MS Word and PDF files.
2. Research before being sent to scientific evaluators is subject to the quotation Turnitin program.
3. Research should be accepted for publication after being judged by scientific evaluators and according to the rules.
4. The publication fee is (100,000 ID) for researchers from Iraqi Universities and (free of charge) for foreign researchers.

Second: To prepare research for publication, authors must follow the following procedures.

1. **The article:**

   The article needs to be typed on one side of A4 paper (Right margin =2.5 cm, left margin =2.5 cm, and 2cm for the top and bottom) with 1.5 space, and the pages must be numbered.

2. **The content organization:**

   MS Word is to be used as follows: "Simplified Arabic" font for the Arabic articles, and "Times New Roman" for the English articles. The Size of the title is 18 bold. The names of the authors will be typed in 11 bold in Arabic and 11 bold in English. Abbreviations, keywords, main headings, the reference, and the acknowledgment will be typed in 14. Subheadings will be in 12 bold. The abstract will be size 12. The body of the article/paper is in size 12. The order of the paper's content will be as follows: The

article heading, the names of authors and their addresses, and the abstract (Both in Arabic and English).

3. **Research paper title:**

The title must be as short as possible and indicate the contents of the subject together with the name (names) of the authors. The names of the authors to whom correspondence is to be made should be indicated with (*) and show his / her email.

4. **The size:**

The paper should contain no more than 25 pages of journal pages including charts and diagrams.

5. **Abstract:**

The abstract should include the purpose and the means of the founding results and the conclusions. It should also contain the knowledge values of the subject of research. It is meant to be no more than 250 words. It should also emphasize the content of the subject and include the keywords used throughout the paper.

6. **Diagrams:**

Figures and diagrams must be given following the explanation referring to the diagram. Each diagram must contain its title below the diagram at the first size of 12. The diagram should be editable in terms of enlargement or reduction within the margins of the paper size. The parts of each diagram must be grouped into drawing parts.

7. **Tables:**

The tables should follow the parts of the main body and should be located below the indicated part of the text. Tables must have titles with a text size of 12. The text used inside the tables should be size 12 and kept within the cells of the table.

8. **References:**

The references used in the paper must be given in order and their numbers given inside the square bracket [ ]. The following instructions are to be followed:

If the reference is a book, the First name of the reference must be given first followed by the other names. Then the title (bold and Italic) of the book, edition, year of publication, the publisher, and place of publication (year of publication).

Example: [1] P. Ring and P. Schuck, "**The Nuclear Many-Body Problem**", First Edition, Springer-Verlag, New York (1980).

(b) If the reference is a research paper or an article in a journal: The name of the author must be given first, the title of the article, the name of the journal, the volume (issue), page (Year). **Example:** [1] Ali H. Taqi, R. A. Radhi, and Adil M. Hussein,

"Electroexcitation of Low-lying Particle-Hole RPA States of ^{16}O with WBP Interaction", Communication Theoretical Physics, 62(6), 839 (2014).

c) If the reference is an M.Sc. or Ph.D. thesis, the name of the anther must be written with the first name first followed by the surname, title of the thesis, the name of the university, and Country (Year).

Example: [1] R. A. Radhi, **"Calculations of Elastic and Inelastic Electron Scattering in Light Nuclei with Shell-Model Wave Functions"**, Ph.D. Thesis, Michigan State University, USA (1983).

(d) If the reference is from the conference. Authors Name, "**Paper Title**", Conference, Country, Publisher, volume, page (Year).

Example: [1] Ali H. Taqi and Sarah S. Darwesh, **"Charge-Changing Particle-Hole Excitation of ^{16}N and ^{16}F Nuclei"**, 3rdInternational Advances in Applied Physics and Materials Science Congress, Turkey, AIP Conf. Proc., 1569, 27 (2013)

Third: Privacy Statement

1. The names and e-mail addresses entered into the journal's website will be used exclusively for the purposes stated in this journal and will not be provided for any other purpose or for any other party.
2. The editor of the journal has the right to change any statement or phrase of the research content he may find necessary to express the work suitable to the general style of the journal.
3. After publishing the paper and its presentation on the journal page, the editors' team will destroy all the scrap papers. The author has no right to ask for them in any case.

Fourth: Modernity of sources:

The percentage of modern references used in the research should not be less than 50% of the total references used in the research. Modernity is measured within the last ten years of the year of submission of the research. For example, when submitting the research in 2018, the references should be from 2008 upwards and not less than 50%. The journal prefers to have at least one of the reference types of research published in the previous journal issues.

Note: For more information, visit:

Iraqi Academic Scientific Journals IASJ: **https://iasj.rdd.edu.iq/journals/journal/issue/**
Or Journal Website: https://isnra.net/index.php/kjps
The Journal can also be e-mailed to kjps@uoalkitab.edu.iq

Table of Contents

Volume: 09 Issue: 02 Dec. 2025

Al-Kitab Journal for Pure Sciences (2025); 9(2):1-19.
https://doi.org/10.32441/kjps.09.02.p1

Al-Kitab Journal for Pure Sciences
ISSN: 2617-1260 (print), 2617-8141(online)

https://isnra.net/index.php/kjps

Currency and Financial Crisis: A Review Study of Prediction Models and Crisis Management Strategies

Haitham Assi Kareem*, Idress Mohammed Husein

Department of Computer Science, College of Computer Science and Information Technology, University of Kirkuk, Kirkuk, Iraq.

*Corresponding Author: haithamassi1994@gmail.com

Citation: Kareem HA, Husein IM. Currency and Financial Crisis: A Review Study of Prediction Models and Crisis Management Strategies. Al-Kitab J. Pure Sci. [Internet]. 2025 Mar. 22;9(2):1-19. DOI: https://doi.org/10.32441/kjps.09.02.p1

Keywords: Currency, Currency Crisis, EWS (Early Warning System), Financial Crisis, Prediction.

Article History

Received	15 Jul.	2024
Accepted	08 Sep.	2024
Available online	22 Mar.	2025

Abstract

Predicting currency and financial crises has garnered a lot of attention and research, with notable developments and a variety of methodological approaches. This review article summarizes current research from 2019 to 2024 with an emphasis on the kinds of datasets, timeframes, and models used. The examination displays a wide range of data, from the 1970s to 2022, with the majority of studies depending on data collected after the 1990s because of its increased dependability and availability. Many models have been used, such as Markov switching models, artificial neural networks (ANN), signal approaches, deep neural decision trees (DNDTs), and traditional econometric models like logit and probit. The results emphasize that there isn't a single model that is always better; rather, they emphasize the significance of choosing models based on context and the advantages that hybrid or ensemble approaches may have. Our review highlights that to improve prediction accuracy, a variety of datasets and models must be used. Because currency crises are inherently complex, a multifaceted strategy that makes use of both conventional econometric and contemporary machine learning techniques is required. To better capture the complex dynamics of economic indicators, future research should investigate higher frequency data and keep improving hybrid methodologies.

This thorough analysis contributes to the current discussion on currency and financial crisis forecasting by offering insightful analysis and directing future research paths.

Keywords: Currency, Currency crisis, EWS (Early Warning System), Financial crisis, Prediction.

أزمات العملة والأزمات المالية: دراسة مراجعة لنماذج التنبؤ واستراتيجيات إدارة الأزمات

هيثم عاصي كريم* & إدريس محمد حسين

قسم علوم الحاسوب في كلية علوم الحاسوب وتكنولوجيا المعلومات، جامعة كركوك، كركوك، العراق

haithamassi1994@gmail.com , idress@uokirkuk.edu.iq

الخلاصة

تحظى عملية التنبؤ بالأزمات النقدية والمالية بقدر كبير من الاهتمام والبحث، مع تطورات ملحوظة ومجموعة متنوعة من الأساليب المنهجية. تلخص هذه المقالة الأبحاث الحالية من عام ٢٠١٩ إلى عام ٢٠٢٤ مع التركيز على أنواع مجموعات البيانات والأطر الزمنية والنماذج المستخدمة. يستعرض البحث أيضا مجموعة واسعة من البيانات المستخدمة في هذه الأبحاث، من سبعينيات القرن العشرين إلى عام ٢٠٢٢، حيث تعتمد غالبية الدراسات على البيانات التي تم جمعها بعد التسعينيات بسبب زيادة موثوقيتها وتوافرها. تم استخدام العديد من النماذج، مثل نماذج التبديل ماركوف، والشبكات العصبية الاصطناعية (ANN)، ونهج الإشارة، وأشجار القرار العصبية العميقة (DNDTs) والنماذج القياسية الاقتصادية التقليدية مثل لوجيت وبروبيت. تؤكد النتائج انه لا يوجد نموذج واحد أفضل من بقية النماذج، بل يعتمد أهمية اختيار النموذج بناءً على السياق والمزايا التي قد تتمتع بها الأساليب الهجينة أو المجمعة وسنسلط الضوء على أنه من أجل تحسين دقة التنبؤ، يجب استخدام مجموعة متنوعة من مجموعات البيانات والنماذج. ولأن أزمات العملة معقدة بطبيعتها، فإن الأمر يتطلب استراتيجية متعددة الأوجه تستفيد من كل من القياس الاقتصادي التقليدي وتقنيات التعلم الآلي المعاصرة. ومن أجل التقاط أفضل للديناميكيات المعقدة للمؤشرات الاقتصادية، ينبغي للبحوث المستقبلية أن تحقق في البيانات ذات التردد الأعلى وتحسين المنهجيات الهجينة باستمرار. ويساهم هذا التحليل الشامل في المناقشة الحالية حول التنبؤ بالعملة والأزمات المالية من خلال تقديم تحليل ثاقب وتوجيه مسارات البحوث المستقبلية.

الكلمات المفتاحية: أزمات العملة، التنبؤ، الأزمات المالية، العملة، نظام الإنذار المبكر.

1. Introduction

1.1. Definition

Currency crises are periods of extreme volatility and depreciation of a country's currency, which can have significant impacts on the economy and society. Price increases for both domestic and imported products and services are one effect of the currency crisis. Customers, however, may not always view price rises similarly. While some price increases could be viewed as justifiable, others might be perceived as exploitative and unfair [1]. A financial crisis

is a disruption to the financial markets that exacerbates issues with moral hazard and adverse selection. Financial markets are therefore unable to effectively direct money to individuals who provide the most profitable investment possibilities [2]. And there are significant occurrences that may have detrimental effects on society and the world economy [3]. Therefore, Early warning systems (EWS) are crucial since they can identify the early warning indicators of a crisis and offer policy solutions to avert or lessen it. However, the majority of EWS rely on ex-post data, which can be delayed and revised frequently and may not accurately represent the status of the economy right now [4].

Financial and currency crises are connected, due to their reliance on each other. They are occurrences that are often analyzed separately because of their unique characteristics and impacts. Financial crises can result in declines as they typically lead to disturbances in financial sectors like stock market collapses or banking emergencies [5]. A rapid devaluation of a country's currency is commonly referred to as a currency crisis [6]. These situations often occur due to market speculation or a loss of trust from investors. To grasp the reasons, processes, and government reactions to these crisis types, researchers distinguish between the two crises in that financial crises often occur by asset bubbles and excessive borrowing while currency crises are commonly associated with balance of payments issues and foreign exchange reserves [7].

1.2. The challenge

Determining and quantifying currency crises objectively is one of the difficulties in analyzing them. The literature has put forth a variety of strategies, including indicators based on market pressure, balance of payments, or currency rates. Among these, the Exchange Market Pressure Index (EMPI) is frequently employed as a combined gauge of currency pressure that accounts for variations in international reserves, interest rates, and exchange rates. Finding the causes or aggravating variables of a currency crisis, such as market expectations, contagion effects, macroeconomic fundamentals, or policy actions, is another difficulty [8]. The identification and analysis of current financial crisis variables is also not easy, assessment of the likelihood and seriousness of potential risks and provision of a scientific foundation for risk mitigation and control constitute early warning systems for financial risk. Building a strong financial risk early-warning mechanism is crucial due to the fragility of the financial system and the severity of the financial crisis [9]. Consequently, it's critical to create reliable and accurate models that can foresee and avert these kinds of problems. However, financial crisis prediction (FCP) is a difficult endeavor that requires handling high-dimensional, complicated data, in addition to choosing the most pertinent features that can reflect the problem's underlying patterns [3].

1.3. Objectives of the study

In this paper, we aim to unify and compile the current state of knowledge on the subject of currency crises and the financial crisis, and we will attempt to collect and summarize the research, theories, methodologies, and results that have been reached. Through our review of existing literature, we can identify trends in research, such as emerging predictive models or evolving crisis indicators, as well as evaluate the strengths and weaknesses of the methodologies used and discuss their applicability, accuracy, and robustness. In this paper, we will attempt to inform policymakers, financial analysts, and researchers about effective strategies for crisis prevention and early warning systems and political interventions. This can help improve financial stability and resilience.

1.4. Importance of predicting crisis

Forecasting currency and financial crises plays a role in upholding stability and averting significant economic downturns. Accurate predictions empower policymakers to proactively address issues thereby minimizing effects on economies and societies. Research has shown that rapid surges in credit and asset values often foreshadow crises underscoring the importance of monitoring these signals for detection [10]. In addition, having a grasp of how types of financial crises, like currency and banking crises, are interconnected can help in creating well-rounded plans to reduce possible weaknesses [11]. It is advantageous to forecast these crises as it helps in safeguarding stability and safeguarding individual national economies [12].

2. Literature review

2.1. Historical overview:

The examination of crisis occurrences within finance has garnered interest in the realm of economics over the past twenty years, particularly concerning the anticipation of financial and currency crises due to their substantial impact on economic activities [13]. Since the 1930s a few academics have introduced the idea of a "financial crisis" for the time and have delved into exploring and researching this business phenomenon [14]. A number of European nations experienced a crisis related to the Exchange Rate Mechanism (ERM) in 1992, which was one of the first currency crises. In December 1994, there was a currency crisis involving the peso. It all started when the Mexican government suddenly decided to devalue its currency, leading to a decline in the peso's value and triggering an economic downturn that saw a substantial decrease in GDP. Despite this, the notable event was the Asian Financial Crisis of 1997 [15]. Initially, two common approaches prevailed in financial crisis analysis: the signal method and the logit model. Despite occurrences of crises, the adoption of early warning models emerged

as a relatively recent development in the late 1990s. Recent studies have delved into utilizing machine learning techniques for predicting crises. These techniques encompass decision trees, networks, random forests, support vector machines, and various deep-learning models [16]. This extensive research endeavor has generated an array of prediction models backed by varied methodologies [13]. There have been three types of models, for understanding currency crises. The first set of models emerged in response to the balance of payment crises in countries, like Argentina, Chile, and Mexico during the 1970s and 1980s. The second-generation models were developed following the Exchange Rate Mechanism (ERM) crisis in 1992 and the crisis of 1994–1995. Lastly, efforts to create third-generation models began after the crisis that occurred between 1997 and 1998. An in-depth look at the literature can help a researcher between a currency crisis and other types of financial crises such as balance of payments crises. The term "financial crisis" seems to be the comprehensive covering forms of instability linked to financial and monetary systems. A balance of payment crisis stems from an imbalance between a deficit in the account and the capital and financial account leading to a currency crisis after foreign reserves are depleted. Many sources suggest that these two concepts are interchangeable. Numerous theories have been proposed to explore the occurrence of currency crises [17].

2.2. Currency crisis

According to [18], using logit regression on monthly data from 1992 to 2011, an early warning system (EWS) was developed to predict currency crises in emerging economies in Asia and Latin America. This system includes analyzing currency crisis history, selecting an ideal cut-off criterion, identifying key predictors, and testing variables using a sound statistical approach. Institutional and macroeconomic factors were used to forecast future crises. EWS's performance was compared with other techniques like the probit model and the signal approach. High foreign conflict combined with weak law and order can also trigger a crisis. Ultimately, a lack of democracy, indicated by high government stability and the absence of internal strife, leads to a currency crisis. The logit model performed better than the probit model and the signal approach in accuracy and timeliness.

Statistika and Maret [19] used a neural network approach (ANN) to identify the Indonesian currency crisis by analyzing macroeconomic data. The authors choose 12 indicators that are often used in literature using monthly data from January 1990 to December 2018. They contrast the ANN model's performance with that of a logit model and a signal approach. They discovered that compared to the other two approaches, the ANN model has a greater accuracy rate and a lower false alarm rate. The most important indicators for forecasting currency crises, including interest rates, foreign reserves, inflation, and exchange rates, are likewise identified by the ANN

model. According to the paper's conclusion, the ANN approach is a useful instrument for creating an early warning system for Indonesia's currency crisis.

Arya and Soenardi [20] use a combination of volatility and Markov switching models to identify currency crises in Indonesia based on real deposit rate indicators, utilizing monthly data from January 1990 to July 2022 and applying ARCH, GARCH, and EGARCH volatility models. They assume that the Markov switching models have two or three states. They use log-likelihood, AIC, BIC, and HQIC criteria to evaluate the models and find that MS-ARCH(1) is the best model for currency crisis modeling on the real deposit rate indicator, detecting crises from 1997 and 2008 and showing how Indonesian crisis eras can be identified using smoothed probabilities from the integrated models. They identify four crisis periods: Jan 1998–Aug 1997, Jun 1998–Oct 1998, Aug 2000–Jun 2000, and Oct 2008–Dec 2008. They conclude that Markov switching models combined with volatility effectively capture data condition changes and are valuable for Indonesia's currency crisis detection.

In Ref. [15], Deep neural decision trees (DNDTs), a method based on decision trees and deep learning neural networks, were used to create a global model for currency crisis prediction by Alaminos et al. They employed a sample of 162 nations, covering both emerging and developed regions, to account for regional heterogeneity in warning indicators. They compared DNDTs with other widely used methods like support vector machines, random forests, and logistic regression. The DNDTs approach achieved an average accuracy of 93.75% for currency crisis prediction, surpassing the other techniques in accuracy, precision, recall, and F1 score. Their research concluded that DNDTs offer tools that contribute to global financial stability and hold significant potential for macroeconomic policy adaptation to currency value decline risks.

Based on interest rates and inflation, Amri, Chamidah, and Sugiyanto [21] created early detection models for currency crises in Indonesia. To simulate the large fluctuations and regime changes of the 1998 and 1997 crises, they combined Markov regime-switching and volatility models, using smoothed probability values to assess the models' effectiveness on monthly data from January 1990 to December 2018. They found that MRS-AR (2,1) is best for inflation, and MRS-GARCH (2,2,0) is most suitable for interest rates. MRS-GARCH (2,2,0) identified currency crises from January to December 1998, while MRS-AR (2,1) identified crises from August 1997 to December 1998. They concluded that Indonesia did not face a currency crisis in 2019 based on the smoothed probability estimates from the two models and proposed using these indicators as early warning systems for currency issues.

Based on the stock price index, Prasasti et al. [22] identified a suitable model and forecasted the Indonesian currency crisis from November 2022 to October 2023, and they made use of three models: a hybrid of the Markov switching model and the volatility model. A situation when the depreciation of the exchange rate surpasses a predetermined threshold is referred to as a currency crisis. The combination model outperforms the others in terms of accuracy, sensitivity, and specificity, they discovered. Additionally, based on the combination model, they projected that Indonesia would not experience a currency crisis between November 2022 and October 2023. Then, based on the stock price index, they concluded that volatility and the Markov switching model could be employed together as an early warning system for Indonesia's currency problem, and they recommended that to prevent a currency crisis, the government and central bank should keep an eye on changes in the stock market and take preventative measures.

Sugiyanto et al. [23] use the real interest rate on deposit indicators from 1990 to 2018 to try and identify Indonesia's currency crisis. To explain the oscillations and regime shifts of the indicator, they used models of volatility and Markov Switching. The MRS-ARCH (2,1) model is suggested as the most appropriate model to elucidate the currency crisis. After analyzing the data using the MRS-ARCH (2,1) model, they came to the following conclusions: There are two states in the model: state 1 is regular, and state 2 is a crisis state. The smoothed probability values indicate that the model can account for the crisis that transpired in 1997/1998 and 2008. Based on the indicator, the model forecasts that there was no indication of a catastrophe in 2019. Ultimately, they concluded that a good way to identify Indonesia's currency issue is to look at the real interest rate on deposits. and the MRS-ARCH (2,1) model is a good fit for explaining how the indicator behaves.

Adams and Metwally [24] used yearly data from 1977 to 2017 to identify the markers of Egypt's currency crisis. Based on 16 economic indicators, they discovered that the following five factors had the best forecasting ability: real interest rate, real exchange rate, USA interest rate, domestic current account, and domestic interest rate spread. They suggested the creation of the market turbulence index (MTI) to gauge the severity of the currency crisis and compare it to other indices. They determined eight episodes of the Egyptian currency crisis that align with historical occurrences. According to their findings, 90.6 percent of non-crisis episodes and 87.5 percent of crisis episodes are accurately predicted by the probit model. The MTI outperforms other indices in reflecting the intensity of the currency crisis, including the Speculative Pressure Index (SPI) and the Exchange Market Pressure Index (EMPI).

In Ref. [25], the recent history of currency crisis (stress periods) and the factors determining their likelihood in India were studied by Mohana Rao and Padhi. Using signal extraction methodology and a logistic regression model for the years 1986–2015, they sought to build an early warning system (EWS) to predict the likelihood of an impending crisis within the 12-month crisis window. They determined 22 crisis months (stress periods), of which only the early ones (1990–1991) had a devaluation; the later ones (after 1991) did not. In terms of accuracy, the logistic regression model performs better than the signal extraction method. They concluded that creating an EWS can be a useful diagnostic tool for tracking how susceptible the Indian economy is to exchange rate fluctuations.

In Ref. [26] a model for forecasting the Iranian currency crisis was presented by Davari et al.; it combined machine learning techniques with macroeconomic indices and classified times of peace and crisis using quarterly data from 1990 to 2018 with logistic regression, support vector machine, and random forest techniques. The most significant indicators are the real effective exchange rate, inflation rate, current account balance, and foreign exchange reserves. The random forest approach has the highest accuracy and reliability. A currency crisis is defined as an exchange rate depreciation of more than 15% in a quarter or more than 25% in a year. The study identified six periods of crisis: 1994Q4, 1995Q1, 2002Q3, 2012Q2, 2018Q2, and 2018Q3. The random forest technique outperforms the other methods and is valuable for forecasting the currency crisis in Iran.

According to [13] a nation's ability to develop depends on its sovereign debt and currencies, which makes international relations and efficient funding crucial. Forecasting sovereign debt and currency crises is important, but current models are not accurate or diverse in terms of geography. David Alaminos and colleagues introduce new predictive models that outperform conventional statistical methods. The models take into account a global sample that includes countries from Africa, the Middle East, Latin America, Asia, and Europe. Significant variables for currency crises are FCF, M2M, M2R, TRO, CACC, DUR, and YEAR; key variables for sovereign debt crises are TDEB, IMFC, FXR, M2R, SCFR, and SBS. Models with high prediction accuracy include fuzzy decision trees, AdaBoost, extreme gradient boosting, and deep learning neural decision trees; some of these models can predict sovereign debt up to 100% of the time, and currency crises up to 99.07%.

Using Egypt as a case study, Mamdouh and Hany [27] suggest the best early warning system (EWS) for foreseeing currency crises in developing nations. The research combines forecasts from separate models using equal weighting (EW) and dynamic model averaging (DMA) techniques, which support time-varying weights. The results show that these combined forecast

methods perform better in both in-sample and out-of-sample predictions than individual models. The research demonstrates that a combination of forecasts provides superior predictive power, which contrasts with prior studies that support particular models, such as Probit, Logit, or extreme value models. In addition to estimating and combining density forecasts rather than point forecasts, the paper recommends future research investigate various combination schemes for other financial crises.

Using the Signal, Logit/Probit, BMA, and 2SLS techniques, Dao and colleagues **[28]** present a novel early warning system (EWS) for predicting currency and systemic banking crises in emerging markets like Vietnam. Focusing on indicators such as the securities index, real effective exchange rate, exports, and banking metrics like M2/reserves and NPLs, the EWS projects a low crisis probability for 2017–2018. Vietnam's economic stability was affected by dollarization and the 2008–2009 global financial crisis. Vietnam, a net importer until 2011, briefly had a trade surplus in 2012, leading to periodic deficits by 2015. Significant currency appreciation weakens export competitiveness, while severe depreciation increases foreign debt risk. From 2002 to 2016, the study's EWS identifies 11 macroeconomic variables influencing currency crises and 15 influencing systemic banking crises, showing a low crisis probability in subsequent years.

To predict currency crises across 17 developing countries, Gulden Poyraz's study uses a dynamic random effects probit model. It highlights the important effects of lagged crisis indicators, particularly the 12th, 3rd, 2nd, and 1st lags, showing short-term state dependence on crisis probability. Their study concludes that, although static models are more common in the literature currently in publication, a dynamic approach can uncover intertemporal relationships and identify actual state dependence in crisis occurrence by using lagged dependent variables. This emphasizes the importance of incorporating endogenous factors into early warning systems to enhance their ability to accurately forecast currency crises **[29]**.

In Ref. **[30]** the goal of the study by Ahmad Googerdchian, Babak Saffari, and Fatemeh Farzina is to use an early warning system to forecast currency crises in Iran. The study uses artificial neural networks, specifically a Multi-Layer Perceptron Neural Network with a Hard-Limit function, along with econometric techniques to analyze seasonal data from 2001 to 2015 and forecast that there won't be a currency crisis in 2019. Important conclusions show that the export index is the main factor affecting Iran's currency stability. The model's 97% predictive accuracy, as demonstrated by comparisons with earlier research, suggests that it is more reliable than traditional econometric techniques, which have higher prediction errors because of serial correlation in time-series data.

2.3 Financial crisis:

Altunöz [31] used the probit model, logit model, and KLR signal methodology to assess the predictability of the 2008 financial crisis in Turkey, selecting nine indicators related to financial stability with data from January 2003 to December 2012. He evaluated the approaches based on lead time, type I and type II errors, and accuracy. The KLR signal technique had a high accuracy rate of 97.5% but a high false alarm rate of 50%. The probit model had a lower accuracy rate of 78.31% and a false alarm rate of 16.67%. The logit model had the highest accuracy rate of 92.18% and a moderate false alarm rate of 33.33%. The lead times were 12 months for the logit model, 10 months for the probit model, and 8 months for the KLR signal method. Altunöz concluded that the logit model is the most effective technique for forecasting the financial crisis due to its high accuracy rate, tolerable false alarm rate, and extended lead time. He recommended monitoring indicators like the credit to GDP ratio, real exchange rate, and current account balance.

In Ref. [32], the authors utilize machine learning methods to anticipate financial problems by integrating multiple models within a sequential prediction framework. This framework covers France, Germany, Italy, and the United Kingdom, using macroeconomic factors like inflation, current account balance, loan growth, and currency rate to forecast crises. They evaluate their predictions out-of-sample, finding that their method can identify systemic financial crises three years ahead with a high signal-to-noise ratio. The approach outperforms any single model in the long run, adapting over time and across nations. Machine learning proves useful for creating macroprudential regulations and forecasting crises, though the method faces limitations, such as small crisis sample size and potential economic structural shifts.

Bluwstein et al. [33] utilized machine learning techniques to analyze macro-financial data from 17 nations between 1870 and 2016 to build early warning models for financial crisis prediction. They found that machine learning models generally outperform logistic regression in forecasting and out-of-sample predictions. Significant indicators of crisis risk include the slope of the yield curve and credit expansion. Machine learning methods like random forests, neural networks, and support vector machines showed better performance than logistic regression, particularly in terms of AUC-PR and AUC-ROC. A framework based on Shapley values revealed that credit growth and yield curve slope are consistently key predictors. Additionally, a flat or inverted yield curve, especially when nominal interest rates are low and credit growth is high, is particularly concerning.

In Ref. [34] Sumaira and colleagues evaluated the performance of traditional distress prediction models before, during, and following financial crises by comparing their predictive accuracy for Pakistani firms between 2001 and 2015. The Z-score model is excellent at predicting insolvency, but the probit model has the best overall accuracy. All models exhibit decreased accuracy during economic downturns. The study emphasizes the importance of defining financial distress broadly and considering warning signs such as listing fees and dividend failures. Metrics like profitability and liquidity show significant differences between troubled and stable firms. The study acknowledges limitations in generalizability and advocates broader research encompassing multiple emerging markets.

Hossein Dastkhan [35] investigates the use of Conditional Value at Risk (CoVaR), a forward-looking systemic risk measure, in an emerging market—the TSE, in particular—in this study. He creates new network-based indices and builds a network representation of firm interconnections based on ΔCoVaR values. As early warning systems, these indices can be used to anticipate firm-level and market-wide downturns and crises. According to the findings, these indicators may be able to predict crises up to seven periods ahead of time. This indicates that investors and policymakers alike may find these indicators useful in managing their portfolios according to risk assessments and in developing micro- and macro-prudential policies to reduce systemic risks.

According to [36] the collapse of the US housing market in 2007 marked the beginning of the global financial crisis, exposing large undervaluation's in mortgage-backed securities and causing a general decrease in bank profitability and liquidity because of intricate financial instruments. Investigations into the effects of securities like mortgage-backed securities, repurchase agreements, and interbank market securities on bank profitability were prompted by predictive models' inability to predict the crisis. Repurchase agreements and banks' return on capital correlated positively, but overall, these factors were not very good at predicting crises. Rather, stable, time-invariant bank characteristics and underlying risks undermined the efficacy of early warning indicators and contributed to the severity of the crisis. To improve crisis anticipation and management in international financial markets, these variables must be included in future prediction models.

During the COVID-19 pandemic, Feixiong-Ma and associates evaluated financial crisis prediction techniques for publicly traded firms. Support vector machines and RPROP artificial neural networks were used to analyze two years' worth of panel financial indicators from 162 different companies. By combining these techniques in a novel way, they were able to create a strong early warning system that improved risk supervision and stability for both listed

businesses and the overall economy. According to the research, combining these algorithms predicts financial crises with accuracy and provides stakeholders—investors, creditors, and regulators—with information about the financial health of the company and risk-reduction tactics. Notwithstanding its merits, the study recommends that nonfinancial indicators and longitudinal data be incorporated into future research for thorough examination and ongoing model validation **[37]**.

High-tech enterprises (HTEs) should embrace sustainable development strategies, according to Houfang Guo, especially for "carbon neutrality" and "carbon peak" objectives. In the face of market competition, he addresses the need for HTEs to manage financial risks using machine learning models like XGBoost, BP neural networks, and logistic regression. The study aims to improve the accuracy of financial crisis early warning (FCEW) systems by combining these models with the stacking method. It examines fusion techniques such as voting and averaging and concludes that the stacking fusion model, particularly when combining logistic regression and XGBoost, produces better performance metrics like accuracy and AUC. Stacking fusion models perform better than single models and other techniques, providing strong predictions essential for sustainable business growth **[38]**.

The temporal convolutional network (TCN), introduced by Shun CHEN, Yi HUANG1, and Lei GE, is an advanced model for financial crisis forecasting that outperforms other deep learning techniques and conventional logit models. TCN processes multiple time points simultaneously, has a larger receptive field than RNNs, and handles long-range dependencies effectively with less computational power. The study uses Shapley value decomposition to interpret the model and finds that real GDP growth and stock prices are important variables in crisis prediction. The study validates the efficacy of TCN using the Jórda-Schularick-Taylor macro-history database, demonstrating precision increases of more than 10% and up to 50% compared to RNNs and logit models. These results highlight the potential of TCN to improve early warning systems and guide policy choices **[16]**.

The goal of the study by Jin Kuang, Tse-Chen Chang, and Chia-Wei Chu **[14]** is to provide a strong financial early warning model for Chinese enterprises amid market competition and economic globalization. The research shows better predictive accuracy with a combined approach using time series methods and the BP neural network algorithm, rather than individual methods. Examining 816 companies listed on the Shanghai Stock Exchange, the study concludes that the BP neural network is the most effective model for forecasting potential crises. Future research should increase sample sizes and integrate internal corporate factors and external economic indicators for more complete prediction models. The results highlight

implications for strengthening crisis management, boosting asset appreciation, encouraging wise investments, and assisting policymakers in resource allocation and economic stability.

3. Summary of Literature Review:

This section offers a thorough overview of studies that have been done on the prediction of currency crises using various machine learning models. A variety of studies are covered in the literature review, demonstrating the variety of dataset types and ranges that researchers in this field have used. We aim to provide a concise and understandable summary by looking at known models used and selecting the models that work best based on the results. The main points of these studies are summarized in **Table 1**, providing a convenient way to quickly review the pertinent data.

Table 1: A Summary of the Studies of Literature Review.

Ref.	Pub. year	Dataset type	Dataset range	Known Models Used in the Study	Best model (depending on the results)
[18]	2022	Monthly data	From 1992 to 2011	logit regression and probit model	logit model
[19]	2023	Monthly data	From January 1990 to December 2018	ANN model, logit model, and signal approach	ANN method with Multilayer Perceptron Backpropagation algorithm
[20]	2023	Monthly data	From January 1990 to July 2022	Combination of volatility and Markov switching models (applying the ARCH, GARCH, and EGARCH volatility models)	MS-ARCH
[15]	2019	Annual data	From 1970 to 2017	deep neural decision trees (DNDTs), Logistic Regression, Support Vector Machines, ANN (Multilayer Perceptron), and AdaBoost	DNDTs
[21]	2020	Monthly data	From January 1990 to December 2018	combined Markov regime-switching and volatility models (applying the MRS-AR (2,1) and MRSGARCH (2,2,0))	MRS-AR (2,1)
[22]	2023	Monthly data	From November 2022 to October 2023	combination of volatility and MARKOV switching models	MSARCH (2,1) model with the AR(1) model
[23]	2019	Annual data	From 1990 to 2018	volatility and Markov Switching	MRS-ARCH (2,1)
[24]	2019	Annual data	From 1977 to 2017	probit model	probit model
[25]	2019	Annual data	From 1986 to 2015	signal extraction methodology and a logistic regression model	logistic regression model
[26]	2022	Quarterly data	From 1990 to 2018	the logistic regression, support vector machine, and random forest techniques	random forest
[13]	2021	Annual data	From 1970 to 2017	Multilayer Perceptron (MLP), Support Vector Machine (SVM), Fuzzy Decision Trees	for the sovereign debt crisis: FDT, AdaBoost, XGBoost, and DNDT. for the prediction of the

Ref.	Pub. year	Dataset type	Dataset range	Known Models Used in the Study	Best model (depending on the results)
				(FDT), AdaBoost, Extreme Gradient Boosting (XGBoost), Random Forest (RF), Deep Belief Networks (DBN), Deep Neural Decision Trees (DNDT)	currency crisis: DNDT, XGBoost, RF, and DBN
[27]	2020	Monthly data	From February 1995 to July 2018	Probit, Logit, Grompit, Switching regression model, equal weighting (EW), and dynamic model averaging (DMA)	EW- and DMA-based EWS
[28]	2022	Monthly data	From January 2002 to December 2016.	the Signal approach, Logit/Probit models, Bayesian Model Averaging (BMA), and Two-Stage Least Squares (2SLS).	the combined approach of these methods.
[29]	2019	Panel data	From 1991 to 2017	The dynamic panel probit model	The dynamic panel probit model
[30]	2021	Seasonal data	From 2001 to 2015	Multi-layer Perceptron Neural Network and Hard-Limit function	Multi-layer Perceptron Neural Network and Hard-Limit function
[31]	2019	Monthly data	From January 2003 to December 2012.	the probit model, the logit model, and the KLR signal methodology	the logit model
[32]	2021	Quarterly data	From 1985q1 to 2019q3	based on model aggregation and is “meta-statistical”	can incorporate any predictive model of crises in the analysis and test its ability to add information
[33]	2023	Annual data	From 1870 to 2016	Neural network, Extreme trees, SVM, Random Forest, Logistic regression, and Decision tree	Machine learning models outperform logistic regression
[34]	2019	Annual data	From 2001 to 2015.	Z-Score, O-Score, Probit, Hazard, and D-Score	The probit model and the Z-score model
[35]	2021	Daily data	From January 2010 and September 2016	Forward-looking Conditional Value at Risk (CoVaR), Network Analysis of Asset Exposures, Network-based Indices (derived from CoVaR values)	Network-based indices based on CoVaR values
[36]	2020	Annual data	From 2004 to 2008	Linear Multiple Regression Analysis, Fixed-Effects Regression Analysis	linear multiple regression analysis
[37]	2020	Panel data	From 2015 to 2016	RPROP artificial neural network and support vector machine	Combine the two methods
[38]	2023	Not mentioned	From 2018 to 2020	logistic regression, XGBoost, and BP neural networks	combine the models using the stacking method
[16]	2024	Annual data	From 1870 to 2016	Temporal Convolutional Network (TCN), Multilayer perception (MLP), Long Short-Term Memory (LSTM) and Gated Recurrent Unit (GRU)	temporal convolutional network (TCN)
[14]	2022	Not mentioned	Not mentioned	the time series forecasting method (an autoregressive integrated moving average (ARIMA)) model, Backpropagation Neural Network (BPNN), and Combined Forecasting Method	combined forecasting method

4. Analysis and methodology:

After studying a large group of previous and more recent research in the field of predicting currency and financial crises, we can conduct a comprehensive analysis and focus on some important points below:

1. Publication Years and Types of Datasets: Through the date of research publication, there is continued interest in and progress in the field of currency and financial crisis prediction, spanning from 2019 to 2023. While monthly data is used in most studies, higher frequency data may be able to capture more subtleties in economic indicators that are important for forecasting currency and financial crises.

2. Dataset Ranges: The datasets span different periods; the most recent data goes back to July 2022, while the oldest data dates to 1970. The diverse range of dataset periods is indicative of distinct historical and economic contexts, thereby augmenting the findings' resilience and applicability. Most research uses data from the 1990s and later, most likely because this is when more complete and trustworthy economic data became available.

3. Models Used in the Studies: Many models have been used, such as deep neural decision trees (DNDTs), artificial neural networks (ANN), signal approaches, Markov switching models, and classic econometric models (logit and probit). The combination of the advantages of contemporary computational methods and classical econometrics through the use of both conventional and sophisticated machine learning models suggests a multidisciplinary approach.

4. Best-Performing Models: The findings show that no single model performs better than all others. The optimal model varies based on the research, dataset, and particular situation. For example, one study determined that the logit model performed best, while other studies found that the ANN method with Multilayer Perceptron Backpropagation, MS-ARCH, DNDTs, and MRS-AR performed best. This variation emphasizes the value of choosing models that are appropriate for the given context as well as the possible advantages of hybrid or ensemble approaches.

The analysis emphasizes how crucial it is to use a variety of models and data sets. Combining different models can potentially result in predictions that are more accurate because they each capture different aspects of the data. The ability of machine learning models to handle intricate, non-linear relationships in economic data is evident in the noticeable shift towards their integration in the prediction of currency and financial crises. The optimal model depends heavily on the context. Model performance is heavily influenced by variables like the dataset period, frequency, and particular economic conditions.

5. Discussion

The efficacy of distinct models in diverse settings implies that a combined or collaborative approach could prove advantageous. Researchers can take advantage of each model's advantages by combining them, which could result in more reliable and accurate predictions. The prevalence of data from the 1990s emphasizes how crucial current economic circumstances are for forecasting currency and financial crises. Nonetheless, incorporating more ancient data can improve the findings' generalizability and offer insightful historical context. The intrinsic complexity and unpredictable nature of currency and financial crises is a significant obstacle. Many variables affect the state of the economy, many of which are hard to measure or forecast. Overfitting is a further drawback, especially with intricate models like artificial neural networks. Ensuring that models generalize well to new data is crucial for reliable predictions. Higher frequency data (weekly or daily, for example) could be explored in future research to capture even more precise economic indicators. To increase prediction accuracy, more research is also required on hybrid and ensemble approaches, which combine machine learning and conventional econometric models. Including a wider range of historical eras and geographical areas in the datasets can improve model robustness and offer a more thorough understanding of currency and financial crises.

6. Conclusions

In this research, we reviewed literature on currency crisis prediction, highlighting the significant progress and diversity in methodologies. Predicting a currency crisis is a complex task due to the numerous variables and uncertainties involved, such as macroeconomic imbalances, external vulnerabilities, institutional weaknesses, political instability, and global shocks. Our review revealed that there is no universally best model or technique for predicting currency crises; each method has its strengths and weaknesses, which depend on factors such as the specific context, country characteristics, model assumptions, and data quality and availability. We examined a variety of methods, including logit and probit models, artificial neural networks, Markov switching models, and deep neural decision trees. Each method's sensitivity, robustness, accuracy, and applicability were discussed. This comprehensive analysis contributes to the body of knowledge on currency crisis prediction, providing insights into the current approaches and models used in the field.

References

[1] Nazari M, Hesaraki A. Fairness Perceptions of Price Increases in the Case of Currency Crisis Affecting Domestic and Foreign Brands. J Advert Sales Manag [Internet]. 2022;3(4):4–16. Available from: http://dx.doi.org/10.1016/j.cviu.2017.00.000

[2] Koh WC, Kose MA, Nagle PSO, Ohnsorge F, Sugawara N. Debt and Financial Crises. SSRN Electron J. 2020;(January).

[3] J U, Metawa N, Shankar K, Lakshmanaprabu SK. Financial crisis prediction model using ant colony optimization. Int J Inf Manage [Internet]. 2020;50(November):538–56. Available from: https://doi.org/10.1016/j.ijinfomgt.2018.12.001

[4] Boonman TM, Jacobs JPAM, Kuper GH, Romero A. Early Warning Systems for Currency Crises with Real-Time Data. Open Econ Rev. 2019;30(4):813–35.

[5] Avdjiev S, Bruno V, Koch C, Shin HS. The Dollar Exchange Rate as a Global Risk Factor: Evidence from Investment. IMF Econ Rev. 2019;67(1):151–73.

[6] Jamal A, Bhat MA. COVID-19 pandemic and the exchange rate movements: evidence from six major COVID-19 hot spots. Futur Bus J [Internet]. 2022;8(1):1–11. Available from: https://doi.org/10.1186/s43093-022-00126-8

[7] Sah A, Patra B. Relation Between Digital Currencies and Other Financial Markets: A Non-Linear and Multivariate Analysis. Asia-Pacific Financial Markets. 2024.

[8] Sutrisno H, Wulansari D, Handoyo RD. Macroeconomic Indicators as A Signal of The Currency Crisis in The Indonesian Economy. Int J Econ Manag. 2022;16(1):1–20.

[9] Chen S, Svirydzenka K. Financial Cycles – Early Warning Indicators of Banking Crises? IMF Work Pap. 2021;2021(116):1.

[10] Greenwood RM, Hanson SG, Shleifer A, Sørensen J. Predictable Financial Crises. SSRN Electron J. 2021;

[11] Hamdaoui M, Ayouni S, Maktouf S. Financial crises: explanation, prediction, and interdependence. Vol. 2, SN Business & Economics. 2022.

[12] Adam Hayes. Currency Crisis: What they are, examples and effects [Internet]. 2024. Available from: https://www.investopedia.com/articles/economics/08/currency-crises.asp#toc-understanding-currency-crisis

[13] Alaminos D, Peláez JI, Salas MB, Fernández-Gámez MA. Sovereign debt and currency crises prediction models using machine learning techniques. Symmetry (Basel). 2021;13(4):1–28.

[14] Kuang J, Chang TC, Chu CW. Research on Financial Early Warning Based on Combination Forecasting Model. Sustain. 2022;14(19).

[15] Alaminos D, Becerra-Vicario R, Fernández-Gámez MA, Ruiz AJC. Currency crises prediction using deep neural decision trees. Appl Sci. 2019;9(23).

[16] Chen S, Huang Y, Ge L. an Early Warning System for Financial Crises: a Temporal Convolutional Network Approach. Technol Econ Dev Econ. 2024;30(3):688–711.

[17] Abdushukurov N. The impact of currency crises on economic growth and foreign direct investment: The analysis of emerging and developing economies. Russ J Econ. 2019;5(3):220–50.

[18] Ferdous LT, Kamal KMM, Ahsan A, Hoang NHT, Samaduzzaman M. An Early Warning System for Currency Crises in Emerging Countries. J Risk Financ Manag. 2022;15(4).

[19] Rosma Dian Pertiwi, Sugiyanto IS. APPLICATION OF ARTIFICIAL NEURAL NETWORK METHOD IN CURRENCY CRISIS DETECTION IN INDONESIA BASED ON MACROECONOMIC INDICATORS ABSTRACT : 2023;(July 1997):51–60.

[20] Arya W, Soenardi B. COMBINED VOLATILITY AND MARKOV SWITCHING MODELS FOR CURRENCY CRISIS DETECTION IN INDONESIA ON REAL DEPOSIT RATE INDICATORS ABSTRACT : Indonesia experienced its worst currency crisis in the mid-1997 and the global currency crisis. 2023;43–50.

[21] Amri IF, Chamidah N, Sugiyanto. Early detection models of currency crises in Indonesia based on inflation and interest rates indicators. J Phys Conf Ser. 2020;1563(1).

[22] Prasasti BA, Sugiyanto S, Subanti S. Early Detection Of Currency Crisis In Indonesia Based On Jci Indicator Using A Combination Of Volatility And Markov Switching Models. J Indones Sos Teknol. 2023;4(3):382–91.

[23] Sugiyanto, Slamet I, Zukhronah E, Subanti S, Sulandari W. Early detection of currency crisis in Indonesia using real interest rate on deposits. AIP Conf Proc. 2019;2202(May).

[24] Adams J, Metwally A. Identifying currency crises indicators: the case of Egypt. African J Econ Manag Stud. 2019;10(2):241–59.

[25] Mohana Rao B, Padhi P. Identifying the Early Warnings of Currency Crisis in India. Foreign Trade Rev. 2019;54(4):269–99.

[26] Davari M, Hasannejad M, Fadaeinejad ME. Presenting a model for predicting currency crises in Iran. J Financ Manag Perspect. 2022;12(37):147–73.

[27] Abdelsalam MAM, Abdel-Latif H. An optimal early warning system for currency crises under model uncertainty. Cent Bank Rev. 2020;20(3):99–107.

[28] Ha D, Nguyen P, Nguyen DK, Sensoy A. Early warning systems for currency and systemic banking crises in Vietnam. Post-Communist Econ [Internet]. 2022;34(3):350–75. Available from: https://doi.org/10.1080/14631377.2021.1965362

[29] Poyraz G. Modelling an early warning system for currency crises: a dynamic panel probit model. Pressacademia. 2019;8(3):181–7.

[30] Farzin F, Googerdchian A, Saffari B. Anticipation of Currency Crisis in Iran Economy with the Use of an Early Warning System. Iran Econ Rev [Internet]. 2021;25(1):69–83. Available from: https://ier.ut.ac.ir/article_81861.html%0Ahttps://ier.ut.ac.ir/article_81861_01a7d2df59a63e35aa0b198d8e988ad1.pdf

[31] Altunöz U. The predictability of the financial crisis with the Probit Model, Logit Model and signal approach: The case of Turkey. IBANESS Congr Ser Econ Bus Manag. 2019;(October).

[32] Fouliard J, Howell MJ, Rey H. Answering the Queen: Machine Learning and Financial Crises. SSRN Electron J. 2021;

[33] Bluwstein K, Buckmann M, Joseph A, Kapadia S, Şimşek Ö. Credit growth, the yield curve and financial crisis prediction: Evidence from a machine learning approach. Vol. 145, Journal of International Economics. 2023.

[34] Ashraf S, G. S. Félix E, Serrasqueiro Z. Do Traditional Financial Distress Prediction Models Predict the Early Warning Signs of Financial Distress? J Risk Financ Manag. 2019;12(2).

[35] Dastkhan H. Network-based early warning system to predict financial crisis. Int J Financ Econ. 2021;26(1):594–616.

[36] Naski L. Leena Naski EARLY WARNING INDICATORS OF THE GLOBAL. 2020;

[37] Feixiong-Ma, Yingying-Zhou, Xiaoyan-Mo, Yiwei-Xia. The Establishment of a Financial Crisis Early Warning System for Domestic Listed Companies Based on Two Neural Network Models in the Context of COVID-19. Math Probl Eng. 2020;2020.

[38] Guo H. The design of early warning software systems for financial crises in high-tech businesses using fusion models in the context of sustainable economic growth. PeerJ Comput Sci. 2023;9.

Al-Kitab Journal for Pure Sciences (2025); 9(2):20-33.
https://doi.org/10.32441/kjps.09.02.p2

Al-Kitab Journal for Pure Sciences
ISSN: 2617-1260 (print), 2617-8141(online)

https://isnra.net/index.php/kjps

An Investigation of the Magnetic and Structural Characteristics of Li-Ni ferrite nanoparticles

Ebtihal G. Khidher

Department of Physics, College of Education for Pure Sciences, University of Kirkuk, Iraq

Corresponding Author: e.gh.abbosh@uokirkuk.edu.iq

Citation: Khidher EG. An Investigation of the Magnetic and Structural Characteristics of Li-Ni ferrite nanoparticles. Al-Kitab J. Pure Sci. [Internet]. 2025 Apr. 13;9(2):20-33. DOI: https://doi.org/10.32441/kjps.09.02.p2.

Keywords: Crystallite Size, Spine1 Ferrites, Sol-Gel Auto-Combustion, Saturation Magnetization.

Received	16 Jan.	2025
Accepted	27 Feb.	2025
Available online	13 Apr.	2025

Abstract:

Nanoparticles of Li-Ni ferrite ($LiNi_{0.5}Fe_2O_4$) were synthesized through the sol-gel auto combustion method, employing lithium nitrate, nickel nitrate, and ferric nitrate as precursors, with citric acid acting as a chelating agent. The samples were annealed at temperatures (as-burnt, from 400 to 800 °C). The impact of various calcination temperatures on the crystalline structure and magnetic characteristics of the $LiNi_{0.5}Fe_2O_4$ nanoparticles was meticulously investigated through X-ray diffraction (XRD) and a vibrating sample magnetometer (VSM).

From XRD analysis, crystallite size D was determined to be the most intense (311) peak using Scherrer's formula. An increase in crystallite size was observed with higher annealing temperatures in the range of 28.50-41.345 nm, while coercivity, with a range 47.9-154.5 Oe, showed an initial rise before decreasing as crystallite size grew. Variations in saturation magnetization (range 6.23-8.02 emu/g) and lattice constant (range 8.291-8.295 °A) displayed a similar trend, decreasing at 400 °C and 600 °C but increasing at 800 °C.

Keywords: Crystallite Size, Spine Ferrites, Sol-Gel; Auto-Combustion, Saturation Magnetization.

دراسة الخصائص المغناطيسية والتركيبية لجسيمات النانوية *Li-Ni* الفراتية

ابتهال غفران خضر

قسم الفيزياء، كلية التربية للعلوم الصرفة، جامعة كركوك، العراق
e.gh.abbosh@uokirkuk.edu.iq

الخلاصة:

تم تحضير الجسيمات النانوية من فيرايت الليثيوم-نيكل ($LiNi_{0.5}Fe_2O_4$) باستخدام تقنية السول-جيل مع الاحتراق الذاتي، حيث استُخدمت نترات الليثيوم، نترات النيكل، ونترات الحديديك كمواد أولية، وتم استخدام حمض الستريك كعامل مخلب. تم تلدين العينات عند درجات حرارة مختلفة (عند الحرق، من ٤٠٠ إلى ٨٠٠ درجة مئوية). تمت دراسة تأثير درجات حرارة التكليس بشكل منهجي على التركيب البلوري والخصائص المغناطيسية لجسيمات $LiNi_{0.5}Fe_2O_4$ النانوية باستخدام حيود الأشعة السينية (*XRD*) ومقياس مغناطيسية العينة الاهتزازي (*VSM*). من تحليل *XRD*، تم تحديد حجم البلورة *D* لأشد قمة (٣١١) باستخدام معادلة شيرر. لوحظت زيادة في حجم البلورات مع ارتفاع درجات حرارة التلدين ضمن نطاق ٢٨,٥٠-٤١,٣٤٥ نانومتر. أظهرت القوة القسرية (٤٧,٩-١٥٤,٥ *Oe*) زيادة أولية ثم انخفاضًا مع زيادة حجم البلورات. كما أظهرت التغيرات في المغناطيسية المشبعة (٦,٢٣-٨,٠٢ *emu/g*) والثابت الشبكي (٨,٢٩١-٨,٢٩٥ *A°*) اتجاهًا مشابهًا، حيث انخفضت عند ٤٠٠°م و٦٠٠°م، لكنها ارتفعت عند ٨٠٠ °م.

الكلمات المفتاحية: حجم البلورات، الفيرايت السبينل، الاحتراق الذاتي؛ السول-جيل، المغناطيسية المشبعة.

1. Introduction:

Ferrite nanoparticles are a significant category of magnetic nanoparticles that have garnered substantial interest due to their extensive uses across many disciplines, from biomedical to industrial [1]. Ferrites have unique magnetic properties, such as the ability to retain magnetism at high temperatures, making them ideal for use in electric motors, transformers, and many other applications [2,3]. Spinel lithium ferrites are characterized by their diverse properties, which can be ascribed to their capacity to accommodate cations of various transition metals inside their lattice structure. Therefore, their structural, optical, magnetic, and electrical properties may vary. Specifically, the compound $Li_{0.5}Fe_{2.5}O_4$ exhibits exceptional features, including high saturation magnetization, low dielectric loss, and a square hysteresis loop, making it a promising magnetic material for use in hybrid nano photocatalysts]4,5[. The rapid progress of wireless communication in the twenty-first century may replace expensive magnetic materials in the fields of antennas and rechargeable lithium-ion batteries.[6] because of its economical price, high Curie temperature, and elevated magnetic permeability.

Ferrite nanoparticles are metal oxides characterised by a spinel structure with the general formula AB_2O_4, wherein A and B represent metallic cations located at distinct crystallographi

csites: tetrahedral (A site) and octahedral (B site)[7]The cations in both places are coordinated to oxygen atoms in tetrahedral and octahedral sites, respectively, as illustrated in **Figure 1**.[8]

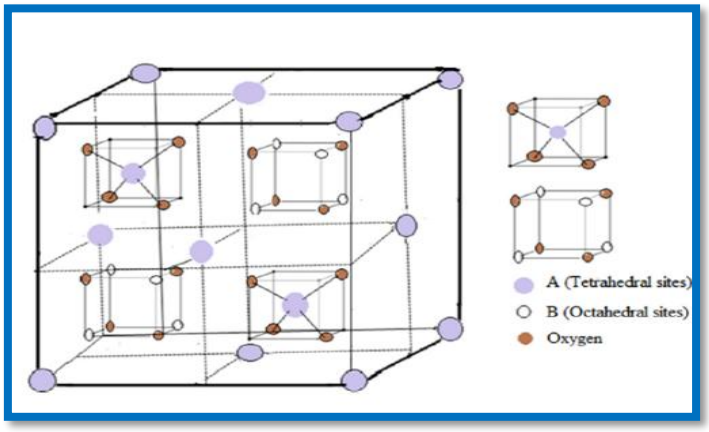

Figure1. Spinel ferrite structure showing tetrahedral and octahedral sites

For a compound to be classified as ferrite, it must contain Fe^{3+} in its chemical formula [9]. Spinel-phase nanocrystalline ferrites $Li_{0.5-0.5x}M_xFe_{2.5-0.5x}O_4$ (where M represents Mg^{2+}, Ni^{2+}, Fe^{2+}, etc) represent one of the most prominent families of nanomaterials due to their wide range of applications, including nano ferrofluids, nanomedical devices, photocatalysts, magnetic devices, microwave devices, and gas sensors [10,11]. The ferrimagnetism of spinel ferrite is attributed to the resultant magnetic moment arising from the antiparallel alignment of magnetic moments at the A and B sites, that is, $\eta_{th} = |\eta_A - \eta_B|$. The replacement of metal cations significantly influences the microstructure and electromagnetic characteristics of lithium ferrite.

Gandomi F. et al. [12], prepared $Li_{0.5}Fe_{2.5}O_4$, $Li\,Mg_{0.5}Fe_2O_4$ and $Li\,Ni_{0.5}Fe_2O_4$ through sol-gel outo-combustion process. The doping of Ni or Mg ions reduces the remanent magnetization (Mr) and saturation magnetization (Ms) of the $LiNi_{0.5}Fe_2O_4$ catalyst. M.F. Warsi et al.[13] prepared praseodymium-substituted nano-crystalline Li-Ni spinel ferrites with different Pr^{3+} contents by micro-emulsion technique. The saturation magnetization (MS) of 41 emu/g and coercivity (HC) of 156.9 Oe for $LiNi_{0.5}Fe_2O_4$ were enhanced through the incorporation of rare earth Pr^{3+} cations.

Innovative methods such as radiofrequency inductively coupled plasma, chemical hydrothermal processes, electrochemical techniques, microwave or non-chemical processing, inert gas condensation, sol-gel auto-combustion, and mechanical milling have been developed for the synthesis of spinel ferrite nanoparticles [14]. The sol–gel auto-combustion process is a prevalent option from this list, utilized in synthesizing materials with various metastable structures, even at very low temperatures, due to its ability to produce products with excellent chemical uniformity. This technology enables the manipulation of physical attributes, including

particle size, shape, and pore structure, by altering the preparation conditions [15]. In addition to the preparation method and metal ion doping, the primary factor affecting the microstructure and performance of ferrite is the sintering temperature.

J. Song et al.[16] investigated the impact of thermal treatment on $Li_{0.35}Nio._3Fe_{2.35}O_4$ using the sol-gel auto-combustion technique. A significant increase in grain size was observed with the rise in annealing temperature. As for coercivity, the value initially increased and subsequently decreased significantly from 115 to 37 Oe with rising annealing temperature. This behavior is attributed to the grain size at 600°C approaching the transitional size between single-domain and multi-domain magnetic regions. R. Paul. Singh et al. [17], prepared magnesium ferrite ($MgFe_2O_4$) nanoparticles using the sol-gel technique, with the samples calcined at different temperatures. The results revealed a significant impact of calcination temperature on the structural and magnetic properties of the nanoparticles. An increase in lattice constant and crystallite size was observed with rising calcination temperature, while coercivity decreased due to the reduction of the pinning effect at the grain boundaries as the calcination temperature increased. According to reports, high sintering temperatures above 1050 °C cause lithium and oxygen to volatilize, changing the stoichiometry of lithium ferrite and so compromising its electrical and magnetic properties [18], significantly reducing the practical use of lithium ferrite.

The structural and magnetic characteristics of $LiNi_{0.5}\ Fe_2O_4$ made using the sol-gel auto-combustion process were investigated in this work. It investigates how temperature changes between 200°C and 800°C affect both its magnetic and crystalline structures.

2. Materials and Methods:

2.1 Material: $LiNi_{0.5}Fe_2O_4$ magnetic nano-powder was prepared using the Sol-Gel Auto-Combustion (SGAC) technique. Lithium nitrate $LiNO_3$, ferric nitrate $Fe\ (NO_3)_3{\cdot}9H_2O$, nickel nitrate $Ni\ (NO_3)_2{\cdot}6H_2O$ citric acid $C_6H_8O_7$ and ammonia with mass 5.745083 g/mol of Lithium nitrate 12.11223 g/mol of Nickel nitrate, 67.3075 g/mol of ferric nitrate and 19.2124 g/mol of citric acid were used as precursors to prepare LiNi0.5Fe2O4 magnetic nano-powders.

2.2 Synthesis $LiNi_{0.5}Fe_2O_4$ magnetic nano-powders: Ferric nitrate, nickel nitrate, and lithium nitrate were dissolved in deionized water at the molar ratios of 2:0.5:1, following the adjustment of the metal nitrate/citric acid ratio at room temperature. Liquid ammonia was added to the mixture to neutralize it to a pH of 7. After that, the neutralized solution was heated to 100°C on a hot plate while being continuously stirred by a magnetic device to evaporate it completely. The solution thickened as the water evaporated, eventually producing an incredibly viscous gel. The gel self-ignited when the temperature was raised to 200°C. The dried gel produced a thick, fluffy powder with a large surface area by continuing a self-sustaining

combustion reaction until it was completely burned. The as-burnt powder was subsequently calcined at various temperatures (400–800°C) for a duration of 3 hours. Experimental observations indicate that all samples exhibited combustible behavior, consistently burning entirely to produce a fine powder.

2.3 Characterization: Phase identification of the calcined powders was performed using a D/MAX-2500 X-ray diffraction (XRD) apparatus with Cu Ka radiation (λ = 1.5405 Å). The samples' magnetic properties were evaluated using a Vibrating Sample Magnetometer (VSM) at room temperature.

3. Results and Discussion

3.1 XRD analysis: The X-ray diffraction for $LiNi_{0.5}Fe_2O_4$ nano particles at various temperatures of calcination (200, 400, 600, and 800 °C) is depicted in **Figure 2**.

The results indicate that with the elevation of calcination temperature, all peaks increase concurrently, leading to narrower and sharper diffraction peaks. This signifies that the increase in particle size within the nucleus leads to a rise in both crystallization density and crystal size ratio.

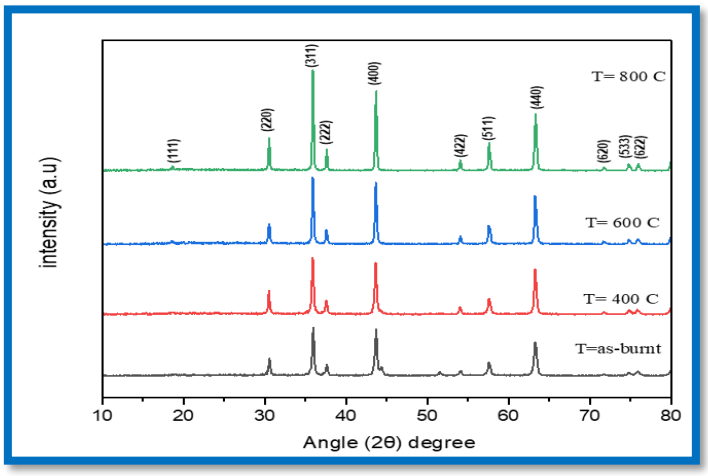

Figure 2. XRD patterns of $LiNi_{0.5}Fe_2O_4$ nanoparticles at various temperatures of calcination

The crystallite size (D) of Li-Ni ferrite, calcined at different temperatures, was determined from the XRD line width of the (311) peak (the greatest intensity peak) using Scherrer's equation **[19]**.

$$D = \frac{k\lambda}{\beta cos\theta} \qquad (1)$$

Where $k = 0.94$ is Scherrer's constant, $\lambda = 1.54$ °A represents the X-ray wavelength, while β denotes the full width at half maximum (FWHM) of the diffraction peak, and θ is the Bragg's angle of diffraction.

Table (1): $LiNi_{0.5}Fe_2O_4$ nanoparticles structural characteristics for as-burnt and different calcination temperatures

Sample	T (°C)	2θ	FWHM	D(nm)	d-spacing (Å)	a (°A)	ρ_x (g/cm3)	LA(°A)	LB (°A)
LiNi0.5Fe2O4	As-burnt	35.98	0.293	28.5003	2.5007	8.294	4.934	3.5914	2.9323
	400	35.91	0.280	29.8249	2.5002	8.292	4.937	3.5907	2.9318
	600	35.94	0.239	34.9443	2.4999	8.291	4.939	3.5902	2.9313
	800	35.94	0.202	41.3458	2.5011	8.295	4.932	3.5919	2.9328

The calcination temperature significantly influenced the FWHM and crystallite size, as shown in **Table 1** and **Figure 3**. The crystallite size (D) is greatest at 800 °C due to the minimum FWHM value, resulting in enhanced crystallinity of the sample. The value rises from 28.50 nm to 41.34 nm with an increase in an annealing temperature.

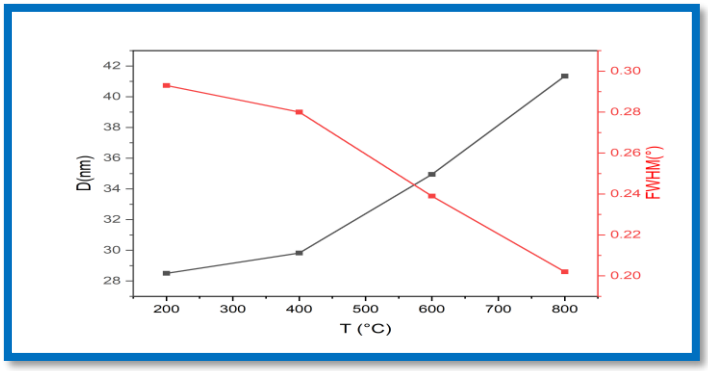

Figure 3. Variation of full width at half maximum (FWHM) and crystallite size as a function of calcination temperature.

The lattice constant (a) exhibits an increase from 8.291 Å to 8.295 Å at calcination temperatures reaching 800 °C, as determined by the following formula **]20[**

$$a = d_{hkl}\sqrt{h^2 + k^2 + l^2} \qquad (2)$$

Where d represents the spacing between the planes, and (h, k, l) denote the Miller indices. A small increase in the lattice constant can be elucidated using Vegard's law, based on the ionic radii of the substituent ions. The substitution of the smaller Fe^{2+} ion (0.64 Å) with the bigger Ni^{2+} ion (0.69 Å) at the octahedral sites is expected to promote an expansion of the unit cell, hence increasing the lattice constant.

X-ray density ρ_x is crucial in evaluating the electromagnetic properties of ferrites, as it is directly linked to the material's crystalline structure and atomic arrangement. These factors significantly influence its electromagnetic characteristics, such as permeability. The equation utilized to find out the X-ray density ρ_x of the samples produced is as **[21]**:

$$\rho_x = \frac{ZM}{Na^3} \qquad (3)$$

Z denotes the number of molecules per unit cell, which is 8 for the spinel structure; M signifies the molecular weight of the corresponding composition; N represents Avogadro's number; and a indicates the lattice constant of the samples. The density (ρ_x) of Li-Ni ferrite ranged between 4.932 and 4.934 g/cm³. The X-ray density was seen to increase with temperature at 400°C and 600°C, then declining at higher temperatures due to its dependence on the lattice parameter a, as shown in **Figure 4**.

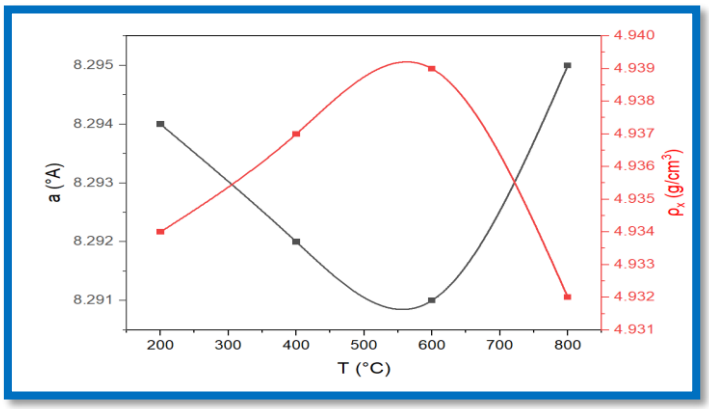

Figure 4. Variation of lattice parameter and X-ray density of the Li-Ni ferrite at various temperatures of calcination

The hopping length is the distance between magnetic ions situated in the tetrahedral (A) and octahedral (B) sites, and it may be calculated using the formulas presented below**[22]**:

$$L_A = 0.25a\sqrt{3} \quad (4)$$

$$L_B = 0.25a\sqrt{2} \quad (5)$$

An alteration in the hopping length on both sides was noticed with an increase in calcination temperature.

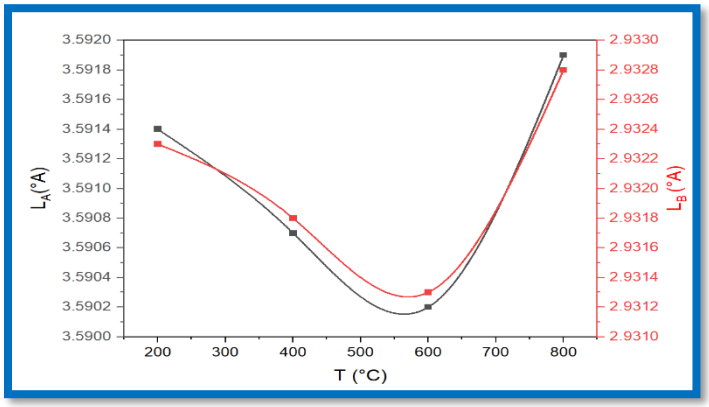

Figure 5. Influence of calcination temperature on the hopping lengths L_A and L_B for Li-Ni ferrite.

As shown in **Figure 5** and **Table 1**, the hopping length L_A is greater than the hopping length L_B , and both vary with temperature changes. This is attributed to the spatial configuration of the tetrahedral sites, which are less constrained compared to the octahedral sites. As the temperature increases, ions such as Fe^{3+} and Ni^{2+} gain kinetic energy, facilitating shifts between

these sites. The lattice parameters are influenced by the reordering of ions, affecting the hopping distances. Furthermore, synthesis conditions, including the annealing process, contribute to the structural arrangement of ions, which in turn impacts the resulting hopping lengths and the associated magnetic properties of the ferrite material.

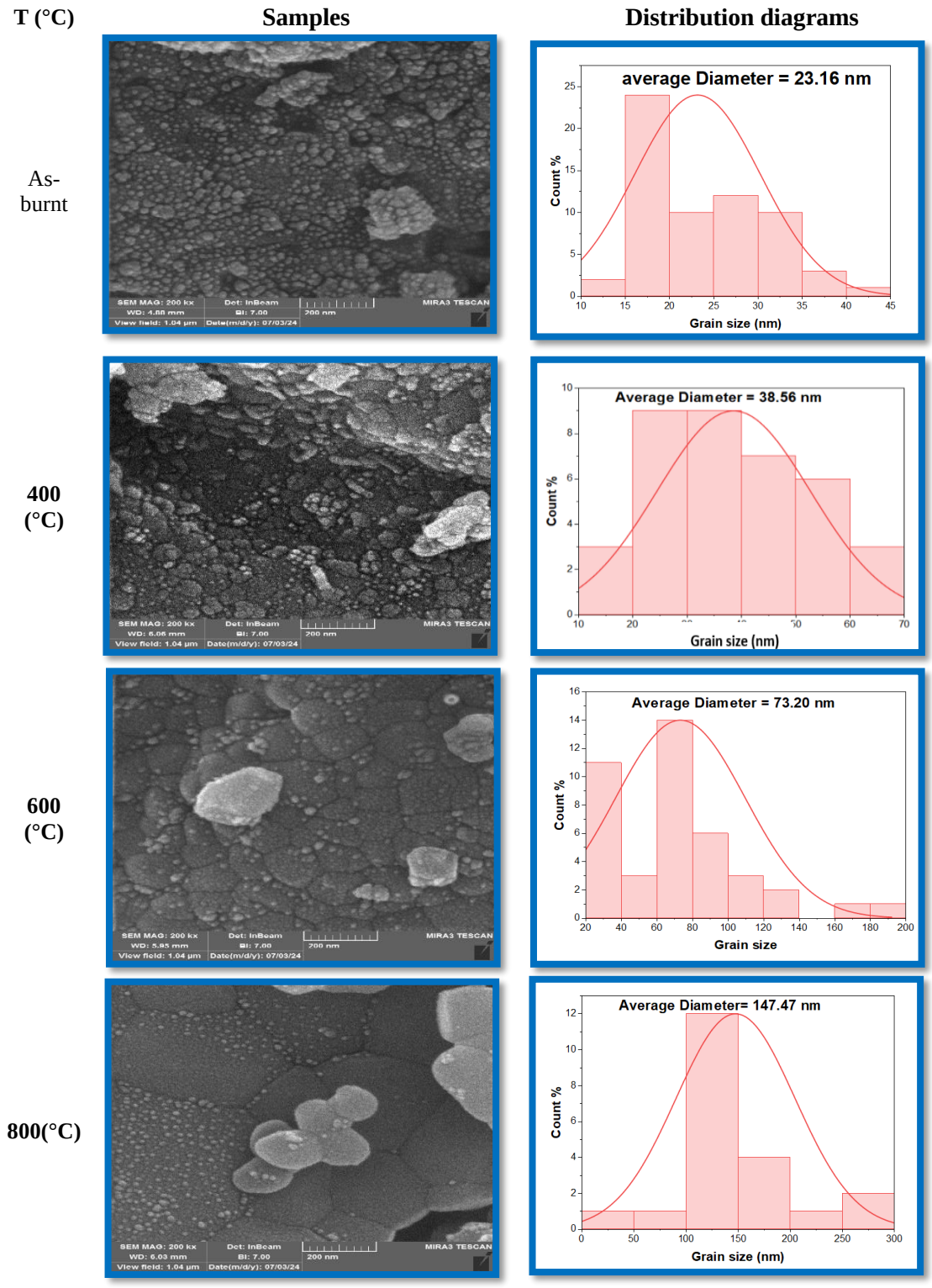

Figure 6. FE-SEM images of $LiNi_{0.5}Fe_2O_4$ nanoparticles at different temperatures.

3.2 FE-SEM: FE-SEM was used to examine the microstructures of the Li-Ni ferrite samples that were synthesized at different calcination temperatures (as-burnt, 400, 600, and 800 °C). The shape of ferrite samples varies from irregular hexagons to spherical aggregates, as seen in **Figure 6**. According to the particle size distribution diagrams shown in **Figure 6** at various calcination temperatures, the samples' grain sizes range from 23.16 nm to 147.47 nm, which is much larger than the values found using Scherrer's formula from XRD analysis, see **Figure 7**. This could be because of lattice strain and molecular structural disorder brought on by the various ionic radii and/or clustering of the nanoparticles. As a result, the XRD approach produces smaller sizes and has stricter criteria. Sintering frequently reduces strain and lattice defects. However, it will result in increased crystallite accumulation, which will lead to an increase in grain size. This is consistent with the pattern of $LiNi_{0.5}Fe_2O_4$ powder grain size at different calcination temperatures.**[23]**

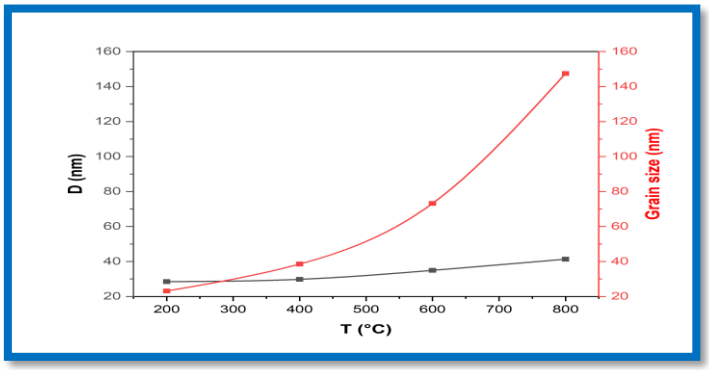

Figure 7. Variation of crystallite size determined by X-ray and grain size of the Li-Ni ferrite at various temperatures of calcination

Table 2: Magnetic properties of $LiNi_{0.5}Fe_2O_4$ nanoparticles for as-burnt and different calcination temperatures.

T(°C)	Ms (emu/g)	Mr (emu/g)	Hc (Oe)	Mr/Ms	*k*(erg/cm3)	$\eta_B(\mu B)$
As-burnt	7.99	2.39	154.3	0.299	1284.2	0.303
400	6.74	2.13	154.5	0.316	1084.7	0.255
600	6.23	1.89	145.9	0.303	946.8	0.236
800	8.02	2.4	47.9	0.299	413.5	0.304

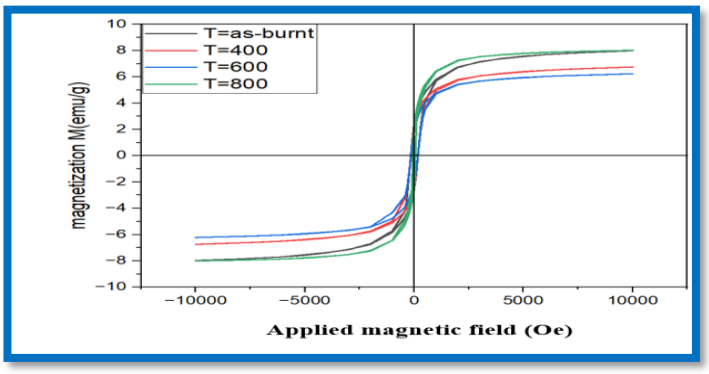

Figure 8. LiNi0.5Fe2O4 nanoparticles hysteresis curves for as-burnt and different calcination temperatures.

3.3 VSM: The M-H loop has been constructed to examine the magnetic characteristics of as-burnt and annealed $LiNi_{0.5}$ Fe_2O_4 nanoparticles. The maximum applied magnetic field was 10 kOe, and measurements were conducted at room temperature. The hysteresis loop provides many magnetic properties, including saturation magnetization (Ms), remanence (Mr), and coercivity (Hc), as shown in **Table 2**.

All samples exhibit soft magnetic characteristics, and the magnetic hysteresis loops get smaller and elongated with rising annealing temperatures, as illustrated in **Figure 8**. The reason is the replacement of the less magnetic Ni^{2+} ions with the magnetic Fe^{3+} ions in the octahedral sublattice of the ferrites, or the occurrence of vacancy crowding in the resulting structure. In general, Extrinsic factors (preparation process, structure, and density) and intrinsic factors (lattice parameter, lattice strain, and cation distribution) significantly affect the material's magnetic behavior.**[24,25]**

The vector sum of a material's magnetic moments per unit mass or volume when the material is magnetized to saturation at a particular temperature while subjected to an external magnetic field is known as saturation magnetization. Neel's model and the cation distribution can be used to explain the samples' magnetism.

This hypothesis posits that exchange interactions are responsible for the magnetic moment in spinel ferrites due to the metal cations located at the A and B sites **[24]**. Magnetic moment (η_B) can be expressed as

$$\eta_B = [M_w \times M_s]/5585 \qquad (6)$$

Where M_w is the molecular weight of the sample, M_s is the saturation magnetization of the sample, and 5585 is the magnetic factor. A decreasing trend is observed in the saturation magnetization and magnetic moment of the nanoparticles at 400 and 600 °C. The decrease in magnetic moment is attributed to the diminished magnetic moments of the A-site (tetrahedral) and B-site (octahedral) lattices, as well as the weakened A-B interactions. The sintering temperature alters the composition of the metal contents. Ni^{2+} and Li^{+} ions predominantly occupy the octahedral sites, with a minority transitioning to the tetrahedral sites as temperature rises **[15]**. The replacement of Fe^{3+} (5μB) with non-magnetic lithium Li^{+} (0μB) leads to a reduction in saturation magnetization at 400 and 600°C; however, at 800°C, the arrangement of Li, Ni, and Fe ions approaches a mixed ferrite state, resulting in an increase of Fe^{3+} (5 μB) in the octahedral position and an elevation of Ni^{2+} (2 μB) in the tetrahedral position, which enhances saturation magnetization. The variations in lattice characteristics and saturation magnetization with respect to annealing temperature are almost the same. **Figure 9** illustrates

the correlation between lattice characteristics and saturation magnetization as a function of calcination temperature.

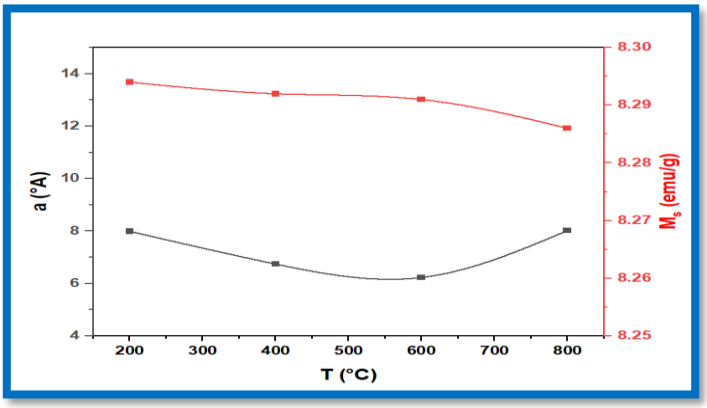

Figure 9. Correlation between lattice parameters (a) and saturation magnetization (Ms) of LiNi0.5Fe2O4 nanoparticles as a function of calcination temperature (T).

Remanent (Mr), usually depends on (M_s), thus by decreasing the saturation magnetization in the prepared samples, remanent magnetization decreases.

Figure 10 illustrates the variation in $LiNi_{0.5}Fe_2O_4$ ferrites' average crystallite size (D) and coercivity (Hc) with respect to calcination temperature (T). The coercivity initially rises and subsequently declines as the crystallite size grows **[26]**. This variation of Hc with crystallite size can be elucidated using the principles of crystal size, single-domain or multi-domain structures, and anisotropy. The anisotropy value was determined using the following equation.:

$$k = \frac{H_c \times M_s}{0.96} \qquad (7)$$

The results are presented in **Table 2**.

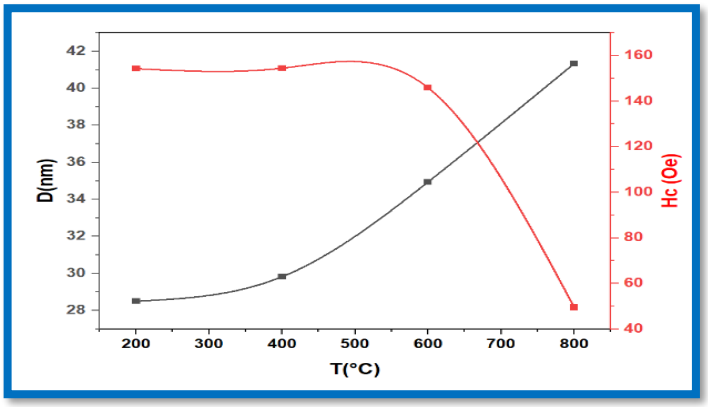

Figure 10. The fluctuation in average crystallite size (D) and coercivity (Hc) of $LiNi_{0.5}Fe_2O_4$ ferrites as a function of calcination temperature (T)

The variation in the anisotropy constant is ascribed to the shape impact of samples manufactured at varying calcination temperatures **[27]**. The hysteresis loops are used to calculate the remanence to saturation magnetization ratio (Mr/Ms) displayed in **Table 2**. The low number also suggests that the ferrites include several domains. According to the results of

this investigation, coercivity peaks at about 400 °C, which is the key temperature at which ferrites change from single-domain to multi-domain behavior.

4. Conclusions

Nano particle Li-Ni ferrites at various calcination temperatures are prepared using the sol-gel auto-combustion technique. The crystallite size D was increased with the calcination temperature up to 800 °C, which was also supported by FE-SEM studies. A maximum saturation magnetization of about 8.02 (emu/g) with a crystallite size of 41.34 nm was obtained at 800 °C, where the variation is almost the same.

5. References

[1] Mullick S. "Ferrites": Synthesis, Structure, Properties and Applications. In 2021. p. 1–61. Available from: https://www.mrforum.com/product/9781644901595-1

[2] Haspers JM. Ferrites: Their properties and applications. In: Modern Materials. Elsevier; 1962. p. 259–341.

[3] Abdulwahab KO, Khan MM, Jennings JR. Ferrites and ferrite-based composites for energy conversion and storage applications. Critical Reviews in Solid State and Materials Sciences [Internet]. 2024 Sep 2;49(5):807–55. Available from: https://www.tandfonline.com/doi/full/10.1080/10408436.2023.2272963

[4] George M, Nair SS, John AM, Joy PA, Anantharaman MR. Structural, magnetic and electrical properties of the sol-gel prepared Li0. 5Fe2. 5O4 fine particles. J Phys D Appl Phys. 2006;39(5):900.

[5] Ahmad M, Shahid M, Alanazi YM, ur Rehman A, Asif M, Dunnill CW. Lithium ferrite (Li0. 5Fe2. 5O4): synthesis, structural, morphological and magnetic evaluation for storage devices. journal of materials research and technology. 2022;18:3386–95.

[6] Zeng H, Tao T, Wu Y, Qi W, Kuang C, Zhou S, et al. Lithium ferrite (Li 0.5 Fe 2.5 O 4) nanoparticles as anodes for lithium ion batteries. RSC Adv. 2014;4(44):23145–8.

[7] Salih SJ, Mahmood WM. Review on magnetic spinel ferrite (MFe2O4) nanoparticles: From synthesis to application. Vol. 9, Heliyon. Elsevier Ltd; 2023.

[8] Issa B, Obaidat IM, Albiss BA, Haik Y. Magnetic nanoparticles: surface effects and properties related to biomedicine applications. Int J Mol Sci. 2013;14(11):21266–305.

[9] Kefeni KK, Msagati TAM, Mamba BB. Ferrite nanoparticles: synthesis, characterisation and applications in electronic device. Materials Science and Engineering: B. 2017;215:37–55.

[10] Gabal MA, El-Shishtawy RM, Al Angari YM. Structural and magnetic properties of nano-crystalline NiZn ferrites synthesized using egg-white precursor. J Magn Magn Mater. 2012;324(14).

[11] Widatallah HM, Johnson C, Gismelseed AM, Al-Omari IA, Stewart SJ, Al-Harthi SH, et al. Structural and magnetic studies of nanocrystalline Mg-doped Li0. 5Fe2. 5O4 particles prepared by mechanical milling. J Phys D Appl Phys. 2008;41(16):165006.

[12] Gandomi F, Peymani-Motlagh SM, Rostami M, Sobhani-Nasab A, Fasihi-Ramandi M, Eghbali-Arani M, et al. Simple synthesis and characterization of Li 0.5 Fe 2.5 O 4, LiMg 0.5 Fe 2 O 4 and LiNi 0.5 Fe 2 O 4, and investigation of their photocatalytic and anticancer properties on hela cells line. Journal of Materials Science: Materials in Electronics. 2019;30:19691–702.

[13] Warsi MF, Gilani ZAA, Al-Khalli NF, Sarfraz M, Khan MAA, Anjum MNN, et al. New LiNi0.5PrxFe2−xO4 nanocrystallites: Synthesis via low cost route for fabrication of smart advanced technological devices. Ceram Int. 2017 Dec 1;43(17):14807–12.

[14] Kaur N, Kaur M. Comparative studies on impact of synthesis methods on structural and magnetic properties of magnesium ferrite nanoparticles, Processing and Application of Ceramics, 8 (2014) 137-143.

[15] Sutka A, Mezinskis G. Sol-gel auto-combustion synthesis of spinel-type ferrite nanomaterials. Front Mater Sci. 2012;6:128–41.

[16] Song J, Wang Z, Gao Y. Effect of heat treatment on structural and magnetic properties of Li–Ni ferrite prepared via sol–gel auto-combustion method. Journal of Materials Science: Materials in Electronics. 2021;32(13):17105–14.

[17] Singh RP, Venkataraju C. Effect of calcinations on the structural and magnetic properties of magnesium ferrite nanoparticles prepared by sol gel method. Chinese journal of physics. 2018;56(5):2218–25.

[18] Surzhikov AP, Malyshev A V, Lysenko EN, Vlasov VA, Sokolovskiy AN. Structural, electromagnetic, and dielectric properties of lithium-zinc ferrite ceramics sintered by pulsed electron beam heating. Ceram Int. 2017;43(13):9778–82.

[19] Ridha SMA. X-ray studies and electrical properties of the zinc-substituted copper nanoferrite synthesized by sol-gel method. Int J Compos Mater. 2015;5(6):195–201.

[20] Mohammad AM, Ridha SMA, Mubarak TH. Dielectric properties of Cr-substituted cobalt ferrite nanoparticles synthesis by citrate-gel auto combustion method. Int J Appl Eng Res. 2018;13(8):6026–35.

[21] Ibrahim MG, Khalf AZ, Ridha SMA. Characterization of Al-Substituted Ni-Zn Ferrites by XRD and FTIR Techniques. Journal of Media,Culture and Communication. 2024 Aug 26;(45):24–39.

[22] Mahmood HN, Razeg KH, Ridha SMA. Study and Analysis of the Structural and Magnetic Properties of Nickel Iron Substituted with Different Proportions of Cerium. Pakistan Journal of Medical & Health Sciences. 2023;17(02):706.

[23] Jumaa JS, Saeed SR, Mohammad AM. Synthesize CoFe2O4/SiO2 nanoparticles and investigate their magnetic, dielectric, and structural characteristics. Passer Journal of Basic and Applied Sciences. 2023;5(2):278–89.

[24] Hassan S, Ahmad M, ur Rehman A, Iqbal MW, Shaukat SF, Abd-Rabboh HSM. Structural, magnetic and electrochemical properties of Al-substituted Ni ferrites for energy storage devices. J Energy Storage. 2022;55:105320.

[25] Kumar Das M, Dey A, Ferdaus J, Chandra Das B, Ahad A, Azizul Hoque M, et al. Investigation of the structural, magnetic, and dielectric properties of Al-substituted Li-Ni-Mn ferrites. Results Phys. 2024 Mar 1;58.

[26] Ramay SM, Saleem M, Atiq S, Siddiqi SA, Naseem S, Sabieh Anwar M. Influence of temperature on structural and magnetic properties of Co 0· 5 Mn 0· 5 Fe 2 O 4 ferrites. Bulletin of Materials Science. 2011;34:1415–9.

[27] Patil RP, Hankare PP, Garadkar KM, Sasikala R. Effect of sintering temperature on structural, magnetic properties of lithium chromium ferrite. J Alloys Compd. 2012;523:66–71.

Al-Kitab Journal for Pure Sciences (2025); 9(2):34-42.
https://doi.org/10.32441/kjps.09.02.p3

Al-Kitab Journal for Pure Sciences
ISSN: 2617-1260 (print), 2617-8141(online)

https://isnra.net/index.php/kjps

Assessing the Radioactivity of Samples Taken during a Dust Storm in the Iraqi City of Hilla

Rawaa M. Obaid[1], Inaam H. Kadhim[2*]

[1]Department of Physics, College of Science, University of Babylon, Iraq.
[2]Department of Physics, College of Education for Pure Science, University of Babylon, Iraq.

*Corresponding Author: pure.inaam.hani@uobabylon.edu.iq

Citation: Obaid RM, Kadhim IN. Assessing the Radioactivity of Samples Taken during a Dust Storm in the Iraqi City of Hilla. Al-Kitab J. Pure Sci. [Internet]. 2025 Apr. 27;9(2):34-42. DOI: https://doi.org/10.32441/kjps.09.02.p3.

Keywords: Specific Activity, Dust Storm, Absorbed Dose, Gamma Radiation, Nai (Tl) Detector.

Article History

Received	23	Aug.	2024
Accepted	16	Oct.	2024
Available online	26	Apr.	2025

Abstract:

The research aims to investigate the distinguishing behaviors and risk indicators in samples of dust storms in Hilla city, Iraq. NaI (Tl) detector was used for the measurements, along with spectrum analysis. The findings of the measurements of elements ^{238}U, ^{232}Th, and ^{40}K's specific activities in samples from dust storms ranged for ^{238}U from 9.2 ± 0.5 to 22.9 ± 0.8 (Bq/kg) at an average 16.92 ± 0.7 (Bq/kg), the range of ^{232}Th's specific activity was between 2.7 ± 0.2 to 11.41 ± 0.5 at the average6.5 ± 0.3 (Bq/kg), whereas the range for ^{40}K was 119.43 ± 2.2 to 174.92 ± 2.6 (Bq/kg) with mean150.34 ± 2.4 (Bq/kg). Furthermore, it is shown that the radium equivalent activity and absorbed dose in dust storm samples average 37.774 Bq/kg and 34.881(nGy/h), respectively, and the external hazard index was 0.102. In contrast, the average of the effective dose of samples was 0.022 mSv/y. The findings of the present study were compared with the global average, the levels were discovered to be within the advised limit according to UNSCEAR.

Keywords: Specific Activity, Dust Storm, Absorbed Dose, Gamma Radiation, Nai (Tl) Detector.

تقييم النشاط الإشعاعي للعينات المأخوذة أثناء العاصفة الغبارية في مدينة الحلة العراقية

رواد مزهر عبيد[1]، انعام هاني كاظم[2]*

[1]قسم الفيزياء، كلية العلوم، جامعة بابل، العراق
[2]*قسم الفيزياء، كلية التربية للعلوم الصرفة، جامعة بابل، العراق

[2]pure.inaam.hani@uobabylon.edu.iq ،[1]sci.rawaa.mizhir@uobabylon.edu.iq

الخلاصة:

يهدف البحث إلى دراسة السلوكيات المميزة ومؤشرات الخطورة في عينات العواصف الغبارية في مدينة الحلة بالعراق، وقد تم استخدام كاشف *NaI(Tl)* للقياسات، إلى جانب تحليل الطيف. وقد تراوحت نتائج قياسات النشاط النوعي للعناصر ^{40}K و^{232}Th و^{238}U في عينات العواصف الغبارية لليورانيوم- ٢٣٨ من ٩,٢ ± ٠,٥ إلى ٢٢,٩ ± ٠,٨ (بيكريل/كجم) بمتوسط ١٦,٩٢ ± ٠,٧ (بيكريل/كجم)، وكان نطاق النشاط النوعي للثوريوم- ٢٣٢ بين ٢,٧ ± ٠,٢ إلى ١١,٤١ ± ٠,٥ بمتوسط ٦,٥ ± ٠,٣ (بيكريل/كجم)، في حين كان نطاق النشاط النوعي للعنصر للبوتاسيوم-٤٠ من ١١٩,٤٣ ± ٢,٢ إلى ١٧٤,٩٢ ± ٢,٦ (بيكريل/كجم) بمتوسط ١٥٠,٣٤ ± ٢,٤ (بيكريل/كجم). علاوة على ذلك، تبين أن متوسط نشاط مكافئ الراديوم والجرعة الممتصة في عينات العواصف الغبارية يبلغ ٣٧,٧٧٤ بيكريل/كجم و ٣٤,٨٨١(*nGy/h*) على التوالي، وكان مؤشر الخطر الخارجي ٠,١٠٢. وعلى النقيض من ذلك، كان متوسط الجرعة الفعالة للعينات ٠,٠٢٢ ميكروسيفرت/سنة. تمت مقارنة نتائج الدراسة الحالية بالمتوسط العالمي، وتبين أن المستويات تقع ضمن الحد الموصى به وفقًا للجنة العلمية التابعة للأمم المتحدة لآثار الإشعاع الذري.

الكلمات المفتاحية: الفعالية النوعية، العاصفة الغبارية، الجرعة الممتصة، إشعاع جاما، كاشف *NaI(Tl)* .

1. Introduction:

The German Association for the Building and Construction Sector has warned that small dust particles in construction sites pose a great risk to health. Sand and dust storms are an important element of Earth's natural biogeochemical cycles, but they are also influenced by human activities such as climate change, inappropriate land management, and water waste. Thus, sand and dust storms contribute to climate change and air pollution [1]. The radiation originates from a variety of sources, both natural and artificial. These include both cosmic radiation and environmental radioactivity from naturally occurring radioactive materials. Naturally, radioactivity is widespread in the Earth's environment, mainly in various geological formations and their disintegration products [2]. The major natural radioactivity sources are the nuclides of very long half-lives that have existed since the Earth's formation, and these nuclides are produced via cosmic rays [3]. The natural radionuclides of concern are mainly uranium(^{238}U), thorium (^{232}Th), or their progenies and potassium (^{40}K) [4]. Long-term exposure to radioactivity and inhalation of radioactive nuclides have serious health effects, such as

cancerous disease. Nuclides' radioactive exposure can cause lung diseases, pancreatic, hepatic, bone, and kidney cancers, and leukemia. These diseases are caused by gamma-radiation, which is capable of traveling long distances through air to affect human beings **[5]**.

The distribution of radionuclides in the environment and their typical concentration levels in soil are of interest to many international studies to determine the levels of radioactivity in soil samples **[6-10]**. Numerous methods exist for uranium to enter the body, including drinking uranium-containing water, inhaling uranium-containing dust particles, or indirectly from nutrient-rich soil layers through the food chain **[11]**. The NaI(Tl) detectors have exceptional absorption efficiency because of the density of the crystal, whilst the detection systems based on these scintillators show high absorption efficiency for low-energy gamma ray detection due to the relatively high atomic number of iodine (Z = 53)**[12].**

There are currently no known baselines for the concentration of naturally occurring radioisotopes, and only a small number of studies on the radioactivity of soil samples in the areas under inquiry have been published. Furthermore, there have been reports of a few people of different ages who have died from cancer instances that have been documented in these areas. Therefore, the goal of this research is to examine the radioactive content of dust storm samples collected from various locations inside Hilla city during the storm. The purpose of the study was to determine whether radioactivity in the storm's dust was dangerous to people or not.

2. Area of Study

Hillah is the Babel provincial capital, which is located in central Iraq between latitudes 32° 28' 59.99" N and longitudes 44° 25' 59.99" E **[13]**. 5119 km^2 is that amount. Located on the Euphrates River, close to the historic city of Babel **[13]**. The physical arrangement of the states comprising the Babel Province is shown in **Figure 1**, along with the sites of sample research.

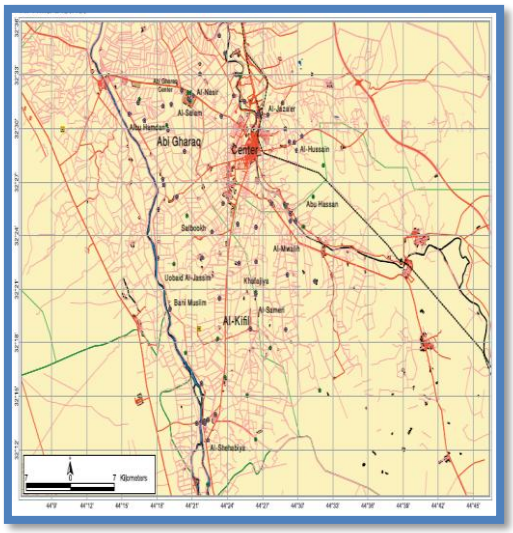

Figure 1: Study area's location on a map [13].

3. Nuclear Detection System:

Nine samples were taken from the dust storm that hit the city of Hillah in May 2022, where a deep container was placed from the beginning of the storm until its end on the roofs of the houses selected for the studied samples. After collecting the samples, they were transferred to the Advanced Nuclear Laboratory of the Physics Department at the College of Education for Pure Sciences at the University of Babylon, and were used. Natural radionuclide activity concentrations were measured using a NaI(Tl) detector comprising a "3 x 3" crystal and a Multi-Channel Analyzer (MCA) at 1024 channels. Gamma-ray spectroscopy observations were analyzed by the MAESTRO-32 software [14]. The lead and stainless steel outside section of the ORTEC cylindrical chamber is split into two pieces. These portions measured 20 cm and 5 cm in breadth, respectively. The evaluation of the whole radiation environment was made easier by the chamber's design. This detector has several advantages, including the ability to easily calibrate the power and its exceptional gamma ray capture capabilities, as **Figure 2.** An energy efficiency calibration using ^{60}Co, ^{133}Ba,^{137}Cs, and ^{22}Na was the first step in the process, which allowed for precise energy values to be obtained.

Figure 2: Detection system

3.1 Sample Measurements: The activity concentration is calculated using the following formulae and hazard indices after determining the radiation background and calibrating the detector's energy and effectiveness.

3.2 Specific Activity (A): Calculations were made to determine the radiologic efficacy of ^{238}U using the energy of ^{214}Bi (1764 keV), the energy of ^{208}Tl (2614 keV) for ^{232}Th, and the energy of ^{40}K (2614 keV) (1460 keV). For computing radionuclide specific activity (A) in soil samples, the following equation was utilized [15]:

$$A = \frac{N.a}{I_\gamma.\varepsilon.m.t.} \pm \frac{\sqrt{N.a}}{I_\gamma.\varepsilon.m.t.} \left[\frac{\text{Bq}}{\text{kg}}\right] \quad (1)$$

,where:

N.a: refers to the area beneath each spectrum's curve after removing background radiation

Iγ: The probabilities of the transition to gamma rays.

m: The specimen's mass

t: Counting time (14400 sec)

ε: The detector's efficiency

3.3 Radium Equivalent (Ra_{eq}): The levels of activity have been described by a radiological index. The formula computes the (Raeq) index of (^{238}U, ^{232}Th, and ^{40}K) **[16]**:

$$(Ra_{eq}\ Bq/kg). = A_U + 1.43A_{Th} + 0.077A_K \quad (2)$$

where: A_U, A_{Th}, and AK stand for the respective activity concentration of (^{238}U.,^{232}Th. and ^{40}K.) in (Bq/kg).

3.4 Absorbed Dose (D_r): The following equation can be used to determine the D_r in air given the abundance of terrestrial cores **[17]**:

$$Dr(\frac{nGy}{h.}) = 0.462A_{.U} + 0.604A_{.Th} + 0.047A_{.K} \quad (3)$$

3.5 Annual Effective Dose (AED): The predicted value was calculated using a conversion factor AED that one person of this (0.7sv/Gy) received. This was then used to determine the comparable effective dosage for a 20% outdoor occupancy and an interior occupancy of (80%) **[18]**:

$$AED\ (mSv/y) = AD(\frac{nGy}{h}) \times 10^{-6} \times 8760\ h \times 0.2 \times 0.7(\frac{sv}{Gy}) \quad (4)$$

3.6 External Hazard Indices (Hex): For the purpose of assessing the radiation risk from gamma rays and other sources, (H_{ex}) may be computed. Depending on the level of specific radiation activity, the following two equations were obtained **[17,18]**:

$$H_{ex} = \frac{Au}{370} + \frac{ATh}{259} + \frac{Ak}{4810} \quad (5)$$

4. Results and Discussion:

Table 1 displays the specific activity for nine dust storm collecting samples from various zones in Babel.

Table 1: Specific activity values for ^{238}U, ^{232}Th, and ^{40}K

Sample No.	*Specific Activity (Bq/kg)*		
	^{238}U	^{232}Th	^{40}K
D1	22.91±0.8	11.41±0.5	174.92±2.6
D2	9.27+0.5	3.86±0.3	147.93±2.4
D3	16.34±0.7	10.48±05	169.68±2.6
D4	15.52±0.6	4.94±0.3	125.34±2.6
D5	19.67±0.7	10.31±.4	168.94±2.6
D6	16.12±0.7	6.45±0.3	123.04±2.2
D7	16.84±0.7	2.72±0.2	151.71±+2.4
D8	20.61±0.8	5.91±0.3	172.15±2.6
D9	15.11±0.6	3.54±0.2	119.43±2.2
Ave± SD	16.93±0.7	6.53±0.3	150.34±2.5
Max± SD	22.91±0. 8	11.41±0. 5	174.92±2.6
Min± SD	9.27±0.5	2.72±0.2	117.43±2.2
UNSCEAR 2008	30	35	400

Table1. shows that the maximum and minimum values of a specific activity for 238U ranged from 9.2 ± 0.5 to 22.91 ± 0.8 (Bq/kg). Sample D2 contained the lowest value, while sample D1 contained the highest value, with a mean of 16.93 ± 0.7 (Bq/kg), as **Figure 3** depicts values of activity level for ^{238}U. The current work's mean is less than 30 (Bq/kg) UNSCEAR calculated global average value is 30 (Bq/kg). Conversely, the max. and min. values of ^{232}Th a specific activity, which range from 2.72 ± 0.26 to 11.41 ± 0.5 (Bq/kg) to an average of 6.5 ± 0.3 (Bq/kg), as **Figure 4**. The current work's mean value of ^{232}Th is smaller than the mean of 35 (Bq/kg). While the maximum and minimum values of a specific activity of ^{40}K range from 119.43 2.2 to 174.92 2.7 (Bq/kg), with a mean is 150.34 2.5 (Bq/kg), as **Figure 5**.

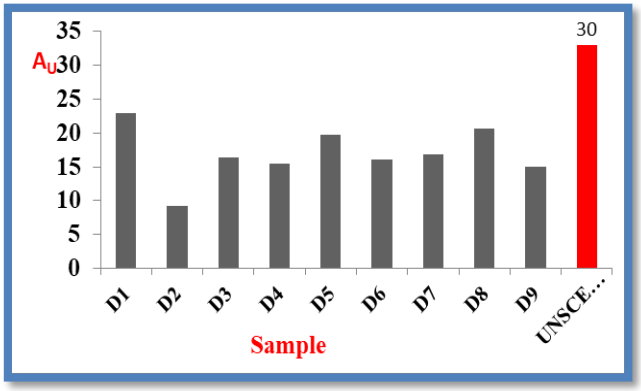

Figure 3: The specific activity of the samples' ^{238}U

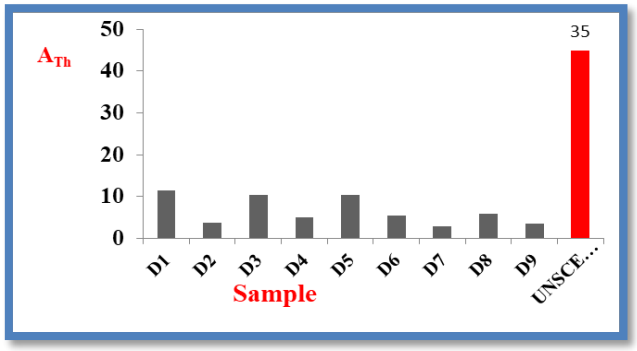

Figure 4: The specific activity of the sample' ^{232}Th

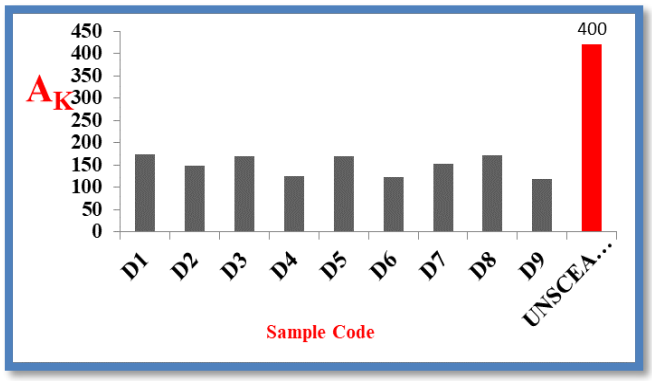

Figure 5: The specific activity of the samples' ^{40}K

Table 2 displays the Radiation Hazard Indices values, while **Figures 6** and **7** depict the Ra_{eq} and D_r, which representative level hazard indices in dust storm samples. In this study.

Table 2: Indicators of risk measured in the current work

Sample No.	Ra_{eq} Bq/kg	D_r(nGy/h)	H_{ex}	AED(mSv/y)
D1	52.685	47.789	0.142	0.029
D2	26.074	24.675	0.070	0.015
D3	44.232	40.182	0.119	0.025
D4	32.173	29.817	0.086	0.018
D5	47.368	43.080	0.127	0.026
D6	33.386	30.7911	0.090	0.018
D7	32.420	30.780	0.087	0.018
D8	42.309	39.399	0.114	0.024
D9	29.317	27.421	0.079	0.016
Ave.	37.774	34.881	0.102	0.022
Max	52.685	47.789	0.142	0.029
Min	26.074	24.675	0.070	0.015
UNSCEAR 2008	370	55	≤ 1	1

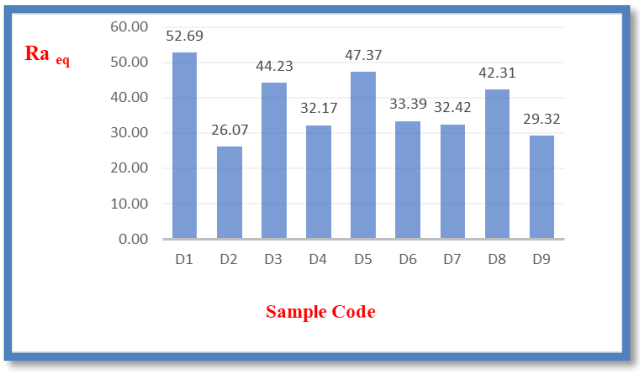

Figure 6: Radium equivalent in dust storm samples

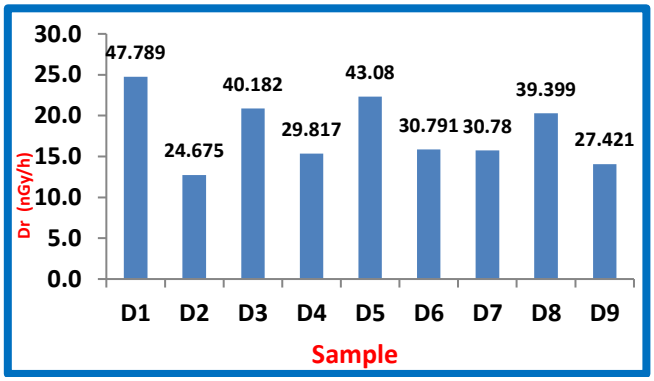

Figure 7: The absorbed dose rate in dust storm samples

It had been noticed from **Table (2)** that the Ra_{eq} values varied from 26.074 to 52.685 (Bq/kg) with an average of 37.774 (Bq/kg), as shown in **Figures (6)** and **(7)**. All dust storm samples had Raeq. values that were fewer than the high value that was advised, 370 (Bq/kg), the D_r value varied between 24.675 (nGy/h) to 47.789 (n.Gy/h). The levels of H_{ex} differed by 0.07 - 0.142 to 0.095 - 0.204, AED values varied by 0.015 to 0.029 (mSv/y), at the average was 0.022

(mSv/y). According to the most recent data, dust storm sample readings for (Ra_{eq}, Dr, H_{ex}, and AED) were below the UNSCEAR and ICRP recommended value [19,20].

5. Conclusions

In the dust storm samples from the Iraqi city of Hillah, the specific activity of ^{238}U, ^{232}Th, and ^{40}K is lower than the global average values. The radiation safety publications UNSCEAR (2008) and ICRP (1993) found that the majority of the radioactive effects, including Ra_{eq}, D_r, H_{ex}, and AED, were below the global average. Thus, dust storms do not pose a radiation risk.

6. References

[1] Taskin H, Karavus M, Topuzogh A, Hindiroglu S, and Karahan G. Radionuclide Concentrations in Soil and Lifetime Cancer Risk Due to the Gamma Radioactivity in Kirklareli. Turkey Journal of Environmental Radioactivity. 2009;100(1): 49-53.

[2] Hasan A, and Hassan S. Measurements of Natural Radiation in Soil of the College of Education, University of Kufa, Al-Najaf Al-Ashraf, Iraq. Pakistan Journal Chemistry. 2011;1(14): 155-160.

[3] Al-Hamdani S, and Mohammed A. Radioactivity Assessment with Different Samples (Soil, Sediment) Selected From AL-Basra Governorate, Iraq. Plant Archives. 2020;20(1): 3103-3110.

[4] Shawkat N. Radioactive pollution and environmental sources in the province of Nineveh. Master Thesis Baghdad University. 2000.

[5] Eral M, Aytas S, Akyil S, and Aslani M. Environmental radioactivity in soil samples from agricultural lands. Environmental Protection Against Radioactive Pollution. 2003; 237-244. Springer Netherlands.

[6] Salman, E, Shakir, A, and Shaker Q. Assessment of radioactivity levels and its associated radiological Hazards in soil of Kifl city/Iraq. Journal of Physics: Conference Series. 2020;1530, IOP Publishing.

[7] Yadav M, Rawat M, Dangwal A, Prasad M, Gusain G, and Ramola R. Levels and effects of natural radionuclides in soil samples of Garhwal Himalaya. Journal of Radioanalytical and Nuclear Chemistry.2014;302(1): 869-873.

[8] Oleiwi M. Assessment of Natural Radioactivity in Some Soil Samples from Kutha District in Babylon Governorate, Iraq. Jordan Journal of Physics. 2021;14(3):267-274.

[9] Abojassim AA, and Rasheed L H. NORM in soil of some locations in Baghdad governorate, Iraq. International Journal of Energy and Environment. 2019;10(3):143-155.

[10] Jassim AZ, Al-Gazaly HH and Abojassim AA. Natural radioactivity levels in soil samples for some locations of Missan Government, Iraq. Journal of Environmental Science and Pollution Research. 2016;2(1): 39-41.

[11] Dia H, Nouh S, Hamdy A and EL-Fiki A. Evaluation of natural radioactivity in a Cultivated Area Around a Fertilizer Factory. Nuclear and Radiation Physics. 2008 ;31(2): 53-62.

[12] Hamad A, and Qadar H. Gamma Rays Spectroscopy by Using a Thallium Activated Sodium Iodide NaI(Tl). Eurasian Journal of Science and Engineering .2018;4(1): 99-111.

[13] Abdul F. School survey atlas. Third Edition.2006.

[14] Ortec. Gamma Ray Spectroscopy Using NaI(Tl). Experiments in Nuclear Science Laboratory Manual. Fourth Edition.2014.

[15] Peksen A, Kurnaz A, Turfan N, and Kibarİ B. Determination of Radioactivity Levels in Different Mushroom Species from Turkey.2021;31(1).doi: 10.29133/yyutbd.797101.

[16] Reda E, Mohammed A, Ali O, Montaser M, and El-Taher A. Natural Radioactivity Levels and Radiological Hazards in Soil Samples Around Abu Kaeqas Sugar Factory. Journal of Environmental Science and Technology. 2018 ;11(1): 28-38.

[17] El-Taher A and Yosif M. The Assessment of the Radiation Hazard Indices due to Uranium and Thorium in Some Egyptian Environmental Matrices. Journal of Physics. D: Applied Physics.2006 ;39(2): 4516-4521.

[18] Alsaedi J, Hasan N. and Abdulhasan A. Natural Radioactivity in Soil Samples from Selected Areas in Nineveh Governorate, Iraq. Nuclear Physics and Atomic Energy. 2020;21(2):187-194.

[19] ICRP International Commission on Radiological Protection. ICRP publication 65, Annals of the ICRP 23(2). - Oxford: Pergamon Press.1993.

[20] UNSCAR United Nation Scientific Committee on the Effects of Atomic Radiation. Exposures from Natural radiation sources. Report of the General Assembly, Annex B, New York.2008.

Al-Kitab Journal for Pure Sciences (2025); 9(2):43-61
https://doi.org/10.32441/kjps.09.02.p4

Al-Kitab Journal for Pure Sciences
ISSN: 2617-1260 (print), 2617-8141(online)

https://isnra.net/index.php/kjps

A Novel Approach in Number Theory for Representing Large Numbers: The Arrow-Free Notation

Laith H. M. Al-Ossmi

College of Engineering, University of Thi-Qar, Thi-Qar Province, Iraq.

*Corresponding Author: laithhady@utq.edu.iq, hardmanquanny@gmail.com

Citation: Al-Ossmi LHM. A Novel Approach in Number Theory for Representing Large Numbers: The Arrow-Free Notation. Al-Kitab J. Pure Sci. [Internet]. 2025 Apr. 26;9(2):43-61. DOI: https://doi.org/10.32441/kjps.09.02.p4.

Keywords: Number Theory, Knuth Up-Arrow Notation, Conway Chained Arrow Notation, Hyperoperation.

Article History

Received	03 Aug. 2024
Accepted	28 Sep. 2024
Available online	26 Apr. 2025

Abstract:

This article introduces a new notation for expressing extremely large numbers, based on the hyperoperation concept in group theory. The method employs a finite sequence of positive integers separated by specific notational symbols, allowing for concise representation through an arrow-free notation: (a_n^b), where b represents the number of copies of a, and n denotes the arrow's number described by a general formula. This recursive definition aims to replace the Knuth up-arrow notation and Conway chained arrow notation, which require the insertion of arrows between or within numbers. The new approach simplifies these expressions, eliminating the need for such symbols and providing a straightforward and concise method for representing large numbers. The aim was to develop a more efficient method, arrow-free notation, reducing the complexity and steps necessary with previous notations.

Keywords: Number Theory, Knuth Up-Arrow Notation, Conway Chained Arrow Notation, Hyperoperation.

نهج جديد في نظرية الأرقام لتمثيل الأعداد الكبيرة: الترميز الخالي من الأسهم

ليث هادي منشد العصامي

كلية الهندسة/ جامعة ذي قار/ محافظة ذي قار/ العراق

hardmanquanny@gmail.com , laithhady@utq.edu.iq

https://orcid.org/0000-0002-6145-9478

الخلاصة:

يتناول هذا المقال ترميزًا جديدًا يتعلق بمفهوم العمليات الفائقة في نظرية الزمر. يتعامل مع طرق التعبير عن بعض الأعداد الكبيرة جدًا. هو ببساطة تسلسل محدود من الأعداد الصحيحة الموجبة مفصولة بترميز خالٍ من الأسهم حيث يكون b هو عدد نسخ a ، و n هو عدد الأسهم، والذي يوصف بالصيغة العامة؛ (a_n^b) كما هو الحال مع معظم الترميزات التوافقية، فإن التعريف تكراري. في هذا المقال، ينتهي الترميز بأن يكون العدد الأيسر مرفوعًا إلى قوة عدد صحيح (عادة ما يكون ضخمًا). تم تصميم هذه الطريقة لتحل محل الطريقتين المستخدمتين سابقًا لتمثيل الأعداد الكبيرة، وهما ترميز السهم الصاعد لـ Knuth وترميز السلسلة المتسلسلة لـ Conway. يبسّط هذا النهج الجديد التعبير عن الأعداد الكبيرة دون الحاجة إلى كتابة الأسهم بين الأعداد أو داخلها، كما كان مطلوبًا في الطرق السابقة. كان هدف هذا البحث هو تحقيق هذه الميزة بهذه الطريقة المبتكرة، التي تبسط عدة خطوات كانت مطلوبة سابقًا من الطريقتين الأخريين، مما يوفر طريقة أكثر بساطة ووضوحًا لتمثيل نفس الحالات. الطريقة بسيطة وواضحة مع خطوات قليلة، مما يجعل من السهل تعلمها وتطبيقها لمعالجة مختلف حالات الأعداد الكبيرة والكبيرة جدًا.

الكلمات المفتاحية: نظرية الأعداد، ترميز السهم المتصاعد لـKnuth ، ترميز أسهم السلسلة لـConway ، العمليات العددية.

1. Introduction:

The notation $x\hat{}y$ for tetration, introduced by Hans Maurer in 1901, has evolved significantly over the years [1]. In 1947, Reuben Louis Goodstein coined the term tetration and named other hyper-operations [2]. Andrzej Grzegorczyk further advanced this field in 1953, leading to the sequence of hyper-operations sometimes being referred to as the Grzegorczyk hierarchy [2,3]. Rudy Rucker's 1995 publication, *Infinity and the Mind*, popularized this notation extensively [4], despite his credit sometimes being mistakenly attributed to its first use. In 1976, Donald E. Knuth developed the Up-arrow notation for hyper-operations [4], which has found significant success on the internet due to its convenience in representing tetration as "$x\hat{}\hat{}y$". More recently, in 1996, John Horton Conway and Richard K. Guy introduced another hyper-operation notation in their book *The Book of Numbers* [2,3]. Large numbers, which significantly exceed those typically encountered in everyday life, such as in simple counting or monetary transactions, are frequently found in fields like mathematics, cosmology, cryptography, and

statistical mechanics. In 2002, Jonathan Bowers developed Array Notation, which extends beyond hyperoperations while still encompassing them **[3]**. Bowers' notation includes an infix notation known as extended operator notation, equivalent in all respects to the current de facto standard notation for hyperoperations **[4,5]**.

In mathematics, large numbers, defined as numbers exceeding one million, are typically represented either using exponents, such as (10^9, or 10^9), or by terms like billion or thousand million, which vary across different numeration systems. The American system of numeration for denominations above one million was originally based on a French system. However, in 1948, the French system was modified to align with the German and British systems **[6,7]**. In the American system, each denomination above one thousand million (the American billion) is 1,000 times the preceding one (for example, one trillion equals 1,000 billion; one quadrillion equals 1,000 trillions). Conversely, in the British system, each denomination is 1,000,000 times the preceding one (for example, one trillion equals 1,000,000 billion), with the exception of the term "milliard," which is sometimes used for one thousand million. In recent years, British usage has increasingly reflected the widespread adoption of the American system **[8]**.

Scientific notation was devised to handle the vast range of values that arise in scientific research. For example, 1.0×10^9 denotes one billion, or a 1 followed by nine zeros: 1,000,000,000. Its reciprocal, 1.0×10^{-9}, represents one billionth, or 0.000000001. Using 10^9 instead of nine zeros alleviates the reader's effort and minimizes the risk of errors associated with counting a long series of zeros to determine the magnitude of the number [9]. In addition to scientific (powers of 10) notation, the following examples illustrate the systematic nomenclature of large numbers based on the short scale. The Avogadro constant **[10]**, for example, is the number of “elementary entities” (usually atoms or molecules) in one mole; the number of atoms in 12 grams of carbon-12 is approximately 6.022×10^{23}, or 602.2 sextillion. The lower bound on the game-tree complexity of chess, also known as the “Shannon number” (estimated at around 10^{120}), or 1 novemtrigintillion. Rayo's number, named after Agustín Rayo, is a large number that has been claimed to be the largest named number **[11]**. At MIT on January 26, it was first defined during a "big number duel", 2007**[12]**. Graham's number, which surpasses what can be represented using power towers (tetration), can nonetheless be expressed using layers of Knuth's up-arrow notation. Nevertheless, there are very specific methods used to write out such huge numbers. Gödel numbers, as well as similar huge numbers used to represent bit-strings in algorithmic information theory, are extraordinarily large, even for mathematical statements of moderate length. One of the earliest mentions of hyperoperations was by Albert Bennett in 1914, where he developed a portion of his theory on commutative

hyperoperations [11,12]. Twelve years later, Wilhelm Ackermann defined a function, denoted as (ϕ), which resembled a sequence of hyperoperations. In a 1947 paper, the Greek mathematician Ruben Goodstein introduced a sequence of operations now known as hyperoperations [12]. He extended these operations beyond exponentiation by adding the subsequent steps, which he suggested be called tetration and pentation. As a function with three arguments, this is recognized as a variant of the original Ackermann function. Nevertheless, some pathological numbers surpass the magnitude of Gödel numbers associated with typical mathematical propositions [10,11]. In general, there are very specific methods used to write out such extremely large numbers, such as:

- Scientific Notation: A way of expressing numbers as a product of a coefficient and a power of 10[11]. For example, 3.2×10^{15} represents 3,200,000,000,000,000.
- Knuth's Up-Arrow Notation: A technique to represent exemplifying very large integers using arrows to denote iterated exponentiation [11]. For instance, $3 \uparrow\uparrow 3$ is $\left(3^{3^3}\right)$, or (3^{27}), which is (7,625,597,484,987).
- Conway's Chain Arrow Notation: An extension of up-arrow notation, useful for representing even larger numbers [12]. For example, $3 \rightarrow 3 \rightarrow 3$ represents a very large number.
- Steinhaus-Moser Notation: A way to represent very large numbers using polygons and the Ackermann function [13]. For example, 2 inside a triangle $(\Delta 2)$ is equivalent to 2^2 or 4, but the notation can escalate quickly to represent vastly larger numbers.
- Hyper-E notation: A notation for expressing extremely large numbers, using "E" to denote a level of exponentiation beyond standard operations [14]. For example, $3E3$ represents (3^{27}).
- Tree notation: Used in certain contexts like Kruskal's tree theorem [11,15], where numbers grow rapidly with tree structures and graph-related operations.

A standardized method for writing very large numbers facilitates their easy sorting in ascending order and provides a clear understanding of how much larger one number is compared to another. These notations represent functions of integer variables that grow at an exceptionally rapid rate as the integer values increase. By applying these functions recursively with large integer arguments, it is possible to construct functions that grow even more quickly. However, functions characterized by vertical asymptotes are not appropriate for defining very large numbers, despite their rapid growth. This is due to the fact that such functions necessitate arguments approaching the asymptote, which involves working with extremely small values, such as reciprocals, rather than directly addressing the construction of large numbers.

2. Materials and methods:

In this paper, we introduce Al-Ossmi's notation, a novel method for expressing extremely large numbers, named after its creator, Al-Ossmi. This notation aims to compactly represent large numbers by providing a clear structure that indicates the base, the level of iteration, and the depth of the operation. By doing so, it offers an efficient and unambiguous method for handling vast numerical values, making it a valuable tool for mathematicians and computer scientists.

Al-Ossmi's arrow-free notation is defined as; $a_n^{(\boldsymbol{b}\ copies\ of\ \boldsymbol{a})}$, where:

- a: The base number.
- b: The number of iterations or the height of the power tower.
- n: The level of operation or the number of arrows in Knuth's notation.

Also, the arrow-free notation developed to be extended to deal with the pentation (iterated tetration), including more complex structures, representing additional levels of nested operations where d and c are variables, such as;

$$a_n^{a_n^{(a_n^a)}},\quad a_{\left(a_n^{(a_n^a)}\right)}^{a_n},\quad \text{or}\quad a_n^{b.c.d.e.f.g},$$

Al-Ossmi's arrow-free notation simplifies the representation of very large numbers by using a compact form that corresponds to $(a \uparrow^n b)$ as in Knuth's up-arrow notation [15], and in Conway's chained arrow notation $a \to b \to n$ [11,16].

3. Results:

The method of writing and representing extremely large numbers is essential in mathematics, as it helps simplify and understand complex calculations and allows for the precise and concise expression of enormous quantities. Using specific symbols and notations to represent these numbers facilitates their handling in various mathematical fields, enhancing the efficiency of computations and analyses. These methods provide valuable tools for mathematicians and scientists who deal with numbers that exceed traditional representation capabilities. In our research, we will focus on the two most well-known methods, Knuth's up-arrow notation and Conway's chained arrow notation.

3.1 Knuth's up-arrow notation: This notation, introduced by Donald Knuth in 1976, is a system designed for representing very large integers [15,16]. It also illustrates the representation of numbers and the execution of arithmetic operations within this base system.

***Definition*:** For all integers a, b, n with $a \geq 0, n \geq 1, b \geq 0$, [16],the up-arrow operators can be formally defined by:

$$a \uparrow^n b = \begin{cases} a^b, & if\ n = 1; \\ 1, & if\ n > 1\ and\ b = 0; \\ a \uparrow^{(n-1)} b\big(a \uparrow^n (b-1)\big), & otherwise \end{cases}$$

This definition employs exponentiation as the base case and tetration as repeated exponentiation, aligning with the hyperoperation sequence but excluding the fundamental operations of succession, addition, and multiplication. The sequence begins with a unary operation (the successor function), for ($n = 0$) and progresses through binary operations such as addition ($n = 1$), multiplication ($n = 2$), exponentiation ($n = 3$), as well as tetration ($n = 4$), and pentation ($n = 5$), among others. This framework is often used to represent hyperoperations with arrows, for example;

- The single arrow ($\uparrow$) represents exponentiation (iterated multiplication);

$$3 \uparrow 2 = 3 \times 3 = 3^2 = 9$$

- The double arrow ($\uparrow\uparrow$) represents tetration (iterated exponentiation);

$$3 \uparrow\uparrow 4 = 3 \uparrow 3 \uparrow (3 \uparrow 3) = 3 \uparrow 3 \uparrow (3^3) = 3 \uparrow 3 \uparrow (27)$$

- The triple arrow ($\uparrow\uparrow\uparrow$) represents pentation (iterated tetration);

$$3 \uparrow\uparrow\uparrow 4 = 3 \uparrow\uparrow 3 \uparrow\uparrow (3 \uparrow\uparrow 3) = 3 \uparrow\uparrow 3 \uparrow\uparrow (3 \uparrow 3 \uparrow 3) = 3 \uparrow\uparrow 3 \uparrow\uparrow \left(3^{3^3}\right)$$

The up-arrow notation general definition is as follows (for $a \geq 0, n \geq 1, b \geq 0$):

$$a \uparrow^n b = a[n+1]b$$

Here, $\uparrow$ stands for *n* arrows, so for example: $3 \uparrow\uparrow\uparrow 5 = 3 \uparrow^4 5$.

Square brackets are another notation for hyperoperations. Exponentiation for a natural power b is defined as iterated multiplication, which Knuth denoted by a single up-arrow:

$a \uparrow b = a^b$, for example, $3 \uparrow 4 = 3 \times 3 \times 3 \times 3 = 3^4 = 81$

Tetration is well-defined as iterated exponentiation, which Knuth denoted by a "double arrow":

$a \uparrow\uparrow b = a \uparrow \big(a \uparrow (\ldots \uparrow a)\big)$, b copies of a's.

Example; $3 \uparrow\uparrow 4 = 3 \uparrow 3 \uparrow (3 \uparrow 3) = 3^{\left(3^{3^3}\right)} = 3^{(7{,}625{,}597{,}484{,}987)}$

Expressions are evaluated from right to left because the operators are right-associative. This results in very large numbers, but the hyperoperator sequence continues beyond pentation. Pentation, defined as iterated tetration, is represented by the "triple arrow":

$a \uparrow\uparrow\uparrow b = a \uparrow\uparrow \big(a \uparrow\uparrow (\ldots \uparrow\uparrow a)\big)$, hence b copies of a's.

Example, $3 \uparrow\uparrow\uparrow 4 = 3 \uparrow\uparrow 3 \uparrow\uparrow (3 \uparrow\uparrow 3) = 3 \uparrow\uparrow 3 \uparrow\uparrow (3 \uparrow 3 \uparrow 3)$

$$= 3 \uparrow\uparrow 3 \uparrow\uparrow \left(3^{3^3}\right) = 3 \uparrow\uparrow 3 \uparrow\uparrow (7{,}625{,}597{,}484{,}987)$$

Hexation, which is the iteration of pentation, is denoted using the "quadruple arrow" notation: $a \uparrow\uparrow\uparrow\uparrow b = a \uparrow\uparrow\uparrow \big(a \uparrow\uparrow\uparrow (..\uparrow\uparrow\uparrow a)\big)$, b copies of a's.

Example, $3 \uparrow\uparrow\uparrow 4 = 3 \uparrow\uparrow\uparrow 3 \uparrow\uparrow\uparrow (3 \uparrow\uparrow\uparrow 3) = 3 \uparrow\uparrow\uparrow 3 \uparrow\uparrow\uparrow \big(3 \uparrow\uparrow (3 \uparrow\uparrow 3)\big)$,

$$= 3 \uparrow\uparrow\uparrow 3 \uparrow\uparrow\uparrow \big(3 \uparrow\uparrow (3 \uparrow 3 \uparrow 3)\big)$$

$$= 3 \uparrow\uparrow\uparrow 3 \uparrow\uparrow\uparrow \big(3 \uparrow\uparrow (7{,}625{,}597{,}484{,}987)\big) \quad \text{and so on.}$$

The general principle is that an *n*-arrow operator unfolds into a right-associative sequence of $(n-1)$-arrow operators. For instance, expressing $a \uparrow\uparrow b$ in traditional superscript notation results in a power tower. If b is a variable or is exceptionally large, the power tower may be denoted with ellipses and an annotation specifying the height of the tower.

$$a \underset{n}{\uparrow\uparrow} \cdots \uparrow b = \underbrace{a \uparrow \cdots \uparrow \big(a \uparrow \cdots \uparrow (\ldots \uparrow \cdots \uparrow a)\big)}_{b \text{ copies of } a}$$

Examples:

$$\mathbf{3} \uparrow\uparrow\uparrow \mathbf{2} = 3 \uparrow\uparrow 3 = 3 \uparrow 3 \uparrow 3 = 3^{3^3} = 7{,}625{,}597{,}484{,}987$$

$$\mathbf{3} \uparrow\uparrow\uparrow \mathbf{3} = 3 \uparrow\uparrow (3 \uparrow\uparrow 3) = 3 \uparrow\uparrow (3 \uparrow 3 \uparrow 3), with;\ 3 \uparrow 3 \uparrow 3 \ copies\ of\ 3.$$

Where; $3 \uparrow 3 \uparrow 3 = 3^{3^3} = 7{,}625{,}597{,}484{,}987 \ copies\ of\ 3.$

$$\mathbf{3} \uparrow\uparrow\uparrow\uparrow \mathbf{4} = 3 \uparrow\uparrow\uparrow 3 \uparrow\uparrow\uparrow (3 \uparrow\uparrow\uparrow 3) = 3 \uparrow\uparrow\uparrow 3 \uparrow\uparrow\uparrow \big(3 \uparrow\uparrow (3 \uparrow\uparrow 3)\big)$$

$$= 3 \uparrow\uparrow\uparrow 3 \uparrow\uparrow\uparrow \big(3 \uparrow\uparrow (3 \uparrow 3 \uparrow 3)\big)$$

$$= 3 \uparrow\uparrow\uparrow 3 \uparrow\uparrow\uparrow \big(3 \uparrow\uparrow (3^{3^3})\big)$$

$$= 3 \uparrow\uparrow\uparrow 3 \uparrow\uparrow\uparrow \big(3 \uparrow\uparrow (7{,}625{,}597{,}484{,}987)\big)$$

where; $3 \uparrow 3 \uparrow 3 = 3^{3^3} = 7{,}625{,}597{,}484{,}987 \ copies\ of\ 3.$

In this notation system, the expression $a \uparrow\uparrow b$ can be represented as a stack of power towers, where each level of the stack illustrates the magnitude of the level above it. If b is a variable or excessively large, this stack may be denoted using ellipses with an annotation indicating its height. Similarly, $a \uparrow\uparrow\uparrow b$ can be represented by multiple columns of these power tower stacks, where each column represents the number of power towers in the stack to its left. This up-arrow notation simplifies the representation of these diagrams while maintaining a geometric framework, such as tetration towers. Although this notation can handle very large numbers, the hyperoperator sequence extends beyond this scope. For extremely large numbers, Knuth's multiple arrows become impractical. In such cases, the *n*-arrow operator ($\uparrow^n$) is useful for describing sequences with a variable number of arrows, or hyperoperators. For numbers that surpass even this notation's capabilities, Conway's chained arrow notation can be employed. While a chain of three elements is comparable to other notations, a chain of four or more elements significantly enhances its capacity.

3.2 Conway chained-arrow notation: Similar to Knuth's, the chained-arrow notation has several properties that are similar to exponentiation, as well as properties that are specific to the operation and are gained from exponentiation. Conway's chained-arrow notation, invented by mathematician John Horton Conway, is a method for representing extraordinarily large numbers [12]. This notation involves a finite sequence of positive integers separated by rightward arrows, such as:

$$2 \to (3 \to 4 \to 5) \to 6 .$$

Like many combinatorial notations, Conway chained arrow notation is defined recursively. Eventually, the notation simplifies to the leftmost number being raised to a very large integer power.

***Definition1*:** A "Conway notation" is defined as follows:

- Any positive integer can be represented as a chain of length 1.
- A chain of length *n*, followed by a right-arrow → and a positive integer, together form a chain of length $(n + 1)$.

Any chain represents an integer, according to the six rules below [10]. Two chains are said to be equivalent if they represent the same integer. Let a, b, n denote positive. Then:

1. An empty chain (or a chain of length 0) is equal to 1.
2. The chain a represents the number a.
3. The chain $(a \to b)$ represents the number (a^b).
4. The chain $(a \to b \to n)$ represents the number $a \uparrow^n b$.

$$a \uparrow\uparrow b = a \to b \to n$$

Examples can become quite intricate rapidly. Here are a few simple instances:

$$2^{2^2} = 2 \uparrow\uparrow 3 = 2 \to 3 \to 2$$

$$4 \uparrow\uparrow 3 = 4 \to 3 \to 2$$

$$5 \uparrow\uparrow\uparrow 2 = 5 \to 2 \to 3$$

Arrow chains do not represent the iterative application of a binary operator. Instead, chains of other infixed symbols $(a \uparrow^n b)$ can frequently be considered in fragments $(a \to b \to n))$ without a change, for example:

$$2^{3^2} = 2^9 = 2 \to (3 \to 2)$$
$$(2^3)^2 = 8^2 = (2 \to 3) \to 2$$

$$2 \uparrow\uparrow\uparrow 4 = 2 \uparrow\uparrow 2 \uparrow\uparrow (2 \uparrow\uparrow 2) = 2 \uparrow\uparrow 2 \uparrow\uparrow (2 \uparrow 2) = \boldsymbol{a \to b \to n = 2 \to 4 \to 3}$$

The sixth rule in Conway's chained-arrow notation is essential. It dictates that for a sequence with four or more elements, ending in a number 2 or higher, the sequence is transformed into one of the same lengths but with a significantly larger penultimate element [12]. The last

element of the sequence is reduced, which simplifies the sequence according to Knuth's detailed procedure. This reduction process continues until the sequence is condensed to three elements, where the fourth rule completes the recursion.

4. The Arrow-Free Notation

The need for new arithmetic operations on very large numbers arises from various practical and theoretical considerations in fields such as science, technology, and mathematics. In this paper, we introduce a modern approach with an arrow-free notation that allows for the representation of numbers so large they are beyond common human experience. Al-Ossmi's arrow-free notation, named after its inventor, represents a function of integer variables that escalate at an exceptionally rapid rate as these integers increase. This notation allows for the recursive construction of increasingly faster-growing functions by applying it with large integer arguments.

***Definition 2*:** For all non-negative integers a, b, n with $a \geq 0, n \geq 1, b \geq 0$, the Al-Ossmi's arrow-free operators can be formally defined by:

$$\boldsymbol{a_n^b} = \begin{cases} a^b\,, & if\ n = 1 \\ 1, & if\ n > 1\ and\ b = 0; \\ a, & if\ n > 1\ and\ b = 1; \\ a_{(n-1)}\ (a_n(b-1)), & otherwise \end{cases}$$

It is important to note that Knuth did not define the "nil-arrow" operator $a \uparrow^0$, whereas Al-Ossmi's notation does include this concept. Furthermore, Al-Ossmi's notation can be extended to negative indices ($n \geq -2$) to align with the entire hyperoperation sequence, albeit with a delay in the indexing, which can be formed as:

$$\boldsymbol{a} \uparrow^{(n-1)} b = \boldsymbol{a}^b_{(n-1)}\ ,\quad for\ (n \geq 0)$$

For $(n = 1)$,we obtain the ordinary exponentiation, hence this definition uses exponentiation; $\boldsymbol{a_1^b} = \boldsymbol{a^b}$,as the base case, and tetration; $\boldsymbol{a_2^b}$ as repeated exponentiation. This approach aligns with the hyperoperation sequence but excludes the three fundamental operations of succession, addition, and multiplication. Alternatively, one may choose to define multiplication as follows:

$$a \uparrow^1 1 = a^1 = \quad \boldsymbol{a_1^1} = a$$

$$a \uparrow^1 b = a^b = \quad \boldsymbol{a_1^b} = a^b$$

$$a \uparrow^0 b = a \times b = \quad \boldsymbol{a_0^b} = a.b$$

The up-arrow operation is right-associative, meaning that is, $a \uparrow b \uparrow c$, is understood to be, $a \uparrow (b \uparrow c)$, instead of, $(a \uparrow b) \uparrow c$, while it is donated by Al-Ossmi's arrow-free notation as:

$$a^{\left(b^{(c^d)}\right)} = a \uparrow (b \uparrow c \uparrow d) = a \uparrow (b.c.d) = \boldsymbol{a^{(b.c.d)}}$$

$$a \uparrow b \uparrow c = a \uparrow (b \uparrow c) = \boldsymbol{a_1^{(b\uparrow c)}} = \boldsymbol{a_1^{(b.c)}} = \boldsymbol{a^{(b.c)}}$$

$$a \uparrow\uparrow b \uparrow c = a \uparrow\uparrow (b \uparrow c) = \boldsymbol{a_2^{(b\uparrow c)}} = \boldsymbol{a_2^{(b.c)}}$$

$$a \uparrow\uparrow\uparrow b \uparrow c = a \uparrow\uparrow\uparrow (b \uparrow c) = \boldsymbol{a_3^{(b\uparrow c)}} = \boldsymbol{a_3^{(b.c)}}$$

Then exponentiation becomes repeated multiplication, $a \uparrow b \uparrow c \uparrow d$ in form of $(a.b.c.d)$, which means; $a^{\left(b^{(c^d)}\right)}$. The formal definition would be donated by Al-Ossmi's arrow-free notation as iterated exponentiation of a power tower of b:

$$a \uparrow b \uparrow c \uparrow d = a \uparrow (b \uparrow c \uparrow d) = \boldsymbol{a_1^{(b\uparrow c\uparrow d)}} = \boldsymbol{a_1^{(b.c.d)}} = \boldsymbol{a^{(b.c.d)}} ,$$

$$a \uparrow b \uparrow c \uparrow d \uparrow e = a \uparrow (b \uparrow c \uparrow d \uparrow e) = \boldsymbol{a_1^{(b\uparrow c\uparrow d\uparrow e)}} = \boldsymbol{a_1^{(b.c.d.e)}} = \boldsymbol{a^{(b.c.d.e)}} ,$$

$$a \uparrow\uparrow b \uparrow c \uparrow d \uparrow e = a \uparrow\uparrow (b \uparrow c \uparrow d \uparrow e) = \boldsymbol{a_2^{(b\uparrow c\uparrow d\uparrow e)}} = \boldsymbol{a_2^{(b.c.d.e)}} ,$$

Hyperoperations extend arithmetic operations beyond exponentiation. Specifically, exponentiation, defined as iterated multiplication for a natural power b, is denoted by a single up-arrow in Knuth's notation. In Al-Ossmi's arrow-free notation, this operation is represented when $(n = 1)$, as:$\left(a_1^b\right)$ which is also donated by: a^b. In this new notation, expressions are evaluated from right to left due to the right-associative nature of the operators. Tetration, which is defined as iterated exponentiation, is represented in Knuth's notation using a "double arrow":

$$a \uparrow\uparrow b = a_2^b = \boldsymbol{a_{n-1}^{(b)}} = \boldsymbol{a^{(b\ copies\ of\ a)}} ,$$

For example;

$$\boldsymbol{3} \uparrow\uparrow \boldsymbol{4} = 3 \uparrow 3 \uparrow 3 \uparrow 3 = \boldsymbol{3^{3^{3^3}}}$$

$$3 \uparrow\uparrow 4 = \boldsymbol{3_2^4 = 3_1 3_1 3_1 3_1} = \boldsymbol{3^{3^{3^3}}}$$

According to this definition, examples of numbers which are written by Knuth's can be rewritten out by the Al-Ossmi's arrow-free notation as following:

$$3 \uparrow\uparrow \boldsymbol{2} = 3 \uparrow 3 = 3_2^{\boldsymbol{2}} = 3_1 3_1 = \boldsymbol{3^3}$$

$$3 \uparrow\uparrow \boldsymbol{3} = 3 \uparrow 3 \uparrow 3 = 3_2^{\boldsymbol{3}} = 3_1 3_1 3_1 = \boldsymbol{3^{3^3}}$$

$$3 \uparrow\uparrow \boldsymbol{4} = 3 \uparrow 3 \uparrow 3 \uparrow 3 = 3_2^{\boldsymbol{4}} = 3_1 3_1 3_1 3_1 = \boldsymbol{3^{3^{3^3}}}$$

$$3 \uparrow\uparrow \boldsymbol{5} = 3 \uparrow 3 \uparrow 3 \uparrow 3 \uparrow 3 = 3_2^{\boldsymbol{5}} = 3_1 3_1 3_1 3_1 3_1 = \boldsymbol{3^{3^{3^{3^3}}}}$$

This process results in exceedingly large numbers, yet the hyperoperator sequence extends further. Pentation, which is defined as iterated tetration and denoted by Knuth using the "triple arrow,"$a \uparrow\uparrow\uparrow b$, and by the arrow-free notation, it is simply represented as: a_3^{b}. According to this definition:

$$3 \uparrow\uparrow\uparrow \mathbf{2} = 3_3^{\mathbf{2}}$$

$$10 \uparrow\uparrow\uparrow\uparrow 5 = 10_4^{\mathbf{5}}$$

Hexation and beyond, which are defined as iterated pentation, are represented using Knuth's "quadruple arrow" notation as $a \uparrow\uparrow\uparrow\uparrow b$. In Al-Ossmi's notation, these operations are expressed as a_4^b. According to this definition:

$$3 \uparrow\uparrow\uparrow\uparrow 2 = 3_4^{\mathbf{2}}$$

$$10 \uparrow\uparrow\uparrow\uparrow\uparrow\uparrow 5 = 10_6^{\mathbf{5}}$$

The sequence of operations begins with a unary operation (hence the successor function for ($n = 0$) and extends through binary operations such as addition ($n = 1$), multiplication ($n = 2$), exponentiation ($n = 3$), tetration ($n = 4$), pentation ($n = 5$), and so on. Different notations have been used to represent these hyperoperations. In Al-Ossmi's notation, the base is represented by *a*, with *b* indicating the number of copies of *a*. Therefore, an *n*-arrow operator in Al-Ossmi's notation translates into a right-associative series of *n*-arrow operators.

Symbolically:

$$a \underbrace{\uparrow\uparrow \cdots \uparrow}_{b \ copies \ of \ a} b = \boldsymbol{a_n^b},$$

Examples:

$$2 \uparrow\uparrow\uparrow 2 = 2 \uparrow\uparrow \mathbf{2} = 2_3^{\mathbf{2}} = 2_2^{\mathbf{2}}$$

$$3 \uparrow\uparrow\uparrow 2 = 3 \uparrow\uparrow \mathbf{3} = 3_3^{\mathbf{2}} = 3_2^{\mathbf{3}}$$

$$3 \uparrow\uparrow\uparrow \mathbf{3} = 3_3^{\mathbf{3}}$$

$$3 \uparrow \mathbf{6} = 3 \uparrow^{\mathbf{23}} \mathbf{6} = 3_{\mathbf{23}}^{\mathbf{6}}$$

$$3 \uparrow^{10^{100}} \mathbf{4} = 3_{10^{(100)}}^{\mathbf{4}} = 3_{10.100}^{\mathbf{4}}$$

$$3 \uparrow^{10^{23.5}} \mathbf{4} = 3_{10^{(23.5)}}^{\mathbf{4}} = 3_{10.(23.5)}^{\mathbf{4}}$$

$$3 \uparrow^{10^{23^5}} \mathbf{4} = 3_{10^{(23^5)}}^{\mathbf{4}} = 3_{10.23.5}^{\mathbf{4}}$$

This flexibility of Al-Ossmi's notation with forms; $\boldsymbol{a_n^b}$, $\boldsymbol{a_n^{b.c}}$ or $\boldsymbol{a_n^{b.c.d.e.f.g.h}}$ **,** all allow for a compact and structured way to represent extremely large numbers. These power tower ($b.c.d.e$) are components to describe complex and extended depth and extend the depth further, representing additional layers of power towers or nested operations. By accurately reflecting the base, height (with nuanced depth like $b.c.d$, indicating an extended height in the power tower), and level of exponentiation, it simplifies understanding and interpreting large numbers. The use of multiple components separated by dots allows for a detailed and nuanced representation of the structure of the large number. This notation captures the nuances of the

structure of these numbers, including the base, height, depth, and level of operations, making it easier to understand and work with extremely large values.

4.1 Compared with Conway's chained notation: Let $(a > 1)$ is the base, $(b > 1)$ is the tower power, and $(n \geq 1)$ is the arrow's number, then Al-Ossmi's arrow-free notation can be written as:

$$a \uparrow^n b = a \to b \to n = \boldsymbol{a_n^b} = (\boldsymbol{a_n} \ldots \boldsymbol{b}\ copies\ of\ \boldsymbol{a}) = \boldsymbol{a}^{(\boldsymbol{b}\ copies\ of\ \boldsymbol{a})}$$

When the number is power by n times, then the Al-Ossmi's notation presents the power tower by adding the base a, arrows number $= n$, and $b =$ number of tower of a , for example:

$$a \to a \to 1 = \boldsymbol{a_1^a} = \boldsymbol{a^a}$$

$$2 \to 2 \to 1 = \boldsymbol{2_1^2} = \boldsymbol{2^2} = \boldsymbol{4}$$

where $\boldsymbol{2_1^2}$ represents 2 with one level of iteration (simple exponentiation), and a height of 2.

$$2 \to (2 \to 2 \to 1) \to 2 = \boldsymbol{2_2^3} = \boldsymbol{2_1 2_1 2_1} = \boldsymbol{2^{2^2}} = \boldsymbol{2^4} = \boldsymbol{16}$$

where $\boldsymbol{2_2^3}$ represents 2 with one level of iteration (simple exponentiation), and a height of 3.

$$2 \to (2 \to 2 \to 2) \to 1 = 2 \to (16) \to 2 = \boldsymbol{2_2^4} = \boldsymbol{2_1 2_1 2_1 2_1} = \boldsymbol{2^{2^{2^2}}} = \boldsymbol{65,536}$$

where $\boldsymbol{2_2^4}$ represents 2 with one level of iteration (simple exponentiation) and a height of 4.

and form rule of (3); we can write it out as; $a_2^{\mathrm{b}} = \boldsymbol{a}^{(\boldsymbol{b}\ copies\ of\ \boldsymbol{a})}$, which is applied in this example:

$$\boldsymbol{10}^{10^{10^{11}}} = 10 \to 10 \to 1 \to (10 \to 11 \to 1) \to 2 = \boldsymbol{10_2^{3^{(11)}}}$$

$$= \boldsymbol{10_1 10_1 10_1^{(11)}} = \boldsymbol{10_2^{3^{(11)}}} = \boldsymbol{10_2^{(3.11)}}$$

where $\boldsymbol{10_2^{3.11}}$ represents 10 with 2 levels of iteration (simple exponentiation), and a height of 10 to the power of 11 and raised 3 times.

$$\boldsymbol{3}^{3^{(56)^2}} = 3 \to (3 \to (56 \to 2 \to 1) \to 1) \to 1 = \boldsymbol{3_1^{3^{(56)^2}}}$$

$$= \boldsymbol{3_1 3_1^{(56)^2}} = \boldsymbol{3}^{\boldsymbol{3}^{(56)^2}} = \boldsymbol{3_1^{3.(3136)}} = \boldsymbol{3_2^{2.(3136)}}$$

Example1:

$$\boldsymbol{10}^{10^{10^{10^{10}}}} = \boldsymbol{10_2^5} = 10_1 10_1 10_1 10_1 10_1$$

Example2:

$$\boldsymbol{10}^{10^{303}} = \boldsymbol{10_2^{2^{(303)}}} = 10_1 10\,{}_1^{(303)}$$

Example3:

$$\boldsymbol{10}^{2^{303}} = \boldsymbol{10_1^{2^{(303)}}} = 10_1^{2.303} = 10^{2.303}$$

The difference between $\boldsymbol{10_1 10\,{}_1^{(303)}}$, regarding $\boldsymbol{10_1^{2.303}}$, is in how exponentially larger the exponent of $\boldsymbol{a_1^{b^{(c)}}}$ compared to the exponent of $\boldsymbol{a^{b^{(c)}}}$. The difference between $\boldsymbol{10_2^{2^{(303)}}}$ and

$\mathbf{10}_{\mathbf{1}}^{\mathbf{2}.(\mathbf{303})}$ lies in the magnitude of the exponent. The exponent itself, 10^{303}, is already a number with 304 digits (a 1 followed by 303 zeros). When you raise 10 to this power, you get a number with 10^{303} digits.

Al-Ossmi's free arrows notation a_n^b for expressing large numbers, $\boldsymbol{a}$ is the base number, $\boldsymbol{b}$ is the height or number of iterations in the power tower, and n is the level or number of arrows in Knuth's up-arrow notation.

Base Case ($n = \mathbf{1}$): Exponentiation: $a_n^b = \ a_1^{\boldsymbol{b}} = \boldsymbol{a^b}$

$$\text{Example: } 2 \uparrow 3 = \mathbf{2_1^3} = 2 \times 2 \times 2 = \mathbf{2^3} = 8$$

Two Levels ($n = \mathbf{2}$): Tetration (iterated exponentiation): $\boldsymbol{a_2^b} = a \uparrow\uparrow b$

$$\text{Example: } \mathbf{2} \uparrow\uparrow \mathbf{3} = 2 \uparrow (2 \uparrow 2) = 2 \uparrow (2^2) = \mathbf{2^{(2^2)}}$$

From the rules of (2 & 3), we find; $\mathbf{2} \uparrow\uparrow \mathbf{3} = \ \mathbf{2_2^3} = \mathbf{2_1}(\mathbf{2_1 2_1}) = \ \mathbf{2^{(2^2)}} = 16$

For $a = 10$, $b = 3$ (height of the tower), and, $(n = 2)$, (level of operation), then form the rules of (2 and 3), we find;

$$10 \uparrow\uparrow 3 = \mathbf{10_2^3} = 10_1(10_1 10_1) = 10^{(10^{10})}$$

Three Levels ($n = \mathbf{3}$): Pentation (iterated tetration):

$\boldsymbol{a_3^b} = a \uparrow\uparrow\uparrow b = a \uparrow\uparrow (\ldots a \uparrow\uparrow a)$, (with b copies of a), then:

$$\boldsymbol{a} \uparrow\uparrow\uparrow \boldsymbol{b} = \boldsymbol{a_n^b} = \ \boldsymbol{a_{(n-1)}^b}\left(\boldsymbol{a_{(n-1)}^{(b\ copies\ of\ a)}}\right),$$

Example, according to Knuth's;

$$\mathbf{2} \uparrow\uparrow\uparrow \mathbf{3} = 2 \uparrow\uparrow (\mathbf{2} \uparrow\uparrow \mathbf{2}) = 2 \uparrow\uparrow (\mathbf{2} \uparrow \mathbf{2}) = 2 \uparrow\uparrow (\mathbf{2^2}) \equiv \mathbf{2} \uparrow\uparrow \mathbf{4}$$

Then according to the Al-Ossmi's arrow-free notation's;

$$\mathbf{2} \uparrow\uparrow\uparrow \mathbf{3} = \mathbf{2_3^3},$$

$$\mathbf{2} \uparrow\uparrow (\mathbf{2^2}) = \mathbf{2} \uparrow\uparrow \mathbf{4} = \mathbf{2_2^{(2_1 2_1)}} = \mathbf{2_2^{(2^2)}} = \mathbf{2_2^{(4)}} = \mathbf{2_2^4}$$

$$\mathbf{2} \uparrow\uparrow\uparrow \mathbf{3} \equiv \mathbf{2} \uparrow\uparrow \mathbf{4} \equiv \mathbf{2_3^3} \equiv \mathbf{2_2^4}$$

Let us prove that; $\boldsymbol{a} \uparrow\uparrow b = \boldsymbol{a} \uparrow (\boldsymbol{a} \uparrow \boldsymbol{a}) = \boldsymbol{a}^{(a^a)}$, which can be written as $\boldsymbol{a_2^b}$.

$$Example;\ \mathbf{10_2^3} = 10 \uparrow\uparrow 3 = 10 \uparrow (\mathbf{10} \uparrow \mathbf{10}) = 10 \uparrow (\mathbf{10^{10}}) \equiv 10^{(10^{10})}$$

$$\mathbf{10_2^3} = \mathbf{10}_1(\mathbf{10}_1\ \mathbf{10}_1) = \mathbf{10}_1(\mathbf{10^{10}}) = \ \mathbf{10^{(10^{10})}} \ = \mathbf{10} \uparrow\uparrow \mathbf{3}$$

By Al-Ossmi's arrow-free notation definition, represents $a \uparrow^n b$ as; a_n^b, which matches our calculation above. Al-Ossmi's notation provides a concise and efficient way to represent very large numbers, combining the simplicity of Knuth's up-arrow notation with a clear structure for understanding the depth and height of power towers.

Example 4:

$$\mathbf{3} \uparrow\uparrow\uparrow \mathbf{4}$$

According to Knuth's;

$$\mathbf{3} \uparrow\uparrow\uparrow \mathbf{4} = 3 \uparrow\uparrow 3 \uparrow\uparrow (\mathbf{3} \uparrow\uparrow \mathbf{3}) = 3 \uparrow\uparrow 3 \uparrow\uparrow (\mathbf{3} \uparrow \mathbf{3} \uparrow \mathbf{3}) = 3 \uparrow\uparrow 3 \uparrow\uparrow \left(\mathbf{3^{3^3}}\right)$$

Then according to the Al-Ossmi's arrow-free notation's;

$$\mathbf{3} \uparrow\uparrow\uparrow \mathbf{4} = \mathbf{3_3^4} = \mathbf{3_2^3 3_2^{(3_1 3_1 3_1)}} = \mathbf{3_2^3 3_2^{\left(3^{3^3}\right)}} = \mathbf{3_2^3 3_2^{(7{,}625{,}597{,}484{,}987)}}$$

General Case ($n \geq 1$): Iterated $(n-1)$ level operation:

$$a_n^b = a \uparrow^n b = a \uparrow^{(n-1)} \left(a \uparrow^{(n-1)} (\dots a \uparrow^{n-1} a)\right), (b \text{ copies of } a)$$

Example 5;

$$\mathbf{5} \uparrow\uparrow\uparrow \mathbf{4} = 5 \uparrow\uparrow (5 \uparrow\uparrow (\mathbf{5} \uparrow\uparrow \mathbf{5})) = 5 \uparrow\uparrow (5 \uparrow\uparrow (\mathbf{5} \uparrow \mathbf{5} \uparrow \mathbf{5} \uparrow \mathbf{5} \uparrow \mathbf{5})),$$

$$\mathbf{5} \uparrow\uparrow\uparrow \mathbf{4} = \mathbf{5_3^4} = \mathbf{5_2^5}\left(5_2^{(5_1 5_1 5_1 5_1 5_1)}\right) = \mathbf{5_2^5}\left(5_2^{\left(5^{5^{5^{5^5}}}\right)}\right)$$

By defining the base (a), height (b), and level (n), it simplifies the notation and makes it easier to interpret and calculate extremely large values. Additional examples such as:

$$\mathbf{2}\left(2^{2^{2^{2^{2^{2^{2^{2^{2^{2^{2^{2^{2^{2^{2^{2}}}}}}}}}}}}}}}\right) = 2 \to 15 \to 2 \to 2 \to 1 = \mathbf{2_2^{16}}$$

$$\mathbf{2}^{4^{4^{4^4}}} = 2 \to (4 \to 4 \to 4 \to 4 \to 4) \to 1 = \mathbf{2_1^4}\left(\mathbf{4_2^5}\right)$$

$$\mathbf{2}^{4^{5^{5^5}}} = 2 \to 4 \to (5 \to (5 \to 5 \to 1) \to 1) \to 1 = \mathbf{2_1^4}\left(\mathbf{5_2^3}\right)$$

$$\mathbf{2}^{3^{5^{5^4}}} = 2 \to 3 \to (5 \to (5 \to 4 \to 1) \to 1) \to 1 = \mathbf{2_1^3}\left(\mathbf{5_2^2}\right)^{\mathbf{4}}$$

$$\boldsymbol{a}^{a^{a^{a^{(3.567)}}}} = a \to (a \to (a \to (a \to 1) \to 3.567 \to 1) \to 1) \to 1$$
$$= \left(\boldsymbol{a_2^4}\right)^{(3.567)}$$

4.2 Discussion: For further clarification, a practical application of the new notation will be demonstrated on a large and diversed set of very big numbers, encompassing the widest possible range of number cases that can be written in this notation, as shown in the following **Table 1**.

Table 1: A set of detailed examples written by Al-Ossmi's arrow- free notation:

Al-Ossmi's notation	*Interpretation*
10_1^2	$10 \uparrow 2 = 10^2 = 100$
10_2^2	$10 \uparrow\uparrow 2 = 10^{10} = 10{,}000{,}000{,}000$
10_2^3	$10 \uparrow\uparrow 3 = 10 \uparrow 10 \uparrow 10$
10_2^4	$10 \uparrow\uparrow 4 = 10 \uparrow 10 \uparrow 10 \uparrow 10$
10_3^3	$10 \uparrow\uparrow\uparrow 3 = 10 \uparrow\uparrow 10 \uparrow\uparrow 10$
10_2^6	$10 \uparrow\uparrow 6 = 10 \to 6 \to 2$
10_3^{11}	$10 \uparrow\uparrow\uparrow 11$, This is simply 10 raised to the power of 11.
10_1^{64}	$10^{4^3} = 10 \uparrow (4 \uparrow 3) = 10 \uparrow 64 = 10 \to (64) \to 1$
3_2^3	$3 \uparrow\uparrow 3 = (3 \uparrow 3 \uparrow 3) = (7{,}625{,}597{,}484{,}987)$
$4_3^2 = 4_2^4$	$4 \uparrow\uparrow\uparrow 2 = 4 \uparrow\uparrow 4 = (4 \uparrow 4 \uparrow 4 \uparrow 4) = 4^{4^{4^4}}$
5_3^4	$5 \uparrow\uparrow\uparrow 4 = 5 \uparrow\uparrow 5 \uparrow\uparrow (5 \uparrow\uparrow 5)$, it is a tetration of 5 repeated 4 times.
3_4^3 $3_{G_n}^3$ $3_{G_{63}}^3$	Graham's Number G: $3 \uparrow^4 3 = 3 \to 3 \to 4$ $G_{n+1} = 3 \uparrow^{G_n} 3$ starting from G_1 to G_{64} $G_{n+1} = 3_3^{G_n}$, for 64 steps: $G_{63+1} = 3_3^{G_{63}}$
$3_{G_{64}}^{10}$	$3 \uparrow^{G_{64}} 10 = 3 \to 10 \to G_{64}$
5_{34}^4	$5 \uparrow^{34} 4 = 5 \to 4 \to 34$
$5_{34}^{\left(411^{300^{12}}\right)}$	$5 \uparrow^{34} \left(411 \uparrow^{300^{12}}\right) = 5 \to (411 \to 300 \to 12) \to 34$
$10_2^{\left(3^{4^{2^5}}\right)}$	$10^{10^{\left(3^{4^{2^5}}\right)}} = 10 \uparrow 10 \uparrow (3 \uparrow 4 \uparrow 2 \uparrow 5)$
$10^{6.12.200.3}$	$10^{6^{12^{200^3}}} = 10 \uparrow (6 \uparrow 12 \uparrow 200 \uparrow 3)$
Al-Ossmi's notation	Interpretation
$10^{3.4.3402.5.3.4.2001}$	$8^{3^{4^{3402^{5^{3^{4^{2001}}}}}}} =$ $= 8 \uparrow \left(3 \uparrow \left(4 \uparrow (3402 \uparrow 5 \uparrow 3 \uparrow 4 \uparrow 2001)\right)\right)$
$10_2^{10.10.303}$	$10 \uparrow\uparrow 10 \uparrow 10 \uparrow 303 = 10 \uparrow\uparrow (10 \uparrow 10 \uparrow 303)$
$100_1^{10^3} = 100_1^{1000}$	$100^{1000} = 100^{10^3}$
100_2^5	$100^{100^{100^{100^{100}}}}$
$100_2^{4^{(12)}} = 100_2^{4.12}$	$100^{100^{100^{100^{12}}}}$
$10_2^{3\times10.(3{,}000{,}000{,}003)}$	$10 \uparrow\uparrow (3 \times 10 \uparrow 3{,}000{,}000{,}003)$

Let's apply the new Al-Ossmi's free arrows notation in case of $\boldsymbol{a_n^{b.c}}$,to describe such the number:$a^{\left(a^{a^c}\right)}$. The given number is a power tower with the base *a* and height 3 exponents, with the topmost exponent being *c*. From the notation definition, the height or number of iterations in the power tower is *b*, and *n* is the level or number of arrows (exponentiation depth).

Example and interpretation: $\boldsymbol{a_2^{(b\ copies\ of\ a)^{(c)}}} = \boldsymbol{a_2^{(b\ copies\ of\ a).c}}$.

Base $(a) = 10$

Height **(***b***)**: The height of the power tower here includes the topmost exponent and any additional exponents as iterations; $\left(a^{a^c}\right)$:

Since the topmost exponent is $\mathbf{10}^{\left(\mathbf{10}^{\mathbf{10}^{12}}\right)}$, we adjust the height to reflect this deep nesting. Level (n): Since this is straightforward exponentiation (second level of up-arrow), $n = 2$.

We describe it in a notation reflecting $\left(3^{(12)}\right)$ height, combining the depth and extending beyond simple iteration count. If we consider it as an iteration extending beyond the simple height, we express it as: $10^{10^{10^{12}}} = 10_2^{3^{(12)}} = 10_2^{3.12}$,

This flexibility of Al-Ossmi's notation with forms; $\boldsymbol{a_n^{b.c}}$ or $\boldsymbol{a_n^{b.c.d.e.f.g.h}}$ allows for a compact and structured way to represent extremely large numbers. These $(b.c.d.e)$ are components to describe complex and extended depth and extend the depth further, representing additional layers of power towers or nested operations. By accurately reflecting the base, height (with nuanced depth like $b.c.d$, indicating an extended height in the power tower), and level of exponentiation, it simplifies understanding and interpreting large numbers. The use of multiple components separated by dots allows for a detailed and nuanced representation of the structure of the large number. This notation captures the nuances of the structure of these numbers, including the base, height, depth, and level of operations, making it easier to understand and work with extremely large values.

The original estimate is then when $(n > 1)$, the value of b indicates to the tetration of the base, a. More precisely, the examples:

$$\mathbf{2_1^3} = 2 \uparrow 3 = \mathbf{2^3} = 8,$$

$$\text{whereas; } \mathbf{2_2^3} = 2 \uparrow\uparrow 3 = 2 \uparrow (2 \uparrow 2) = \mathbf{2^{(2^2)}} = \mathbf{16}$$

$$\text{note that; } \mathbf{2_3^3} = 2 \uparrow\uparrow\uparrow 3 = 2 \uparrow\uparrow (2 \uparrow\uparrow (2 \uparrow 2 \uparrow 2)) = 2 \uparrow\uparrow \left(2 \uparrow\uparrow \left(\mathbf{2^{2^2}}\right)\right)$$

Therefore, compared with notations such as Conway's chained and Knuth's, the value of n is related to the number of arrows, while it is by Al-Ossmi's notation indicates that we deal with a tetration process, thus value of n in Al-Ossmi's does not help to determine the exact value of the number. Al-Ossmi's arrow-free notation easily helps to write out extremely large power towers, as it is listed in **Table 2** and **3**.

Table 2: Systems of key Notations for Arithmetic Operators.

Arithmetic	Standard	Ackermann's	Knuth's	Conway's	Al-Ossmi's
Exponentiation	a^b	ack(a,b,2)	$a \uparrow b$	$a \to b \to 1$	$\boldsymbol{a^b}$
Tetration	${}^{b}a$	ack(a,b,3)	$a \uparrow\uparrow b$	$a \to b \to 2$	$\boldsymbol{a_2^b}$
Pentation	b^a	ack(a,b,4)	$a \uparrow\uparrow\uparrow b$	$a \to b \to 3$	$\boldsymbol{a_3^b}$
Hexation	-	ack(a,b,5)	$a \uparrow\uparrow\uparrow\uparrow b$	$a \to b \to 4$	$\boldsymbol{a_4^b}$
Fundamental rule	-	ack(a,b,n)	$a \uparrow^n b$	$a \to b \to n$	$\boldsymbol{a_n^b}$

Where:
a, b, n are positive integers, hence:
a is the base number,
b copies of a,
n is the arrow number.

Table 3: Al-Ossmi's free arrows notation of a set of extremely huge numbers in form of titration exponential express.

Number Name	*Exponential Notation*	*Al-Ossmi's notation*
Skewes number	$10^{10^{10^{34}}}$	$10_2^{3.34}$
Pentalogue	$10^{10^{10^{10^{10}}}}$	10_2^5
Millyllion	$10^{2^{1002}}$	$10_1^{2.1002}$
Gigillion	$10^{3\times10^{3,000,000,000+3}}$	$10_1^{3\times10^{3,000,000,000+3}}$
Ecetonplex	$10^{10^{303}}$	$10_2^{2.303}$
Heskironduplex	$10^{10^{10^{600}}}$	$10_2^{3.600}$
Googolduplexichime	$10^{10^{10^{1000}}}$	$10_2^{3.1000}$
Guppyduplexitoll	$10^{10^{10^{2000}}}$	$10_2^{3.2000}$
Googolduplexibell	$10^{10^{10^{5000}}}$	$10_2^{3.5000}$
Millinillion	10^{3003}	10_1^{3003}
Millinillinillion	$10^{3000003}$	$10_1^{3000003}$
Hepta-taxis	$10 \uparrow\uparrow\uparrow 7$	10_3^7
Hexa-taxis	$10 \uparrow\uparrow\uparrow 6$	10_3^6
Penta-taxis	$10 \uparrow\uparrow\uparrow 5$	10_3^5
Boogafive	$5 \uparrow\uparrow\uparrow 5$	5_3^5
Tetra-taxis	$5 \uparrow\uparrow\uparrow 4$	5_3^4
Gigaexpofaxul	$10 \uparrow\uparrow\uparrow (5+98)$	$10_3^{(5+98)}$
Two	$2 \uparrow 1$	$2_1^1 = 2^1 = 2$

5. Conclusions

In this paper, we introduce a novel notation for expressing extremely large numbers, named Al-Ossmi's notation after its creator. This notation aims to compactly represent large numbers by providing a clear structure that shows the base, the level of iteration, and the depth of the operation. By doing so, it offers an efficient and unambiguous method for handling vast numerical values, making it a valuable tool for mathematicians and computer scientists.

Al-Ossmi's arrow-free notation is defined as; a_n^b , $a_n^{b.c}$, or $a_n^{b.c.d.e}$, where:

- *a*: The base number.
- *b,c,d,e etc.*: The number of iterations or the height of the power tower.
- *n*: The level of operation or the number of arrows in Knuth's notation.

The original estimate is then this notation can be extended to include more complex structures, such as a_n^b , $a_n^{b.c}$, or $a_n^{b.c.d.e.f.g}$, to represent additional levels of nested operations, where *d* and *c*, are variables. Al-Ossmi's arrow-free notation simplifies the representation of very large numbers by using a compact form that corresponds to $(a \uparrow^n b)$ in Knuth's notation

and $a \to b \to n$ in the Conway's chained arrow notation. It combines these notations into a concise and easily readable format, reducing the complexity and length of numerical expressions. This notation is more standardized and better recognized within the mathematical community, making it effective for communicating and working with extremely large numbers. It is less cumbersome than writing multiple up-arrows or chaining arrows and is easy to write and understand once the rules are clear. To facilitate the adoption of Al-Ossmi's notation, detailed documentation and examples are provided. This includes practical applications in various fields such as physics, astronomy, and large number theory, where extremely large numbers are common. Al-Ossmi's arrow-free notation utilities in different fields, in physics or astronomy, this notation can simplify expressions and calculations involving vast quantities. In combinatorial mathematics or proofs involving large number theory, it provides clarity and precision.

6. Acknowledgements

Grateful acknowledgment is made to the following individuals for their significant support, time, and kindness in the production of this paper: my family, including Mrs. Angham Saleh, Noor Al-zehraa, Nada, Fatima Al-zehraa, and Omneya.

Author's declaration: Conflicts of Interest: None. I hereby confirm that all figures and tables in the manuscript are original. Additionally, figures and images not created by me have been included with permission for re-publication, as documented in the manuscript.

7. References

[1] Rucker R. Infinity and the Mind: The Science and Philosophy of the Infinite. Princeton (NJ): Princeton University Press; 2019.

[2] Chambart P, Schnoebelen Ph. Pumping and counting on the Regular Post Embedding Problem. In: Proceedings of ICALP 2010. Lecture Notes in Computer Science. Vol. 6199. Springer; 2010. p. 100–111.

[3] Munafo R. Versions of Ackermann's Function. Large Numbers at MROB [Internet]. 2019 [cited 2025 Apr 26]. Available from: https://mrob.com/pub/math/largenum-ackermann.html

[4] Dufourd C, Jancar P, Schnoebelen Ph. Boundedness of Reset P/T nets. In: Proceedings of ICALP'99. Lecture Notes in Computer Science. Vol. 1644. Springer; 1999. p. 301–310.

[5] Figueira D, Figueira S, Schmitz S, Schnoebelen Ph. Ackermann and primitive recursive upper bounds with Dickson's lemma. In preparation.

[6] Munafo R. Inventing New Operators and Functions. Large Numbers at MROB [Internet]. 2019 [cited 2025 Apr 26]. Available from: https://mrob.com/pub/math/largenum-invent.html

[7] Arjun K, Rathie JM. Generalizations and variants of Knuth's old sum. Combinatorics (math.CO); Complex Variables (math.CV) [Preprint]. 2022. https://doi.org/10.48550/arXiv.2205.05905

[8] Caldarola F, Maiolo M. On the topological convergence of multi-rule sequences of sets and fractal patterns. Soft Comput. 2020;24(23):17737–49.

[9] Caldarola F, Maiolo M, Solferino V. A new approach to the Z-transform through infinite computation. Commun Nonlinear Sci Numer Simulat. 2020;82:105019.

[10] Conway JH, Guy RK. The Book of Numbers. New York (NY): Springer-Verlag; 1996. p. 59–62.

[11] Caldarola F, d'Atri G, Maiolo M, Pirillo G. The sequence of Carboncettus octagons. In: Sergeyev YD, Kvasov D, editors. Numerical Computations: Theory and Algorithms NUMTA 2019. Lecture Notes in Computer Science. Vol. 11973. Cham: Springer; 2020. p. 373–80.

[12] Antoniotti L, Caldarola F, d'Atri G, Pellegrini M. New approaches to basic calculus: an experimentation via numerical computation. In: Sergeyev YD, Kvasov D, editors. Numerical Computations: Theory and Algorithms NUMTA 2019. Lecture Notes in Computer Science. Vol. 11973. Cham: Springer; 2020. p. 329–42.

[13] Antoniotti L, Caldarola F, Maiolo M. Infinite numerical computing applied to Hilbert's, Peano's, and Moore's curves. Mediterr J Math. 2020;17(3):99.

[14] Caldarola F, Cortese D, d'Atri G, Maiolo M. Paradoxes of the infinite and ontological dilemmas between ancient philosophy and modern mathematical solutions. In: Sergeyev YD, Kvasov D, editors. Numerical Computations: Theory and Algorithms NUMTA 2019. Lecture Notes in Computer Science. Vol. 11973. Cham: Springer; 2020. p. 358–72.

[15] Caldarola F, d'Atri G, Mercuri P, Talamanca V. On the arithmetic of Knuth's powers and some computational results about their density. In: Sergeyev YD, Kvasov D, editors. Numerical Computations: Theory and Algorithms NUMTA 2019. Lecture Notes in Computer Science. Vol. 11973. Cham: Springer; 2020. p. 381–8.

[16] Caldarola F, Gianfranco D. On the Arithmetic of Knuth's Powers and Some Computational Results about Their Density. In: Sergeyev YD, Kvasov D, editors. Numerical Computations: Theory and Algorithms. Part I, Chapter: 33. Lecture Notes in Computer Science. Vol. 11973. Cham: Springer; 2020. p. 381–8. https://doi.org/10.1007/978-3-030-39081-5_33.

Al-Kitab Journal for Pure Sciences (2025); 9(2):62-83.
https://doi.org/10.32441/kjps.09.02.p5

Al-Kitab Journal for Pure Sciences
ISSN: 2617-1260 (print), 2617-8141(online)

https://isnra.net/index.php/kjps

Approximate Solutions of Nonlinear Integral Equations Using the Cubic B-Spline Scaling Method

Mohammed Jabbar Adaay Al-Sharea

Department of Mathematics, College of Science, University of Azad, Iran.

Corresponding Author: Mohammedalshara1975@gmail.com

Citation: AL-SHAREA MJA. Approximate Solutions of Nonlinear Integral Equations Using the Cubic B-Spline Scaling Method. Al-Kitab J. Pure Sci. [Internet]. 2025 Apr. 28;9(2):62-83. DOI: https://doi.org/10.32441/kjps.09.02.p5.

Keywords: Fixed Point Method, Non-Linear Fredholm Integral Equation, Cubic B-Spline Wavelets, Scaling Functions, Darbo Condition.

Received 31 Jul. 2024
Accepted 15 Oct. 2024
Available online 28 Apr. 2025

Abstract:

This paper examines a category of general nonlinear integral equations. These equations also include many special cases, such as functional equations and nonlinear integral equations of the Volterra type. In order to approximate the solutions to numerous physical, chemical, and biological issues, we implemented an approach that incorporates the fixed-point method and semi-vertical cubic scaling functions. We also obtain a numerical solution to the integral equation. Numerical examples illustrate the accuracy and validity of this method.

Keywords: Fixed Point Method, Non-Linear Fredholm Integral Equation, Cubic B-Spline Wavelets, Scaling Functions, Darbo Condition.

الحلول التقريبية للمعادلات التكاملية غير الخطية باستخدام طريقة قياس الشريحة B المكعبة

محمد جبار عداي الشرع

قسم الرياضيات/ التحليل العددي/ كلية العلوم/ جامعة آزاد الإسلامية/ إيران
Mohammedalshara1975@gmail.com

الخلاصة:

تتناول هذه الورقة فئة من المعادلات التكاملية غير الخطية العامة. تتضمن هذه المعادلات أيضًا العديد من الحالات الخاصة، مثل المعادلات الوظيفية والمعادلات التكاملية غير الخطية من نوع فولتيرا. من أجل تقريب الحلول للعديد من القضايا الفيزيائية والكيميائية والبيولوجية، قمنا بتنفيذ نهج يتضمن طريقة النقطة الثابتة ودوال التحجيم التكعيبي شبه العمودية، نحن نحصل أيضًا على حل عددي للمعادلة التكاملية. توضح الأمثلة العددية دقة وصلاحية هذه الطريقة.

الكلمات المفتاحية: طريقة النقطة الثابتة؛ معادلة فريدهولم التكاملية غير الخطية؛ الموجات المكعبة ذات شكل متعرج ؛ وظيفة القياس، شرط داربو.

1. Introduction:

An integral equation is an equation with an unknown function, x(s), under the integral sign [1-4]. The conventional form of this Equation in x(s) is as follows.

$$x(t) = f(t) + \lambda \int_{9(t)}^{f(t)} k(t.s)u(s)\,ds, \qquad (1)$$

k(t,s) is a function that consists of two variables and is referred to as the kernel of the Equation, while λ is a constant parameter. The limits of integration are β(t) and g(t). The function x(s) appears, defined under the integral sign, as well as the interior and exterior of the sign. The functions f(t) and k(t,s) have been given previously, and the limits of integration g(t) and f(t) can be constants, variables, or a combination of a constant and a variable. Integral equations have multiple forms, and there are two ways to distinguish the Equation, which depend on the limits of integration.

1- If the limits of integration are constant, the Equation is referred to as the Fredholm equation and is expressed in the following representation.

$$x(t) = f(t) + \lambda \int_{a}^{b} k(t.s)u(s)\,ds \qquad (2)$$

2- When one of the limits of integration is a constant, and the other is a variable, the equation is considered a Volterra equation and is expressed in the following manner.

$$x(t) = f(t) + \lambda \int_{a}^{x} k(t.s)u(s)\,ds, \qquad (3)$$

Additionally, two varieties of equations are contingent upon the form of the function x(s), which is defined as follows:

1- The integral Equation is referred to as a Volterra or Fredholm equation of the first kind if the unknown function x(s) is present exclusively within the integral sign.

2- A Volterra or Fredholm equation of the second kind is defined as an equation in which

The unknown function u(s) is present both within and outside the integral sign. Suppose the Function f(s) equals zero in Volterra or Fredholm equations. The integral Equation is referred to as a homogeneous equation. The Fredholm integral equation of the second kind is called nonlinear if the function x(s) that appears under the integral sign is nonlinear. Additionally, it is expressed in the subsequent manner ($e^{-cos^2(\frac{1}{2})} . sin^2(x)$…..), etc. Accordingly, the Equation has been formulated as follows.

$$x(t) = f(t) + \lambda \int_{9(t)}^{f(t)} k(t.s) F\big(u(s)\big)\, ds, \qquad \textbf{(4)}$$

We want to clarify in this introduction that Fredholm's integral equations can be derived from boundary value problems, and it is essential to remember Eric Fredholm's work on integral equations and the applied theory from the year (1866-1927). The Swedish scientist developed the theory of integral equations, and his research paper, presented in 1903 in the Acta Mathematica, played a fundamental role in establishing operator theory. Integral equations play a prominent role in applied mathematics, and non-linear integral equations have significant practical importance, as shown by numerous studies in the field of knowledge, encompassing biology, traffic theory, optimal control theory, economics, and other engineering sciences **[5-8]**. Numerous sources have examined functional integral equations' existence and analytical behaviour **[5, 9, 10]** using non-compactness measure techniques and fixed-point theories. In references **[10]**, scholars Jalilian and Aghanjani presented numerous results related to the existence and unified universal gravity and the local gravity of solutions to the functional integral Equation.

$$x(t) = (Kx)(t) = f\left(t, x\big(\alpha(t)\big), \int_0^{\beta(t)} u\left(t, s, x\big(\gamma(s)\big)\right) ds\right), \qquad t \in [0, \infty] \qquad \textbf{(5)}$$

These results were presented through the measure of non-compactness. These results were reached by the scientists Jalilian and Aghanjani, who worked to improve and expand upon the findings that emerged in other studies. Most functional integral equations are not amenable to analytical solutions; therefore, numerical methods are indispensable. Consequently, numerical methods are implemented to ascertain an Approximately calculated solution. The numerical solution of integral equations can be approached using projection, iterative, and Nystrom methods **[11-12]**; the references include the definitions of the collocation approaches **[13, 14-17]**. Galerkin methods are used to find numerical solutions for Fredholm integral equations, as outlined in the references **[13, 14, 17-21]** Spline functions, wavelets, product integration,

homotopy analysis approaches, homotopy perturbation, Adomian decomposition method, interpolation of polynomials methods, suboptimal trajectories, and multigrid methods are all viable alternatives. The Nystrom procedures are mentioned in the references **[11-14, 21, 22]**. In a few articles, the approximate numerical representation of the solution has been analyzed. Composition techniques are the foundation of Numerical approaches to solving functional integral equations **[23-30]**, homotopy perturbation methods **[25,26-32]**, Lagrange and Chebyshev interpolation methods **[27,28,32-38]**. The various studies in most numerical methods addressed by previous research transform the integral Equation into a linear or non-linear algebraic equation system. This paper presents a numerical solution for an integral equation utilizing a hybrid iterative approach that combines the fixed-point method with trapezoidal scaling functions. The method does not rely on any equation-solving system. The objective of employing this method for non-linear functional integral equations is to achieve a more precise solution with less error. We successfully attained favorable outcomes with this strategy and further elaborated on the findings presented in other investigations. The investigation is structured as follows: In the first section, the scholars Jalilian and Aghanjani provide an introduction to integral equations and a definition of equation number **(5)**. The second section of the research provides the definitions necessary for effectively composing this scientific paper. In the third section, we examined several findings that pertain to having existed and the allure of the aforementioned integral Equation. In the fourth section, we introduced the development of cubic B-spline functions within the interval [0.1], as documented in sources **[39-42]**. In the fifth section, we provide an explanation of the strategy used in this research's solution method and the method by which we approach the genuine solution. Conversely, in the final section, we provided numerical examples to demonstrate the precision of this methodology and contrasted the accuracy of these numerical results with those from prior research.

2. Background Concepts

We provide some definitions and findings in this section relevant to the rest of the paper. BC($\mathcal{R}_+$) is a branch with limited space, but operations continue on $\mathcal{R}_+$, furnished with a conventional standard. $||z|| = \sup\{|z(t)| : t \in \mathcal{R}_+, \}$.Let E Let be an infinite-dimensional Banach space containing the zero element. element θ and norm $\|\cdot\|$ Indicate the closed ball with radius r and center at x by writing B(z, r). Closure and convex property of Z, a nonempty subset of E, are shown by the symbols Z and Conv Z, respectively. Let also m_E be all relatively compact combinations: their family and n_E denote the family of all nonempty bounded subsets of E. We employ the concept found in **[4]** for the non-compactness metric.

Definition 1. When a mapping v: $m_E \rightarrow \mathcal{R}_+$ meets specific requirements, it can indicate non-compactness in E.

1. a family ker u = {X ∈ m_E : u(x) = 0} is not-empty and ker x ⊂ n_E.
2. X⊂ Y ⇒ v(X) ≤ v(Y).
3. u(Z) = u(Z).
4. u(Conv x) = u(x).
5. u(λX + (1 − λ)Y) ≤ λu(x) + (1 − λ)u(Y) for λ∈ [0, 1].
6. write an equation of closed originating from sets (Xn) from nE such that X_{N+1} ⊂ Xn(n = 1, 2, . . .) and if $\lim_{n\to\infty} x(X) = 0$ consequently, the intersection emerged. $X_\infty = \bigcap_{n=1}^{\infty} X_n$ is nonempty. Given the Example of Banas and Goebel, we present a Darbo-type fixed-point theorem.[9]

Theorem (1): I will define E as a closed, convex, limited, and not-empty subset of the Banach space divided into sub-sets C.

Let L: E → E a constant was present. Mapping presupposes that there is a consistent. Z.∈ [0, 1) thus, u(F(X)) ≤ kw(X) before every non-empty sub-group of C that. Subsequently, L contains a fix-point within the set C. For any not empty bounding sub-set X of BC($\mathbb{R}_+$), x ∈ X, T >0 and ∈ ≥ 0 let

$$w^T(x,\epsilon) = \sup\{|x(s) - x(s)|: t, s \in [0,T], |t-s| \leq \in\}$$

$$w^T(x,\epsilon) = \sup\{u^T(x,\epsilon): x \in X\},$$

$$w_0^T(x) = \lim_{€\to\infty} u_0^T(x,€),$$

$$w_0^T(x) = \lim_{T\to\infty} u_0^T(x),$$

X(t) = x(t) : the variables x ∈ X},

diam the function X(t) = sup{|x(t) − y(t)| : x, y ∈ X

And

$$\mu(X) = w_0\ (x) + \lim_{T\to\infty} \text{sup diam the function X(t)} \qquad (6)$$

Banas has demonstrated in [43] that the function μ measures non-compactness via space. BE($\mathcal{R}_+$). The solution to the equation as operative from the BE($\mathcal{R}_+$) included in BE ($\mathcal{R}_+$)

$$(F\ x)(t) = x(t) \qquad (7)$$

We will discuss the introduction: the attractiveness to Eq. (7).

Definition 2: [9] If a ball B(x_0, r) exists in space, then solutions to Eq. (7) are locally attractive. BC($\mathbb{R}_+$) so that for Any two solutions that are arbitrary to Eq. (7) that are part of B(x_0, r) ∩Ω that is in our possession.

$$\lim_{t\to\infty}\left(x(t)-y(t)\right)=0 \quad (8)$$

Resolving the Eq. (7) is locally alluring at a uniform rate (or, similarly, asymptotic stability) if the limit (4) is consistent concerning $B(x_0,r)\cap\Omega$,

Theorem 2: There is a minimum of one solution to Eq. (5) in BC($\mathcal{R}_+$) for all of (5)'s solutions that have uniform local attraction.

Proof: This section presents a summary of the proof necessary for the subsequent sections. Refer to [10] for additional information.

First, the authors designed operator K in [2]; hence, for any x ∈ BC(R+)

$$(Hx)(t)=f\left(t,x(\alpha(t)),\int_0^{\beta(t)}u\left(t,s,x(\gamma(s))\right)ds\right),$$

(Hx) is clearly continuous on $\mathbb{R}_+$.Next, for each arbitrarily fixed t ∈ $\mathbb{R}_+$

$$|(Mx)(t)|\le n\,|x(\alpha(t))|+M_0,$$

Where $M_0=\sup\{|f(t,0,0)|:t\in R+\}+\Psi(2D)$,

$$r=\frac{M_0}{1-n}.$$

Subsequently, they demonstrated that given A set that is not vacant X ⊂ (Br), μ(HX) < nμ(X), with n ∈ U(0,1). Accordingly, the Eq. (1) of functional integration is at least one solution in British Columbia. ($\mathcal{R}$+), and(x) has a fixed- -point in (Br) for the operator H. based on Theorem 1. Every solution to Eq. (5) contained within the A member of the Ker μ group is ball Br

Corollary 1. If f (t, s, 0) is constrained by additional Constraints 1–4, then the solutions to the integration of the formula (5) are as follows: are generally attractive, as stated in Theory 2. Sufficient evidence. See [27].

3- Cubic B-Aspline Scaling and Wavelet Function on [0.1]

In L2(R), you can utilize scaling functions to increase the size of any function. Extending these functions outside the integration domain is possible because they are specified across the natural line. This article considers B-spline scaling functions with compact support built for the bounded interval [0,1]. When using order m semi-orthogonal B-spline scaling functions, the requirement.

$$2^{J_0}\ge g$$

Has to be met for there to be one full inner scaling function. $\omega_{4,k}^{(j)}(x)$ represents these scaling functions. We'll employ scaling functions for cubic B-splines (cardinal B-splines of order g = 4). As a cubic spline, its scaling is denoted.

$$A_4(x) = \omega_4(x) = \begin{cases} \frac{1}{6}x^3 & 0 \le x < 1 \\ \frac{1}{6}(-3x^3 + 12x^2 - 12x + 24) & 1 \le x < 2 \\ \frac{1}{6}(3x^3 - 12x^2 + 60x - 44) & 2 \le x < 3 \\ \frac{1}{6}(4 - x)^3 & 3 \le x < 4 \\ 0 & \text{otherwise} \end{cases}$$

Furthermore, the shape of its two-scale relation is

$$\omega_4(x) = \frac{1}{8}\omega_4(2x) + \frac{4}{8}\omega_4(2x-1) + \frac{6}{8}\omega_4(2x-2) + \frac{4}{8}\omega_4(2x-3) + \frac{1}{8}\omega_4(2x-4)$$

$$\omega_{4,-3}^{(3)}(x) = \begin{cases} (1-8x)^3 & 0 \le x < \frac{1}{8} \\ 0 & \text{otherwise} \end{cases}$$

With boundary scale, for example, the scaling factors used for j_0= j = 3 and m = 4 are enumerated below.

$$\omega_{4,-2}^{(3)}(x) = \begin{cases} 896x^3 - 288x^2 + 24x & 0 \le x < \frac{1}{8} \\ 2(1-4x)^3 & \frac{1}{8} \le x < \frac{2}{8} \\ 0 & \text{otherwise} \end{cases}$$

$$\omega_{4,-1}^{(3)}(x) = \begin{cases} -\frac{1408}{3}x^3 + 96x^2 & 0 \le x < \frac{1}{8} \\ \frac{896}{3}x^3 - \frac{576}{3}x^2 + 36x - \frac{3}{2} & \frac{1}{8} \le x < \frac{2}{8} \\ -\frac{1}{6}(4x-3)^3 & \frac{2}{8} \le x < \frac{3}{8} \\ 0 & \text{otherwise} \end{cases}$$

$\omega_{4,-1}^{(j)}(x) = \omega_{4,k}^{(3)}(2^{j-3}x), k = -3,-2,-1 \quad j = 3,4 \dots \dots \dots$

$\omega_{4,5}^{(3)}(x) = \omega_{4,-1}^{(3)}(1-x),$

$\omega_{4,6}^{(3)}(x) = \omega_{4,-2}^{(3)}(1-x)$

$\omega_{4,7}^{(3)}(x) = \omega_{4,-3}^{(3)}(1-x)$

$\omega_{4,k}^{(j)}(x) = \omega_{4,2^j-k-4}^{(3)}(1-2^{j-3}x), \quad k = 2^j - 3, \dots \dots, 2^j - 1, \quad j = 3,4 \dots \dots \dots$

Inner scaling:

$$\omega_{4,0}^{(3)}(x)=\begin{cases}\frac{256}{3}x^3 & 0\le x<\frac{1}{8}\\ -256x^3-128x^2-16x+\frac{2}{3} & \frac{1}{8}\le x<\frac{2}{8}\\ 256x^3-256x^2+80x-\frac{22}{3} & \frac{2}{8}\le x<\frac{3}{8}\\ \frac{32}{3}(1-2x)^3 & \frac{3}{8}\le x<\frac{1}{2}\\ 0 & \text{Otherwise}\end{cases}$$

$$\omega_{4,1}^{(3)}(x)=\begin{cases}\frac{1}{6}(8x-1)^3 & \frac{1}{8}\le x<\frac{2}{8}\\ -256x^3+224x^2-60x+\frac{31}{6} & \frac{2}{8}\le x<\frac{3}{8}\\ 256x^3-352x^2+156x-\frac{131}{6} & \frac{3}{8}\le x<\frac{1}{2}\\ \frac{1}{6}(5-8x)^3 & \frac{1}{2}\le x<\frac{5}{8}\\ 0 & \text{Otherwise}\end{cases}$$

$$\omega_{4,2}^{(3)}(x)=\begin{cases}\frac{4}{3}(4x-1)^3 & \frac{2}{8}\le x<\frac{3}{8}\\ -256x^3+320x^2-128x+\frac{50}{3} & \frac{3}{8}\le x<\frac{1}{2}\\ 256x^3-448x^2+256x-\frac{142}{3} & \frac{1}{2}\le x<\frac{5}{8}\\ \frac{1}{6}(6-8x)^3 & \frac{5}{8}\le x<\frac{3}{4}\\ 0 & \text{Otherwise}\end{cases}$$

$$\omega_{4,3}^{(3)}(x)=\begin{cases}\frac{1}{6}(8x-3)^3 & \frac{3}{8}\le x<\frac{1}{2}\\ -256x^3+416x^2-220x+\frac{229}{6} & \frac{1}{2}\le x<\frac{5}{8}\\ 256x^3-544x^2+380x-\frac{521}{6} & \frac{5}{8}\le x<\frac{3}{4}\\ \frac{1}{6}(7-8x)^3 & \frac{3}{4}\le x<\frac{7}{8}\\ 0 & \text{Otherwise}\end{cases}$$

$$\omega_{4,4}^{(3)}(x)=\begin{cases}\frac{1}{6}(8x-4)^3 & \frac{1}{2}\le x<\frac{5}{8}\\ -256x^3+416x^2-220x+\frac{229}{6} & \frac{5}{8}\le x<\frac{3}{4}\\ 256x^3-544x^2+380x-\frac{521}{6} & \frac{3}{4}\le x<\frac{7}{8}\\ \frac{1}{6}(7-8x)^3 & \frac{7}{8}\le x<1\\ 0 & \text{Otherwise}\end{cases}$$

$$\omega_{4,k}^{(j)}(x) = \omega_{4,k}^{(3)}\left(2^{j-3}x - k\right), \quad k = 0,1, \dots \dots .. 2^j - 4 \quad j = 3,4 \dots \dots \dots$$

$$\psi_4(x) = \frac{1}{8!}\omega_4(2x) + \frac{124}{8!}\omega_4(2x-1) + \frac{1677}{8!}\omega_4(2x-2) + \frac{7904}{8!}\omega_4(2x-3) + \frac{18482}{8!}\omega_4(2x-4) - \frac{24264}{8!}\omega_4(2x-5) + \frac{18482}{8!}\omega_4(2x-6) - \frac{7904}{8!}\omega_4(2x-7) + \frac{1677}{8!}\omega_4(2x-8) - \frac{124}{8!}\omega_4(2x-9) + \frac{1}{8!}\omega_4(2x-10)$$

Cubic B-spline wavelet $\psi_4(x)$ is shown in Fig.3. The system's inner and border wavelet analysis is obtained through the application of **[8, 11].**

4. Functional Approximation

A function f (x) specified in the interval [0,1] can be rendered in the cubic B-spline scale field FJ_0

For any fixed positive integer J_0 as

$$\mathrm{g(x)} = \sum_{i=-3}^{2^{j_0-1}} c_{j_0.i}\varphi_{4.i}^{(3\ )}(x) + \sum_{i=3}^{j_0}\sum_{k=-3}^{2^i-4} d_{i.k}\Psi_{4.k}^{(i)}(x) = C^T\Psi(x) \qquad (9)$$

Where $\varphi_{4.i}^{(j_0)}$ and $\Psi_{4.k}^{(i)}$are wavelet and scaling functions should eq (9)'s infinite series be shortened, respectively. And for j=3, it can be expressed as follows:

$$\mathrm{g(x)} = \sum_{i=-3}^{7.} c_{j_0.i}\varphi_{4.i}^{(j_0)}(x) + \sum_{i-3}^{j_0}\sum_{k=-3}^{2^i-4} d_{i.k}\Psi_{4.k}^{(i)}(x) = C^T\Psi_{\cdot}(\mathrm{x}) \qquad (10)$$

Where C and $\Psi(x)$ are $(2^{j_0+1}+5)$x1 vectors given bye

$$\mathrm{C}=\text{"}[c_{-3,\dots\dots\dots},c_{7,,}d_{3,-3,\dots\dots\dots\dots}d_{3.4\dots\dots\dots\dots\dots}d_{j0,-3\dots\dots\dots\dots\dots}d_{j2^j-4\ ,}]^{.T}\text{ "} \qquad (11)$$

$$\Psi = [\varphi_{4.-3}^{(3)} \dots \dots .. \varphi_{4.-3}^{(3)}, \Psi_{4.-3}^{(3)} \dots \Psi_{4.-3}^{(3)} \dots \Psi_{4.4}^{(3)} \dots \dots \Psi_{j_0.2^j-3}^{(3)}]^{.T} \qquad (12)$$

With

$$C_1 = \int_0^1 f(x)\varphi_{4.1}^{(3)}(x)\,dx, \dots . i = -3, \dots \dots 7. \qquad (13)$$

$$d_{j.k} = \int_0^1 f(x)\psi_{4.1}^{(j)}(x)\,dx, \dots . j = 3, \dots J_0. k = -3 \dots \dots 2^{J_0} - 4, \qquad (14)$$

Where $\varphi_{4.1}^{(3)}$ and $\psi_{4.k}^{(j)}$ have dual purposes. of $\varphi_{4.1}^{(3)} i = -3, \dots \dots 7$ and $\psi_{4.k}^{(j)} = j = 3, \dots J_0$ According to. By using linear combinations, these can be obtained. Of

$\varphi_{4.1}^{(3)}$ and $\psi_{4.k}^{(j)}$

$$\varphi = [\varphi_{4.-3}^{(3)}{}_{,}(x)\varphi_{4.-2}^{(3)}(x) \dots \dots .. \varphi_{4.-7}^{(3)}(x)\ ]^{.T} \qquad (15)$$

$$\Psi = [\Psi_{4.-3}^{(3)}(x) \dots \Psi_{4.4}^{(3)}(x) \dots \dots \Psi_{4.2^j-4}^{(3)}(x)]^{.T} \qquad (16)$$

Using(9)-(13),(15,16) We obtain

$$\int_0^1 \phi(x)\phi^T(x)\,dx = L_1 \qquad (17)$$

$$\begin{vmatrix}
\frac{1}{56} & \frac{7}{640} & \frac{31}{13440} & \frac{1}{566720} & 0 & 0 & 0 & 0 & 0 & 0 & 0 \\
\frac{7}{640} & \frac{31}{1120} & \frac{5}{256} & \frac{29}{6720} & \frac{1}{26880} & 0 & 0 & 0 & 0 & 0 & 0 \\
\frac{31}{13440} & \frac{5}{256} & \frac{183}{4480} & \frac{283}{10080} & \frac{239}{80640} & \frac{1}{40320} & 0 & 0 & 0 & 0 & 0 \\
\frac{1}{6720} & \frac{29}{6720} & \frac{283}{10080} & \frac{151}{2520} & \frac{397}{13440} & \frac{2}{672} & \frac{1}{40320} & 0 & 0 & 0 & 0 \\
0 & \frac{1}{26880} & \frac{239}{80640} & \frac{397}{13440} & \frac{151}{2520} & \frac{397}{13440} & \frac{2}{672} & \frac{1}{40320} & 0 & 0 & 0 \\
0 & 0 & \frac{1}{40320} & \frac{2}{672} & \frac{397}{13440} & \frac{151}{2520} & \frac{397}{13440} & \frac{2}{672} & \frac{1}{40320} & 0 & 0 \\
0 & 0 & 0 & \frac{1}{40320} & \frac{2}{672} & \frac{397}{13440} & \frac{151}{2520} & \frac{283}{10080} & \frac{29}{6720} & \frac{1}{6720} & 0 \\
0 & 0 & 0 & 0 & \frac{1}{40320} & \frac{2}{672} & \frac{397}{13440} & \frac{151}{2520} & \frac{283}{10080} & \frac{29}{6720} & \frac{1}{6720} \\
0 & 0 & 0 & 0 & 0 & \frac{1}{40320} & \frac{239}{80640} & \frac{283}{10080} & \frac{183}{4480} & \frac{5}{256} & \frac{31}{13440} \\
0 & 0 & 0 & 0 & 0 & 0 & \frac{1}{26880} & \frac{29}{6720} & \frac{5}{256} & \frac{31}{1120} & \frac{7}{640} \\
0 & 0 & 0 & 0 & 0 & 0 & 0 & \frac{1}{6720} & \frac{31}{13440} & \frac{7}{640} & \frac{1}{56}
\end{vmatrix}$$

L is [11 × 11].

Assume ϕ(x) serves dual functions. Of ϕ(x) as presented in the Equation

$\varphi = [\varphi_{4.-3}^{(3)}{}_{,}(x)\varphi_{4.-2}^{(3)}(x) \ldots\ldots\ldots \varphi_{4.-7}^{(3)}(x)\ ]^T$

Using (8) (9) (11)

$$\int_0^1 \phi(x)\phi^T(x)\,dx = K11$$

where the identity matrix is [11 × 11]. Consequently, we obtain

$$\bar{w}=\phi^{-1}\omega \qquad (18)$$

Theorem 3: Let $e_j(x)$ denote the approximate errors of f in (9) using cubic B-spline scaling function within space Vj; therefore, || = O$e_j(x)$ (2^{-4j}).

Proof. By using (9) and (10). We get

$$e_j(x) = \sum_{i=j}^{\infty} \sum_{k=-3}^{2^i-4} d_{i.k} \Psi_{4.k}^{(i)}(x)$$

By putting

$c_j = max\{|\psi^1(x)|; k = -3, \dots \dots 2^i - 4\}$ We obtain

And

$$\sum_{k=-3}^{2^i-4} \left| d_{i.k} \Psi_{4.k}^{(i)}(x) \right| \leq \alpha\beta c_i \frac{2^{-4!}}{4!}$$

As a result,

$$\left| e_j(x) \right| \leq \frac{1}{4!} \alpha\beta \sum_{i=j}^{\infty} c_i 2^{-4!}$$

The current inequality allows us to get

$$\left| e_j(x) \right| = O(2^{-4!}) \quad \textbf{(19)}$$

The order of error depends on the level j. as ()demonstrates. The approximation error will decrease with increasing degree of j.

5. Method of Solvation

This part outlines our primary approach, which combines the fixed point with the cub-spline scale function. Next, we consider the method's convergence.

5.1 The New Numerical Method's Description: When considering the integral Eq. (5). To streamline this procedure, assume that each value of t is confined to the interval where the maximum level of β(t) is constant. assume t ∈ [0, a] without losing generality. Allow me to

$$0 = t_0 \leq t_1 \leq t_m = a.,$$

By G locations in [0, a].

That are evenly separated. By the proof, K is a continuous operator on (Br) and had a fix-point x in the Br—theorem 2**.** Eq. (1) has at least one solution in Br under the assumptions 1–4. Additionally, evenly locally appealing solutions for problems (1). This section provides a concise overview of the evidence required in the subsequent sections. For additional information, please refer to **[6]**.

Initially, parameter G was defined by the creators in **[6]**. in a way that ensures that for any x ∈ Br,

$$x(t) = (\mathrm{K}x)(t) = f \cdot \left(t, x(\alpha(t)), \int_0^{\beta(t)} u\left(t, s, x\left(\gamma(s)\right)\right) ds \right) \quad ,$$

Now, we treat operator H using the fix-point approach. for $\boldsymbol{x_0}$ (t) ∈ *Br* as well as Points t_I (i = 1, . . …….. ,G)

$$x_{k+1}(t_i) = (H_k)(t_i) = f \cdot \left(t_i, x_k(\alpha(t)), \int_0^{\beta(t)} u\left(t_i, s, x_k\left(\gamma(s)\right)\right) ds \right) K = 0,1,. \qquad (20)$$

The integral is to be approximated. Numerically inside the intervals [0, β(t_i)] in (21) and $x_{N+1}(t)$, we apply A Simpson rule that is composite and applies to equally distant L points. Today, we utilize cub-spline scaling methods as the foundation for our estimations. $x_{N+1}(t)$ to get ready for the following iteration. $x_{N+1}(t)$We can immediately calculate using the coefficients of the scaling functions (5)–(14) from the previous section without having to solve any systems of algebraic equations as

$z_i = \int_0^1 . x_{k+1}(t) \varpi_{4.I}^{(3)}(t)\, dt \, , J = -3, \ldots . 7$

where, as previously stated

$[\varpi_{4.-3}^{(3)}(t), \varpi_{4.-2}^{(3)}(t), \ldots \ldots . \varpi_{4.7}^{(3)}(t)]^T = P^{-1} \, [\omega_{4.-3}^{(3)}(t), \ldots \ldots . \omega_{4.7}^{(3)}(t)]^T$

Given the values of xk+1(ti) (i = 1,..., H), we compute cj. By employing the composite Simpson rule, we arrive at the following;

$x_{k+1}(t) \approx \sum_{i=-3}^{7} c_j \varphi_{4.}^{(3)}(t)$ **(21)**

We repeat the iterations until the difference between subsequent iterations, $x_k(t)$, is as small as we need for the appropriate level of precision. The end values of $x_{k+1}(t)$ correspond to an operator's M fixed point k at that level of precision. Consequently, we make an approximation of Equation (5). The following briefly describes the numerical approach.

5.2 There is a Relationship Between Teachers K and G: The teacher k represents the number of iterations within the fixed-point method, while G, according to the assumptions of Theory (2), are distant and central points within the interval [0. a]. Through the practical application of numerical examples, we continue with the iterations until we achieve a small difference between consecutive iterations. These small differences are essential for achieving high accuracy, ensuring that the terminal parameters x(t) converge to a stationary point for operator Z. Therefore, we are approaching an accurate solution to the Eq. (5). We observe the accuracy of the method used through the numerical examples in examples **[7]** and **[8]**, comparing them with the methods used in previous studies. We notice that an increase in k and G leads to an increase in accuracy and a decrease in the absolute error rate. The iterations keep increasing until the approximate solutions get closer to the exact solutions.

6- Results:

This article illustrates the method's accuracy by presenting numerical illustrations for the integral equation eq(5). We utilized the symbol k to represent the number of iterations in the fixed-point method. And K to Represent the approximate value x(t) in the iteration X(t), which is based. On this, we can calculate the absolute error ratio to x(t) in iteration k as follows: is represented with $x_{K(}t_{i)}$

$$|(X(t)) - x_{K+1}(t)|$$

Hence, it is possible to determine the most significant (absolute error in iteration K as an

$$\|x - x_K\| = max\left|x(t_{i)} - x_{K(}t_{i)}\right|$$

Furthermore, one can compute the discrepancy located between the approximate at K and K+1 as

$$\left|x_{K+1}(t) - x_{K(}t_{)}\right|.$$

As a result, we acquire

$$\|x - x_K\| = max\left|x_{K+1}(t) - x_{K(}t_{i)}\right|$$

We used different values of k and G to solve the following numerical examples. In these examples, we applied the formulas in the articles above (17) and (18) to derive approximate numerical solutions. The calculations and results were carried out using Mathematics 8.

Example (1) : non-linear Fredholm–Hammerstein equation that follows

$$x(t) = sin\left(\frac{\pi}{2}t\right) - 2te^{-t}ln(3) + e^{-t}\int_0^1 .\frac{4ts + \pi tsin(\pi s)}{x(s)^2 + s^2 + 1}ds,$$

Table 1: Absolute errors for Example 1 across various values of K.

t	k=2	k=5	k=10
0	0	0	0
0.1	0.127890×10^{-1}	0.953012×10^{-5}	0.362567×10^{-9}
0.2	0.214093×10^{-1}	0.167951×10^{-4}	0.119137×10^{-8}
0.3	0.227909×10^{-1}	0.197670×10^{-4}	0.139588×10^{-7}
0.4	0.169766×10^{-1}	0.149812×10^{-4}	0.402300×10^{-7}
0.5	0.797177×10^{-2}	0.497886×10^{-4}	0.934621×10^{-7}
0.6	0.384727×10^{-4}	0.334333×10^{-5}	0.378213×10^{-7}
0.7	0.472688×10^{-2}	0.660849×10^{-5}	0.269398×10^{-7}
0.8	0.631157×10^{-2}	0.612657×10^{-5}	0.301620×10^{-7}
0.9	0.572703×10^{-2}	0.453392×10^{-5}	0.464820×10^{-7}
1	0.410323×10^{-2}	0.290023×10^{-5}	0.301723×10^{-8}

Possesses an exclusive, precise resolution

. $x(t) = sin\left(\frac{\pi}{2}t\right)$. Functional, the value of β(t) is 1, and γ(t) is equal to t.

$$f(t, x, y) = sin\left(\frac{\pi}{2}t\right) - 2te^{-t}ln(3) + e^{-t}y$$

And

$$u(t,s,x)\frac{4ts+\pi tsin(\pi s)}{x^2+s^2+1},$$

Are continuous functions that meet Theorem 2's presumptions. see

ϕ(t) Equal t, k Equals 0, m(t) = e^(-t), where D = 1.24575

We make a decision $x_0(t)=\sin\left(\frac{\pi}{2}t\right)-2te^{-t}\ln(3)\in[-r,r]$, where $r=\frac{M_0}{1-n}.=3.82984.$

Table 1 displays the absolute values of defects for (G = 200 and L = 200) mesh points. The errors associated with a single iteration are represented by absolute values in **Table 2**. for varied numbers of mesh points. Furthermore, errors are diminished by conducting additional iterations. Refer to Figure 1. Where the [$\log10(\|x_k-x\|)=\log10\ (\max|x_k(t_i)-x(t_i)|)$, to t_i = i/10 for any (i = 0, 1…… , 10)

Example (2): Examine the subsequent information. Kind (42, 43) of non-linear function integral equation of the Volterra.

$$x(t)=\frac{t}{1+t^2}\,x(t)+\int_0^t e^{-t}\ \frac{sx(s)}{1+|x(s)|}ds$$

Table 2: Absolute Errors within the EX.1 K Equal 10, L Equal 200, many G variables

t	G=50	G=100	G=200
0	0	0	0
0.1	0.170303×10^{-5}	0.449863×10^{-5}	0.362567×10^{-9}
0.2	0.307753×10^{-5}	0.805820×10^{-5}	0.119137×10^{-8}
0.3	0.409215×10^{-5}	0.104431×10^{-4}	0.139588×10^{-7}
0.4	0.478569×10^{-5}	0.117460×10^{-4}	0.402300×10^{-7}
0.5	0.521326×10^{-4}	0.121565×10^{-4}	0.934621×10^{-7}
0.6	0.540250×10^{-4}	0.1200099×10^{-4}	0.378213×10^{-7}
0.7	0.548649×10^{-4}	0.116624×10^{-4}	0.269398×10^{-7}
0.8	0.547760×10^{-4}	0.110637×10^{-4}	0.301620×10^{-7}
0.9	0.542085×10^{-4}	0.105845×10^{-4}	0.464820×10^{-7}
1	0.532832×10^{-4}	0.101492×10^{-4}	0.301723×10^{-7}

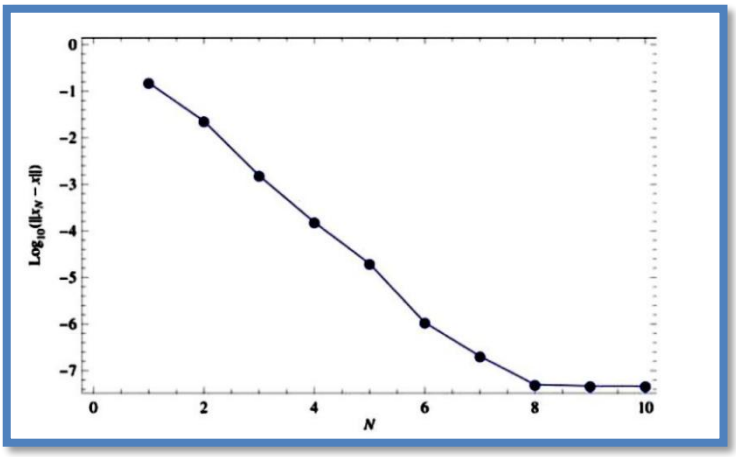

Figure 1: Ex(1) Illustrates the Logarithm of t the Utmost Error Occurring During Every Iteration.

Which has a unique, precise solution. The value of x(t) is zero. The formulas are: α(t) = β(t) = γ(t) = t: We can ascertain t by employing fundamental mathematics. the solution to which is unique and exact x(t) = 0. The functions α(t), β(t), and γ(t) are all defined as t.

$$f(t,s,x)\frac{tx}{1+t^2}+y,$$

And

$$u(t,s,x)=e^{-t}\frac{sx}{1+|x|}$$

Satisfying the requirements of the second theorem with ϕ(t) Equal t, k Equal 1/2, m(t) Equal 1, and D = 0.270671, The procedure is implemented. where x_0(t) Equal 0.5 ∈ Br, where r = 1.08268. **Table 3** displays the exact error values, while Figure 2 depicts the logarithm of the highest error associated with iterations, especially for G equals 80 and L equals 50 mesh points.

Example (3): We investigate the non-linear Volterra functional integral problem using proportional delay.

$$x(t)=\cos(t)-\sin\left(\frac{e^{-\cos^2(\frac{1}{2})}-e^{-1}}{1+t^2}\right)+\sin\left(\int_0^{t/2}\frac{\sin(2s)e^{-x^2(s)}}{1+t^2}ds\right),$$

Table3: Fundamental errors for Example 2 over several levels of K

t	k=5	k=25	k=50
0	0	0	0
0.1	0.462407×10^{-5}	0.808969×10^{-13}	0.306027×10^{-20}
0.2	0.131506×10^{-3}	0.268324×10^{-12}	0.107748×10^{-19}
0.3	0.790865×10^{-3}	0.275392×10^{-12}	0.171832×10^{-19}
0.4	0.243661×10^{-2}	0.300346×10^{-12}	0.114517×10^{-19}
0.5	0.512032×10^{-2}	0.649454×10^{-10}	0.156528×10^{-18}
0.6	$0.0.835707\times10^{-2}$	0.635856×10^{-9}	0.148931×10^{-17}
0.7	0.114419×10^{-1}	0.316263×10^{-8}	0.185272×10^{-16}
0.8	0.138099×10^{-1}	0.802217×10^{-8}	0.131274×10^{-15}
0.9	0.151984×10^{-1}	0.129801×10^{-7}	0.334904×10^{-15}
1	0.156251×10^{-1}	0.149012×10^{-7}	0.439281×10^{-15}

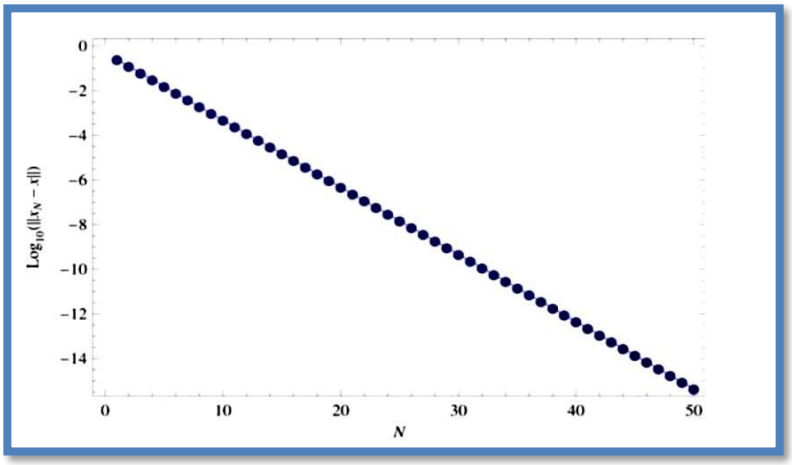

Figure 2: The logarithm of the highest error associated with every iteration in Example 2.

Which possesses the precise solutions x(t) = cos(t). The functions such as β(t) = t - (1 - q)t for q = 1/2 and γ(t) Equal t can be readily demonstrated to be continuous. Additionally, α(t) may be Any continuous operation that satisfies Condition 1.

$$f(t,x,y)=\cos(t) - \sin\left(\frac{e^{-\cos^2(\frac{1}{2})}-e^{-1}}{1+t^2}\right) + \sin(y)$$

And $$u(t,s,x)=\cos(t)- \sin\left(\frac{e^{-x^2}\sin(2x)}{1+t^2}\right)$$

Meet the conditions of Theorem 2, given k = 0, m(t) = 1, ϕ(t) = t, with D ranging from 0.25. We

Derive r = 1.5 and utilize $x_0(t)= \cos(t)- \sin\left(\frac{e^{-\cos^2(\frac{1}{2})}-e^{-1}}{1+t^2}\right) \in$ Br

The preliminary function. Both **Table 4** and the following figure illustrate the absolute errors with the logarithm of the highest Iteration-related absolute errors for L = 100 and G = 200 centered within the range [0,2].

Table 4: Approximate Errors for the Third Example for Various Values of K

t	k=2	k=5
0	0	0
0.2	0.234328×10^{-7}	0.239081×10^{-7}
0.4	0.146720×10^{-7}	0.360304×10^{-7}
0.6	0.323011×10^{-6}	0.914190×10^{-7}
0.8	0.863026×10^{-6}	0.637923×10^{-9}
1	0.205252×10^{-5}	0.284243×10^{-9}
1.2	0.539092×10^{-5}	0.878520×10^{-7}
1.4	0.113864×10^{-4}	0.593672×10^{-7}
1.6	0.154702×10^{-4}	0.506919×10^{-7}
1.8	0.252727×10^{-4}	0.231660×10^{-7}
2	0.852385×10^{-7}	0.116951×10^{-8}

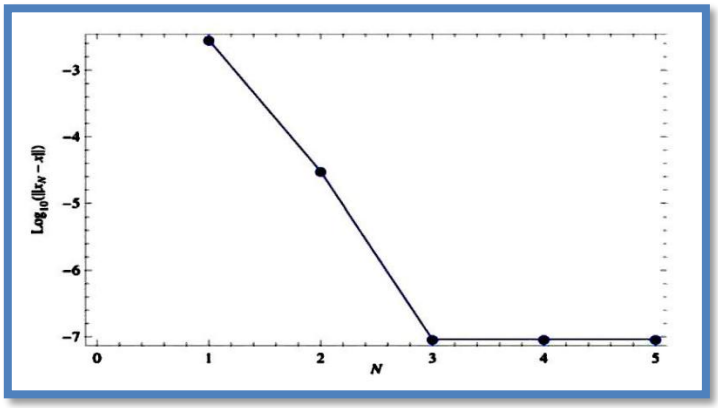

Figure 3. Logarithm of the greatest error associated with each repetition in Example (3).

Example (4): The subsequent non-linear integral Equation for Volterra function

$$x(t) = e^{-t\sqrt{t}} - \frac{t^2(1+e^{-t\sqrt{t}}x(t))}{2(1+t^4)} + \left(\frac{t^2}{1+t^4}\right) e^{-\left|\int_0^{t\sqrt{t}} \frac{2e^{-s}x(\sqrt[3]{s^2})}{(1+x(\sqrt[3]{s^2})^2)} ds\right|}$$

Contains a precise solution. The value of x(t) is equal to e. The functions to use are α(t) = t, β(t) = t, and γ(t) Equal 3.

Comply with the first condition of Theorem 2. Furthermore, functions as well

$$f(t,x,y) = e^{-t\sqrt{t}} - \frac{t^2(1+e^{-t\sqrt{t}x})}{2(1+t^4)} + \left(\frac{t^2}{1+t^4}\right)e^{-|y|}$$

And $$u(t,s,x) = \frac{2e^{-t}x}{1+x^2}$$

Fulfilled the criteria of Theorem 2–4 using n = 0.111641, ϕ(t) Equal t, G(t) = $t^2/(1+t^4)$, D = 0.5, and M_0 = 2. Thus, we have r = 2.25134 and choose $x_0(t) \in Br$. The extent of errors

Table 5: Absolute Errors of Example 4fore $x_0(t)$ =0.5and Different Value of K

t	K=2	K=5	K=10
0	0	0	0
0.1	0.116062×10^{-4}	0.302756×10^{-6}	0.302763×10^{-6}
0.2	0.150179×10^{-3}	0.164254×10^{-6}	0.163322×10^{-6}
0.3	0.597392×10^{-3}	0.518220×10^{-6}	0.551065×10^{-6}
0.4	0.139726×10^{-2}	0.963558×10^{-6}	0.626378×10^{-6}
0.5	0.237648×10^{-2}	0.135418×10^{-5}	0.213892×10^{-6}
0.6	0.319742×10^{-2}	0.444057×10^{-5}	0.933230×10^{-7}
0.7	0.356863×10^{-2}	0.811830×10^{-5}	0.411882×10^{-7}
0.8	0.342076×10^{-2}	0.110323×10^{-4}	0.286523×10^{-6}
0.9	0.291232×10^{-2}	0.133351×10^{-4}	0.152142×10^{-6}
1	0.22864×10^{-2}	0.136016×10^{-4}	0.216699×10^{-6}

Table 6:Absolute errors of Example 4for K=5 and different values of $x_0(t)$

t	$x_0(t)$=0.5	$x_0(t)$ = 1	$x_0(t)$=2
0	0	0	0
0.1	0.302756×10^{-6}	0.302762×10^{-6}	0.302777×10^{-6}
0.2	0.164254×10^{-6}	0.163079×10^{-6}	0.161031×10^{-6}
0.3	0.518220×10^{-6}	0.562475×10^{-6}	0.637346×10^{-6}
0.4	0.963558×10^{-6}	0.420642×10^{-6}	0.419744×10^{-6}
0.5	0.135418×10^{-5}	0.165281×10^{-5}	0.595858×10^{-5}
0.6	0.444057×10^{-5}	0.553731×10^{-5}	0.188352×10^{-4}
0.7	0.811830×10^{-5}	0.140381×10^{-4}	0.417234×10^{-4}
0.8	0.110323×10^{-4}	0.251467×10^{-4}	0.680604×10^{-4}
0.9	0.133351×10^{-4}	0.133351×10^{-4}	0.880009×10^{-4}
1	0.136016×10^{-4}	0.397919×10^{-4}	0.991856×10^{-4}

Table 5 provides details of the iterations, which correspond to G = 150 and L = 100 mesh points. **Table 6** displays the maximum inaccuracy values for a single iteration according to various initial locations and a consistent number of mesh points. **Figure 4** illustrates how increasing the number of repetitions reduces mistakes.

Example (5): Examine the integral Equation shown below **[10]**.

$$x(h) = \frac{sin\left(hx(\sqrt[3]{h})\right)}{1+h^2} + arctan\left(\int_o^{\sqrt{1}} \frac{\sqrt[4]{1+sx^2(s^2)+}}{(1+h^7)} \frac{hs^{11}(1+x^4(x^2))}{(1+x^4(x^2))}\right) ds.$$

Using basic math, we can determine that

$$\propto (h) = \sqrt[3]{t},\ \beta(h) = \sqrt{h},\ y(t) = h^2$$

$$x(h) = \frac{sin\left(hx(\sqrt[3]{h})\right)}{1+h^2}, +arctan(y)$$

And

$$u(t.s,x) = \frac{\sqrt[4]{1+sx^2(s^2)+ts^{11}(1+x^4)}}{(1+h^7)(1+x^4)}$$

Fulfill the requirements of Theory 2 accompanied by { D = 1.0184, k = 0.5, m(t) = 1, and ϕ(t) = h.} As a result, we determine that the beginning function belongs to the ball Br and get(r = 4.07362.) In contrast, since f (t, x, 0) is a function restricted in its range, Corollary 1's requirement are met. As a result, there is at least one solution to the integral Equation, and These solutions possess universal appeal. Upon completing 50 cycles, we ascertain the mistake for (L = 50 and G is equal to 80) mesh points.$\|x_{N+1} - x_N\|$ = maxi $|x_{N+1}(t_i) - x_N(t_i)|$ = 2.37155 × 10−8, where h_i = i/10 where i = 0, 1, ..., 10. In the figure, the response is an approximation obtained after 50 iterations. as demonstrated by the explanation that follows x(t) is an element of Br

Example (6): Examine: Kindly assess the presented non-linear Fredholm integral. [44,45]

$$x(t) = 1 + te - \int_o^1 (t+S)e^{X(S)}\,dS.$$

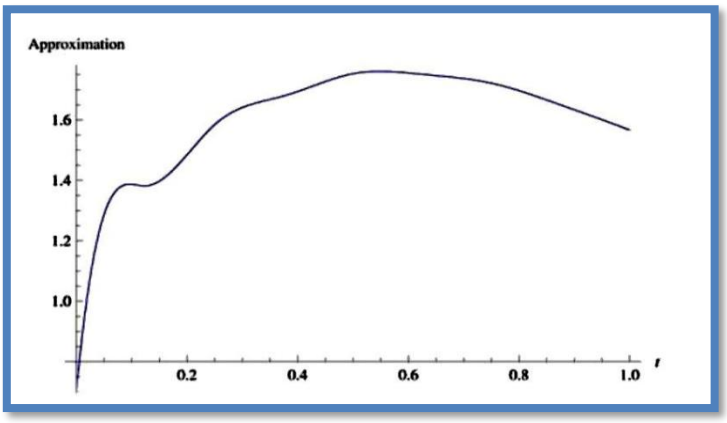

Figure 4: Approximation Solution of Example 5 after 50 Iteration

The precise solution is x(t) = t. This section addresses the solution of the integral Equation utilizing our suggested method and juxtaposes prior results with the new findings delineated in **Table 7** for K = 30, G = 200, and L = 200.

Example (7): The following integral Equation

$$x(t) = sin(t)^2 + 1 - \int_0^t 3\,sin(t-s)x\,(s)^2\,ds$$

Table 7:As shown in Figure 3, the absolute errors are as follows: K=30, G=200, and D=200.

t	Methodology of[44]	Methodology [45]	Methodologically presented
0	2×10^{-3}	2.58×10^{-6}	8.96539×10^{-10}
0.2	1×10^{-2}	7.35×10^{-6}	7.99324×10^{-9}
0.4	2×10^{-2}	7.93×10^{-6}	$4.23015 \times 10^{--8}$
0.6	1×10^{-2}	2.55×10^{-6}	8.28779×10^{-9}
0.8	0×10^{-3}	3.98×10^{-6}	2.82284×10^{-7}
1	1×10^{-2}	2.64×10^{-6}	5.62541×10^{-8}

Table 8:Contains The Solutions to Example 7: K = 10, G = 250, And D = 200, With Both Exact And Approximate Values

t	Methodology of[44]	Methodology of[45]	Methodologically presented	PERFECT RESOLUTION
0	1.0000	1.00000	1.000000000	1.000000000
0.1	0.9952	0.99500	0.995004165	0.995004165
0.2	0.9800	0.98006	0.980066580	0.980066577
0.3	0.9554	0.95533	0.955336485	0.955336489
0.4	0.9210	0.92105	0.921060993	0.921060994
0.5	0.8775	0.87756	0.877582565	0.877582561
0.6	0.8255	0.82531	0.825335614	0.825335614
0.7	0.7648	0.76482	0.764842185	0.764842187
0.8	0.6969	0.69669	0.696706707	0.696706709
0.9	0.6217	0.62159	0.621609968	0.621609968
1	0.5405	0.54028	0.540302303	0.540302305

The exact answer is x(t) Equal cos(t). This Equation fails to satisfy the following criteria: to theory 2, we employ the technique described in this article. Furthermore, the findings of our investigation have been compared with the results **[46,47] Table 8**.

7. Conclusion

In this research paper, we applied fixed-point technique with cubic B-Spline scaling function to obtain a numerical solution for a set of non-linear integral equations without the need for algebraic systems. Using the numerical examples and the obtained results, as well as equation number (5), we found that the results are highly accurate and closely approximate the exact solution. We compared these results with those obtained from previous studies and observed the accuracy of this method. Since the accuracy of this method depends on using larger values for G and K, we note that the accuracy will improve with larger values. We continue the iterations until we reach a precise solution that approaches the true solution. This method is free from scenarios, problems, or excessive computational costs, and it is applicable to equations with larger and more complex dimensions. This method has no adverse effects on more complex equations.

8. References

[1] Arbabi F, Li FJJoSE. Buckling of variable cross-section columns: integral-equation approach. 1991;117(8):2426-41.

[2] Hochstadt H. Integral equations: John Wiley & Sons; 1989.

[3] Jerri AJ. Introduction to integral equations with applications: John Wiley & Sons; 1999.

[4] Kanwal RP. Linear integral equations: Springer Science & Business Media; 2013.

[5] Argyros IKJBotAMS. Quadratic equations and applications to Chandrasekhar's and related equations. 1985;32(2):275-92.

[6] Deimling K. Non-linear functional analysis: Springer Science & Business Media; 2013.

[7] Hu S, Khavanin M, Zhuang WJAA. Integral equations arising in the kinetic theory of gases. 1989;34(3-4):261-6.

[8] Precup R. Methods in non-linear integral equations: Springer Science & Business Media; 2002.

[9] Banaś J, Dhage BCJNAT, Methods, Applications. Global asymptotic stability of solutions of a functional integral equation. 2008;69(7):1945-52.

[10] Aghajani A, Jalilian YJCiNS, Simulation N. Existence and global attractivity of non-linear functional integral equation solutions. 2010;15(11):3306-12.

[11] Sommariva AJNA. A fast Nyström-Broyden solver by Chebyshev compression. 2005;38(1):47-60.

[12] Petryshyn WJJoM, Mechanics. Projection methods in non-linear numerical functional analysis. 1967;17(4):353-72.

[13] Pata V. Fixed point theorems and applications: Springer; 2019.

[14] Maleknejad K, Torabi P, Mollapourasl RJC, Applications Mw. Fixed point method for solving non-linear quadratic Volterra integral equations. 2011;62(6):2555-66.

[15] Maleknejad K, Nosrati Sahlan MJIJoCM. The method of moments for solution of second kind Fredholm integral equations based on B-spline wavelets. 2010;87(7):1602-16.

[16] Maleknejad K, Nedaiasl KJC, Applications Mw. Application of Sinc-collocation method for solving a class of non-linear Fredholm integral equations. 2011;62(8):3292-303.

[17] Maleknejad K, Karami M, Rabbani MJAm, computation. Using the Petrov–Galerkin elements to solve Hammerstein integral equations. 2006;172(2):831-45.

[18] Maleknejad K, Almasieh H, Roodaki MJCiNS, Simulation N. Triangular functions (TF) method for solving non-linear Volterra–Fredholm integral equations. 2010;15(11):3293-8.

[19] KtMAR S, SLOAN IJMC. A new collocation-type method for Hammerstein equations. 1987;48:585-93.

[20] Kelley CJTJoIE. Approximation of solutions of some quadratic integral equations in transport theory. 1982:221-37.

[21] Kaneko H, Noren RD, Padilla PAJJoC, Mathematics A. Superconvergence of the iterated collocation methods for Hammerstein equations. 1997;80(2):335-49.

[22] Guoqiang HJJoc, mathematics a. Extrapolation of a discrete collocation-type method of Hammerstein equations. 1995;61(1):73-86.

[23] Guoqiang H, Liqing ZJAm, computation. Asymptotic error expansion of a collocation-type method for Hammerstein equations. 1995;72(1):1-19.

[24] Brutman LJNA. Applying the generalized alternating polynomials to the numerical solution of Fredholm integral equations. 1993;5:437-42.

[25] Borzabadi AH, Fard OSJJoC, Mathematics A. A numerical scheme for a class of non-linear Fredholm integral equations of the second kind. 2009;232(2):449-54.

[26] Atkinson KE. The numerical solution of integral equations of the second kind: Cambridge University Press; 1997.

[27] Atkinson K, Han W. Theoretical numerical analysis: Springer; 2005.

[28] Pour-Mahmoud J, Rahimi-Ardabili MY, Shahmorad SJAM, Computation. Numerical solution of the system of Fredholm integro-differential equations by the Tau method. 2005;168(1):465-78.

[29] Maleknejad K, Arzhang AJAM, Computation. The numerical solution of the Fredholm singular integro-differential equation with Cauchy kernel using the Taylor-series expansion and Galerkin method. 2006;182(1):888-97.

[30] Dinghua XJJoSU. Numerical solutions for non-linear Fredholm integral equations of the second kind and their superconvergence. 1997;1(2):98-104.

[31] Babolian E, Shahsavaran AJJoC, Mathematics A. Numerical solution of non-linear Fredholm integral equations of the second kind using Haar wavelets. 2009;225(1):87-95.

[32] Maleknejad K, Karami MJAm, computation. Numerical solution of non-linear Fredholm integral equations by using multiwavelets in the Petrov–Galerkin method. 2005;168(1):102-10.

[33] Hackbusch W, Sauter SAJAom. On the efficient use of the Galerkin method to solve Fredholm integral equations. 1993;38(4):301-22.

[34] Xiao J-Y, Wen L-H, Zhang DJAM, Computation. Solving second kind Fredholm integral equations by periodic wavelet Galerkin method. 2006;175(1):508-18.

[35] Atkinson KEJSJoNA. The numerical evaluation of fixed points for completely continuous operators. 1973;10(5):799-807.

[36] Han GJBNM. Asymptotic error expansion for the Nyström method for non-linear Fredholm integral equations of the second kind. 1994;34(2):254-61.

[37] Babolian E, Abbasbandy S, Fattahzadeh FJAM, Computation. A numerical method for solving a class of functional and two-dimensional integral equations. 2008;198(1):35-43.

[38] Ebrahimi N, Rashidinia JJAM, Computation. A collocation method for linear and non-linear Fredholm and Volterra integral equations. 2015;270:156-64.

[39] Biazar J, Ghazvini H, Eslami MJC, Solitons, Fractals. He's homotopy perturbation method for systems of integro-differential equations. 2009;39(3):1253-8.

[40] Rashed MJAM, Computation. Numerical solution of functional differential, integral, and integro-differential equations. 2004;156(2):485-92.

[41] Rashed MJAM, Computation. Numerical solutions of functional integral equations. 2004;156(2):507-12.

[42] Banaś J, Rzepka BJAML. An application of a measure of noncompactness in the study of asymptotic stability. 2003;16(1):1-6.

[43] Burton T, Zhang BJAML. Fixed points and stability of an integral equation: nonuniqueness. 2004;17(7):839-46.

[44] Borzabadi AH, Kamyad AV, Mehne HHJAM, Computation. A different approach for solving the non-linear Fredholm integral equations of the second kind. 2006;173(2):724-35.

[45] Babolian E, Fattahzadeh F, Raboky EGJAM, Computation. A Chebyshev approximation for solving non-linear integral equations of Hammerstein type. 2007;189(1):641-6.

[46] [Razzaghi M, Ordokhani YJMPiE. Solution of non-linear Volterra-Hammerstein integral equations via rationalized Haar functions. 2001;7(2):205-19.

[47] Sepehrian B, Razzaghi MJMPie. Solution of non-linear Volterra-Hammerstein integral equations via single-term Walsh series method. 2005;2005(5):547-54.

Al-Kitab Journal for Pure Sciences (2025); 9(2):84-103.
https://doi.org/10.32441/kjps.09.02.p6

Al-Kitab Journal for Pure Sciences
ISSN: 2617-1260 (print), 2617-8141(online)

https://isnra.net/index.php/kjps

Assessment of IoMT-Based Remote Patient Monitoring Used to Support Healthcare System in Kirkuk City

Lamees S. Ahmed, Abdulrahman Ikram Siddiq*

Department of Electronic and Control Engineering, Technical College Kirkuk, Northern Technical University, Iraq.

*Corresponding Author: draisiddiq@ntu.edu.iq

Citation: Ahmed LS, Siddiq AI. Assessment of IoMT-based Remote Patient Monitoring used to Support Healthcare System in Kirkuk City. Al-Kitab J. Pure Sci. [Internet]. 2025 Apr. 29;9(2):84-103. . DOI: https://doi.org/10.32441/kjps.09.02.p6.

Keywords: Iomt, Iot, Healthcare, Remote Patient Monitoring, Telemedicine, Iot Cloud, Iot Platform, Reliability.

Article History

Received	31 Aug.	2024
Accepted	14 Oct.	2024
Available online	29 Apr.	2025

Abstract:

Recently, Internet of Medical Things (IoMT)-based telemedicine applications are acquiring increasing attention. This is due to their benefits, especially during pandemic circumstances. A popular example is the Remote Patient Monitoring (RPM) system, whose performance crucially depends on the components used, mainly the available Internet connectivity. Since similar RPM systems operating in different areas can perform differently, the reliability of these systems is questionable. Therefore, in this paper, the reliability of an RPM system is assessed and tested under realistic operation conditions in Kirkuk city. The purpose is to figure out to what extent the RPM system is applicable under the locally available technologies. Extensive tests by using a 12 Mbps optical Internet connection and two different cloud platforms show that the system encountered a maximum delay of about 59 seconds with an average availability exceeding 98%. The tests proved the robustness of the system, and it is henceforth recommended for practical application in Kirkuk city to support the healthcare system.

Keywords: Iomt, Iot, Healthcare, Remote Patient Monitoring, Telemedicine, Iot Cloud, Iot Platform, Reliability.

تقييم نظام مراقبة المرضى عن بعد المعتمد على تقنية IoMT المستخدم لدعم نظام الرعاية الصحية في مدينة كركوك

لميس سعدي احمد & عبد الرحمن إكرام صديق*

قسم تقنيات الإلكترونيك والسيطرة، الكلية التقنية كركوك، الجامعة التقنية الشمالية، كركوك، العراق
lamies.saadi23@ntu.edu.iq, draisiddiq@ntu.edu.iq*

الخلاصة:

تحظى تطبيقات التطبيب عن بعد المرتكزة على شبكات إنترنت الأشياء الطبية (IoMT) باهتمام متزايد. وذلك لفوائدها خاصة في ظل ظروف انتشار الامراض والاوبئة من الأمثلة الشائعة على ذلك نظام مراقبة المريض عن بعد (RPM) الذي يعتمد أدائه بشكل حاسم على المكونات المستخدمة، وخاصة جودة خدمة الاتصال بالإنترنت المتاحة وهذا يعني أن أنظمة RPM نفسها التي تعمل في مناطق مختلفة من العالم يمكن أن يكون مستوى اداءها متباينا، مما يجعل من موثوقية هذه الأنظمة موضع شك. تم في هذا البحث تقييم واختبار موثوقية نظام RPM في ظل ظروف تشغيل واقعية في مدينة كركوك. ان الغرض من ذلك هو معرفة مدى إمكانية تطبيق نظام RPM في ظل التقنيات المتاحة محليًا. أظهرت الاختبارات المكثفة باستخدام اتصال إنترنت بصري بسرعة ١٢ ميجابت في الثانية ومنصتين سحابيتين مختلفتين أن اقصى تاخير يبلغ حوالي ٥٩ ثانية و بمتوسط توفر (Availability) يتجاوز ٩٨٪. لقد أثبتت الاختبارات ان هذا النظام يتمتع باعتمادية عالية بالنسبة لتطبيقات مراقبة المرضى عن بعد ويمكن ان يدعم ويحسن نظام الرعاية الصحية في مدينة كركوك.

الكلمات المفتاحية: إنترنت الأشياء الطبية، إنترنت الأشياء، الرعاية الصحية، مراقبة المرضى عن بعد، التطبيب عن بعد، سحابة إنترنت الأشياء، منصة إنترنت الأشياء، الموثوقية.

1. Introduction

The Internet of Things (IoT) is a concept that encompasses the interaction between Internet-connected devices less need for human-to-human or human-to-computer communication. These devices can offer services globally [1], in ways that were previously unimaginable. In contrast to the conventional paradigm, all entities in IoT realm are regarded as intelligent objects that are interconnected [2]. However, IoT-based technologies have significantly contributed to the transformation of the healthcare sector into a technologically advanced domain, with the aim of enhancing patient care. The Internet of Medical Things (IoMT), is the result of applying IoT in healthcare. It combines different medical devices and sensors with the Internet to enable immediate gathering and examination of patient data [3].

The deployment of IoMT in the healthcare sector brings substantial advantages, such as the ability to provide effective and prompt medical assistance using precise and continuous monitoring data [1]. However, the concept of green hospitals evolving as a model for future hospitals [4], when equipped with IoMT technologies, can significantly enhance the healthcare

ecosystem, particularly for individuals utilizing remote monitoring systems [5]. Remote monitoring systems rely heavily on the processing and analysis of real-time data obtained by bio-sensors [2].

The core of IoMT-based healthcare systems is the IoT platform. It provides the required services and applications such as data transfer, storage, and processing. The Arduino IoT Cloud and Blynk are popular platforms for developing IoT-based applications in the healthcare sector. The Arduino Cloud is the standard and compatible platform for Arduino controllers and peripherals. Also, the effectiveness of the Blynk platform has been emphasized through its successful usage in many IoMT applications [6]. Both platforms are widely applied in remote health monitoring systems due to their flexibility, ease of use, and very good compatibility with different types of sensors and devices [7]. The quality and reliability of these services highly depend on many factors, including the Internet connectivity and the sensors and actuators [8],[9]. Then, IoMT-based healthcare systems may encounter serious challenges such as delay and data loss when they use unstable Internet connectivity, which is the case in many places.

However, the application of IoMT in Kirkuk city in Iraq can be very beneficial to the healthcare system in the city. As the population and hence the demand for healthcare services increases, the infrastructure of healthcare in the city is overstretched. Also, access to specialized care can become difficult for people from far-flung areas or living far away from the city center, and thus, on-time access to healthcare gets compromised. Therefore, this entails that an effective and reliable telehealth monitoring system becomes very important in helping to surmount such challenges by providing a system through which healthcare providers monitor the health status of their patients remotely However, IoMT acquires more importance in cases like the spread of infectious diseases where it would be preferable to monitor patients remotely without having to visit health facilities and hospitals frequently except in a situation of critical need.

The objective of this study is to design, implement, and test the performance of a medical IoT-based remote patient monitoring system. In order to highlight the impact of the IoT platform on the performance of the system, the system is implemented and tested by using two popular IoT platforms, namely the Arduino IoT and Blynk platforms. Extensive tests under realistic operation conditions have been conducted. The system's real-time operation and reliability have been evaluated by focusing on several key numerical performance metrics such as maximum delay, maximum and average data loss, uptime, and availability. By conducting this evaluation, this study aims to show the significance of developing and deploying such a system in Kirkuk city.

The rest of the paper is organized as follows: A comprehensive literature review on the works related to the context of this paper is presented in Section 2. In Section 3, the IoMT system model is described in terms of implementation and workflow. Then, in Sections 4 and 5, the reliability metrics and the adopted test procedure are presented. Section 6 presents the results obtained from testing the system under realistic operation conditions. Reliability calculations and related comments are also given in Section 6. Finally, conclusions and recommendations are given in Section 7.

2. Literature Review

Many designs and implementations of Remote Patient Monitoring (RPM) that used different sensors and actuators were presented in the literature, such as [3],[10],[11], and [12]. They collectively showed the advantages of IoMT-based RPM including: The ability of healthcare providers to collect and evaluate patient data from a distance, decreasing the necessity for frequent visits to healthcare institutions, real-time collection and updating of health data and triggering alerts and notifications to healthcare practitioners enabling them to stay informed about the health status of their patients even when they are not physically present in the hospital.

However, the performance of IoMT RPM greatly relies on the capabilities of the used communication infrastructure. Therefore, these reported advantages of IoMT cannot be directly generalized for all implementations of IoMT [13]. One main reason is that the performance of the RPM system is governed by the available Internet connectivity. Slow service can significantly cause undesired delays and data losses, even if the IoT platform is working properly. Such cases may cause serious hazards to patients' lives. Therefore, it is important to test and evaluate the reliability of the implemented RPM system for the specific components used to build the system, to know to what extent this system is dependable [14].

Reliability is essential in healthcare operations as it ensures that systems can effectively manage and counteract external stresses, such as patient demand and resource availability. A reliable healthcare system contributes to performance enhancement and customer satisfaction, which are critical in delivering quality care [15]. Beyond life-threatening issues, unreliable systems can result in significant financial losses for healthcare providers. This can affect the overall reputation of healthcare institutions, making reliability a key factor in operational success. The increasing demand for new technologies necessitates robust reliability measures to ensure these systems can handle various scenarios without failure [16]. Healthcare systems are complex and high-risk, involving various components that must work together reliably. This complexity necessitates a thorough reliability analysis to identify weak links and potential failure points. Reliability analysis allows for the identification of weak links within the system,

enabling targeted improvements. This process helps in redesigning systems to enhance reliability and reduce the likelihood of failures [17].

The study [18] emphasizes the reliability of IoMT-based biomedical measurement systems (BMS) through accurate measurements essential for diagnosing diseases like heart conditions and neurological disorders. Validation against standard methods shows promising results, with low mean absolute differences in blood sugar measurements. Advanced signal processing techniques significantly improve data quality, enhancing the reliability of ECG signal classification. Addressing environmental challenges and employing multidisciplinary approaches are crucial for maintaining consistent performance in real-world applications.

In [19], the importance of reliability in telemedicine systems was studied for real-time remote health monitoring. It proposed solutions to mitigate electromagnetic interference and packet delay. The study reported the need for secure, efficient, and effective communication systems to support healthcare delivery. Next, a complete design and implementation of a wireless clinical monitoring system was presented in [20] for measuring pulse and oxygen saturation from patients. A clinical trial was conducted over seven months in a cardiology unit with 41 patients. The system demonstrated high reliability with an average availability of 99.68%. However, the reliability of the sensors for measuring oxygen and pulse was lower at 80.85%, with occasional disconnections. The performance was improved by increasing the sampling rate and implementing a disconnection alarm system. The analysis showed that the system was effective in detecting clinical deterioration. The results indicate the feasibility of using wireless networks for patient monitoring in hospitals [17]. The study [21] presents a comprehensive analysis of IoMT applications, highlighting their reliability through systematic methodology, diverse applications, and technological support, while also addressing potential challenges that could affect their implementation in healthcare systems.

An experimental performance test was presented in [22]. The presented tests were conducted on what is called Health Monitoring for All (HM4All) with a remote vital signs monitoring system based on a ZigBee body sensor network (BSN). The system involved six ECG sensors operating in two modes: ECG mode, which transmits ECG waveform data and heart rate (HR) values, and HR mode, which only transmits HR values. The non-beacon-enabled star network maintained a 100% delivery ratio (DR) without hidden nodes. When the network topology was changed to a 2-hop tree, the performance slightly degraded, resulting in an average DR of 98.56%. However, further investigation revealed that individual sensing devices experienced transitory periods with low DR.

The study in [23] aimed to assess the reliability of a real-time health monitoring system in the homes of older adults. The "Mobile Care Monitor" system was installed in nine homes for two weeks, featuring a wireless wristwatch with sensors and additional devices. Results showed system reliability between 73% and 92%, with data concurrence exceeding 88%. Usability metrics ranged from 82% to 97% after a firmware update for the pulse oximeter. Watch-wearing adherence was about 80%, and the study achieved 88% effectiveness in collecting potential measurements, indicating the system's high effectiveness in providing accurate remote health data.

In [24], the regional limitations were taken into consideration. The study evaluated what is called the “Mashavu” telemedicine system in rural Kenya. It was found that it provided about 90% of the same medical advice as face-to-face consultations, with a high level of diagnostic consistency. The system was capable of enhancing healthcare access, reducing travel costs, and creating job opportunities. At the same time, it faced limitations such as potential bias and diagnostic gaps. Future improvements were suggested to focus on quality control and expanding diagnostic capabilities.

However, COVID-19 has shown the significance of IoMT-based RPM systems. In [25], an IoT-based health monitoring system was presented that is designed for individuals diagnosed with COVID-19. It created a prototype measuring instrument for blood oxygen levels that precisely measures oxygen levels with an average error of 0.01 to 1%. It was proved that the system was efficient and helpful in monitoring patients infected with COVID-19 remotely.

The impact of using different data transmission protocols was investigated in [26]. The delays were measured in remote patient monitoring systems using Advanced Message Queuing Protocol (AMQP) and Constrained Application Protocol (CoAP) protocols. The findings indicated that the AMQP protocol can perform better for larger data packets and high-load scenarios, while the CoAP protocol was more efficient for small, frequent updates. The study underscored the need to select appropriate protocols to ensure effective and reliable data transmission in remote patient monitoring systems. With the aim of improving healthcare delivery in rural areas, the research in [27] presented an IoT-based real-time RPM system. The system used the MQTT data transmission protocol to transmit ECG data to a web server, enabling remote monitoring via smartphones or computers. The conducted experiments showed no packet loss or errors in both private (LAN) and public (WAN) networks. It supported both real-time and store-and-forward ECG monitoring, with real-time mode facing challenges like transmission delays. The use of Message Queuing Telemetry Transport (MQTT) protocol ensured low bandwidth and low power consumption.

The study [28] emphasizes the importance of reliable data delivery in the Internet of Things (IoMT) for applications like smart hospitals and traffic monitoring. It highlights the challenges of higher bandwidth and computational resources compared to traditional IoT devices, and the impact of increasing multimedia data on transmission, processing, and storage. The study also highlights the subjective quality of experience (QoE) as a significant factor in network performance evaluation, influencing perceived service reliability.

Based on the presented literature so far, it is clear that the effectiveness of IoMT-based RPM systems depends heavily on the performance of system components, mainly on the Internet service and IoT platform. Therefore, it is crucial to thoroughly test and evaluate the reliability of the specific components used in the system to ensure dependability and to recommend the system for suitable healthcare services.

3. System model

3.1 System Design: The schematic diagram of the designed healthcare IoMT system is shown in **Figure 1**. The system can be divided into three main parts. The first is the cloud platform, which serves as the system's backbone, providing communication infrastructure, data storage, retrieval, analysis, and security for all devices connected to it. The second is the healthcare room, which is designed to accommodate the patient. The medical sensors are connected to a microcontroller equipped with a Wi-Fi module. This microcontroller collects data from the medical sensors and sends it to the cloud. Another microcontroller collects environmental data and sends it to the cloud. All controllers can receive commands from a remote healthcare provider to control patient and environment-related actuators such as valves of nutrition bags, lights, and fans. Each patient microcontroller is connected to a local display screen, which displays sensor readings and emergency situation suggestions.

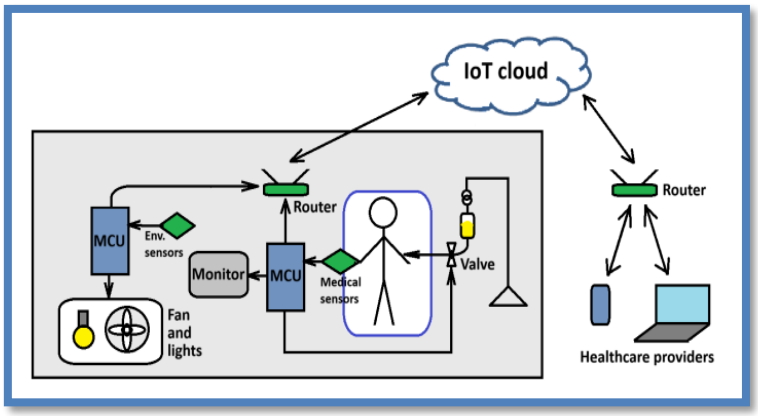

Figure 1: The designed IoMT system.

The third part of the designed system is the remote healthcare provider devices. Healthcare providers (like doctors, nurses, and home health agencies) use devices connected to the IoT

platform through the Internet to receive patient data and cloud alerts. These devices have simple, clear, and user-friendly interfaces for monitoring patients and issuing control commands.

3.2 System Workflow: The designed IoMT system uses data collection, transmission, storage, and analysis mechanisms to ensure that the data is accurate, reliable, and secure, enabling effective remote patient monitoring and healthcare delivery. Before the system is operational, the microcontrollers are set to be connected to the Internet through a local Wi-Fi wireless router. The microcontrollers are also well defined within the cloud platform, such that suitable cloud variables are assigned to the streams of collected data initiated from medical and environmental sensors. The available cloud options and services are suitably customized to correctly accommodate and display the data on the dashboards of the platform. Control buttons are added to the dashboards as a means for the healthcare providers to control actuators.

The privacy and security of data access from both sides of the designed system (sending data to the cloud and accessing dashboards for monitoring and control) are achieved by limiting access to authorized devices only according to their Media Access Control (MAC) addresses. The collected sensor data on the cloud server is analyzed, and in accordance with notifications and alerts, is generated to inform healthcare providers when abnormalities and emergency cases occur. These alerts are determined by setting upper and lower bounds for the normal ranges of every measured parameter. Alerts are initiated by the cloud server once a value exceeds normal limits. In similar systems, a monitor is also used to display the sensor readings of each patient. In this research, the function of this monitor is extended to display suggestions and recommendations in abnormal situations, and most importantly, in the case of losing Internet connectivity. These suggestions are pre-programmed inside the patient microcontroller, and they are related to the reading of the sensors according to recommendations obtained from specialized consultants.

The designed system is easily scalable. It is open to deal with more patients by just iterating replicas of the hardware and software modules used for one patient. The cloud platform can easily be modified to accommodate more patients (and maybe more sensors and functions) by upgrading the usage plan according to the available options.

3.3 System Hardware Implementation: The designed IoMT-based healthcare system is implemented using hardware and software modules to perform its specified functions. The utilized hardware components are as follows:

1. Microcontrollers: Three Node MCU esp8266 modules are used, two for patient circuits and one for environmental parameters. The characteristics of this microcontroller and

the integrated Wi-Fi module make it a suitable choice for connecting sensors and actuators.

2. Medical sensors

- The MAX30100: is a device that monitors heart rate and pulse oximetry, using light-emitting diodes and an Infra-Red sensor. It uses an analog signal processing unit to improve output signal quality and operates on input voltages from 1.8V to 3.3V. The sensor has an accuracy range of 96.17%-97.67% for blood oxygen saturation level and 92.35%-99.65% for heart rate.

- DS18B20: is a digital thermometer that offers 9-bit to 12-bit Celsius temperature measurements, with an operating temperature range of -55°C to +125°C and accuracy of ±0.5°C. It connects via a one-wire bus, requiring only a single data line and Vcc and GND for microcontroller interfacing.

3. Room environment sensors

- The DHT11: is a temperature and humidity sensor with a calibrated digital output. It measures temperature in the 0°C to +50°C range with a ±2°C accuracy and relative humidity in the 20 to 90% range with a ±5% accuracy.

- MQ-135: is a gas sensor that detects harmful gases and smoke using both digital and analog output pins. The digital output gives a high signal when gas concentration exceeds a threshold, while the analog output voltage ranges from 0 to 4.2V. The detection range varies based on the gas being measured.

4. Actuators: The designed IoMT system consists of two actuators and two electronic switches. They are controlled by the healthcare providers through the control buttons on the dashboard. Two of these actuators are used to control the solenoid valves for the purpose of controlling the flow of nutritional fluid into the patients' bodies. The two switches are implemented by relays to control the ON/OFF operation of the fan and lights in the healthcare room.

4. IoMT reliability metrics

The undesired effects of communication impairments on the performance of the implemented IoMT system are the delay in data delivery, data losses and inaccuracy of received data. These effects can be measured and the reliability of the system can be assessed by evaluating several key numerical metrics. These metrics help in forming a clear idea of the extent to which the system is performing as expected. These metrics include:

A. **Latency and Response Time:** Calculating the average and maximum time required to deliver a data entity. These metrics help in understanding the range of response times and identifying any outliers or extreme delays. This metric is essential for assessing how quickly and efficiently a network operates, impacting user experience and system quality. A low reaction time indicates rapid task handling by the network. However, if

it's high, it could indicate that the network is crowded, has experienced problems, or has become ineffective [29].

B. **Uptime and Availability**

- Mean Time Between Failures (MTBF): This metric measures the average time the system operates without failure. It is calculated by dividing the total operational time, called the uptime, by the number of failures [30].

$$\text{MTBF} = \frac{uptime}{number\ of\ failures} \quad (1)$$

- Mean Time To Repair (MTTR): This metric measures the average time taken to repair the system after a failure. It is calculated by dividing the total time of failure, called the downtime, by the number of failures [31].

$$\text{MTBF} = \frac{downtime}{number\ of\ failures} \quad (2)$$

- Availability: Often expressed as a percentage, availability is calculated by using the formula [32].

$$\text{Availability} = \frac{\text{MTBF}}{\text{MTBF+MTTR}} \times 100\% \quad (3)$$

C. **Data Integrity:** Sometimes known as the Error Rate and it is the number of errors detected in the data transmitted or stored, usually expressed as errors per million (EPM) or simply as a percentage ratio of the number of errors to the total number sent data items [29].

5. Test procedure

In order to measure the previous metrics, the following procedure has been applied:

1. Software tools have been implemented to measure the system performance defined by delay, data loss, and EPM. The *Teraterm* serial port monitor software is used to record the values of the transmitted sensor data, together with the transmission time, to be used as a reference for the measurements. Also, as one facility offered by the cloud platform, the data on their exact arrival time is recorded.
2. The system operated for 24 hours for 10 days, and the system performance parameters were measured and recorded to observe how the system performs under various realistic network conditions. The sensor's data are replaced by previously recorded real patient data obtained from the same sensors. The data represent the sensor readings for 24 hours. The data were stored and fed to the system continuously and repeatedly throughout the period of the system test. This is done because of the difficulty in performing this test on a human for this relatively long period, and since the focus of this research is to evaluate the impact of communications impairments on system performance.
3. The collected data is systematically analyzed according to the metrics defined to assess the reliability of the system.
4. The procedure is repeated for two different cloud platforms.

6. The Results

According to the test procedure, the implemented IoMT system is first tested over the Arduino IoT platform. Artificially generated data representing the medical and environmental sensors is generated and sent to the cloud sequentially. The system is supplied by an uninterruptible power source to maintain continuous operation for 24 hours for 10 days. Internet connectivity is maintained through the popularly available optical service, with a maximum bit rate of about 12 Mbps. So, the system will operate under real conditions, and the recorded measurements can give a reasonable idea about its reliability.

The first measured parameter is the time delay, defined as the period between data transmission and reception time. The maximum delay is the performance-limiting parameter, so it is measured as shown in **Table 1**. Although in detailed tests the delay is measured for each received data item, in this table only the maximum delay within each test hour is recorded. This is because some sent data items are lost. It can be observed that there is no regular pattern. This is because the delay is the result of many interrelated parameters. The significant conclusion from this table is that the maximum encountered delay didn't exceed one minute, making the implemented system suitable for telemedical applications that allow a delay time not exceeding a minute.

Table 1: Maximum delay (sec) by using the Arduino IoT platform.

Hour	Test day									
	1	2	3	4	5	6	7	8	9	10
0	10.968	40.231	**46.987**	12.456	30.985	0.762	9.542	22.876	33.761	0.987
1	10.959	14.13	4.891	20.987	31.987	0.981	10.988	20.988	33.981	**39.987**
2	12.902	**43.099**	4.89	33.761	40.987	0.543	10.988	19.876	10.987	38.876
3	10.924	14.046	4.883	28.991	15.672	0.877	12.987	17.988	15.987	**35.876**
4	10.91	14.036	4.878	30.987	**41.988**	0.988	15.988	17.999	16.987	34.987
5	18.179	13.992	4.873	31.771	23.765	12.988	17.543	18.988	16.976	**33.769**
6	10.823	14.004	4.866	**33.991**	23.987	13.988	19.679	13.988	20.876	23.981
7	10.961	**43.742**	4.864	19.987	28.876	14.988	18.988	13.988	21.988	19.987
8	10.903	14.021	**58.397**	12.877	17.987	15.988	19.987	12.988	22.876	30.877
9	10.974	14.028	**58.351**	12.543	20.871	12.987	12.988	20.987	23.876	31.988
10	25.681	14.163	2.575	17.988	22.987	19.988	11.658	23.987	24.987	**31.658**
11	25.633	14.913	9.106	17.987	**42.987**	19.988	10.877	22.765	25.987	30.469
12	25.627	35.334	9.16	20.988	**43.988**	20.987	12.988	22.765	25.987	29.437
13	25.571	35.29	23.103	21.988	**42.987**	23.988	19.987	21.982	22.987	40.987
14	46.342	15.175	46.687	48.333	11.368	31.678	**49.721**	16.46	11.952	10.365
15	46.329	13.405	46.68	48.32	11.257	31.656	**49.705**	22.482	10.346	8.802
16	46.315	13.582	46.669	48.311	47.078	31.652	**49.69**	17.885	10.397	8.708
17	46.298	13.438	46.656	48.298	11.395	33.432	**49.68**	18.174	10.398	8.751
18	46.305	13.493	46.645	48.292	12.881	2.324	**50.275**	16.535	36.402	47.362
19	46.321	13.538	46.625	48.276	12.829	0.338	**50.224**	16.535	37.502	47.35
20	46.266	13.914	46.618	**48.264**	12.801	0.478	9.238	18.361	37.685	47.34
21	48.539	14.029	46.608	**49.397**	12.783	0.443	9.367	18.958	36.197	47.294
22	**50.772**	21.275	46.597	15.205	12.77	0.243	13.432	16.502	36.141	26.959
23	25.749	28.381	**38.862**	15.114	13.788	0.408	9.266	26.953	36.157	28.976

In order to take the variation in Internet quality of service during the day, the maximum and average time delay at each test hour (averaged over the 10 test days) are plotted in **Figure 2** versus test time ranging from 0 (12 AM) through 23 (11 PM). The general pattern shows increased delay during the times of intense use of the Internet around 9 AM and the evening period, but without exceeding 59 seconds for the whole test period. Also, the tests show an average delay between about 16 and 32 seconds over 24 hours.

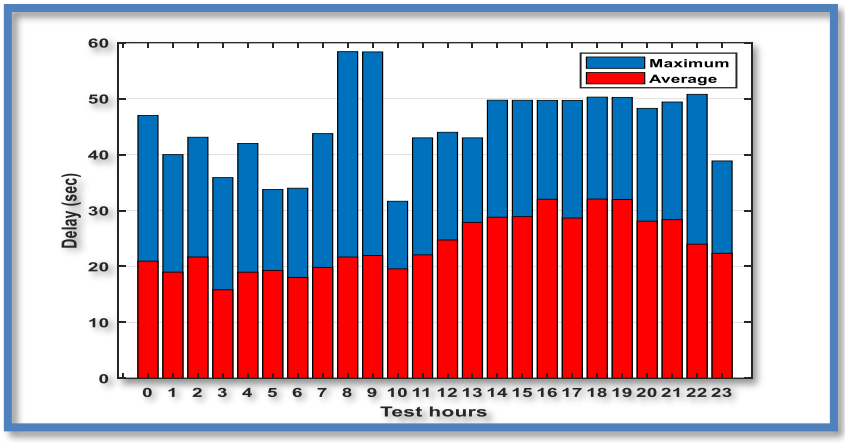

Figure 2: Delay per hour for Arduino IoT platform.

Similarly, to consider the possible daily variation in Internet service quality, the maximum and average delay within each test day, are plotted in **Figure 3**. The plot shows that the delay is not constant over different days, but instead, it is affected by the Internet service. The importance of this plot is that it gives practically encountered delay ranges, which are beneficial in evaluating and making decisions whether the implemented system is suitable for a specific telemedicine application or not.

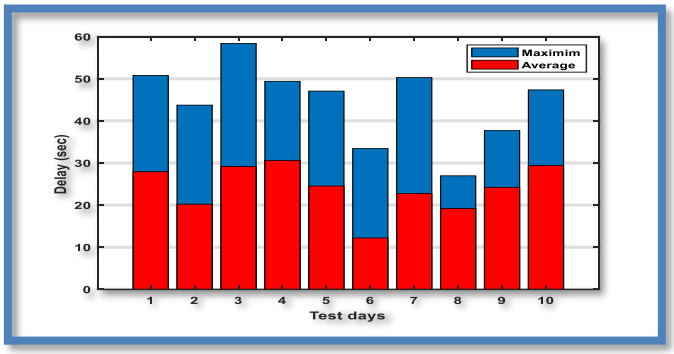

Figure 3 Delay per day for Arduino IoT platform.

Next, data loss is measured. A data item is considered to be lost if it was sent from the microcontroller and wasn't received at the platform. The percentage of the amount of lost data within each test hour is measured as shown in **Table 2**. From the first overview, it may be stated that the implemented system with the Arduino IoT platform could deliver the sensor readings with limited losses. However, odd cases of high loss percentage may practically occur, like

88.33% at hour 19/ day 7, due to unexpected interruption in Internet service, but the tests over a continuous 10 days showed that such a severe case is very rare. The data loss measurements also show the correlation with the Internet usage load. That is, relatively more data losses are expected in the morning and evening periods, which are the periods of high activity of Internet users.

Table 2: Percentage data loss for Arduino IoT platform.

Hour	Test day									
	1	2	3	4	5	6	7	8	9	10
0	0	0	**1.66**	1.66	0	0	0	0	0	0
1	0	0	0	0	**3.33**	0	0	0	0	0
2	0	0	0	1.66	0	**3.33**	0	0	0	0
3	0	0	0	0	0	0	0	0	0	5
4	0	0	0	0	0	0	0	0	0	0
5	0	0	0	0	0	0	0	**1.66**	0	0
6	0	0	0	0	0	0	0	0	0	0
7	0	0	0	0	0	0	0	0	0	0
8	0	0	**15**	0	0	0	0	0	0	0
9	8.33	0	**13.33**	0	0	0	0	0	1.66	0
10	**5**	0	3.33	0	0	0	1.66	0	0	0
11	0	**35**	1.66	0	0	0	0	0	0	0
12	0	**11.66**	0	0	3.33	0	0	0	1.66	0
13	**1.66**	0	0	0	0	0	0	0	0	0
14	0	0	0	0	0	0	0	0	0	0
15	0	0	0	0	0	0	0	0	0	0
16	0	0	0	0	0	0	0	0	**1.66**	0
17	0	0	0	0	0	**5.00**	0	0	0	0
18	0	0	0	0	**16.66**	1.66	0	0	5.00	6.66
19	0	0	0	0	0	0	**88.33**	0	0	0
20	0	10.00	0	0	0	0	**16.66**	0	0	0
21	6.66	0	0	**31.66**	0	5.00	0	0	0	0
22	3.33	0	3.33	**6.66**	0	0	0	0	0	0
23	0	0	0	**18.33**	1.66	0	0	3.33	0	0

In addition to the amount of data lost, it is important to take into account the time periods during which data loss fully occurs, known as the downtime, because it is one of the direct factors that determines the reliability of the system. **Table 3** shows the system reliability calculations. The uptime is the sum of the time periods during which the system is properly operational. The downtime is measured as the length of the periods during which data was being lost. Each separate downtime period is considered as a single failure, regardless of how many data items were lost within this period. For example, if the system is operating properly and suddenly a single data item (or more but continuously) is lost and then system resumed correct operation, this is considered as a single failure. On this bases, the MTBF, MTTR and hence the system availability are calculated as shown in **Table 3**. The results show that the availability ranges from 95.76% to 99.79%, with the daily average percentage data loss, calculated as the EPM, in the range from 4.44% to 0.21%. These results indicate a high level of reliability of the implemented system under realistic operation conditions.

Table 3: Reliability calculations for Arduino IoT platform.

Day	Total Up time (minutes)	Total Down time (minutes)	Number of failures	MTBF (minute)	MTTR (minute)	Availability (%)	EPM (%)
1	1425	15	5	285	3	98.96	1.04
2	1406	34	3	468.67	11.33	97.64	2.36
3	1417	23	6	236.17	3.83	98.40	1.6
4	1404	36	4	351	9	97.50	2.5
5	1425	15	4	356.25	3.75	98.96	1.04
6	1431	9	5	286.2	1.8	99.38	0.62
7	1379	61	3	459.67	20.33	95.76	4.44
8	1437	3	2	718.5	1.5	99.79	0.21
9	1434	6	4	358.5	1.5	99.58	0.42
10	1433	7	2	716.5	3.5	99.51	0.49

Moreover, in order to figure out the effect of the adopted IoT platform, the same implemented system with the same hardware and software modules has been tested over a different IoT platform, namely the well-known Blynk IoT platform. The same test procedure is applied, and the system is again tested for 24 hours for 10 days. The delay measurements are presented in **Table 4**. Fortunately, the maximum encountered delay is also less than 59 seconds, but it should be noted that on average, the system suffered from less delay time. So the implemented system over the Blynk platform seems to be relatively faster than the case of the Arduino platform. As shown in **Figure 4**, the average delay ranges from 5.5 to about 17 seconds, which is less than that in **Figure 2**. Similar comments also hold for the daily-based delay measurements shown in **Figure 5** and **Figure 3**.

Table 4: Maximum delay (sec) by using the Blynk IoT platform.

Hour	Test day									
	1	2	3	4	5	6	7	8	9	10
0	0.325	2.654	0.795	0.431	10.872	0.221	2.871	2.761	20.431	**24.651**
1	0.35	0.323	1.792	0.981	13.987	0.297	2.971	2.871	12.871	**23.541**
2	0.347	0.372	1.75	0.432	6.971	0.371	4.981	1.761	**21.981**	20.761
3	0.354	0.357	1.789	0.543	15.871	0.541	6.981	2.321	**25.981**	21.871
4	0.641	0.372	0.79	0.411	**20.761**	0.193	4.871	1.981	19.981	17.987
5	0.372	0.388	0.788	0.521	**21.876**	0.479	7.981	1.871	20.991	21.651
6	0.386	0.402	1.76	0.763	9.761	0.179	7.543	2.981	29.981	**33.549**
7	0.614	9.591	0.786	0.659	22.871	0.183	5.348	3.981	**32.853**	32.651
8	0.397	0.433	0.784	0.459	23.654	0.198	3.541	3.761	**33.871**	23.548
9	0.606	0.446	1.781	0.329	**22.951**	0.461	3.841	10.871	20.439	18.651
10	0.602	0.796	7.418	0.981	**21.295**	0.279	2.981	15.654	18.571	19.981
11	3.278	0.541	24.276	1.92	9.942	0.628	2.251	1.679	**38.622**	24.666
12	0.279	0.481	9.255	1.097	16.046	0.635	0.771	1.664	**38.614**	24.682
13	0.272	0.504	25.228	1.105	19.079	0.632	0.772	**58.773**	38.604	24.708
14	4.247	0.493	3.601	0.179	7.096	0.646	8.224	**58.783**	38.594	24.716
15	1.244	0.385	1.586	0.141	2.083	0.646	1.225	**58.814**	21.905	40.241
16	0.245	1.359	1.57	0.205	0.9399	0.683	2.212	**58.808**	25.09	41.23
17	1.231	0.358	1.55	0.174	2.318	0.693	2.209	4.355	**25.688**	24.725
18	0.931	0.34	1.532	0.199	14.698	0.69	0.805	4.345	21.566	**24.737**
19	0.926	0.32	1.513	0.203	1.678	0.447	0.815	3.342	21.574	**24.741**
20	0.92	0.3	1.496	0.219	0.668	0.47	0.823	**51.491**	21.574	24.788
21	**28.22**	0.278	1.477	0.234	0.652	0.472	0.83	26.633	21.583	24.784
22	1.771	0.259	1.456	0.248	**27.922**	0.465	0.994	2.632	21.608	24.788
23	1.763	0.24	1.441	0.264	11.056	0.534	1.005	2.603	21.61	**24.807**

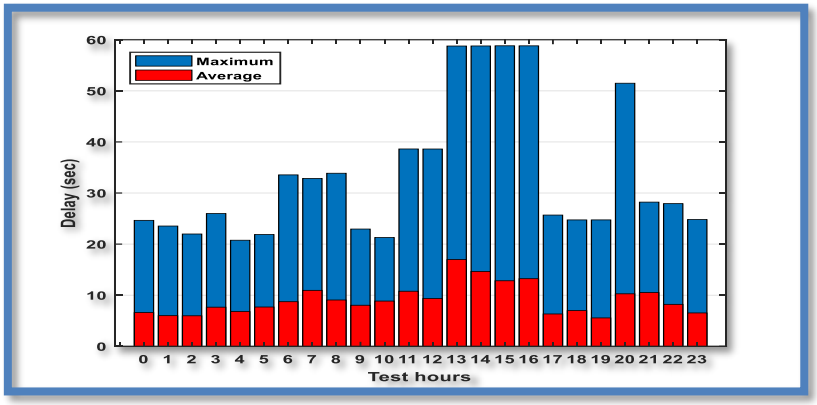

Figure 4 Delay per hour for Blynk IoT platform.

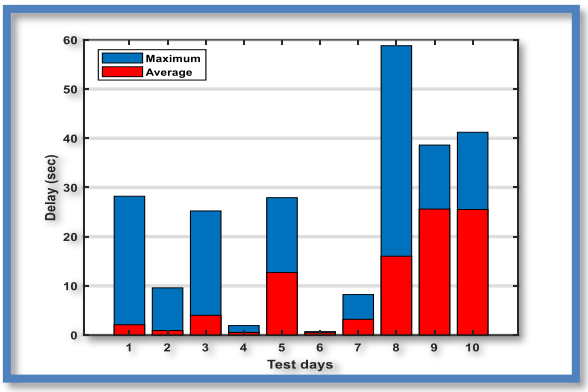

Figure 5 Delay per day for Blynk IoT platform.

Additionally, an important consideration when evaluating system latency is its comparison to commonly accepted standard latency values for various IoMT-based applications. **Table 5** outlines the key telemedicine applications and their acceptable delay thresholds. The implemented system is categorized under non-critical periodic monitoring. Based on the extensive testing, the overall average delay values not exceeding 32 and 17 seconds observed in the system fall well within the acceptable range for this class of telemedical applications.

Table 5 Latency of main telemedicine applications.

Application class	Latency requirement	Reason	Example
Critical	**Low**, typically less than 330 ms. [33],[34]	These applications require immediate feedback or action to ensure patient safety.	Remote surgery and urgent emergency response systems.
Non-Critical Monitoring	**Moderate**, typically up to several seconds. [35], [36]	These systems can tolerate delays without compromising patient safety or care.	Routine patient monitoring and wearable health devices for fitness tracking.
Long-Term Data Analysis	**High**, can tolerate delays of several minutes or even hours. [35]	These applications are typically not time-sensitive and are used for long-term health management rather than immediate interventions.	Predictive analytics and historical data review.

Next, the percentage data loss for the Blynk platform is measured as shown in **Table 6**. As compared with the case of Arduino IoT platform, the Blynk based system suffered from slightly more amounts of data loss. Although a maximum loss of 75% happened at hour 17/ day 10, it is clearly a rare situation related with a temporary degradation in Internet service. But, in total,

the losses in the Blynk platform are more as compared with the case of the Arduino IoT platform. This can have a negative impact on reliability.

Table 6: Percentage data loss for Blynk IoT platform.

Hour	Test day									
	1	2	3	4	5	6	7	8	9	10
0	**3.33**	0	0	0	0	0	0	0	0	0
1	0	0	0	0	0	0	0	0	**5**	0
2	0	0	0	0	0	0	0	0	0	0
3	0	0	0	0	0	0	0	0	0	0
4	0	0	0	0	0	0	0	**1.66**	0	0
5	0	0	0	0	0	**1.66**	0	0	0	0
6	0	0	0	**1.66**	0	0	0	0	0	0
7	0	0	0	0	**3.33**	0	0	0	0	0
8	**15**	0	0	0	0	0	5	0	0	0
9	13.33	**41**	15	0	0	0	0	0	0	1.66
10	3.33	**45**	16.66	0	0	0	0	0	0	0
11	0	0	1.66	0	**3.33**	0	0	0	0	0
12	0	0	0	0	**6.66**	0	0	0	0	0
13	0	0	1.66	0	3.33	0	0	**20**	0	0
14	0	0	0	0	0	0	0	0	**1.66**	1.66
15	0	0.66	0	0	**13.33**	0	0	0	0	1.66
16	0	0	0	0	0	0	0	20	1.66	**26.66**
17	0	0	0	0	10.00	0	0	0	25.00	**75.00**
18	**10.00**	0	0	0	0	3.33	0	0	0	0
19	0	0	0	0	0	0	0	0	0	0
20	0	0	0	0	0	0	0	**15.00**	0	0
21	**3.33**	0	0	3.33	0	0	0	3.33	0	0
22	0	0	0	0	**1.66**	0	1.66	0	0	0
23	0	0	0	0	0	0	0	0	0	0

The reliability calculations are shown in **Table 7**. The relatively large loss peak at the tenth test day has reduced system availability to 95.56%, which is by itself can be considered as a high percentage. For the rest of the test days, the availability is higher and reaches 99.79%. However, as a way of validation for the availability results and the related reliability metrics, the EPM is calculated as the average loss per day from **Table 6**. As shown in **Table 7**, the EPM perfectly complements the availability values.

Table 7: Reliability calculations for Blynk IoT platform.

Day	Total Up time (minutes)	Total Down time (minutes)	Number of failures	MTBF (minute)	MTTR (minute)	Availability (%)	EPM (%)
1	1411	29	7	201.57	4.14	97.99	2.01
2	1388	52	4	347	13	96.39	3.61
3	1419	21	4	354.75	5.25	98.54	1.46
4	1437	3	3	479	1	99.79	0.21
5	1415	25	11	128.64	2.27	98.26	1.74
6	1437	3	2	718.5	1.5	99.79	0.21
7	1436	4	2	718	2	99.72	0.28
8	1404	36	8	175.5	4.5	97.5	2.5
9	1420	20	4	355	5	98.61	1.39
10	1376	64	5	275.2	12.8	95.56	4.44

Based on the presented results and findings, it can be stated that the implemented system can be relied on as a successful remote patient monitoring tool built by using the available Internet service and technical components in the local region of Kirkuk city. It can positively contribute

to the healthcare sector as described in section 1. Finally, it worth noting that the specifications of the implemented system in terms of sensors types, accuracy, delay, loss rate, etc., may fit many telemedical applications whose requirements match these specifications. But at the same time, it may be not suitable for others. That is, the implemented IoMT system becomes not suitable for telemedical applications that are delay sensitive and do not have the suitability to withstand such values of time delay, data loss, etc.

7. Conclusions

In this paper, an IoMT system has been designed and implemented for remote patient health monitoring. The system has been tested to evaluate its reliability under practical conditions. Two different popular IoT platforms, namely the Arduino and Blynk, have been used to compare their impact on the performance of the system. The conducted tests have provided a practical experimentation results for the implemented system under realistic operation conditions and locally available facilities. Data is sent in this system with a variable time delay depending on the connection status, but it does not exceed 59 seconds in the worst circumstances. The tests show the Blynk IoT platform cause less delay as compared with the Arduino IoT platform. Also data transmission involved losses, and although rarely, high loss rates may appear. But the tests for 24 hours over 10 days have shown that the system can achieve average availability of more than 98% for both of the tested platforms. Therefore, as a conclusion, it can be stated that the tested platforms seem to be equivalently reliable, with Blynk having an advantage in terms of the delayed time.

However, the implemented system is not without limitations. On the shelf sensors were used for two reasons: first to prove the concept with a limited budget, second their accuracy is suitable for the target RPM system. Even though, the used sensors and circuitry have enabled a high reliability system.

Possible future work may be applied to test different system configurations to suit different telemedical applications, such as tele-surgery, requiring more accurate sensory, less delay and less loss rate. However, performance improvement by examining selective system customizations could be a wide field of many future works. The cost of the system may be studied and analyzed to optimize system resources according to different requirements and practical limitations. Further system performance improvement may be investigated by examining the individual and collective effects of specific factors and system components.

In summary, the implemented system has been built by using locally available resources. The tests showed it is accurate enough and reliable for RPM with limited delay and loss rate. It is customizable to suit a wide range of medical applications. Therefore, a possible collaboration

with the healthcare agencies in Kirkuk city may be held in order to bring the system into actual practical operation to support and improve the healthcare system.

8. References

[1] Ree MD, Vizár D, Mantas G, Bastos J, Kassapoglou-Faist C, Rodriguez J, editors. A Key Management Framework to Secure IoMT-enabled Healthcare Systems. 2021 IEEE 26th International Workshop on Computer Aided Modeling and Design of Communication Links and Networks (CAMAD); 2021 25-27 Oct. 2021.

[2] Al-Turjman F, Nawaz MH, Ulusar UD. Intelligence in the Internet of Medical Things era: A systematic review of current and future trends. Computer Communications. 2020;150:644-60.

[3] Khan MA, Din IU, Kim B-S, Almogren A. Visualization of remote patient monitoring system based on internet of medical things. Sustainability. 2023;15[10]:8120.

[4] Alkaabi A, Aljaradin M. Green Hospitals for the Future of Healthcare: A Review. Al-Kitab Journal for Pure Sciences. 2022;6[2]:31-45.

[5] Abdullah A, Ismael A, Rashid A, Abou-ElNour A, Tarique M. Real time wireless health monitoring application using mobile devices. International Journal of Computer Networks & Communications (IJCNC). 2015;7[3]:13-30.

[6] Hasan D, Ismaeel A. Designing ECG monitoring healthcare system based on internet of things blynk application. Journal of applied science and technology trends. 2020;1[2]:106-11.

[7] Chinnamadha N, Ahmed RZ, Kalegowda K. Development of health monitoring system using smart intelligent device. Indonesian Journal of Electrical Engineering and Computer Science (IJEECS). 2022;28[3]:1381-7.

[8] Turcu CE, Turcu CO. Internet of things as key enabler for sustainable healthcare delivery. Procedia-Social and Behavioral Sciences. 2013;73:251-6.

[9] Saini P, Ahuja R, Sai V. Wireless Sensor Networks and IoT Revolutionizing Healthcare: Advancements, Applications, and Future Directions. Emerging Technologies and the Application of WSN and IoT: CRC Press; 2024. p. 228-50.

[10] Malasinghe LP, Ramzan N, Dahal K. Remote patient monitoring: a comprehensive study. Journal of Ambient Intelligence and Humanized Computing. 2019;10:57-76.

[11] Vishnu S, Ramson SJ, Jegan R, editors. Internet of medical things (IoMT)-An overview. 2020 5th international conference on devices, circuits and systems (ICDCS); 2020: IEEE.

[12] Guntur SR, Gorrepati RR, Dirisala VR. Internet of Medical things: Remote healthcare and health monitoring perspective. Medical big data and internet of medical things: CRC Press; 2018. p. 271-97.

[13] Jabirullah M, Ranjan R, Baig MNA, Vishwakarma AK, editors. Development of e-health monitoring system for remote rural community of India. 2020 7th International conference on signal processing and integrated networks (SPIN); 2020: IEEE.

[14] Moore SJ, Nugent CD, Zhang S, Cleland I. IoT reliability: a review leading to 5 key research directions. CCF Transactions on Pervasive Computing and Interaction. 2020;2:147-63.

[15] Hejazi T-H, Badri H, Yang K. A Reliability-based Approach for Performance Optimization of Service Industries: An Application to Healthcare Systems. European Journal of Operational Research. 2019;273[3]:1016-25.

[16] Gawanmeh A, Al-Hamadi H, Al-Qutayri M, Shiu-Kai C, Saleem K, editors. Reliability analysis of healthcare information systems: State of the art and future directions. 2015 17th International Conference on E-health Networking, Application & Services (HealthCom); 2015 14-17 Oct. 2015.

[17] Zaitseva E, Levashenko V, Kostolny J, Kvassay M. New methods for the reliability analysis of healthcare system based on application of multi-state system. Applications of Computational Intelligence in Biomedical Technology. 2016:229-51.

[18] Ahmed I, Balestrieri E, Lamonaca F. IoMT-based biomedical measurement systems for healthcare monitoring: A review. Acta IMEKO. 2021;10[2]:174-84.

[19] Albahri OS, Albahri AS, Mohammed K, Zaidan A, Zaidan B, Hashim M, et al. Systematic review of real-time remote health monitoring system in triage and priority-based sensor technology: Taxonomy, open challenges, motivation and recommendations. Journal of medical systems. 2018;42:1-27.

[20] Chipara O, Lu C, Bailey TC, Roman G-C, editors. Reliable clinical monitoring using wireless sensor networks: experiences in a step-down hospital unit. Proceedings of the 8th ACM conference on embedded networked sensor systems; 2010.

[21] Dwivedi R, Mehrotra D, Chandra S. Potential of Internet of Medical Things (IoMT) applications in building a smart healthcare system: A systematic review. Journal of oral biology and craniofacial research. 2022;12[2]:302-18.

[22] Fernandez-Lopez H, Afonso JA, Correia JH, Simoes R. Remote patient monitoring based on zigbee: Lessons from a real-world deployment. Telemedicine and e-Health. 2014;20[1]:47-54.

[23] Charness N, Fox M, Papadopoulos A, Crump C. Metrics for assessing the reliability of a telemedicine remote monitoring system. Telemedicine and e-Health. 2013;19[6]:487-92.

[24] Qin R, Dzombak R, Amin R, Mehta K. Reliability of a telemedicine system designed for rural Kenya. Journal of primary care & community health. 2013;4[3]:177-81.

[25] Gunawan I, B. A. C P, Suhartini, Sudianto A, Sadali M, Faturrahman I, et al., editors. Prototype Health Monitoring For Quarantined Covid 19 Patients Based On The Internet Of Things (IoT). 2022 International Conference on Science and Technology (ICOSTECH); 2022 3-4 Feb. 2022.

[26] Tsvetanov F, Pandurski M. Delay of Transmitted Data in the Remote Patient Monitoring System through AMQP and CoAP. International Journal of Online & Biomedical Engineering. 2024;20[7].

[27] Yew HT, Ng MF, Ping SZ, Chung SK, Chekima A, Dargham JA, editors. Iot based real-time remote patient monitoring system. 2020 16th IEEE international colloquium on signal processing & its applications (CSPA); 2020: IEEE.

[28] Zikria YB, Afzal MK, Kim SW. Internet of multimedia things (IoMT): Opportunities, challenges and solutions. Sensors. 2020;20[8]:2334.

[29] Miracle NO. The role of network monitoring and analysis in ensuring optimal network performance. International Research Journal of Modernization in Engineering Technology and Science https://doi org/1056726/irjmets59269. 2024.

[30] Thawkar DR. Down Time Analysis In Process Industry-A Case Study. Weekly Science Research Journal. 2013;1[24]:1-10.

[31] Aguilar A, editor Lowering Mean Time to Recovery (MTTR) in Responding to System Downtime or Outages: An Application of Lean Six Sigma Methodology. 13th Annual International Conference on Industrial Engineering and Operations Management; 2023.

[32] Todmal YS, Shinde P, Sisodia V, editors. Analysis of breakdowns and implementing optimal maintenance of engine cylinder block machines for improving operational availability. Proceedings of the International Conference on Industrial Engineering and Operations Management Presented at the 2nd Indian International Conference on Industrial Engineering and Operations Management, Warangal, India; 2022.

[33] Bailo P, Gibelli F, Blandino A, Piccinini A, Ricci G, Sirignano A, et al. Telemedicine applications in the Era of COVID-19: telesurgery issues. International Journal of Environmental Research and Public Health. 2021;19[1]:323.

[34] Xu S, Perez M, Yang K, Perrenot C, Felblinger J, Hubert J. Determination of the latency effects on surgical performance and the acceptable latency levels in telesurgery using the dV-Trainer® simulator. Surgical endoscopy. 2014; 28:2569-76.

[35] Alam MM, Ben Hamida E. Surveying wearable human assistive technology for life and safety critical applications: Standards, challenges and opportunities. Sensors. 2014; 14[5]:9153-209.

[36] Fadhel AA, Hasan HM. Reducing Delay and Packets Loss in IoT-Cloud Based ECG Monitoring by Gaussian Modeling. International Journal of Online & Biomedical Engineering. 2023;19[6].

Al-Kitab Journal for Pure Sciences (2025); 9(2):104-127.
https://doi.org/10.32441/kjps.09.02.p7

Al-Kitab Journal for Pure Sciences
ISSN: 2617-1260 (print), 2617-8141(online)

https://isnra.net/index.php/kjps

Polyphenols of Mulberry White (*Morus alba L.*) Leaves as a Source of Functional Food: A Review

Hagar F. Forsan[1]*, Menatalla R. Fayed[2], Noureldin M. Farahat[3],Ezzeldeen M. Alswerky[4], Walaa M. Gabr[5], Asmaa E. Abd El-Hak[6], Mohamed A. Fouda[7], Mennat-Allah Safwat[8]

[1]*Animal Production Research Institute (APRI), Agricultural Research Center (ARC), Dokki, Giza, Egypt, [2] Faculty of Pharmacy, Sinai University, North Sinai, Egypt, [3] Faculty of Pharmacy, Alexandria University, Alexandria, Egypt, [4] Faculty of Science, Islamic University of Gaza, Gaza, Palestine, [5]Faculty of Science, Mansoura University, Dakahlia, Egypt, [6] Faculty of Agriculture, Ain Shams University, Cairo, Egypt, [7] Faculty of Agriculture, Tanta University, Gharbia, Egypt, [8] Faculty of Pharmacy, Alazhar University, Cairo, Egypt.

*Corresponding Author: hagarfathy@pg.cu.edu.eg

Citation: Forsan HF, Fayed MR, Farahat NM, Gabr WM, Alswerky EM, Abd El-Hak AE, Fouda MA, Safwat MA. Polyphenols of Mulberry White (Morus alba L.) Leaves as a Source of Functional Food: A Review. Al-Kitab J. Pure Sci. [Internet]. 2025 Apr. 30; 9(2):104-128. DOI: https://doi.org/10.32441/kjps.09.02.p7.

Keywords: Mulberry Leaves; Phenolic Compounds; Extraction; Metabolism; Health Benefits.

Article History
Received 05 Sep. 2024
Accepted 27 Oct. 2024
Available online 30 Apr. 2025

Abstract:

Mulberry is a plant that grows in temperate to subtropical climates. Mulberry leaves are economically feasible due to their historical importance in sericulture, so their production increases yearly, but the large output leads to a large percentage of residues. As a result, it was largely accumulated, creating controversial consequences, rather than being reintegrated into the manufacturing process for a new function. However, this residue in mulberry leaves naturally contains high levels of bioactive compounds, especially polyphenols. Mulberry leaves have a vital pharmaceutical potential role as antibacterial and antioxidant. Mulberry leaves have many health benefits, such as anticancer, antiviral, and anti-obesity etc. However, many extraction methods can benefit different uses as food innovation, leading to added-value products. So, the current review article provides a comprehensive discussion concerning extraction methods, metabolism, health effects such as Anticancer, Antidiabetic**,** Anti-obesity, Activity of anticonvulsant, Antiatherosclerosis, and SARS-CoV-2 inhibition, and various uses in the food industry.

Keywords: Mulberry Leaves; Phenolic Compounds; Extraction; Metabolism; Health Benefits.

بولي فينولات أوراق التوت (*Morus alba L.*) كمصدر للغذاء الوظيفي: مقال مرجعي

هاجر فتحي فرسان[١]، منة الله رضا فايد[٢]، نورالدين محمد فرحات[٣]، عزالدين محمد السويركى[٤] ، ولاء محمد جبر[٥] ، اسماء عماد عبدالحق[٦] ، محمد أشرف فودة[٧] ، منه الله صفوت[٨]

[١]معهد بحوث الإنتاج الحيواني، مركز البحوث الزراعية ،الدقي، الجيزة، مصر/ [٢] كلية الصيدلة، جامعة سيناء، شمال سيناء، مصر/ [٣]كلية الصيدلة، جامعة الإسكندرية، الإسكندرية، مصر/ [٤] كلية العلوم، الجامعة الإسلامية، غزة، فلسطين/ [٥] كلية العلوم، جامعة المنصورة، الدقهلية، مصر/ [٦] كلية الزراعة، جامعة عين شمس، القاهرة، مصر/ [٧] كلية الزراعة، جامعة طنطا، الغربية، مصر/ [٨] كلية الصيدلة، جامعة الأزهر، القاهرة، مصر

hagarfathy@pg.cu.edu.eg, su.14011384@su.edu.eg, D06201915411@alexu.edu.eg, eswerky@students.iugaza.edu.ps, alaa300@std.mans.edu.eg, asmaa_emad@agr.asu.edu.eg, mohammed30935346@agr.tanta.edu.eg, Mennat-allahAbdelsalam5928@azhar.edu.eg

الملخص:

ينمو نبات التوت بكثافة في المناطق ذات المناخ المعتدل وشبه الاستوائي. وتكتسب أوراق التوت أهمية اقتصادية نظرًا لدورها التاريخي في تربية دودة القز، مما أدى إلى زيادة إنتاج نبات التوت سنويًا. إن الزيادة الكبيرة في الإنتاج تتسبب في تراكم كميات كبيرة من المخلفات. هذه المخلفات تراكمت بمرور الوقت بشكل كبير، مما أوجد تحديات بيئية واقتصادية. وُجد أن مخلفات أوراق التوت تحتوي على مستويات مرتفعة من المركبات النشطة بيولوجيًا، وخاصة البوليفينولات. تلعب أوراق التوت دورًا مهمًا في المجال الصيدلاني، حيث تتمتع بخصائص مضادة للأكسدة والبكتيريا. كما أن لها فوائد صحية متعددة، منها الوقاية من الإصابة بمرض السرطان، والوقاية من السمنة، كما أنها مضادة للفيروسات وغيرها. وُجد أن هناك العديد من طرق الاستخلاص التي يمكن الاستفادة منها في مختلف المجالات، بما في ذلك الابتكار الغذائي، مما يساهم في إنتاج منتجات ذات قيمة مضافة. يستعرض هذا المقال بشكل شامل طرق الاستخلاص، والتمثيل الغذائي، والفوائد الصحية لأوراق التوت، مثل مكافحة السرطان، ومكافحة السكري، ومكافحة السمنة، والوقاية من التشنجات، والحد من تصلب الشرايين، وتثبيط فيروسSARS-CoV-2 ، فضلاً عن الاستخدامات المتنوعة في الصناعة الغذائية.

الكلمات المفتاحية: أوراق التوت، المركبات الفينولية، الاستخلاص، التمثيل الغذائي، الفوائد الصحية.

1. Introduction:

The Morus genus (Moraceae) has about 19 members, most are in the northern temperate zone. White, black, and red mulberries are the highest prevalent types. *Morus alba* is the most common species grown in South Europe, Turkey, Southwest Asia, and Central Asia. This plant's various morphological components (fruits, leaves, roots, and stems) have been used for various purposes. The primary contents are fruits and leaves **[1]**. In a circular and sustainable bioeconomy, organic agricultural wastes like mulberry leaves are utilized as extraction material, and recovery chemicals are reinserted into the production chain. scientists use different recovery procedures to acquire bioactive compounds. Mulberry leaves have therapeutic benefits **[2]**. Mulberry leaves are also used as an anti-hyperglycemic supplement by people with diabetes in

Japan and Korea, high blood pressure, alcohol hangovers, throat infections, irritations, and infections. Mulberry tea usage has risen in recent decades due to its hypoglycemic, depressive, antioxidant, and hepatoprotective properties [3]. Mulberry leaves are approved as a great source due to the high concentration of protein, carbohydrates, vitamins, microelements, and dietary fiber. It is also high in flavonoids, alkaloids, phenolic acids, and gamma-aminobutyric acid [4]. Chlorophyll, the green pigment found in mulberry leaves, plays a crucial role in photosynthesis, allowing plants to convert light energy into chemical energy. In addition to its primary role in plants, chlorophyll in mulberry leaves offers several health benefits when consumed by humans [5]. Anti-HIV, antioxidative, hypotensive, cytotoxic, hypoglycemia, hepatoprotective, neuroprotective, and anti-inflammatory activities are all present in these bioactive molecules. They've also been used to treat antibacterial and anti-obesity conditions. Plants have since been exploited in phytotherapeutic activities and other industrial uses as a source of pharmacologically bioactive compounds, mainly for medications that treat various ailments. Various plants require the ability to scavenge free radicals for the food business [6]. Caffeic acid, kaempferol-3-O-(6-malonyl)–glucoside, quercetin-3-O-(6-malonyl)–glucoside, caffeoylquinic acids, and quercetin-3-O-glucoside are among phenolic acids and flavonoids found in Mulberry leaves [7], Figure 1 [8]. This review aims to thoroughly explain extraction techniques, metabolism, anticancer, antidiabetic, anti-obesity, anticonvulsant, anti-atherosclerosis, and SARS-CoV-2 inhibitory health effects, as well as diverse applications in the food sector.

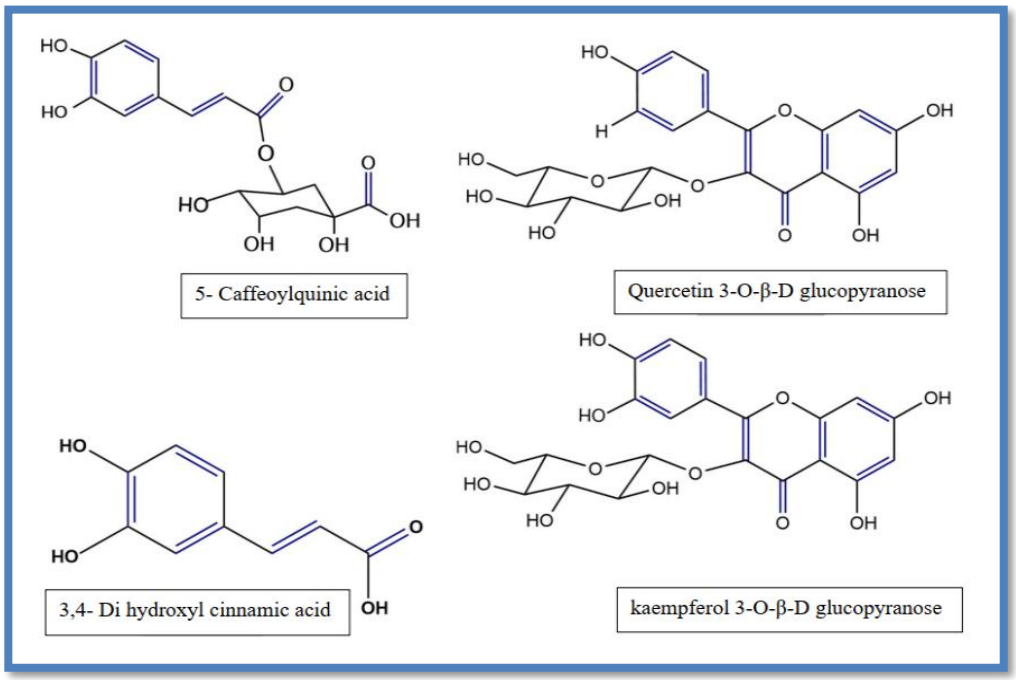

Figure 1: Phenolic acids identified from Mulberry leaves [7, 8].

2. Extraction methods

2.1 Low-pressure liquid chromatography (LPLC)

2.1.1 Mulberry leaf sample preparation: Researchers used dried plant material from mulberry leaves. The materials were sieved after being reduced to a fine powder to find the optimal particle size for green tea catechin extraction. The powder was maintained in airtight jars and kept at a temperature of 4°C [9].

2.1.2 Extraction: The following steps were used to extract lipids from Mulberry leaves in the first instance. n-hexane (250 mL) was used to homogenize dried Mulberry leaves (10 g), centrifuged at 4390 g for 5 minutes after being homogenized for 10 minutes in an ice bath. In the following step, the residue was added after removing the supernatant to 250 mL precooled alcohol/water combination (8:2, by volume) to create the final product. Separate extractions were performed on the mixture using a homogenizer at 5000 rpm for 5 minutes and a centrifuge at 4390 g for 5 minutes. Two supernatants were mixed and dehydrated in a RE-52AA rotary evaporator at 50°C. Each extraction's dry residue was dissolved in an 8/2 methanol/water solution. The solution was filtered through a filter membrane (0.22 m; 25 mm Luer syringe filter) and stored at 80°C till analysis. Each extraction took two steps. The residue was preserved for upcoming use. Solvent for extraction was discovered in an 8:2 binary mixture of water, organic solvents (e.g., acetone), and other organic solvents. Diamonsil C18 reversed-phase column with methanol as solvent (250 nm 4.6mm, 5 m, Dikma, Beijing). Mobile phases A and B were 0.01 % phosphoric acid (A) and 0.01 % acetonitrile (B), with gradient elution as follows: 18-23 % B; 29-36 % B; 36-43; 43-50 % B. The column was also set at 30°C with 0.9 mL/min flow [10, 11].

3. Quantitative phenolic analysis of black mulberry leaf extracts

Low-pressure liquid chromatography with SPD-M10AVP diode array detector (200–550 nm), CTO-10 column oven, LC-10 ADP pump, Reodayn Valve type 7725i manual sample injection, and CBM-10A communications bus module. The following materials were dissolved in 50 mL MeOH in a volumetric flask 50 mL: (80:20; v/v) rutin trihydrate, hydroxycinnamic acid, color Serial dilutions in a MeOH: H2O (80:20; vol/vol) solvent phase yielded concentrations of 10–500 g/mL. The Low-pressure liquid chromatography was used to test seven standard solution concentrations (10–500 g/mL). In this case, an Intersil ODS-3 reverse phase column (25 cm 4.6mm, 5 m particle size) was used. It was done at 1 mL/min using 20 L of standards and extracts. All solutions were filtered using a 0.45 m syringe filter before Low-pressure liquid chromatography analysis. The mobile phase was acetic acid (vol/vol) and

MeOH (solvent A) (solvent B). Conditions of gradient were nominal values: 0 (100), 3, 95 (95), 18, 80 (25), 75 (75), 60 (60), 55 [12], 65 (40), and 100 (100). During the acquisition of the chromatograms, the UV spectra of each chemical were obtained using a diode array detector. For gallic acid monohydrate, (—) –gallocatechin, vanillic acid, ellagic acid, trans-ferulic acid, hydroxycinnamic acid, kaempferol, (+)–catechin, and (—) –epicatechin, the maximum wavelengths were 280 nm for gallic acid monohydrate, (—) –gallocatechin, vanillic acid, ellagic acid, trans-ferulic acid [13].

4. High-performance liquid chromatography

4.1 Collection and preparation of samples of Mulberry leaves: In High-Performance Liquid Chromatography (HPLC) analysis, the collection and preparation of samples of mulberry leaf extracts is a critical step to ensure accurate and reliable results. The process typically begins with the collection of fresh or dried mulberry leaves, which are then thoroughly cleaned to remove any dirt or contaminants. The leaves are air-dried or oven-dried and ground into a fine powder to increase the surface area for extraction. In this process, heating the Mulberry leaves to 55°C and drying it for 6–8 hours is a typical approach to remove moisture, ensuring the stability of bioactive compounds. Pulverizing the dried Mulberry leaves into a powder increases its surface area, facilitating more efficient extraction of polyphenols or other compounds during further analysis. Storing the powder at 2°C until use helps preserve the integrity of these bioactive compounds, preventing degradation from environmental factors like light or heat. This method ensures that the Mulberry leaves remains in good condition for subsequent studies or extractions

4.2 Free phenolic extraction: A RE-52AA rotary evaporator was used to dry two supernatants at 50°C. The "two supernatants" refer to the liquid fractions obtained from two distinct extraction steps that utilize different solvents or methods. The first supernatant is derived from an initial extraction using a non-polar solvent, such as n-hexane, which is typically employed to extract lipid or non-polar compounds. After homogenizing the dried mulberry leaves with n-hexane, centrifugation separates the mixture, yielding a supernatant rich in lipid-soluble compounds. The second supernatant comes from a subsequent extraction using a different solvent system, often a mixture of alcohol and water (for instance, ethanol and water in an 8:2 ratio), aimed at isolating free phenolic compounds that are more soluble in polar solvents. Following this extraction, the mixture undergoes centrifugation again, resulting in a supernatant containing the desired free phenolics. Both supernatants are then dried separately using a rotary evaporator at 50°C, concentrating their respective bioactive compounds before

further analysis or processing. This method effectively ensures the extraction of both lipid-soluble and phenolic compounds from the mulberry leaves.

Or make a methanol and water solution to dissolve the dry extraction residue. The solution was filtered using 0.22 m membrane filters and preserved till analysis at 80°C. Each extraction took two steps. The remnants were preserved for future use. Various organic solvents, such as ethanol, were used to create 8:2 binary mixtures of organic solvents and water to determine the best extraction solvent **[14]**. The following steps were used to extract lipids from the Mulberry leaves in the first instance. n-hexane (250 mL) was used to homogenize dried mulberry leaves (10 g), which were centrifuged at 4390 g for 5 minutes after being homogenized for 10 minutes in an ice bath **[15]**. The final product was made by removing the supernatant and mixing it with 250 mL precooled alcohol and water (8:2, by volume). The mixture was homogenized (5000 rpm, 5 minutes) and centrifuged separately (4390 g, 5 minutes).

4.3 Bound phenolic extraction: After phenolics were extracted freely, Mulberry leaves residues were used to hydrolyze bound phenolics in acetone **[15]**. The substance was subjected to both alkaline and acid hydrolyzed, and alkaline hydrolysis was performed **[16]**. The residue was hydrolyzed under nitrogen gas flow for 1.5 hours with 2 M NaOH (100 mL). HCl (6 M) was added six times to obtain pH 2. This extract was vaporized to dryness at 45°C. The dried Mulberry leaves extracts were reconstituted in methanol 80%, filtered, and kept at –80°C. Acid hydrolysis was performed using the Dongxiao method. This was followed by 1.5 hours at 85°C in a mix of methanol and concentrated sulfuric acid (90:10) with nitrogen gas flow. The mix was neutralized to pH 2 using NaOH (10 M) for six extractions. This extract evaporated to dryness at 45°C.

The Dongxiao technique was used to achieve acid hydrolysis. After that, 1.5 hours at 85°C with nitrogen gas flow were spent in a combination of methanol and concentrated sulfuric acid (90:10). The mix was neutralized to pH 2 using NaOH for six extractions (10 M). At 45°C, this extract evaporated to dryness. Dietary supplements should not be taken with dried extracts. Dried extracts should be approached with caution when it comes to their use in dietary supplements for several important reasons. Firstly, these extracts can exhibit potency variability due to differences in raw material quality, extraction methods, and processing conditions, leading to inconsistent concentrations of active compounds and making it challenging to determine effective dosages for health benefits. Additionally, the drying process can cause the degradation or loss of sensitive bioactive compounds, as exposure to heat, light, and oxygen may break down certain vitamins, antioxidants, and phytochemicals, thereby diminishing their

efficacy in the final product. Furthermore, improperly purified dried extracts may harbor contaminants like pesticides, heavy metals, or microbial toxins, posing significant health risks, particularly since dietary supplements are often not adequately regulated. The lack of standardization in many dried extracts complicates matters further, as consumers cannot be assured of specific active ingredient levels, making it difficult to understand their health impacts. Moreover, the potent biological effects of dried extracts can lead to interactions with medications, potentially causing adverse effects or diminishing the effectiveness of prescribed treatments, especially for those with pre-existing health conditions or multiple prescriptions. Finally, while some dried extracts show promise in preliminary studies, there is often limited clinical evidence supporting their safety and efficacy, which hinders confident recommendations for their use. For these reasons, consumers must consult healthcare professionals before using dietary supplements containing dried extracts, ensuring informed choices tailored to their specific health needs and conditions.

4.4 Total Polyphenol Content (TPC) determination

4.4.1 Extraction of Mulberry leaves: To create Mulberry leaves extract, approximately 200 mg of Mulberry leaves powder was properly weighed and combined with 20 mL of a solution containing ethanol and deionized water (70:30, vol/vol). The mixture was put in an ultrasonic cleaning bath (KQ-2200DB, 100W, Kunshan, China) and removed twice for a total of 20 minutes at 30 °C each time. The extracts were filtered via filter paper to remove any impurities. Last but not least, the filtrate was diluted with 70 % (vol/vol) ethanol in water to get 50 mL **[17]**.

4.4.2 Determination of Total Polyphenol Content (TPC): Using a slightly modified Folin-Ciocalteu technique, total polyphenols in Mulberry leaves were shown to be substantial. 40 ul of Folin-Ciocalteu reagent (2N) was mixed with the samples. A blank sample of 40 ml ethanol 70% ethanol was combined with diluted Folin-Ciocalteu solution and used for instrument auto zeros. The mixture was neutralized for 1–2 hours at room temperature before adding 1.2 mL of 7.5 percent sodium carbonate solution to test for pollutants. The absorbance was measured at 765 nm. The total polyphenol concentrations were expressed as gallic acid equivalents (y=0.6812x+0.0314, R2=0.9975, calibration range 0.0078125 mg/mL to 0.5 mg/mL, and absorbance 0.0308 and 0.3678, respectively). Total polyphenols as gallic acid equivalents **[17]**.

The Total Polyphenol Content of mulberry juice can be determined using the Folin-Ciocalteu colorimetric method, which is a widely used technique for quantifying polyphenols. In this

process, the Folin-Ciocalteu reagent, a mixture of phosphomolybdate and phosphotungstate, reacts with polyphenols present in the juice. When polyphenols reduce these complexes, a blue color develops, with the intensity of the color directly proportional to the polyphenol concentration. The absorbance of the solution is then measured spectrophotometrically, typically at a wavelength of around 765 nm. The results are compared to a standard, often gallic acid, and expressed as gallic acid equivalents **[18]** to quantify the total polyphenol content in the mulberry juice **[19]**.

5. HPLC determination of phenolic

The HPLC setup for analyzing phenolic compounds involves several critical components for effective separation and quantification. Column Specification: An ADME column (5 µm, 250 × 4.6 mm) is employed, which is suitable for separating a wide variety of phenolic compounds based on their polarity and size. Mobile Phase Composition: The method utilizes a mobile phase comprising phosphoric acid and water (0.2:100) as one solvent, alongside acetonitrile as the second solvent, enhancing the solubility of phenolic compounds in an acidic environment for improved separation. Gradient Program: A gradient elution method is employed with varying percentages of acetonitrile (solvent B) over specific intervals, which facilitates the optimized separation of phenolic compounds. The program involves starting at a lower percentage, gradually increasing to 30%, then 40%, decreasing to 20%, increasing again to 35%, and reaching 71% before decreasing to 76%. This approach allows for the elution of different phenolic compounds at distinct times, thereby enhancing resolution. Flow Rate and Temperature: A standard flow rate of 1 mL/min is maintained, striking a balance between resolution and analysis time, while the column temperature is kept at 25°C to ensure consistent performance of the stationary phase. Detection Wavelengths: Chromatograms are acquired at 280 nm and 350 nm, which are optimal wavelengths for detecting many phenolic compounds due to their strong UV absorbance at these points. Overall, this HPLC method accurately detects and quantifies phenolic compounds, making it suitable for analyzing samples such as mulberry leaves and other plant extracts **[20, 21]**.

6. Health-promising effects of polyphenols in Mulberry leaves

Polyphenols found in mulberry leaves offer a variety of health benefits. These benefits range from managing blood sugar levels and lipid profiles to safeguarding organs from oxidative stress and inflammation. Their physiological effects, which include antioxidant, anti-inflammatory, and antimicrobial properties, position them as strong candidates for both disease prevention and treatment. Besides, they play a role in protecting essential organs such as the

heart, brain, liver, and skin from damage. Such health advantages emphasize the considerable potential of polyphenols in the fields of pharmaceutical development and dietary supplements aimed at enhancing overall health and longevity.

6.1 Neurocognitive effects: Recent studies have also suggested that some gut microbiota (gm)-derived phenolic metabolites may have neurocognitive effects, such as improving memory and cognitive function **[22-24]**. Phenolic metabolites can have direct neurocognitive impacts by passing through the blood-brain barrier (BBB) and boosting levels of neurotransmitters like dopamine, which are examples of indirect brain effects. The primary purpose of this crucial physiological barrier is to keep dangerous compounds out of the brain, but it can also keep xenobiotics like polyphenols out. Thus, the effects of phenolic compounds (PCs) on the central nervous system (CNS) largely depend on their capacity to pass through the BBB **[25]**. The production of phenolic metabolites by the microbiota has been well-studied, but their permeability across the blood-brain barrier has just recently come to light **[26]**.

6.2 Anticancer: Mulberry leaves, derived from Morus species, contain a high concentration of polyphenols, which are natural substances with various biological activities, including properties that may help fight cancer. The main types of polyphenols found in mulberry leaves are flavonoids (like quercetin, rutin, and isoquercitrin), phenolic acids (including caffeic acid and gallic acid), and stilbenes. These compounds have been thoroughly researched for their potential health advantages, such as antioxidant, anti-inflammatory, and anticancer effects. Polyphenols in mulberry leaves function as strong antioxidants, neutralizing harmful free radicals that can damage DNA and contribute to cancer development by minimizing oxidative stress and shielding cells from mutations that may lead to cancer. They also exhibit anti-inflammatory properties, as compounds like quercetin and rutin have been shown to block pro-inflammatory cytokines and enzymes (such as COX-2), which play a role in the progression of cancer. Also, polyphenols encourage apoptosis (programmed cell death) in cancerous cells through pathways such as caspase activation, which helps eliminate compromised or cancerous cells while preserving healthy ones. What's more, specific polyphenols, such as quercetin, hinder the growth and spread of cancer cell lines (including breast, lung, and liver) by obstructing essential signaling pathways related to cell cycle progression, such as the PI3K/Akt and MAPK pathways. They also impede angiogenesis, the process of forming new blood vessels necessary for tumor growth, by downregulating the expression of vascular endothelial growth factor (VEGF). Flavonoids like rutin inhibit the migration and invasion of cancer cells, thereby decreasing metastasis by interfering with metalloproteinases (MMPs) that break down

the extracellular matrix. Research has shown that polyphenols from mulberry leaves can inhibit the proliferation of liver cancer cells, induce apoptosis through the mitochondrial pathway, and exhibit cytotoxicity against breast cancer cells by modulating estrogen receptor signaling. In models of colon cancer, these polyphenols suppress tumor growth and lower carcinogenesis risk by influencing GM and reducing inflammation. Overall, the polyphenols in mulberry leaves demonstrate major anticancer potential by fighting oxidative stress, inflammation, tumor growth, and metastasis. Although these findings indicate that mulberry leaves may be an effective supplement for cancer prevention and treatment, further clinical trials in humans are essential to validate these outcomes [27].

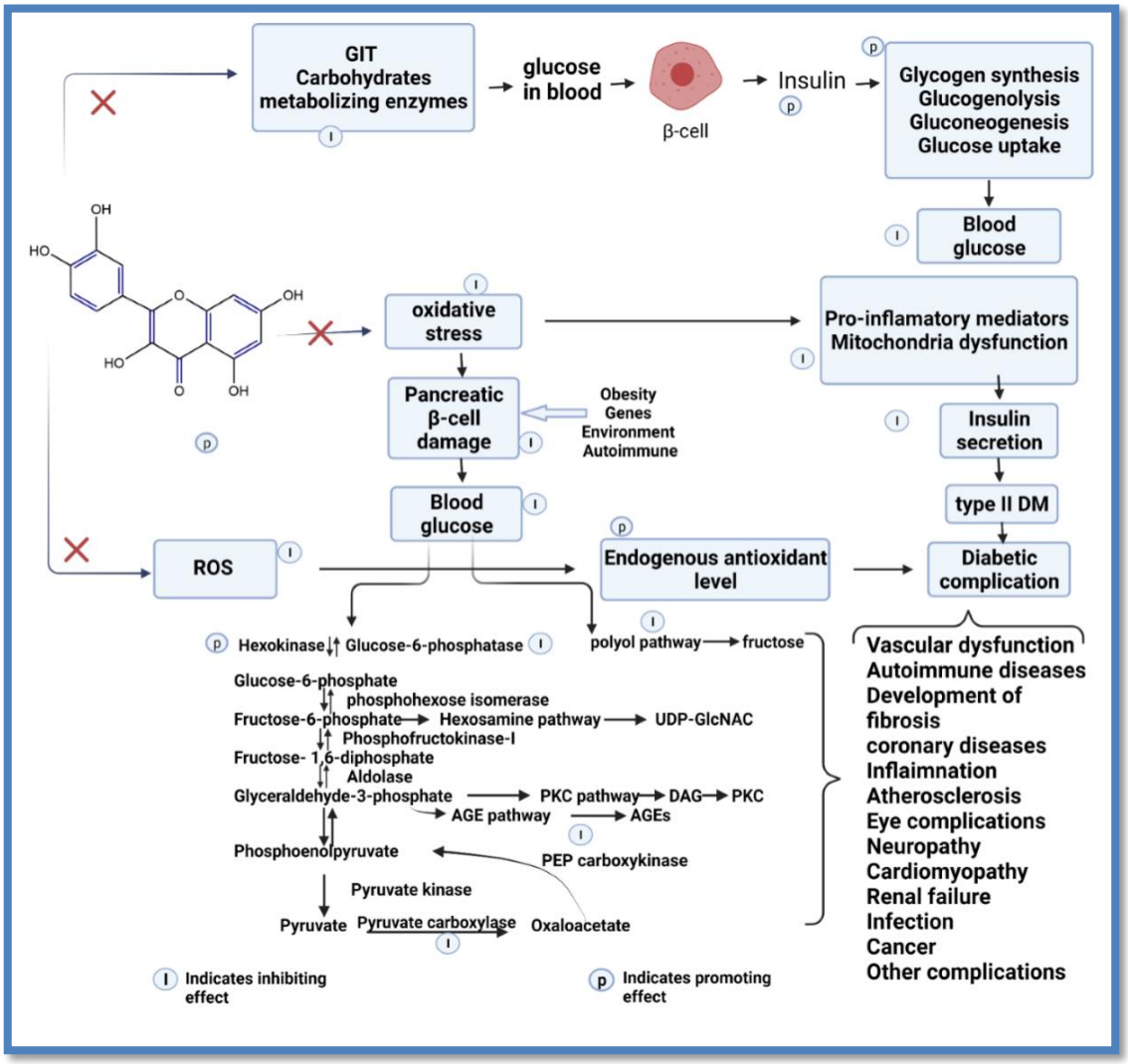

Figure 2: Antidiabetic mechanisms of dietary polyphenols. Adapted with permission from Ref. [28] Copyright 2024, Wiley

6.3 Antidiabetic: Consumption of dietary polyphenols reduces diabetes risk problems such as vascular dysfunction and failure for renal, protects pancreatic islet cells, reduces apoptosis, increases cell proliferation, decreases oxidative stress, activates insulin signaling, and

stimulates insulin secretion are some of the insulin-dependent and insulin-independent approaches that have been studied in vivo and in vitro as shown in **Figure 2** and **Figure 3 [28]**. High blood glucose impacts small-molecule medications' absorption, distribution, biotransformation, and excretion. Medication bioavailability and polyphenols in food vary depending on daily dosages, component complexity, and dietary interaction. Dietary polyphenols are little absorbed and quickly excreted. Only 5–10% of polyphenols are absorbed, while 90% of polyphenols digested are excreted in the colon. The majority of clinical drugs are properly absorbed and delivered. Carbohydrate, protein, and lipid metabolism are all affected by high blood sugar. The mechanisms that control these biochemical processes often also engage in phytochemical biotransformation. Thus, hyperglycemia impacts the bioavailability of dietary polyphenols. For example, diabetic mice show higher Cmax and AUC of mangiferin, baicalin, wogonoside, and oroxyloside **[29]**. Phlorizin bioavailability increased in rats with type 2 diabetes **[30]**. Diabetic rats absorbed more cynaroside and other antioxidants than non-diabetic rats. The Zucker diabetic fatty rat demonstrated lower Cmax values for catechin, epicatechin, quercetin, and resveratrol conjugated metabolites than the Zucker diabetic fatty rat **[31]**. methylation flavan-3-ol, resveratrol, and quercetin bioavailability metabolite considerably reduced in Zucker fatty diabetic rats **[31]**. Research on hyperglycemia-induced alterations in phytochemical bioavailability has stalled. Finding out how hyperglycemia affects dietary polyphenol bioavailability will allow us to use these polyphenols better and enhance clinical outcomes, as illustrated in **Figure 4**.

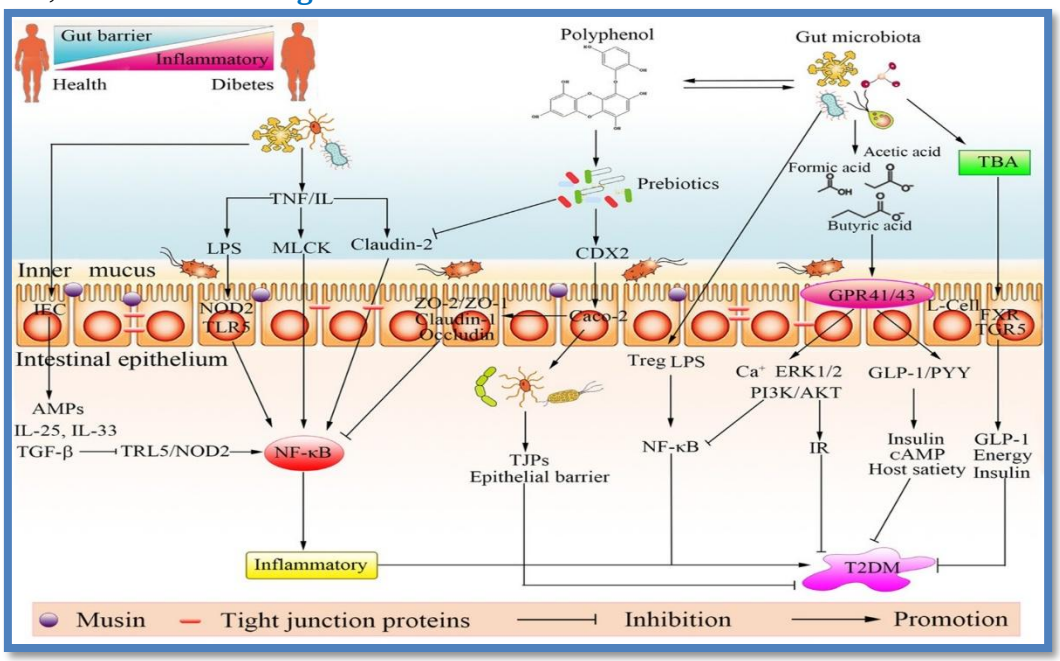

Figure 3: Polyphenols and gut microbiota diabetes effects. Adapted with permission from Ref. [28] Copyright 2024, Wiley.

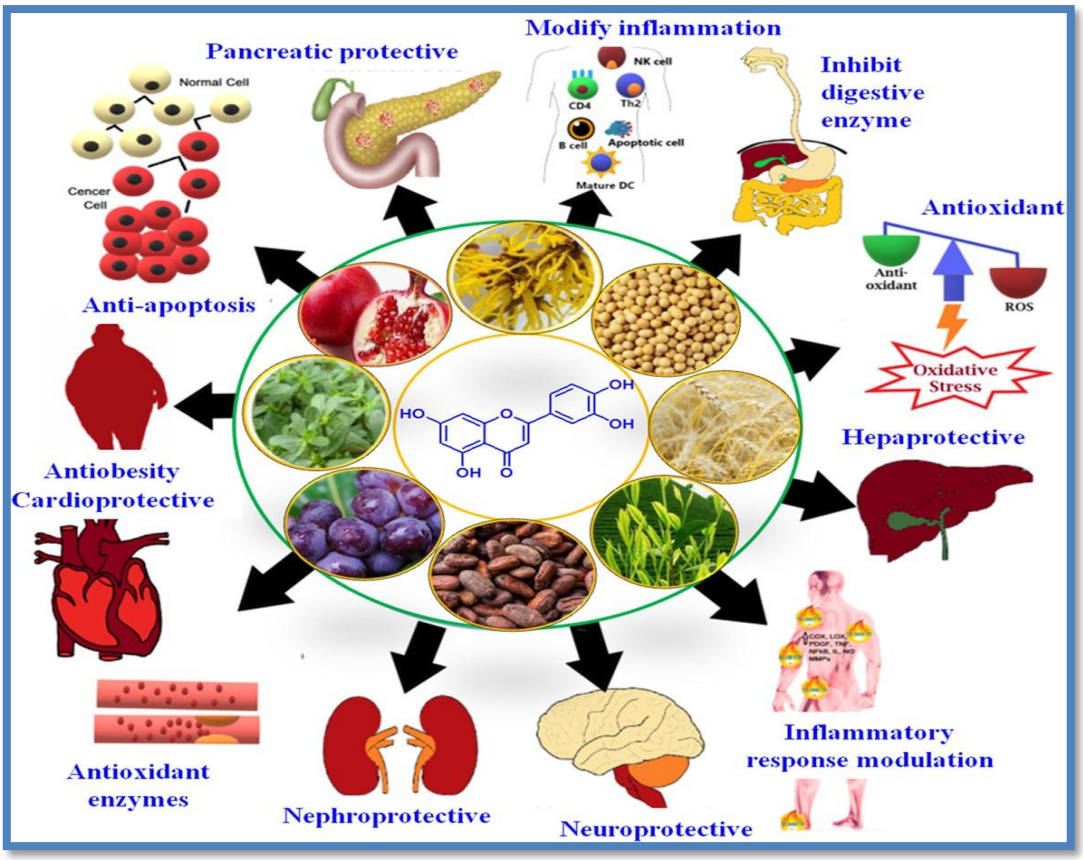

Figure 4: Dietary polyphenols Antidiabetic effects. Adapted with permission from Ref. [28] Copyright 2024, Wiley.

6.4 Anti-obesity: Mulberry leaves may help in managing obesity thanks to their high levels of polyphenols, particularly flavonoids like quercetin and rutin, which play a role in several mechanisms. They assist in regulating blood glucose and insulin sensitivity by inhibiting carbohydrate-digesting enzymes, such as alpha-glucosidase and alpha-amylase, which slow sugar absorption and prevent blood sugar spikes. Mulberry leaf extracts also improve lipid metabolism, encouraging the breakdown of fats and blocking the formation of new fat cells (adipogenesis), while also affecting genes related to fat metabolism, thereby aiding in weight loss. Besides, their anti-inflammatory and antioxidant properties may help diminish chronic inflammation and oxidative stress, which are often associated with complications related to obesity, such as insulin resistance and metabolic syndrome. By inhibiting pancreatic lipase, these extracts can reduce fat absorption, which further supports weight loss. In addition, some studies indicate that mulberry leaves may influence appetite by affecting hunger-related hormones, although further research is necessary to verify this effect in humans. In summary, mulberry leaves present promising advantages for managing obesity through the enhancement of glucose metabolism, reduction of fat accumulation, and improvement of metabolic health [32].

6.5 Activity of anticonvulsant: Mulberry leaves are rich in polyphenols, including flavonoids and phenolic acids, which have demonstrated potential anticonvulsant properties in various studies. These polyphenols may affect neurotransmitter systems, particularly gamma-aminobutyric acid (GABA) receptors, which are critical for managing neuronal excitability and preventing seizures. By altering GABAergic activity, polyphenols from mulberry leaves might assist in stabilizing nerve cell function and decreasing the likelihood of seizures. What's more, the antioxidant qualities of these compounds can safeguard neurons against oxidative stress, a condition frequently linked to seizure disorders. Mulberry leaves may also exhibit anti-inflammatory properties that help diminish neuroinflammation, another contributor to seizures. Although animal studies have indicated encouraging anticonvulsant effects, further clinical research involving humans is necessary to thoroughly evaluate their potential as a natural treatment for seizure disorders **[33]**.

6.6 Anti-atherosclerosis: Research has explored the potential anti-atherosclerosis benefits of mulberry leaves. Atherosclerosis is a condition characterized by the buildup of plaque in the arteries, which can lead to cardiovascular issues. These leaves are rich in bioactive compounds such as flavonoids, alkaloids, and polysaccharides. These compounds may assist in lowering lipid levels, reducing inflammation, and preventing oxidative stress, all of which are essential in fighting atherosclerosis. The lipid-lowering properties of mulberry leaves include lowering LDL cholesterol and triglycerides, which greatly contribute to the development of arterial plaque. Their anti-inflammatory effects may help to reduce chronic inflammation, an important factor in the advancement of atherosclerosis. What's more, mulberry leaves are abundant in antioxidants, which help neutralize free radicals and lessen oxidative stress, thereby shielding the arteries from harm. These leaves also aid in regulating blood sugar levels, a benefit that is especially important for those with diabetes, as this condition can often hasten atherosclerosis. While these findings are encouraging, additional clinical studies involving humans are necessary to fully determine the impact of mulberry leaves in preventing or treating atherosclerosis. It is advisable to seek guidance from a healthcare professional before adding it to a treatment plan **[34]**.

6.7 SARS-CoV-2 inhibition: The polyphenols present in mulberry leaves (Morus species) have garnered significant attention for their potential antiviral properties, particularly in inhibiting SARS-CoV-2, the virus responsible for COVID-19. Research indicates that polyphenols, including flavonoids like quercetin, rutin, and kaempferol, as well as phenolic acids such as caffeic acid and gallic acid, may exhibit several mechanisms of action against

SARS-CoV-2. Notably, certain polyphenols can bind to viral proteins, such as the spike protein and main protease (Mpro), thereby blocking the virus's entry into host cells or inhibiting its replication. Additionally, their strong antioxidant properties can mitigate oxidative stress induced by viral infections, enhancing cellular health and improving the immune response. The anti-inflammatory effects of these compounds may help modulate immune responses, potentially reducing the risk of cytokine storms associated with severe COVID-19 cases. Furthermore, polyphenols can influence immune cell activity, promoting the activation and proliferation of cells involved in combating viral infections. Some studies also suggest that polyphenols may affect the expression or activity of ACE2 receptors, which serve as entry points for SARS-CoV-2, thus potentially reducing viral load. While the evidence surrounding the antiviral effects of mulberry leaf polyphenols against SARS-CoV-2 is promising, further research, including clinical trials, is essential to establish their efficacy and potential therapeutic applications in managing COVID-19 **[35]**.

So far, the Centers for Disease Control and Prevention (CDC) has identified no effective treatment for COVID-19. Polyphenols have not been extensively studied in the scientific community for possible antiviral activities besides SARS-CoV-2 yet. It can help lower SARS-CoV-2 mortality and morbidity by giving patients beneficial antiviral or anti-inflammatory treatments. These properties make several naturally occurring polyphenols ideal candidates for use as a preventive drug to reduce viral infection rate and the danger of a virus-caused inflammatory reaction **[36-38]**. Polyphenols have molecular potential as viral protease inhibitors because of their strong hydrogen bonding affinity for proteins and minimal toxicity. They have a strong affinity for proteins and have few harmful side effects. Polyphenol binding to the spike protein may be similar. The Spike protein of coronaviruses is the individual viral membrane protein that allows cells to enter. It explains what viral tropism is by the virus's capacity to bind to the cell membrane. So, the CoV-2 spike protein stops spike-mediated fusion of the membrane, which stops the virus from entering **[39]**.

ACE2 is a potential therapeutic target because it allows SARS-CoV-2 into host cells. A screening investigation found polyphenols promising for ACE2 ligands to prevent virus entry with a strong binding. It may reduce the severity of COVID-19 lung injury by regulating the expression of the antioxidant ACE2 **[40]**.

Research that showed resveratrol stopped the Middle East respiratory syndrome coronavirus (MERS-CoV) from replicating in vitro by blocking the production of nucleocapsid and RNA proteins led to the idea that polyphenols might stop SARS-CoV-2 RdRp. Preclinical and clinical

studies are needed to improve the findings, but none are currently happening. Also, the formulation of these polyphenol-based nutraceuticals should be considered. Concerns about low bioavailability and high levels of active polyphenols in the respiratory system, which is where most infections come from, should be addressed with aerosol delivery methods like inhalers and nebulizers **[39].**

6.8 Antimicrobial activity: Mulberry leaves are rich in polyphenols, including flavonoids and phenolic acids, which show major antimicrobial properties against various pathogens. These polyphenols can inhibit bacterial, fungal, and viral growth by disrupting the membranes of microbial cells, interfering with their enzymatic functions, and diminishing biofilm formation, an essential factor for the survival and virulence of microbes. Research has indicated that substances found in mulberry leaves, such as quercetin, rutin, and chlorogenic acid, are particularly effective against dangerous bacteria like *Staphylococcus aureus*, *Escherichia coli*, and *Salmonella typhimurium*. Besides, extracts from mulberry leaves have been found to inhibit fungal pathogens, including *Candida albicans*, and to exhibit antiviral properties against specific viral strains. This broad-range antimicrobial activity positions mulberry polyphenols as a promising natural option for infection management and overall health enhancement **[41]**.

6.9. Antioxidative effect: Various results showed that mulberry leaves were highly protective against free radicals and oxidative stress-induced tissue damage. The antioxidant capabilities of mulberry leaf extract have been quantified, showing values ranging from 1.89 to 2.12 mM Trolox equivalent per gram of dried leaves for one measurement method, and a higher range of 6.12 to 9.89 mM Trolox equivalent per gram of dried leaves for another method. The variation in antioxidant capacity between measurement methods suggests the importance of employing different assays to fully assess the antioxidant potential of plant extracts. The extract's ability to donate electrons lowered Fe3 to Fe2. All tests on mulberry leaves demonstrated a dose-dependent antioxidative effect. Previous positive controls, ascorbic acid and butylated hydroxytoluene (BHT), showed a stronger but less apparent effect. Phenoxenic acid and flavonoids have antioxidant effects **[42]**. According to earlier studies, the mulberry leaf extract fractions with the highest phenolic and flavonoid content exhibited the strongest antioxidant activity. This is supported by the substantial link between antioxidant content and efficacy **[43]**.

7. The metabolism of polyphenols

Polyphenols are extensively metabolized in the body's tissues or by bacteria in the intestines, for non-absorbed portions and fractions are re-excreted in bile. Polyphenols are converted to

O-glucuronides, sulfate esters, and O-methyl ethers in the body. Firstly, this conjugation occurs in the intestinal barrier, as evidenced by quercetin perfusion studies in living rats. When tested, quercetin glucuronides (QGs) were generated in the gut mucosa and secreted to the gut lumen or serosal side. Rat's gut has the most glucuronyl transferase activity. The conjugates then travel to the liver to be metabolized and eliminated. Citronella catechins, for example, are heavily methylated. Only half of the catechin perfused into the rat stomach was O-methylated before getting to the liver, whereas the catechin produced in the bile was 99 % catechin**.** In contrast, only O-methylated in mesenteric plasma was half of the catechin. Except for some flavonoids like phloretin, which was identified in both conjugated (90%) and non-conjugated (10%) forms in rat plasma, plasma contains almost no free aglycones**.** There were two kinds of phloretin in rat plasma: one that was conjugated and one that wasn't. There were also free flavonoid aglycones in tests that used therapeutic doses of flavonoids, which suggests that the conjugation routes may have been saturated. By joining glucuronides and sulfate groups, these compounds may form anionic derivatives that are quickly flushed out of the body. The biological properties of polyphenol-conjugated derivatives are unknown due to the lack of commercial standards **[44]** as shown in **Figures 3,4,** and **5**.

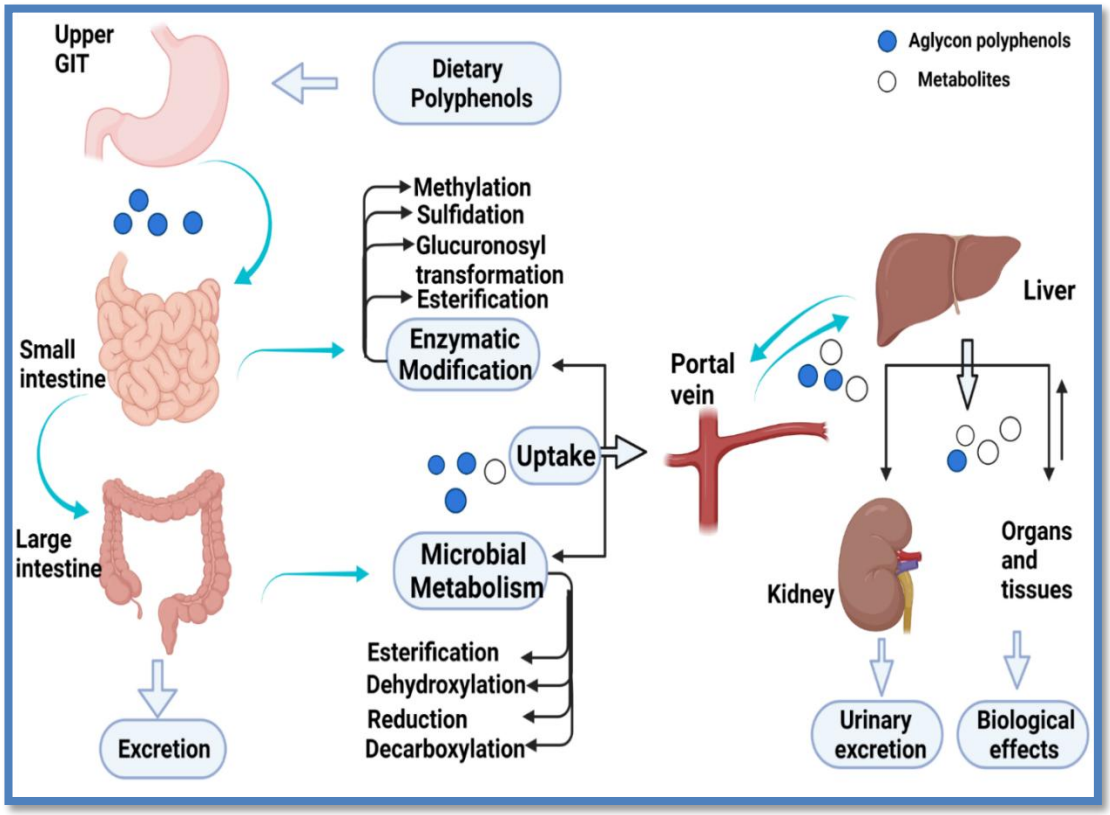

Figure 5: Dietary polyphenols' absorption and metabolism. Aglycon polyphenols are represented by blue dots, and their metabolites are represented by white dots. Adapted with permission from Ref. [44] Copyright 2024, MDPI

8. Food Processing utilization

Mulberry leaves (Morus species) are gaining recognition in food processing due to their rich nutritional and functional properties, offering diverse applications in various products. They can be processed into powders or extracts and utilized as nutraceutical ingredients, thanks to their abundance of bioactive compounds such as flavonoids, polyphenols, vitamins, and minerals. Dried mulberry leaves are also popular in herbal tea production, known for their antioxidant properties and appealing health benefits, making them a preferred choice for natural beverages. Their mild, slightly sweet flavor allows them to serve as natural flavoring agents in a range of food products, including beverages, sauces, and snacks. Additionally, mulberry leaves can provide natural colorants to enhance food aesthetics without synthetic additives and act as natural preservatives, extending the shelf life of products through their antioxidant properties. They can be incorporated into fermented products, promoting the growth of beneficial microorganisms, and added to functional snacks like energy bars and chips, enhancing nutritional profiles and supporting health benefits such as improved blood sugar regulation. Furthermore, mulberry leaves can also be processed into animal feed, contributing essential nutrients to livestock health **[45]**.

Mulberry leaves have emerged as a novel raw material food source. Several studies have been conducted on manufacturing Mulberry leaves-enhanced foods containing ordinary foods, healthy foods, and seasonings, among others (granule beverages, bitter melon, biscuits, and vinegar). The production of Mulberry leaves juice beverages or yogurt attempts to reinvent Mulberry leaves and create healthier and novel foods. When it comes to tea, Mulberry leaves have been utilized for centuries, as documented in the "Compendium of Material Medica." Mulberry tea comes in a variety of flavors and variations in China. Mulberry tea has been established as a local standard in some locations, and two companies have obtained trademark protection for mulberry tea [44]. Mulberry leaves tea can lower blood sugar levels and have antioxidative effects that help stop many ailments. Mulberry leaves were shown to be highly nutritious, with amino acids and polyphenols when fermented with Mauri yeast **[44].** A methanolic extract of Mulberry leaves improved the storage period of minced beef.

Foods that contain antioxidant chemicals derived from residual sources may have a greater shelf life because they are less susceptible to lipid peroxidation and are less susceptible to oxidative damage because they scavenge oxygen radicals. These effects may also be transferred to people, perhaps increasing the impact of particular foods on human health due to their

enhanced antioxidant potential. However, to increase the polyphenol content of plant meals, meticulous control of the production process is required**.**

Due to the advancement of nano-sized functional food components containing polyphenols, food safety and quality have increased, smart packaging has been developed, targeted distribution of compounds has been achieved, and the sensory qualities of food items have improved. Nanoparticles such as cyclodextrins, gelatin, casein and whey proteins, zein, chitosan, and complex nanoparticles are commonly employed as Nanocarriers in pharmaceuticals and other applications. These carriers protect sensitive polyphenols while also preserving the beneficial polyphenolic properties of the polyphenols. The delivery of these particles is improved due to their nanoscale dimensions. Future research should focus on the validation of suitable methods for the characterization of nanomaterials in complex matrices and measuring their reactivity and in vitro degradation to facilitate safety-risk assessments. For example, nanomaterials such as ENPs, used in food-packaging materials, should be addressed for their potential toxicity. The utilization of native Nanocarriers, such as casein micelles, as an alternative strategy could be explored. The GRAS status of casein micelles has been confirmed. It should be remembered that numerous health benefits associated with polyphenols have not been proven in vivo research, and that the use of polyphenols may be harmful to one's health when consumed in large quantities. Certainly, more people should be educated about nanotechnology and polyphenols and informed of the benefits and concerns associated with them **[46]**.

9. Externalities

9.1 Cultivation area conditions and nitrogen amount: A quantitative study in some Chinese cities shows the difference in the amount of different polyphenolic compounds in both fresh and dried leaves, indicating the temperature's effect on mulberry leaves' polyphenols. The Guangxi area has products with more antioxidant activity than Guangdong and Chongqing. The phenolic compounds are the major compounds with antioxidant activity in mulberry leaves. The different components may be due to different temperatures, as lower temperatures are more suitable for these extracts. The nitrogen amount in the soil also affects the number of different extracts; increasing the nitrogen content decreases both flavonol and chlorogenic acid and increases other materials **[47]**. Harvest and processing times: the levels of polyphenolic compounds decrease with the increase of harvest time, while the amount increases with increasing heat processing time, which must be taken into consideration **[48]**.

9.2 The solvent used for extraction and PH: An experiment proved that the content of polyphenols in methanol extract was more than that in water, ethanol, and acetone, respectively **[49]**. The most appropriate pH for polyphenolic extraction is the neutral pH **[50].**

9.3 Temperature: Polyphenolic compounds in mulberries remained almost unchanged at 60° C and below, while decreasing significantly with the temperature above 70° C. The polyphenol extractions are stored at 5 °C in the dark to remain stable for 30 days. Then, the content decreases gradually **[49]**.

9.4 The Economic and Medical Significance of Mulberry: A Source of Antimicrobial, Antioxidant, and Therapeutic Advantages: Mulberry is economically important directly or indirectly due to its important role in the industry, medical, and environmental fields. Mulberry by-products have anti-microbial, anti-hyperglycemic, anti-hyperlipidemic effects, etc., which can be used very well in the pharmaceutical industry **[51]**. Polyphenols exhibit Gram-positive inhibitory impact, especially toward Bacillus cereus, Staphylococcus aureus, Micrococcus luteus, and Listeria monocytogenes, while having little effect on Gram-negative bacteria as Escherichia coli and Pseudomonas aeruginosa, and no effect on Candida albicans. Some polyphenols inhibit α-amylase as α-amylase activity is connected to its substitution **[52]**. Polyphenols in mulberries have an antioxidant effect, which can be used in heat stroke. Polyphenols can also be used in treating sore throats. Also, due to the antioxidant effects, polyphenols can be used as anti-aging factors in animal models that need more investigation **[53]**.

9.5 Safety: Many studies on mice were done to see the safety and the side effects of mulberry, but it was proved that mulberry leaf ingestion is safe. An experiment on mice for 2 weeks shows the safety of the leaves' products, and another study on mice for 90 days finds no serious side effects **[53].**

9.6 Zero waste process: In this process, all materials are in a circular system, meaning the same material will be used many times till almost complete consumption. In this strategy, no product or by-product is wasted. All will be recycled. The zero-waste technique is used in many fields, including agriculture, which means it can be used in mulberry by-products **[54].**

10. Conclusions

In a circular and sustainable bioeconomy, organic agricultural wastes are utilized as extraction material, and recovery chemicals are reinserted into the production chain. scientists use different recovery procedures to acquire bioactive compounds. Optimization of extraction techniques is required to boost production yields while being environmentally benign and economically viable. The purpose of the recent review was to emphasize the importance and

applicability of various contexts of Morus species. It is abundantly obvious from the foregoing discussion that mulberry is a useful medicinal plant with the vitality of tremendous potential. Recently developed approaches to functional applications revealed that Morus species and their bioactive phytochemicals exhibit a varied range of biomedical activities, as well as antioxidants, anti-diabetic, hypolipidemic, anti-obesity, anti-hypertensive, and anti-atherosclerosis, among others. Morus extraction methods, metabolism, and a variety of food industry applications were also discussed. In general, a New study on the phytochemical and pharmacological aspects of Mulberry leaves is needed. Mulberry leaves have several potential applications.

11. References

[1] Khadivi A, Hosseini A-S, Naderi A. Morphological characterizations of Morus nigra L., M. alba L., and M. alba L. var. nigra. Genetic Resources and Crop Evolution. 2024;71(4):1635-42.

[2] Regolo L, Giampieri F, Battino M, Armas Diaz Y, Mezzetti B, Elexpuru-Zabaleta M, et al. From by-products to new application opportunities: the enhancement of the leaves deriving from the fruit plants for new potential healthy products. Frontiers in Nutrition. 2024;11:1083759.

[3] Garrett NR, Pink RC, Lawson C. Contribution of extracellular particles isolated from Morus sp.(mulberry) fruit to their reported protective health benefits: an in vitro study. International Journal of Molecular Sciences. 2024;25(11):6177.

[4] Pongworn S, Wongsa J, Vatanyoopaisarn S, Thumthanaruk B, Uttapap D, Lamsal B, et al. Influence of dietary mulberry leaf on the nutritional composition of mulberry silkworm, Bombyx mori L. at different developmental stages. Journal of Insects as Food and Feed. 2024;1(aop):1-14.

[5] Wang Y, Jin W, Che Y, Huang D, Wang J, Zhao M, et al. Atmospheric nitrogen dioxide improves photosynthesis in mulberry leaves via effective utilization of excess absorbed light energy. Forests. 2019;10(4):312.

[6] Manzoor S, Qayoom K. Environmental Importance of Mulberry: A Review. Journal of Experimental Agriculture International. 2024;46(8):95-105.

[7] Li R, Wang J, Liu J, Li M, Lu J, Zhou J, et al. Mulberry leaf and its effects against obesity: a systematic review of phytochemistry, molecular mechanisms and applications. Phytomedicine. 2024:155528.

[8] Thabti I, Elfalleh W, Hannachi H, Ferchichi A, Campos MDG. Identification and quantification of phenolic acids and flavonol glycosides in Tunisian Morus species by HPLC-DAD and HPLC–MS. Journal of Functional Foods. 2012;4(1):367-74.

[9] Vuong QV, Golding JB, Stathopoulos CE, Nguyen MH, Roach PD. Optimizing conditions for the extraction of catechins from green tea using hot water. Journal of separation science. 2011;34(21):3099-106.

[10] Guo N, Jiang Y-W, Kou P, Liu Z-M, Efferth T, Li Y-Y, et al. Application of integrative cloud point extraction and concentration for the analysis of polyphenols and alkaloids in mulberry leaves. Journal of Pharmaceutical and Biomedical Analysis. 2019;167:132-9.

[11] Gao M-Z, Cui Q, Wang L-T, Meng Y, Yu L, Li Y-Y, et al. A green and integrated strategy for enhanced phenolic compounds extraction from mulberry (Morus alba L.) leaves by deep eutectic solvent. Microchemical Journal. 2020;154:104598.

[12] Laurent RS, O'Brien LM, Ahmad S. Sodium butyrate improves locomotor impairment and early mortality in a rotenone-induced Drosophila model of Parkinson's disease. Neuroscience. 2013;246:382-90.

[13] Algan Cavuldak Ö, Vural N, Akay MA, Anlı RE. Optimization of ultrasound-assisted water extraction conditions for the extraction of phenolic compounds from black mulberry leaves (Morus nigra L.). Journal of Food Process Engineering. 2019;42(5):e13132.

[14] Kim JongMin KJ, Chang SangMok CS, Kim InHo KI, Kim YoungEun KY, Hwang JiHwan HJ, Kim KyoSeon KK, et al. Design of optimal solvent for extraction of bio-active ingredients from mulberry leaves. 2007.

[15] Chu Y-F, Sun J, Wu X, Liu RH. Antioxidant and antiproliferative activities of common vegetables. Journal of agricultural and food chemistry. 2002;50(23):6910-6.

[16] Nuutila A-M, Kammiovirta K, Oksman-Caldentey K-M. Comparison of methods for the hydrolysis of flavonoids and phenolic acids from onion and spinach for HPLC analysis. Food chemistry. 2002;76(4):519-25.

[17] Zhang D-Y, Wan Y, Hao J-Y, Hu R-Z, Chen C, Yao X-H, et al. Evaluation of the alkaloid, polyphenols, and antioxidant contents of various mulberry cultivars from different planting areas in eastern China. Industrial Crops and Products. 2018;122:298-307.

[18] Lavialle M, Champeil-Potokar G, Alessandri JM, Balasse L, Guesnet P, Papillon C, et al. An (n-3) polyunsaturated fatty acid–deficient diet disturbs daily locomotor activity, melatonin rhythm, and striatal dopamine in Syrian hamsters. The Journal of nutrition. 2008;138(9):1719-24.

[19] Fu L, Xu B-T, Gan R-Y, Zhang Y, Xu X-R, Xia E-Q, et al. Total phenolic contents and antioxidant capacities of herbal and tea infusions. International journal of molecular sciences. 2011;12(4):2112-24.

[20] Kotásková E, Sumczynski D, Mlček J, Valášek P. Determination of free and bound phenolics using HPLC-DAD, antioxidant activity and in vitro digestibility of Eragrostis tef. Journal of Food Composition and Analysis. 2016;46:15-21.

[21] Gundogdu M, Canan I, Gecer MK, Kan T, Ercisli S. Phenolic compounds, bioactive content and antioxidant capacity of the fruits of mulberry (Morus spp.) germplasm in Turkey. Folia Horticulturae. 2017;29(2):251-62.

[22] Forsan HF. Diet and Sleep Disorders. In: Mohamed W, Kobeissy F, editors. Nutrition and Psychiatric Disorders, Nutritional Neurosciences: Springer Nature Singapore Pte Ltd; 2024. p. 421.

[23] Forsan HF, Abd El-Hak AE, Ahmad E, Alswerky EM, Elagezy FK, Yassin M, et al. Toward Better Science-Based Advice on Nutrition. Nutrition and Psychiatric Disorders2024. p. 183.

[24] Forsan HF, Hassan RS. Novel Nutraceutical Milk Compound in Alzheimer's Prevention. In: Mohamed E, editor. Handbook of Neurodegenerative Disorders. Singapore: Springer; 2023.

[25] Velásquez-Jiménez D, Corella-Salazar DA, Zuñiga-Martínez BS, Domínguez-Avila JA, Montiel-Herrera M, Salazar-López NJ, et al. Phenolic compounds that cross the blood–brain barrier exert positive health effects as central nervous system antioxidants. Food & Function. 2021;12(21):10356-69.

[26] Domínguez-López I, López-Yerena A, Vallverdú-Queralt A, Pallàs M, Lamuela-Raventós RM, Pérez M. From the gut to the brain: the long journey of phenolic compounds with neurocognitive effects. Nutrition Reviews. 2024:nuae034.

[27] Chan EWC, Wong SK, Tangah J, Inoue T, Chan HT. Phenolic constituents and anticancer properties of Morus alba (white mulberry) leaves. Journal of integrative medicine. 2020;18(3):189-95.

[28] Sun C, Zhao C, Guven EC, Paoli P, Simal-Gandara J, Ramkumar KM, et al. Dietary polyphenols as antidiabetic agents: Advances and opportunities. Food Frontiers. 2020;1(1):18-44.

[29] Xiao J, Hogger P. Dietary polyphenols and type 2 diabetes: current insights and future perspectives. Current medicinal chemistry. 2015;22(1):23-38.

[30] Wang Z, Tang C, Dai F, Xiao G, Luo G. HPLC determination of phenolic compounds in different solvent extracts of mulberry leaves and antioxidant capacity of extracts. International journal of food properties. 2021;24(1):544-52.

[31] Chen TY, Ferruzzi MG, Wu QL, Simon JE, Talcott ST, Wang J, et al. Influence of diabetes on plasma pharmacokinetics and brain bioavailability of grape polyphenols and their phase II metabolites in the Zucker diabetic fatty rat. Molecular nutrition & food research. 2017;61(10):1700111.

[32] Liao S, Long X, Zou Y, Liu F, Li Q. Mulberry leaf phenolics and fiber exert anti-obesity through the gut microbiota-host metabolism pathway. Journal of Food Science. 2021;86(4):1432-47.

[33] Rayam S, Kudagi B, Sufyan U, Buchineni M, Pathapati RM. Assessment of Morus alba (Mulberry) leaves extract for anti convulsant property in rats. Int J Basic Clin Pharmacol. 2019;8:520-3.

[34] Zeni ALB, Moreira TD, Dalmagro AP, Camargo A, Bini LA, Simionatto EL, et al. Evaluation of phenolic compounds and lipid-lowering effect of Morus nigra leaves extract. Anais da Academia Brasileira de Ciências. 2017;89(04):2805-15.

[35] Thabti I, Albert Q, Philippot S, Dupire F, Westerhuis B, Fontanay S, et al. Advances on antiviral activity of Morus spp. plant extracts: human coronavirus and virus-related respiratory tract infections in the spotlight. Molecules. 2020;25(8):1876.

[36] Forsan HF, Rahman ARA, Safwat M, Abduljabar RS, Riad OK. COVID-19: A review of immune-enhancing nutrients and supplements. 2022.

[37] Safwat M-A, Abdul-Rahman AR, Forsan HF, Abduljabar R, Riad O. COVID-19; Immunology, pathology, severity and immunosuppressants. Azhar International Journal of Pharmaceutical and Medical Sciences. 2021;1(1):1-12.

[38] Bhuiyan FR, Howlader S, Raihan T, Hasan M. Plants metabolites: possibility of natural therapeutics against the COVID-19 pandemic. Frontiers in medicine. 2020;7:444.

[39] Williamson G, Kerimi A. Testing of natural products in clinical trials targeting the SARS-CoV-2 (Covid-19) viral spike protein-angiotensin converting enzyme-2 (ACE2) interaction. Biochemical pharmacology. 2020;178:114123.

[40] Albalaty J, Forsan F, Awad S, Elsadek E, Rahman A, Badawy M, et al. SARS-CoV-2 vaccines from A to Z: A review of the current challenges. Global Nest Journal. 2023:148-71.

[41] Sánchez-Salcedo EM, Mena P, García-Viguera C, Hernández F, Martínez JJ. (Poly) phenolic compounds and antioxidant activity of white (Morus alba) and black (Morus nigra) mulberry leaves: Their potential for new products rich in phytochemicals. Journal of Functional Foods. 2015;18:1039-46.

[42] Forsan HF, Awad SS. Cyanidin: Advances on Resources, Biosynthetic Pathway, Bioavailability, Bioactivity, and Pharmacology. In: Xiao J, editor. Handbook of Dietary Flavonoids. Cham: Springer International Publishing; 2023. p. 1-50.

[43] Jan B, Parveen R, Zahiruddin S, Khan MU, Mohapatra S, Ahmad S. Nutritional constituents of mulberry and their potential applications in food and pharmaceuticals: A review. Saudi journal of biological sciences. 2021;28(7):3909-21.

[44] Cipolletti M, Solar Fernandez V, Montalesi E, Marino M, Fiocchetti M. Beyond the antioxidant activity of dietary polyphenols in cancer: the modulation of estrogen receptors (ERs) signaling. International journal of molecular sciences. 2018;19(9):2624.

[45] Yu Y, Li H, Zhang B, Wang J, Shi X, Huang J, et al. Nutritional and functional components of mulberry leaves from different varieties: Evaluation of their potential as food materials. International Journal of Food Properties. 2018;21(1):1495-507.

[46] Marranzano M, Rosa RL, Malaguarnera M, Palmeri R, Tessitori M, Barbera AC. Polyphenols: Plant sources and food industry applications. Current pharmaceutical design. 2018;24(35):4125-30.

[47] Hao J-Y, Wan Y, Yao X-H, Zhao W-G, Hu R-Z, Chen C, et al. Effect of different planting areas on the chemical compositions and hypoglycemic and antioxidant activities of mulberry leaf extracts in Southern China. PloS one. 2018;13(6):e0198072.

[48] Lee WJ, Choi SW. Quantitative changes of polyphenolic compounds in mulberry (Morus alba L.) leaves in relation to varieties, harvest period, and heat processing. Preventive Nutrition and Food Science. 2012;17(4):280.

[49] Arabshahi-Delouee S, Urooj A. Antioxidant properties of various solvent extracts of mulberry (Morus indica L.) leaves. Food chemistry. 2007;102(4):1233-40.

[50] Sugiyama M, Takahashi M, Katsube T, Koyama A, Itamura H. Effects of applied nitrogen amounts on the functional components of mulberry (Morus alba L.) leaves. Journal of agricultural and food chemistry. 2016;64(37):6923-9.

[51] Rohela GK, Shukla P, Kumar R, Chowdhury SR. Mulberry (Morus spp.): An ideal plant for sustainable development. Trees, Forests and People. 2020;2:100011.

[52] Cui H, Lu T, Wang M, Zou X, Zhang Y, Yang X, et al. Flavonoids from Morus alba L. leaves: Optimization of extraction by response surface methodology and comprehensive evaluation of their antioxidant, antimicrobial, and inhibition of α-amylase activities through analytical hierarchy process. Molecules. 2019;24(13):2398.

[53] Liu D, Meng S, Xiang Z, He N, Yang G. Antimicrobial mechanism of reaction products of Morus notabilis (mulberry) polyphenol oxidases and chlorogenic acid. Phytochemistry. 2019;163:1-10.

[54] Sheng C, Shi X, Ding Z, Chen Y, Shi X, Wu Y, et al. Effects of mulberry leaf extracts on activity and mRNA expression of five cytochrome P450 enzymes in rat. Brazilian Journal of Pharmaceutical Sciences. 2021;57:e18059.

Al-Kitab Journal for Pure Sciences (2025); 9(2):128-139.
https://doi.org/10.32441/kjps.09.02.p8

Al-Kitab Journal for Pure Sciences
ISSN: 2617-1260 (print), 2617-8141(online)

https://isnra.net/index.php/kjps

Monkeypox Virus: A Review

Huda Mawlood Taher*, Hiyam Jamal Ibrahim, Bayan Mohammed Mahdi

Department of Biology, College of Education for Pure Sciences, University of Kirkuk, Iraq.

*Corresponding Author: huda.mawlood@uokirkuk.edu.iq

Citation: Taher HM, Ibrahim HJ, Mahdi BM. Monkeypox Virus: A Review. Al-Kitab J. Pure Sci. [Internet]. 2025 May. 02 ;9(2):128-139. DOI: https://doi.org/10.32441/kjps.09.02.p8.

Keywords: **Monkeypox**, **virus, Pathogenicity**.

Article History

Received	14	Oct.	2024
Accepted	04	Dec.	2024
Available online	02	May.	2025

Abstract:

Monkeypox is a disease caused by the monkeypox virus, which is related to the smallpox virus. It is a double-strand DNA virus enclosed in an envelope and a member of the Orthopoxvirus genus within the Orthopoxviridae family. This disease was spread in West and Central African countries and other regions as well. It transmits through direct contact with the skin lesions of an infected person, as well as through respiratory droplets and contaminated materials. Monkeypox is generally less severe than smallpox, and most people recover completely from it; however, it is still serious, especially for young children, pregnant women, and people with weakened immune systems**.** It causes pain, fever, rash, and swollen lymph nodes.

Keywords: Monkeypox, Virus, Pathogenicity.

فيروس جدري القرود: مراجعة

هدى مولود طاهر*، هيام جمال إبراهيم، بيان محمد مهدي

قسم علوم الحياة ، كلية التربية للعلوم الصرفة، جامعة كركوك، العراق
huda.mawlood@uokirkuk.edu.iq, plantanatomy@uokirkuk.edu.iq, bayanmohammad@uokirkuk.edu.iq

الخلاصة:

جدري القرود هو مرض يسببه فيروس جدري القرود وهو قريب من فيروس الجدري، وهو فيروس ثنائي السلسلة محاط بغلاف وهو من جنس فيروسات الأورثوبوكس ضمن عائلة الفيروسات الأورثوبوكس. انتشر هذا المرض في دول غرب ووسط أفريقيا ومناطق أخرى أيضًا. ينتقل من خلال الاتصال المباشر بآفات الجلد لدى الشخص المصاب، وكذلك من خلال قطرات الجهاز التنفسي والمواد الملوثة. جدري القرود أقل خطورة من الجدري بشكل عام ويتعافى منه معظم الناس تمامًا، ولكنه لا يزال خطيرًا، وخاصة الأطفال الصغار والنساء الحوامل والأشخاص الذين يعانون من ضعف في جهاز المناعة. حيث يسبب ألمًا وحمى وطفح جلدي وتضخم الغدد اللمفاوية.

الكلمات المفتاحية: جدري القرود، فيروس، إمراضية.

1. Introduction

Monkeypox (MPXV) is a viral infection transmitted from animals to humans that leads to a skin rash resembling smallpox, and the likelihood of death is much lower in monkeypox compared to smallpox [1]. Two chief groups of monkeypox virus have been discovered in West and Central Africa, with the former linked to another serious disease [2]. Numerous instances in the recent epidemic are linked to sexual transmission, particularly between individuals who are recognized as bisexual, gay or engage in sex with men [3]. Firstly, the monkeypox virus was discovered in monkeys [4]. Monkeypox was reported in 1958 in monkeys that were transported from Singapore to Denmark [5]. The initial incident in humans was identified in a 9-month-old boy, Zaire, in 1970 (currently known as the Democratic Republic of the Congo) [6]. Since that period, monkeypox has established itself as a common disease in the DRC where it has expanded to various African nations, particularly in West and Central Africa. The initial documented monkeypox condition outside of Africa was reported in 2003. (97.962)cases of monkeypox have been recorded on June 30, 2024, in nearly 120 countries, 110 of which have not historically announced it [7].

The monkeypox virus comes in two types: clade I and clade II [8]:

- Clade I causes more severe illnesses and deaths. Up to 10% of cases in some outbreaks have resulted in deaths, however, the death toll from more recent outbreaks has been lower. Clade I is prevalent in Central Africa.

- Clade II is the type that caused the global epidemic that began in 2022. It's not as serious. Over 99.9% of people make it out alive. Clade II is prevalent in West Africa.

2. Transmission methods of monkeypox virus

There is currently no known method of MPXV transmission to humans. It is assumed that handling monkeypox-infected animals directly by touch, bite, scratch, and indirectly causes the primary animal-to-human infection [9]. It is believed that the respiratory system, mucous membranes, and damaged skin let the virus enter the body (eyes, nose, and mouth), Secondary human-to-human transmission frequently occurs as a result of respiratory droplets, direct or indirect contact with bodily fluids, solid lesions, contaminated surfaces, and contaminated clothing. Extended interactions with patients increase the risk of infection for hospital staff and family members [10]. Generally, asleep in the same bed or room, alive in an identical home, and eating or drinking from the same dish were hazardous behaviors connected with person-to-person transmission [11]. Also, it has been established that sleeping outside or on the ground and residing close to or visiting a forest increase the likelihood of coming into contact with animals and, consequently, the risk of the monkeypox virus dispersal from animal to human [12]. Using toilet and sterility and washing wear did not have a significant connotation with obtaining monkeypox [13]. During the 2003 occurrence in the US, daily contact with sick animals and cleaning their cages were found to be dangerous factors for developing monkeypox [14].

3. Epidemiology

Human monkeypox infections have been reported in African countries, the most affected countries are Nigeria, the Democratic Republic of the Congo, and the Central African Republic, which has only a few hundred cases reported [15], together with a very great rise in case numbers above the previous thirty years [16], with national observation data showed in assumed cases from 2001 to 2018: from fewer than 500 cases to more than 2500 cases [15]. The majority of cases reported in the 1970s and 1980s involved young children, while the average age at identification in Nigeria during the 2017–2018 epidemic was 20-29 years old [17].

In Africa, both person-to-person and animal-to-person transmissions have been acknowledged. Transmission of zoonotic organisms happens by connection with the lesions or biological fluids of an infested animal [18]. These associates happen during hunting, butchering, or game consumption. Person-to-person transmission occurs mainly by contact with biological fluids, infected skin lesions of patients, and polluted resources such as bedding also can be transferable. The cause of transmission in Africa is unknown, and studies have found

significant differences in the amounts of suspected person-to-person and animal-to-person transmissions. Of the 122 patients in Nigeria, 10 had contact with animals and 36 had contact with people who had an interrelated skin lesion [17]. Intra-familial communications have been reported for viral clades 1 and 2 [19]. Sexual transmission has been reported in uncommon cases in African countries [20]. Chains of transmission are commonly stumpy up to seven transmission goings on within a lone household have been reported [21].

4. Pathogenicity

Symptoms of infection of monkeypox include headaches, body aches, chills, sore throat, fever, fatigue, swollen lymph nodes, malaise, and a severe rash that develops into blisters or papules that crust over and heal [22]. Monkeypox Lymphadenopathy appears in MPXV infections but may be misdiagnosed as chickenpox [23]. Numerous patients experience different diseases including few or no lesions, which are restricted to the genital perianal area, hurt, and hemorrhage [24].

The beginning monkeypox signs varieties start from 6 to 21 days, and naturally, the infection restores to its personnel in 2–4 weeks [25]. Monkeypox Virus infections may cause lengthy viral DNA remaining in the higher respiratory tract that persists later in the skin lesion resolves, but it's inexact if this is connected with communicable virus transmission [26]. The common monkeypox Virus infection patches up on their particular. Though, it is more severe, and potency needs hospitalization in immunosuppressed patients and young children [27]. HIV-1-infected people have lengthy monkeypox disease, greater lesions, secondary microbial skin infections, and genital abscesses [22]. Also, monkeypox Virus may be diffused through the placenta in the pregnancy and clue to fetal death [28].

In several cases, possibly life-threatening problems such as encephalitis secondary infection of the instrument, and bronchopneumonia [23]. An additional rare but serious, long-term problem of monkeypox is the loss of vision resulting from infection of the tissue damage and eye cornea [28]. The overall mortality rate differs depending on patient age, infection types, and localization of the occurrence. Also, it is more fatal in children than in adults [29].

5. Immune response

The first line of defense against a monkeypox infection is thought to be the innate immune system. Innate immune cells, which produce inflammatory cytokines, and type I interferons, such as monocytes and NK cells, play a vital role. However, NK cells and cytotoxicity can be overcome by monkeypox [30]. Th2-related cytokines (IL-4, IL-5, IL-6, and IL-10) are elevated in response to monkeypox infection, whereas Th1-associated cytokines (IL-2, IL-12, TNF-α,

and IFN-γ) stay within the normal range, suggesting complex immune deregulations during the infection [31]. Antibody response, which is a key component of adaptive immunity, is essential for eliminating monkeypox. Detection of specific IgG and IgM antibodies in infected individuals is commonly used for diagnosis, while B cells play a crucial role in providing protection against monkeypox through vaccination [30]. Also, T cells contribute to the protecting responses to monkeypox, as T cell response to monkeypox has been identified in healthy persons, especially persons born before the year 1976 who likely expected the smallpox vaccine, which affords cross defense against monkeypox [32].

Some factors affect the immune response to monkeypox disease, people who have had smallpox in the past tend to be more immune to monkeypox because of the relationship between the viruses and the presence of cross-immunity, leading to a more robust genetic makeup and immune reaction. Younger people tend to have a stronger immune response to the monkeypox virus compared to older people, due to the immune system declining with age [33]. But immune-compromised persons like persons with cancer, HIV, and organ transplant receivers are at a greater hazard of constricting monkeypox and my knowledge of elongated recovery periods and their conceded immune status hinders their bodies' capability to effectually conflict with the monkeypox virus, as **Figure 1 [34]**.

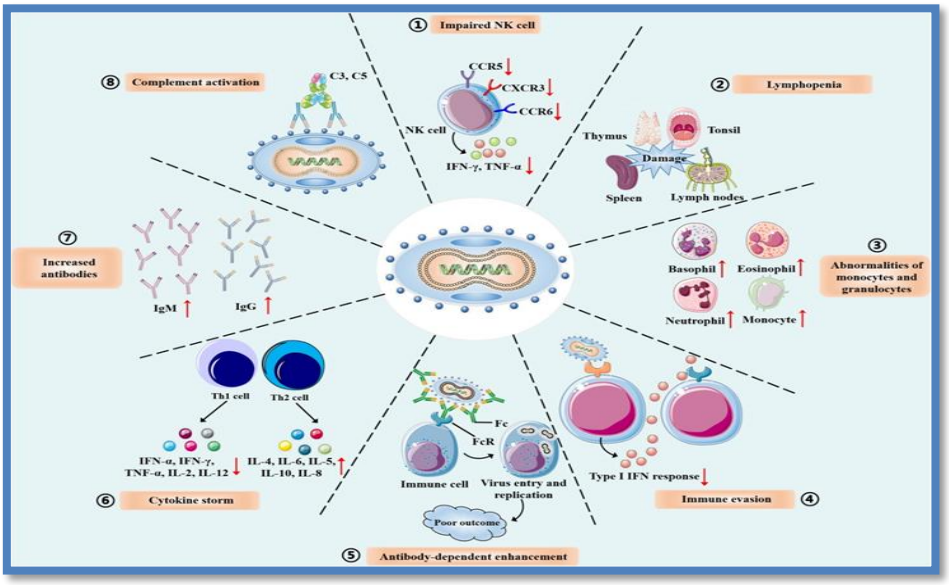

Figure 1: The immunopathogenesis of monkeypox virus [34]

6. Diagnosis methods

Diagnosis is considered the key to detection and keeping monkeypox under control. We can simply distinguish monkeypox from other orthopox viruses by electron microscopy. Clinical characteristics can help differentiate poxvirus infections from other causes of vesiculopustular

eruptions, a laboratory examination is necessary for a conclusive diagnosis [35]. IgM and IgG ELISA, immune fluorescent antibody assay, PCR, electron microscopy, virus isolation, and histopathology analysis are laboratory diagnostic methods for monkeypox [36]. We can distinguish between a herpes virus and poxvirus infection by using immunohistochemistry analysis with monoclonal or polyclonal antibodies against all orthopox viruses [37]. Electron microscopes have played a chief role in viral diagnosis, they can be the main mode for diagnosis of poxvirus infection. We can be detected under electron microscopy the characteristic morphology of poxvirus [36]. The definitive identification of MPXV often involves virus isolation in the culture of mammalian cells and their characterization using different PCR techniques, either by sequencing of amplicons or by restriction fragment length polymorphism analysis [38]. Also, the accessibility of many real-time PCR assays that use monkeypox Virus definite targets has improved in recent years [39]. A new rapid method for identifying orthopox viruses was created using a DNA microarray with the TNF receptor gene crmB [40].

The main diagnostic problem is distinguishing between monkeypox and varicella. Laboratory authorization can be done by PCR technique of vesicle liquid or scab in active disease, however when disease determination, testing of convalescent stage serum specimen for anti varicella virus IgM can be done[36]. Identifying anti-poxvirus antibodies in a person who has not ever been vaccinated and has a past of serious infection and skin rash suggests a diagnosis of monkeypox [40].

7. Prevention

The prevention of the monkeypox virus in healthcare clinicians and specialists is an additional challenge since they are normally in close contact with infected people [41]. To decrease the infection risk, healthcare professionals should follow the commendations such as carefully handled connection with special protective equipment such as gloves, a gown, eye protection, and a fitted N95 mask (**Figure 2**) [42]. Patients with disbelieved monkeypox infections should also be hidden, and their skin lesions must be covered with a gown or cloth, and be placed in isolation, if at all possible, in a single-person room [43]. Patients should remain in the home and border contact with others for 3–6 weeks and evade close contact such as sexual connection with someone exposed or infected with the monkeypox virus, persons should maintain good hand sanitization and respiratory system by wearing a fitted mask and lidding coughs and sneeze with the bend of a limb after taking visitors at home, proper cleaning are advised [44]. The obtainable documents show that smallpox vaccination might ensure 85% cross-protection against monkeypox [45].

Samples such as scabs or cutaneous tissues should be handled with care because the simplicity of transmission by direct contact or air particles, and instantaneous ring vaccination and quarantine are considered the simply actual public health protecting procedures as there is no effective, approved antiviral healing for monkeypox [46].

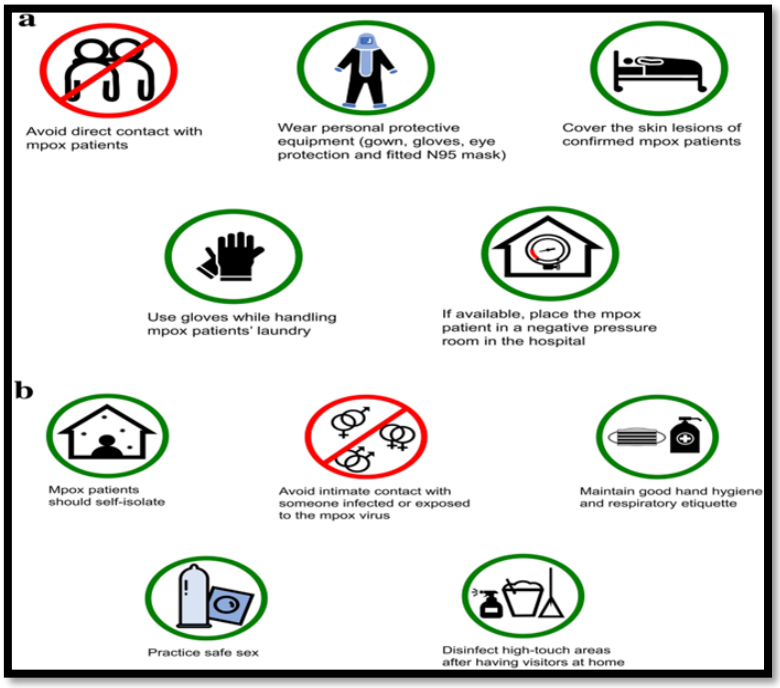

Figure 2: Prevention ways from monkeypox virus [42].

8. Treatment

Most individuals infected with monkeypox infection recover without medicinal treatment, while patients with gastrointestinal warning signs such as nausea, and diarrhea will need oral or venous rehydration to decrease losses of gastrointestinal fluid [47]. The number of antivirals might be effective in handling monkeypox infection [48]. Tecovirimat also known as ST-246 or TPOXX completely that chemical considered the best antiviral directed for treating smallpox in adults and children weighing over 3 kg [49]. Double therapy with brincidofovir and tecovirimat can be used in patients with severe infection. Tecovirimat mechanisms inhibit viral envelope protein VP37, which controls the final steps of virus maturation and release from infected cells, thereby inhibiting virus spread within the infected host [50]. Even though the efficiency of this agent in persons contrary to monkeypox has not been tried, revisions have informed advanced persistence from deadly monkeypox virus infections in recoverin at treated animals associated to palliative treated animals at changed periods of disease [51]. In some research studies, tecobilimatosis has been used in combination with vaccinia immune globulin in patients with difficult-to-administer smallpox vaccination, such as those with vaccinia

eczema and advanced vaccine reactions [52]. The CDC New protocol enables us of Tecovirimat in non-variola orthopoxvirus infections as monkeypox [53]. It also includes information for pediatric patients under 13 kg to open an oral capsule and combine the liquid or soft food inside of it [54]. It was also approved to utilize brincidofovir for treating smallpox in the US in the meantime in 2021 [55]. Brincidofovir by oral considered an equivalent to the intravenous drug cidofovir, a lesser amount of kidney toxicity related to cidofovir, these medicines work throw inhibit the viral DNA polymerase [56]. Clinical documents about the efficacy of cidofovir against monkeypox in humans are unknown, but the in vitro activity and efficacy of cidofovir against lethal monkeypox virus infections in animals are known. The efficacy of cidofovir against monkeypox in humans is missing, yet in vitro activity and efficiency against fatal monkeypox virus infections in animals have been informed [57]. Liver function examinations must be prepared before and through treatment with brincidofoviras, these medications may lead to a rise the serum transaminases and serum bilirubin. It can use Vaccinia hyperimmune globulin which is qualified by the FDA for cooperation of certain complications of vaccination [58]. VIG subsidy for patients with severe immunodeficiency in T-cell function, and use of VIG must be under IND application [59].

9. Conclusions

The public health importance of monkeypox disease cannot be underestimated, as the potential for person-to-person transmission is an issue not only among household residents but also among caregivers of sick individuals. Also, the monkeypox virus has the potential to spread via zoonotic reservoirs.

10. References

[1]Centers for Disease Control and Prevention. Monkeypox-2024 Available from: https://www.cdc.gov/ poxvirus/monkeypox/index.html

[2] Durski KN, McCollum AM, Nakazawa Y, et al. Emergence of monkeypox in West Africa and Central Africa, 1970–2017. *Wkly Epidemiol Rec*. 2018;93(11):125–132.

[3] Monkeypox virus infection in the united states and other non- endemic countries—2022. https://emergency.cdc.gov/han/2022/ han00466.asp.

[4] Guarner J, Del Rio C, Malani PN. Monkeypox in 2022—what clinicians need to know [published online ahead of print. *JAMA*. 2022. https://doi.org/10.1001/jama.2022.10802

[5] Von Magnus P, Andersen EK, Petersen KB, Birch Andersen A. A pox-like disease in cynomolgus monkeys.*Acta Pathol Microbiol Scand* 1959; 46**:** 156–76.

[6] Breman JG, Kalisa R, Steniowski MV, Zanotto E, Gromyko AI, Arita I. Human monkeypox, 1970–79. *Bull World Health Organ.* 1980; 58(2):165–182.

[7] Monkeypox Outbreak Global Map | monkeypox | Poxvirus | CDC 2023. https://www.cdc.gov/poxvirus/mpox/ 2023 June.

[8] Sabeena S. The changing epidemiology of monkeypox and preventive measures: an update. *Arch Virol* 2023; 168:31.

[9] Jezek Z, Grab B, Szczeniowski M, Paluku KM, Mutombo M. Clinico-epidemiological features of mon- keypox patients with an animal or human source of infection. *Bull World Health Organ*. 1988; 66 (4):459–464.

[10] Vora S, Damon I and Fulginiti V. Severe eczema vaccinatum in a household contact of a smallpox vaccinee. *Clin Infect Dis*. 2008.

[11] Burnett JC, Henchal EA, Schmaljohn AL, Bavari S. The evolving field of biodefence: therapeutic developments and diagnostics. *Nat Rev Drug Discov*. 2005; 4:281–97.

[12] Nolen LD, Osadebe L, Katomba J, Likofata J, Mukadi D, Monroe B, et al. Extended human-to-human transmission during a monkeypox outbreak in the Democratic Republic of the Congo. *Emerg Infect Dis*. 2016; 22(6):1014–1021.

[13] Olson VA, Laue T, Laker MT, et al. Real-time PCR system for detection of orthopoxviruses and simultaneous identification of smallpox virus. *J Clin Microbiol* 2004; 42:1940–6.

[14] Chittick G, Morrison M, Brundage T, Nichols WG. Short-term clinical safety profile of brincidofovir: a favorable benefit–risk proposition in the treatment of smallpox. *Antiviral Res*. 2017. https://doi.org/10.1016/j.antiviral.2017.01.009

[15] Bunge EM, Hoet B, Chen L, et al. The changing epidemiology of human mon- keypox-a potential threat? A systematic review. *PLoS Negl Trop Dis* 2022;16(2): e0010141.

[16] Beer EM, Rao VB. A systematic review of the epidemiology of human monkey- pox outbreaks and implications for out- break strategy. *PLoS Negl Trop Dis* 2019; 13(10):e0007791.

[17] Yinka-Ogunleye A, Aruna O, Dalhat M, et al. Outbreak of human monkeypox in Nigeria in 2017-18: a clinical and epidemiological report. *Lancet Infect Dis* 2019; 19:872-9

[18] Doshi RH, Alfonso VH, Morier D, et al. Monkeypox rash severity and animal ex- posures in the Democratic Republic of the Congo. *Ecohealth* 2020;17:64-73.

[19] Besombes C, Gonofio E, Konamna X, et al. Intrafamily transmission of mon- keypox virus, Central African Republic, 2018. *Emerg Infect Dis* 2019;25:1602-4.

[20] Vandenbogaert M, Kwasiborski A, Gonofio E, et al. Nanopore sequencing of a monkeypox virus strain isolated from a pustular lesion in the Central African Re- public. *Sci Rep* 2022;12:10768.

[21] Nolen LD, Osadebe L and Katomba J. Extended human-to-human transmission during a monkeypox outbreak in the Democratic Republic of the Congo. *Emerge Infect Dis* 2016;22:1014-21.

[22] Ogoina, D.; Iroezindu, M.; James, H.I.; Oladokun, R.; Yinka-Ogunleye, A.; Wakama, P.; Otike-Odibi, B.; Usman, L.M.; Obazee, E and Aruna, O.Clinical Course and Outcome of Human Monkeypox in Nigeria. *Clin. Infect. Dis.* 2020, 71, e210–e214.

[23] Jezek, Z.; Szczeniowski, M.; Paluku, K.M.; Mutombo, M. Human Monkeypox: Clinical Features of 282 *Patients. J. Infect. Dis*. 1987;156: 293–298.

[24] WHO. Monkeypox. Available online: https://www.who.int/news-room/fact-sheets/detail/monkeypox. 2022 July.

[25] Adler, H.; Gould, S.; Hine, P.; Snell, L.B.; Wong, W.; Houlihan, C.F.; Osborne, J.C.; Rampling, T.; Beadsworth, M.B and Duncan, C.J. Clinical features and management of human monkeypox: A retrospective observational study in the UK. *Lancet Infect. Dis*. 2022.

[26] Osadebe, L.; Hughes, C.M.; Lushima, R.S.; Kabamba, J.; Nguete, B.; Malekani, J.; Pukuta, E.; Karhemere, S.; Tamfum, J.-J.M;. Okitolonda, E.W.; et al. Enhancing case definitions for surveillance of human monkeypox in the Democratic Republic of Congo. *PLOS Negl. Trop. Dis*. 2017, 11, e0005857

[27] Huhn, G.D.; Bauer, A.M.; Yorita, K.; Graham, M.B.; Sejvar, J.; Likos, A.; Damon, I.K.; Reynolds, M.; Kuehnert, M.J. Clinical Characteristics of Human Monkeypox, and Risk Factors for Severe Disease. *Clin. Infect. Dis*. 2005; 41: 1742–1751

[28] Mbala, P.K.; Huggins, J.W.; Riu-Rovira, T.; Ahuka, S.M.; Mulembakani, P.; Rimoin, A.W.; Martin, J.W.; Muyembe, J.-J.T. Maternal and Fetal Outcomes Among Pregnant Women with Human Monkeypox Infection in the Democratic Republic of Congo. *J. Infect. Dis.* 2017;216: 824–828

[29] Damon, I.K. Status of human monkeypox: Clinical disease, epidemiology and research. *Vaccine* 2011; 29: D54–D59.

[30] Hussein, F. K., Mahmoud, A. J., and Yousif, B. J. Estimation of Immunoglobulin A, Immunoglobulin G, and Immunoglobulin M Antibody Levels in Laboratory Mice Balb/c Infected with Entamoeba histolytica and Treatment with Aqueous Extracts of Cyperus rotundus and Thymus serpyllum. *Polytechnic Journal*.2020; 10(1), 21.

[31] Yi X.M, Lei Y.L, Li M, Li Z, Li S. The monkeypox virus-host interplays. *Cell Insight*. 2024:100185

[32] Estep RD, Messaoudi I, O'Connor MA, Li H, Sprague J, Barron A, et al. Deletion of the monkeypox virus inhibitor of complement enzymes locus impacts the adaptive immune response to monkeypox virus in a nonhuman primate model of infection. *Journal of virology*. 2011;85(18):9527-42.

[33] Shchelkunov SN. An increasing danger of zoonotic orthopoxvirus infections. *PLoS pathogens*. 2013;9(12):e1003756.

[34] Adler H, Gould S, Hine P, Snell LB, Wong W, Houlihan CF, et al. Clinical features and management of human monkeypox: a retrospective observational study in the UK. *The Lancet Infectious Diseases.* 2022;22(8):1153-62

[35] Kulesh DA, Loveless BM, Norwood D, et al. Monkeypox virus detection in rodents using real-time 3f-minor groove binder TaqMan assays on the Roche Light Cycler. *Lab Invest* 2004; 84:1200–8.

[36] Bayer-Garner IB. Monkeypox virus: histologic, immunohistochemical and electron-microscopic findings. *J Cutan Pathol* 2005; 32:28–34.

[37] Gentile M, Gelderblom HR. Rapid viral diagnosis: role of electron microscopy. *New Microbiol* 2005; 28:1–12.

[38] Damon IK, Esposito JJ. Poxviruses that infect humans. In: Murray PR, Baron EJ, Jorgensen JH, Pfaller MA, Yolker MH, eds. Manual of clinical microbiology. 8th ed. Washington, DC: *ASM Press*, 2003:1583–91

[39] Taher, H. M. Levels Estimation of Iron, Zinc and Copper in the Serum of Children Infected with Giardiasis. *Al-Kitab Journal for Pure Sciences*.2024; *8*(02), 120-124.

[40] Lapa S, Mikheev M, Shchelkunov S, et al. Species-level identification of orthopoxviruses with an oligonucleotide microchip. J Clin Microbiol 2002; 40:753–7.

[41] Guarner J, Del Rio C, Malani PN. Monkeypox in 2022-what clinicians need to know. *JAMA*. 2022;328(2):139–40.

[42] Centers for Disease Control and Prevention. Impact of monkeypox outbreak on select behaviors. 2022. https://www.cdc.gov/poxvirus/monkeypox/response/2022/amis-select behaviors.html#:~:text=In%20an%20online%20survey%20of,encounters%2C%20and%205 0%25%20reported%20reducing. Accessed 19 Oct 2022.

[43] Rimoin AW, Mulembakani PM, Johnston SC, Lloyd Smith JO, Kisalu NK, Kinkela TL, et al. Major increase in human monkeypox incidence 30 years after smallpox vaccination campaigns cease in the Democratic Republic of Congo. *Proc Natl Acad Sci USA*. 2010;107(37):16262–7.

[44] Centers for Disease Control and Prevention. Monkeypox and smallpox vaccine guidance. 2022. https://www.cdc.gov/poxvirus/monkeypox/clinicians/smallpox-vaccine.html. Accessed 26 Sept 2022.

[45] Amer, F., Khalil, H. E., Elahmady, M., ElBadawy, N. E., Zahran, W. A., Abdelnasser, M.and Tash, R. M. E. Monkeypox: Risks and approaches to prevention. *Journal of infection and public health*.2023; 16(6), 901-910.

[46] Guarner J, Del Rio C, Malani PN. Monkeypox in 2022-what clinicians need to know. *JAMA*. 2022;328(2):139–40.

[47] Reynolds MG, McCollum AM, Nguete B, Lushima RS, Petersen BW. Improving the care and treatment of monkeypox patients in low-resource settings: applying evidence from contemporary bio- medical and smallpox biodefense research. *Viruses*. 2017. https:// doi.org/10.3390/v9120380.

[48] Adler H, Gould S, Hine P, et al. Clinical features and management of human monkeypox: a retrospective observational study in the UK. *Lancet Infect Dis*. 2022;S1473–3099(22)00228-6. https://doi. org/10.1016/S1473-3099(22)00228-6.

[49] TPOXX (tecovirimat) [Package Insert]. Corvallis, OR: SIGA Technologies, Inc. 2018. https://www.accessdata.fda.gov/drugs atfda_docs/label/2018/208627s000lbl.pdf. Accessed 2022 May.

[50] Russo AT, Grosenbach DW and Chinsangaram J. An overview of tecovirimat for smallpox treatment and expanded anti-ortho- poxvirus applications. *Expert Rev Anti Infect Ther*. 2021. https:// doi.org/10.1080/14787210.2020.1819791.

[51] Grosenbach DW, Honeychurch K, Rose EA, et al. Oral tecovirimat for the treatment of smallpox. *N Engl J Med*. 2018. https://doi.org/ 10.1056/nejmoa1705688.

[52] Quenelle DC, Buller RML, Parker S, et al. Efficacy of delayed treatment with ST-246 given orally against systemic orthopox- virus infections in mice. *Antimicrob Agents Chemother*. 2007. https://doi.org/10.1128/AAC.00879-06.

[53] Marcinak J, Vora S, Weber S, et al. Household transmission of vaccinia virus from contact with a military smallpox vaccine Illinois and Indiana. *Morb Mortal Wkly Rep*. 2007.

[54] Taher, H. M. The effect of aqueous and alcoholic extract of Opuntia ficus indica on biochemical parameters and kidney function in rats infected with Echinococcosis. *GSC Biological and Pharmaceutical Sciences*.2023; *25*(2), 244-248.

[55] Hahne S, Macey J, Binnendijk RV, et al. Progressive vaccinia in a military smallpox vaccine—United States. *Pediatr Infect Dis J*. 2009. https://doi.org/10.1097/inf.0b013e3181b18ed0

[56] US Food and Drug Administration: FDA approves drug to treat smallpox. https://www.fda.gov/drugs/drug-safety-and-availabili ty/fda-approves-drug-treat-smallpox. Accessed 2022 May.

[57] Bakr, M.M., Taher, H. M. & Mohamed, A. H. The Effect of Entamoeba Histolytica Infection on Levels of Adiponectin and Histamine in Children. *Bahrain Medical Bulletin*.2022; 44(2).

[58] Lanier R, Trost L, Tippin T, et al. Development of CMX001 for the treatment of poxvirus infections. *Viruses*. 2010. https://doi. org/10.3390/v2122740.

[59] Rice AD, Adams MM, Wallace G, et al. Efficacy of CMX001 as a post exposure antiviral in New Zealand white rabbits infected with rabbit pox virus, a model for orthopoxvirus infections of humans. *Viruses*. 2011. https://doi.org/10.3390/v3010047.

Al-Kitab Journal for Pure Sciences (2025); 9(2):140-153.
https://doi.org/10.32441/kjps.09.02.p9

Al-Kitab Journal for Pure Sciences
ISSN: 2617-1260 (print), 2617-8141(online)

https://isnra.net/index.php/kjps

Landfill Site Suitability Assessment Based on GIS and Multicriteria Analysis: A Case Study of Kirkuk City

Hana Kareem Shekho*, Muntadher Aidi Shareef

Northern Technical University, Engineering Technical College of Kirkuk, Surveying Engineering Department, Iraq

*Corresponding Author: hana.kareemgs@ntu.edu.iq

Citation: Shekho HK, Shareef MA. Landfill Site Suitability Assessment Based on GIS and Multicriteria Analysis: A Case Study of Kirkuk City. Al-Kitab J. Pure Sci. [Internet]. 2025 May. 07;9(2):140-153. DOI: https://doi.org/10.32441/kjps.09.02.p9.

Keywords: Landfill, Geographic Information System (GIS), Analytic Hierarchy Process (AHP), Convolutional Neural Network (CNN), Kirkuk, Multicriteria Analysis, Suitability Assessment.

Article History

Received	01	Aug.	2024
Accepted	09	Dec.	2024
Available online	07	May.	2025

Abstract:

This study looks at the environmental and socioeconomic aspects of possible landfill locations in Kirkuk City, Iraq, as well as their spatiotemporal appropriateness. This study used different types of data, including Landsat satellite imagery, soil texture, groundwater level, and slope. The Analytic Hierarchy Process (AHP) was utilized for multi-criteria decision analysis of possible landfill sites, linear regression was employed for population projection, and a Convolutional Neural Network (CNN) was utilized for Normalized Difference Vegetation Index (NDVI)/ Normalized Difference Built-up Index (NDBI) prediction. The suitability ratings for prospective dump sites were produced using the AHP-based Geographic Information Index (GIS) techniques. The results reveal that the selection of landfill locations minimizes environmental effects and advances environmentally sound waste management. The technique provides a framework for assessing the appropriateness of dump sites in various geographical areas. Moreover, the projections for the future emphasize Kirkuk City's need for upgraded waste management facilities. Furthermore, urban planners and politicians in Kirkuk City may benefit greatly from this research's data-driven approach to landfill site selection, which takes social and environmental concerns into account and has implications for sustainable waste management techniques.

Keywords: Landfill, Geographic Information System (GIS), Analytic Hierarchy Process (AHP), Convolutional Neural Network (CNN), Kirkuk, Multicriteria Analysis, Suitability Assessment.

تقييم مدى ملاءمة موقع المكب بناء على نظم المعلومات الجغرافية وتحليل متعدد المعايير: دراسة حالة مدينة كركوك

هانا كريم شيخو*، منتظر عيدي شريف

الجامعة التقنية الشمالية، الكلية التقنية الهندسية كركوك، قسم هندسة المساحة، العراق

hana.kareemgs@ntu.edu.iq, muntadher.a.shareef@ntu.edu.iq

الخلاصة:

نظرت هذه الدراسة في الجوانب البيئية والاجتماعية والاقتصادية لمواقع مدافن النفايات المحتملة في مدينة كركوك بالعراق، فضلا عن ملاءمتها الزمانية المكانية. تم استخدام أنواع مختلفة في هذه الدراسة بما في ذلك صور الأقمار الصناعية لاندسات، وملمس التربة، ومستوى المياه الجوفية، والمنحدر. واستخدمت عملية التسلسل الهرمي التحليلي (*AHP*) لتحليل القرار متعدد المعايير لمواقع المكب المحتملة، واستخدمت الانحدار الخطي لإسقاط السكان، واستخدمت الشبكة العصبية التلافيفية (*CNN*) للتنبؤ ندفي/ندبي. وأنتجت تقييمات الملاءمة لمواقع التفريغ المرتقبة باستخدام تقنيات نظم المعلومات الجغرافية القائمة على برنامج التكيف الهيكلي. تم الكشف عن النتائج أن اختيار مواقع مدافن النفايات يقلل من التأثير البيئي ويعزز الإدارة السليمة بيئيا للنفايات. وتوفر هذه التقنية إطارا لتقييم مدى ملاءمة مواقع تفريغ النفايات في مختلف المناطق الجغرافية. علاوة على ذلك، تؤكد التوقعات المستقبلية على حاجة مدينة كركوك إلى تحسين مرافق إدارة النفايات. علاوة على ذلك، قد يستفيد المخططون والسياسيون الحضريون في مدينة كركوك بشكل كبير من نهج هذا البحث القائم على البيانات لاختيار مواقع دفن النفايات، والذي يأخذ في الاعتبار الاهتمامات الاجتماعية والبيئية وله آثار على تقنيات الإدارة المستدامة للنفايات.

الكلمات المفتاحية: مكب النفايات، نظم المعلومات الجغرافية، التسلسل الهرمي التحليلي، الشبكة العصبية التلافيفية، كركوك.

1. Introduction:

Every nation on the planet deals with a variety of environmental issues [1]. Municipal solid waste management is becoming a global concern that many municipalities are facing, especially in hilly cities. Additionally, the UN's goal for global sustainability now includes municipal waste management as an emerging problem because of the population increase [2–4].

The aim of solid waste management is to dispose of waste in the most environmentally friendly way feasible [5]. The locals who are immediately touched by a region's solid waste program help to achieve this. Households, workplaces, small businesses, and commercial establishments all have their solid trash collected. This is regarded as a unique waste stream in the EU. The term "MSW" refers to this type of trash as well as waste produced during building, restoration, and demolition. MSW includes items like glass, bricks, concrete, inert materials, paper and cardboard, yard trash, metal, plastic and rubber, electronic waste, and miscellaneous garbage. Municipalities across the world classify MSW in different ways. It is composed of both

biodegradable and non-biodegradable elements as well as organic and inorganic components. Many different approaches are used worldwide to reduce the production of solid waste. The most popular strategies for reducing solid waste are garbage disposal, recovery, reuse, recycling, and prevention. Another tactic used to prevent any environmental problems is the regular storage of solid waste. One of the major worldwide concerns that is particularly noticeable in developing countries is the disposal of municipal solid waste (MSW) [6]. Finding, evaluating, and planning for landfill sites is one of the most important steps in the MSW disposal process [7,8].

According to their research, the number of households, employment, and population expansion all have a big influence on trash generation rates. Predicting a 70.6% rise in garbage by 2031, the LSTM model proved to be the most accurate in predicting future trends in waste. Planning effective waste management systems to accommodate the predicted rise in trash creation would need careful consideration of this forecast.

The aim of this study is to provide a framework for assessing the appropriateness of dump sites in various geographical areas. This framework is based on the Analytic Hierarchy Process (AHP) [9], which was utilized for multi-criteria decision analysis of possible landfill sites, linear regression was employed for population projection, and a convolutional neural network (CNN) [10] was utilized for NDVI/NDBI prediction [11–13].

2. Literature Review

A number of review papers discussed GIS-based multicriteria spatial decision support systems for landfill siting suitability analysis. The factors considered for utilizing MCDA for landfill site suitability assessment [16]. The use of MCDA in tackling waste management problems emphasized the increasing complexity of waste management due to growing waste volumes and environmental concerns [17]. The review covered various MCDA techniques used in real-life waste management scenarios, highlighting their advantages and disadvantages compared to other approaches .

In [18] it was discussed that the challenges in solid waste management due to the increasing quantities and complexity of waste generated worldwide. They presented the importance of MCDA models in addressing the various dimensions and conflicting criteria involved in waste management. The study reviewed the current practices and methods of MCDA in SWM, emphasizing the need for tools to assess system performance comprehensively [18].

Abujayyab et al. (2016) discussed GIS modelling for landfill site selection, focusing on the criteria and methods used for selection as the key challenges in determining landfill-siting input criteria, as discussed in the article, include the complexity of procedures, the need to consider

environmental, economic, and social impacts, compliance with regulations, public acceptance, and the extensive evaluation required for selecting suitable landfill sites [19].

Abujayyab et al. (2017) explored the use of MCDA in GIS modeling for landfill site selection from 1997 to 2014 as the study focused on stages such as the selection of weights and decision rules in the models [20]. It identified strengths and limitations of using MCDA for landfill site selection and suggested the potential use of Artificial Neural Networks (ANN) for enhanced validation and accuracy [20].

Mat et al. (2017) discussed the criteria and decision-making techniques used in solving landfill site selection problems, it highlighted the importance of selecting appropriate landfill sites and the use of GIS and MCDA techniques in this process [21]. More recently, the review by Mohammed et al. (2019) discussed how the combination of GIS-based tools and decision analysis techniques has significantly expanded in various fields of research over the last few decades, allowing for the automation and analysis of spatial data [22].

3. Materials and methods:

3.1 Overview: The process for determining whether possible landfill sites are suitable and analyzing the spatiotemporal dynamics of several elements' influence is shown in **Figure 1**. The technique incorporates many data sources, such as population data from 2004 to 2024, Landsat satellite photos from 2004, 2014, and 2024, and climatic data including air temperature, rainfall, relative humidity, wind speed, and wind direction. Furthermore, soil texture, steady groundwater level, and slope GIS data are used.

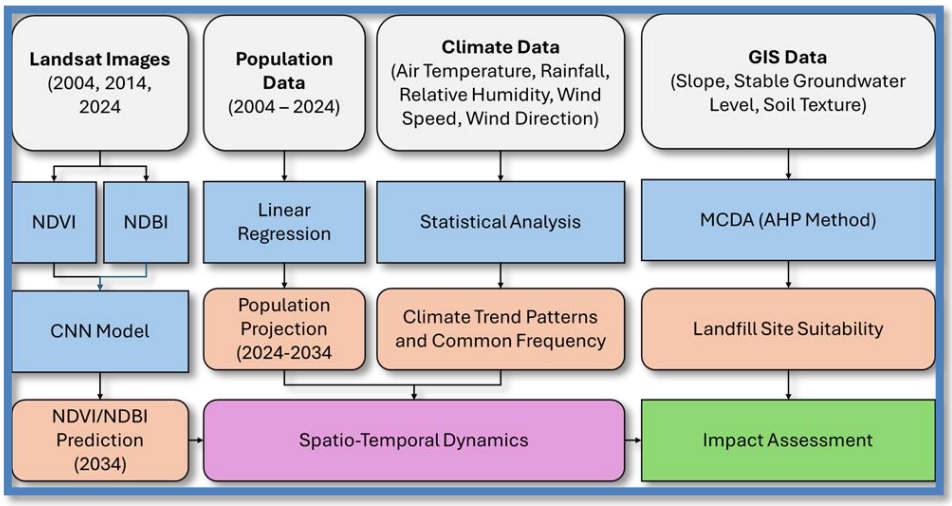

Figure 1: Flowchart of the proposed methodology overview

3.2 Study Area: This research focuses on Kirkuk City, the capital of the Kirkuk Governorate, which is situated in northern Iraq, along with its surrounding neighborhoods, including Taza and Leylan. Situated between the flat plains and the foothills of the Zagros

Mountains, Kirkuk City is located at 35°28'N 44°25'E. With a population that is expected to surpass 1.1 million by 2023 due to both natural growth and migration, this large metropolitan area is experiencing tremendous population increase. Significant urban sprawl has occurred in the city and its environs, with industrial zones primarily located on the periphery and residential and commercial sectors predominating in terms of land use. Figure 2 shows the study area.

Geographically, Kirkuk City is bordered to the north by the Zagros Mountains, to the east by the city of Sulaymaniyah, to the south by the Hamrin Mountains, and to the west by the Lower Zab Mountains. The area is around 250 kilometers away from Baghdad. The three districts of Kirkuk City, Laylan, and Taza comprise the 1368.34 km2 that make up the Kirkuk study area. Its landscape is varied, with heights ranging from 192 to 713 meters above sea level and features both flat sections and quite steep hills.

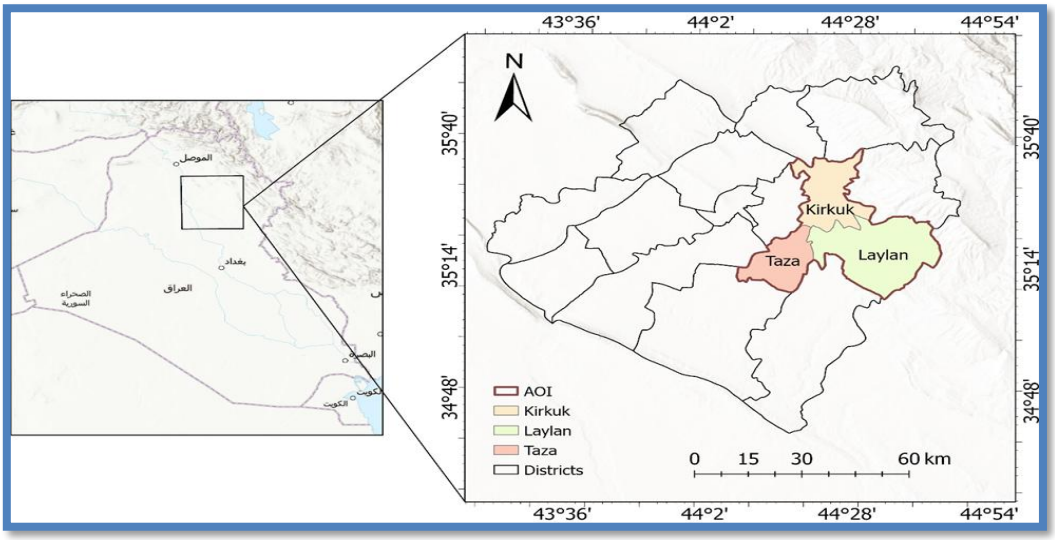

Figure 2: Map of the study including three districts of Kirkuk province (Kirkuk city, Laylan, and Taza).

3.3 Datasets

3.3.1 Landsat Data: Four images total from Landsat satellites were used in the investigation. As shown in **Table 1**. The dataset contains atmospherically corrected surface reflectance and land surface temperature derived from the data produced by the Landsat 8 OLI/TIRS sensors.

Table 1: Information on Landsat images obtained for this study.

Landsat Image	Sensor	Row	Path	Date	Cloud Cover	Processing Level
Image 2004-1	LANDSAT 5 TM	035	169	2004-03-18	18.00	L1TP
Image 2004-2	LANDSAT 5 TM	036	169	2004-03-18	2.00	L1TP
Image 2014	LANDSAT 8 OLI TIRS	035	169	2014-03-28	30.88	L1TP
Image 2024	LANDSAT 8 OLI TIRS	035	169	2024-03-01	1.35	L1TP

3.3.2 Population Data: The Department of Urban Planning in Kirkuk provides the demographic figures. The information was collected annually between 2004 and 2023. In terms of population, Kirkuk is the largest of the three cities. Between 2004 and 2023, the population

grew gradually, from 566,000 to 1,075,000. According to the data, the population is growing by between 30,000 and 40,000 people every year on average. Although Taza is a smaller city than Kirkuk, its population has been increasing more quickly. The population of Taza rose from 12,715 in 2004 to 51,119 in 2023. With the population growing by about 2,000 per year in the earlier years and then by about 3,000 to 4,000 per year in the more recent years, the growth rate seems to be quickening. In terms of population, Laylan is the smallest of the three cities. Between 2004 and 2023, its population grew from 14,887 to 20,881. The population of Laylan is growing by a few hundred each year, which seems to be a slower pace of growth than that of Kirkuk and Taza.

3.3.3 Climate Data: The Kirkuk station's meteorological section provides climatic data. The monthly statistics were collected between 2014 and 2023. Included in the climatic variables are air temperature, precipitation, relative humidity, wind direction, and wind speed.

3.3.4 GIS Data: Three primary factors—the soil texture and steady groundwater level—were taken into consideration while determining the viability of a landfill site. The research area's DEM data was used to derive the slope. With a spatial resolution of 30 m, the DEM was acquired from ASTER GDEM (https://gdemdl.aster.jspacesystems.or.jp/). The soil texture was taken from a 1:250000 scale raster map of the Iraqi Geological Survey.

3.4 Methods

3.4.1 Remote Sensing Indices: This investigation made use of several indices. These consist of NDBI and NDVI. The density of greenness on the ground surface is indicated by the NDVI measure, which is why it was chosen in this study. As such, it is an important factor to take into account while choosing a suitable landfill site. Equation (1) was utilized to create the NDVI using the Landsat-8 OLI dataset, as shown in reference [13].

$$NDWI = \rho_{green} - \rho_{NIR} / \rho_{green} + \rho_{NIR} \quad (1)$$

Where ρ_{green} and ρ_{NIR} are the green and the near infrared satellite image bands, respectively.

The size and geographic distribution of the research area's urban built-up areas are evaluated using the NDBI and related computations. It also offers a thorough overview of the land cover in cities. This study's NDBI map was produced using the Landsat-8 OLI dataset. For relevant computations, the near-infrared (NIR) and shortwave infrared (SWIR) bands were used, as shown in Equation (1) [14].

3.4.3 CNN

3.4.3.1 CNN Background: Convolutional operations are used on 2D input data, such as photographs or spatial grids, in order to extract significant features and patterns. This is the fundamental theory of CNNs [15]. In a regular Neural Network, there are three types of layers:

Input Layers: It's the layer in which we give input to our model. The number of neurons in this layer is equal to the total number of features in our data (number of pixels in the case of an image). Hidden Layer: The input from the Input layer is then fed into the hidden layer. There can be many hidden layers depending on our model and data size. Each hidden layer can have different numbers of neurons, which are generally greater than the number of features. The output from each layer is computed by matrix multiplication of the output of the previous layer with learnable weights of that layer and then by the addition of learnable biases, followed by an activation function, which makes the network nonlinear. Output Layer: The output from the hidden layer is then fed into a logistic function, like sigmoid or softmax, which converts the output of each class into the probability score of each class.

3.4.3.2 Patch Extraction: The input images are usually processed in discrete areas, known as patches, using CNNs. The input image is divided into smaller patches, or tiles, as part of the patch extraction process. These patches are then fed into the CNN's convolutional layers. The input picture is frequently padded with zeros around the borders prior to patch extraction. The purpose of this padding is to guarantee that patches close to the image's edge may be removed without running out of data. The size of the patches being extracted determines how much padding is needed.

3.4.3.3 Proposed CNN Architecture: One convolutional layer, one flattening layer, and two fully connected dense layers make up the CNN design that the study suggests. With data from 2014 and 2024, this CNN model is intended to forecast the NDVI and NDBI for the year 2034. The input data is passed through 32 convolutional filters of size 2x2 by the model's first layer, a 2D convolutional layer. The input shape is (3, 3, 2), where the number of channels (corresponding to NDVI and NDBI data) is represented by 2 and the spatial dimensions of the input data are represented by 3x3. This layer's output is subjected to the ReLU activation function. The convolutional layer's output is flattened into a 1D vector by the flattening layer, which prepares it for the fully connected layers that follow. The ReLU activation function is applied to the output by the following fully connected layer in the model, which consists of 16 neurons.

3.5 Validation: The actual observed data for 2024 was compared with the model's predictions as part of the validation procedure. The NDVI and NDBI values for 2024 were predicted by the algorithm after it had been trained using data between 2004 and 2014. The performance of the model was then assessed by comparing the projected values for 2024 with the actual observed values for 2024.

4. Results and Discussions

4.1 Results of NDVI/NDBI Prediction: Figure 1 shows the NDVI changes for a study region in 2004, 2014, and 2024. Higher values (darker green) in the NDVI indicate denser vegetation, whereas lower values (yellow/brown) indicate scant or no vegetation, such as in urban or desolate environments. A variety of plant densities were observed in the study region in 2004. Some areas, especially in the northern and southern parts, have extremely thick vegetation (dark green). Significant regions with moderate to low plant cover, which are represented by yellow and lighter green hues, are found as well; these areas are thought to be urban or developed areas. The research area's total vegetation density seems to have decreased by 2014. Particularly in the central and eastern sections, the forested areas have given way to urban or arid areas. The size of the dark green, high NDVI zones has shrunk, suggesting more urban or arid territory. The trend of declining vegetation density is expected to continue in 2024. A reduced percentage of the study area is currently covered by the highest, darkest green NDVI values, especially in the central and eastern parts. Comparing this year to last, there has been greater growth in the yellow, arid/urban regions. The NDVI variations between 2004 and 2024 indicate that the study area's vegetation is gradually getting less dense and dispersed. This may be brought on by things like changes in farming techniques that result in less plant cover, deforestation, or urban growth.

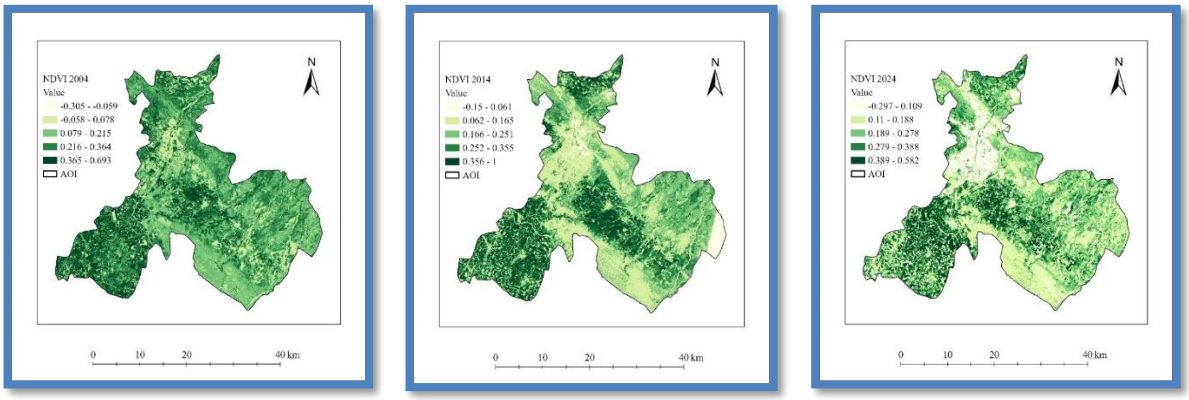

Figure 3: NDVI maps of the study area, (a) 2004, (b) 2014, and (c) 2024.

The maps in **Figure 1** depict the NDBI for the research area for the years 2004, 2014, and 2024. Oranges and reds denote greater values, indicating the presence of urban and arid areas. The NDBI values are represented using a color scale. Over the course of the three years, the mapped area's two main regions, the center and the southeast, have seen the greatest concentration of urban and desolate lands, shown by orange and red. These areas probably belong to large cities or metropolitan areas. The greater regions covered in orange and red on the 2014 map compared to the 2004 image indicate an increase in the size of urban and desolate

lands between 2004 and 2014. The growth of urban and arid regions is evident in the 2024 image, which has even more areas covered in orange and red than the 2014 map had. The temporal variations point to a continuous pattern of urban sprawl and the spread of arid areas over time, with the pace of expansion seeming to be faster between 2014 and 2024 than it was between 2004 and 2014.

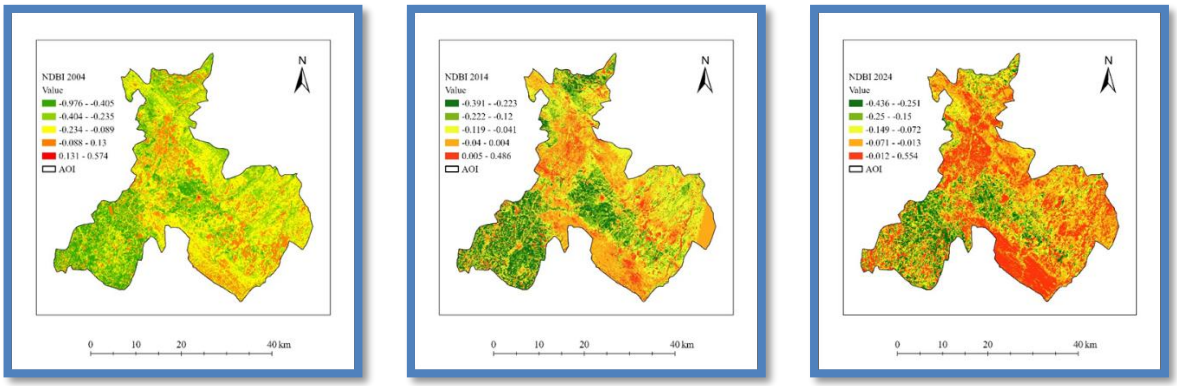

Figure 4: NDBI maps of the study area, (a) 2004, (b) 2014, and (c) 2024.

The NDVI for the research region in 2024 and the expected NDVI for 2034 are displayed in Figure 3. The NDVI readings show different degrees of plant density and health, ranging from -0.297 to 1 (green to red hues). Lower values (redder colors) denote scant or stressed vegetation, whereas higher values (greener shades) indicate denser and healthier plant cover. In comparison to 2024, the regional distribution of vegetation appears to have shifted dramatically, with some places seeing a loss of vegetation and others seeing a gain. The yellow/beige tint indicates where certain regions with moderate to high NDVI values in 2024 are expected to have little to no vegetation in 2034. The 2034 NDVI forecast shows that there won't be any appreciable changes to the plant cover.

These plant cover changes may have an influence on landfill siting because of the following possible effects. Because of possible ecological effects, places with sparse vegetation can be a better fit for landfill development than those with extensive vegetation. The anticipated alterations in the plant cover can be a result of infrastructure growth, urbanization, or other changes in land use that could affect whether possible landfill locations are suitable. To reduce soil erosion and regulate surface runoff, vegetation cover is essential. Variations in plant types may have an impact on surface water runoff and leachate management at landfills. During the site selection process, it may be necessary to take vegetation into account since it might affect the visual effect and public impression of a possible landfill site. Significant changes in the amount of vegetation might have an influence on the surrounding ecosystems, sometimes necessitating mitigation strategies or careful site selection to reduce effects on species or habitats that are vulnerable.

The NDBI for 2024 and the expected NDBI for 2034 are depicted in Figure 4. Warmer hues (yellow, orange, and red) indicate higher amounts of built-up or barren regions, whereas cooler colors (green) indicate vegetated areas. The NDBI values vary from -0.436 to 0.1. Compared to 2024, there seems to have been a considerable shift in the geographic distribution of developed and undeveloped regions, with certain places becoming more urbanized. It is anticipated that certain places with moderate to low NDBI values in 2024 will have high NDBI values (red) in 2034, suggesting a rise in built-up or bare areas, most likely because of urban growth or expansion. It is anticipated that certain regions with high 2024 NDBI values would have lower 2034 NDBI values (green), indicating a possible reduction in built-up areas or opportunity for revegetation or redevelopment.

The alterations in developed and undeveloped regions may have consequences for the location of landfills because of the subsequent elements and their effects. While locations with less built-up areas may provide more possible sites, areas with rising urbanization may have limited acreage available for landfill construction. Transportation networks and infrastructure may be easier to reach in urbanized regions, which might make it easier to move garbage to possible disposal locations. Higher densities of impermeable surfaces may be found in highly developed regions, which might increase surface runoff and require more thorough stormwater management at landfill sites. Potential landfill locations may get closer to residential areas because of increased urbanization, which might cause residents to worry about noise, odor, and other annoyances. Redevelopment of brownfields and the cleanup of previously constructed sites might be opportunities in regions with declining built-up areas and should be taken into consideration when choosing where to locate landfills.

4.2 Results of Landfill Site Suitability Assessment: A weighted average of the soil type weights, stable groundwater level, and criteria slope from earlier studies is used to assess the area's appropriateness for landfills. A map illustrating the research region's landfill suitability is shown in Figure 5. The appropriateness is broken down into five categories, as indicated by the map: very low, low, moderate, high, and very high. Several colored zones on the map represent different degrees of appropriateness for the establishment of a landfill. The areas for the five appropriateness levels—219.25, 305.30, 181.49, 304.10, and 354.84 km2—are displayed in the chart. The research region's northern regions exhibit varying degrees of eligibility for disposal locations. The red and yellow hues indicate that the region's eastern and southeast have very low and low suitability ratings, respectively. The land's southernmost portion is more favorable—in fact, exceptionally suited. Four landfill sites were chosen based on the suitability map and the accessible lands (**Figure 5**).

Site 3 is the ideal option since it implies typically flat terrain with low population density and a shallow water table, among other critical features. It has the largest population (16.922), the lowest slope (1.955), the highest landfill compatibility score (0.316), and a stable groundwater level (204.159m). It is also the closest to cities (3522.0m) and water (817.6m), which may or may not be useful depending on the circumstances. Even yet, the present landfill is rather far away (15120.5m). Site 1 is feasible as well, having the lowest slope (1.867), population (9.909), and NDVI (0.101, indicating little vegetation), in addition to having an intermediate landfill suitability (0.283). Although it is closer to water (1192.2m) than Sites 2 and 4, its closeness to towns and cities (2878.6m and 3735.4m) may provide issues.

Table 2: Weights for the landfill site suitability criteria provided by the experts questioned in this study and AHP methodology.

Main Criteria	Weight	Sub–criteria	Sub–Weights
Slope	0.310	0 – 3	0.163
		3 – 6	0.111
		6 – 9	0.034
		9 – 35.638	٠
Groundwater stable level	0.333	0.388 - 112	0.173
		113 - 224	0.136
		225 - 336	0.018
		337 - 448	0.005
		449 - 560	٠
Soil types	0.356	Injana Formation	0.050
		Kirkuk group	0.011
		Valley Fill Deposits	0.038
		Sheet Runoff Deposits	0.072
		Bai Hassan Formation	0.026
		Slope Deposits	0.074
		Poly Genetic	0.072
		Jaddala and Ayanah Formation	0.011
Sum	1		1

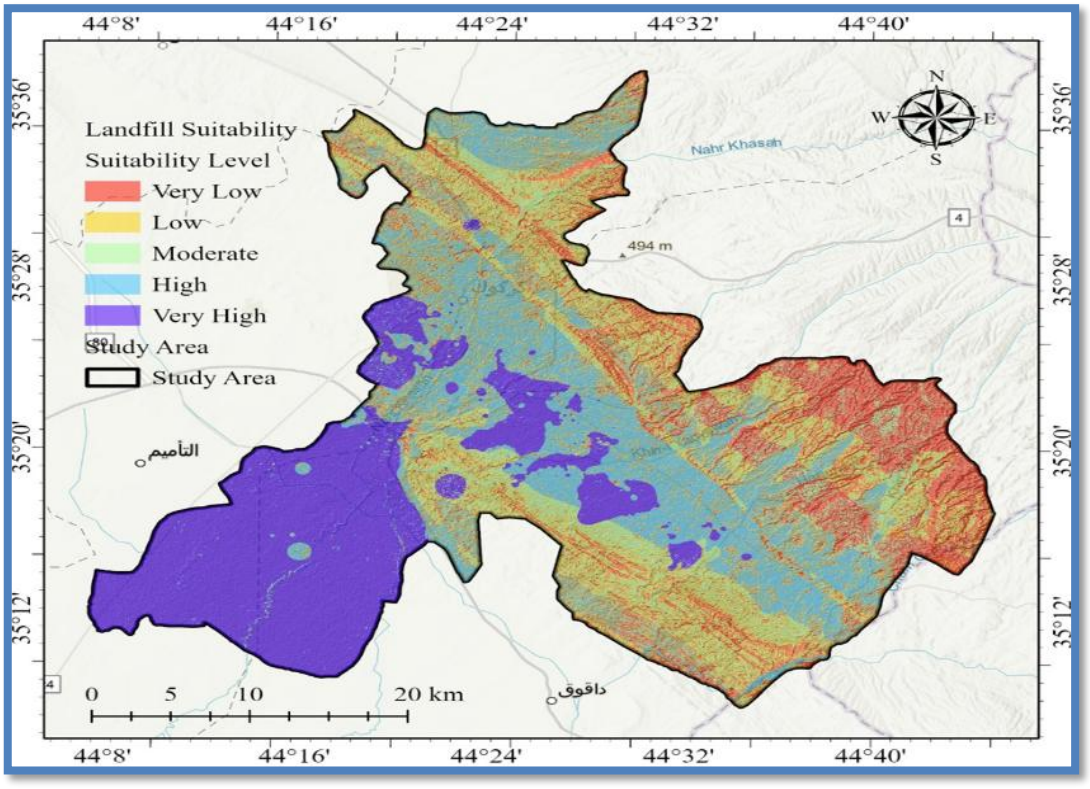

Figure 5: Map of landfill suitability in the study area.

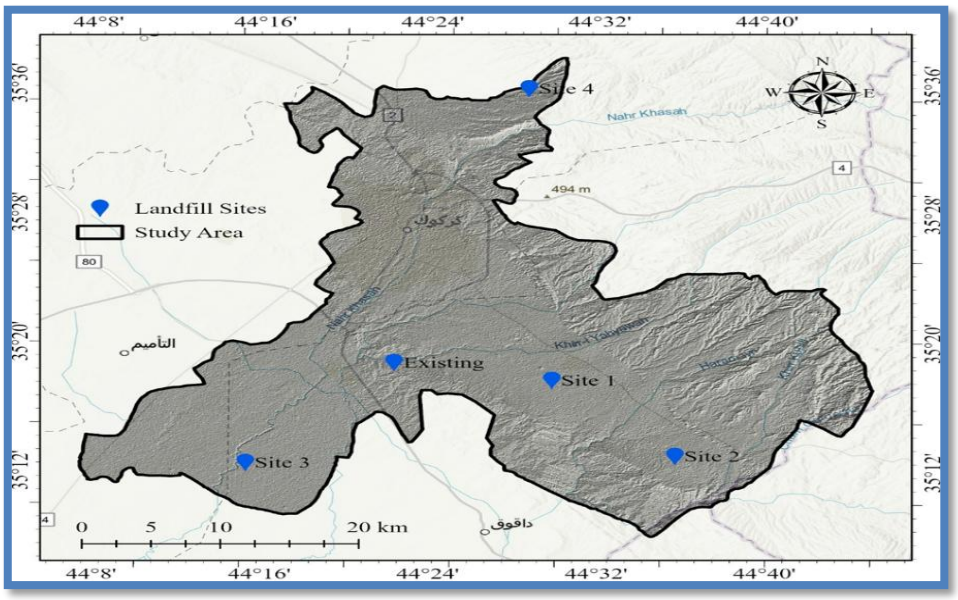

Figure 6: Map of landfill site locations including the existing and selected sites.

4. Conclusions

Significant trends in land use changes, climatic patterns, and population increase were found in Kirkuk City throughout our analysis. These patterns point to a significant rise in solid waste creation in the future, as do population estimates. The study developed a methodology for the spatiotemporal assessment of possible landfill sites to overcome this difficulty. This approach considers social, economic, and environmental aspects, such as land cost, population density, soil texture and groundwater levels. The study selected landfill locations that minimize environmental effects and enhance sustainable waste management by combining these through a multi-criteria decision analysis. For Kirkuk City urban planners, this study offers insightful information. The methodology of data-driven landfill site selection provides a model for comparable assessments in other areas. Moreover, the anticipated rise in trash production highlights the pressing necessity for enhanced waste management facilities inside the city. By putting our suggestions into effect, Kirkuk City's waste management procedures may have a more sustainable future.

6. References

[1] Mushtaq J, Dar AQ, Ahsan N. Spatial–temporal variations and forecasting analysis of municipal solid waste in the mountainous city of north-western Himalayas. SN Appl Sci. 2020 Jul;2(7):1161.

[2] Srivastava A, Jha PK. A multi-model forecasting approach for solid waste generation by integrating demographic and socioeconomic factors: a case study of Prayagraj, India. Environ Monit Assess. 2023 Jun;195(6):768.

[3] Tv R, Aithal BH, Sanna DD. Insights to urban dynamics through landscape spatial pattern analysis. Int J Appl Earth Obs Geoinformation. 2012 Aug;18:329–43.

[4] Grimm NB, Grove JM, Pickett STA, Redman CL. Integrated Approaches to Long-Term Studies of Urban Ecological Systems. In: Marzluff JM, Shulenberger E, Endlicher W, Alberti M, Bradley G, Ryan C, et al., editors. Urban Ecology [Internet]. Boston, MA: Springer US; 2008 [cited 2024 Jul 30]. p. 123–41. Available from: http://link.springer.com/10.1007/978-0-387-73412-5_8

[5] Abdel-Shafy HI, Mansour MSM. Solid waste issue: Sources, composition, disposal, recycling, and valorization. Egypt J Pet. 2018 Dec;27(4):1275–90.

[6] Aslam B, Maqsoom A, Tahir M, Ullah F, Rehman M, Albattah M. Identifying and Ranking Landfill Sites for Municipal Solid Waste Management: An Integrated Remote Sensing and GIS Approach. Buildings. 2022 May 6;12(5):605.

[7] Zhang Z, Liu N, Zhao L. Spatio-temporal evolution and driving factors of waste disposal facilities in China. J Environ Plan Manag. 2024 Jul 2;67(8):1805–29.

[8] Wang Y, Li Z, Zheng X. The Microclimatic Effects of Ecological Restoration in Brownfield based on Remote Sensing Monitoring: The Case Studies of Landfills in China. Ecol Eng. 2020 Oct;157:105997.

[9] Ishizaka A. Analytic Hierarchy Process and Its Extensions. In: Doumpos M, Figueira JR, Greco S, Zopounidis C, editors. New Perspectives in Multiple Criteria Decision Making [Internet]. Cham: Springer International Publishing; 2019 [cited 2024 Jul 30]. p. 81–93. (Multiple Criteria Decision Making). Available from: http://link.springer.com/10.1007/978-3-030-11482-4_2

[10] Abdullahi HS, Sheriff RE, Mahieddine F. Convolution neural network in precision agriculture for plant image recognition and classification. In: 2017 Seventh International Conference on Innovative Computing Technology (INTECH) [Internet]. Luton: IEEE; 2017 [cited 2024 Jul 30]. p. 1–3. Available from: http://ieeexplore.ieee.org/document/8102436/

[11] Macarof P, Statescu F. Comparasion of NDBI and NDVI as Indicators of Surface Urban Heat Island Effect in Landsat 8 Imagery: A Case Study of Iasi. Present Environ Sustain Dev. 2017 Oct 1;11(2):141–50.

[12] Lima GC, Silva MLN, Curi N, Silva MAD, Oliveira AH, Avanzi JC, et al. Evaluation of vegetation cover using the normalized difference vegetation index (NDVI). Ambiente E Agua - Interdiscip J Appl Sci. 2013 Aug 29;8(2):204–14.

[13] Borgogno-Mondino E, Lessio A. Estimation and mapping of NDVI uncertainty from Landsat 8 OLI datasets: An operational approach. In: 2015 IEEE International Geoscience and Remote Sensing Symposium (IGARSS) [Internet]. Milan, Italy: IEEE; 2015 [cited 2024 Jul 30]. p. 629–32. Available from: http://ieeexplore.ieee.org/document/7325842/

[14] Bhatti SS, Tripathi NK. Built-up area extraction using Landsat 8 OLI imagery. GIScience Remote Sens. 2014 Jul 4;51(4):445–67.

[15] Wiatowski T, Bolcskei H. A Mathematical Theory of Deep Convolutional Neural Networks for Feature Extraction. IEEE Trans Inf Theory. 2018 Mar;64(3):1845–66.

[16] X. Zhang et al., "Using biochar for remediation of soils contaminated with heavy metals and organic pollutants," Environ. Sci. Pollut. Res., vol. 20, no. 12, pp. 8472–8483, 2013, doi: 10.1007/s11356-013-1659-0.

[17] C. Achillas, N. Moussiopoulos, A. Karagiannidis, G. Banias, and G. Perkoulidis, "The use of multi-criteria decision analysis to tackle waste management problems: A literature review," Waste Manag. Res., vol. 31, no. 2, pp. 115–129, 2013, doi: 10.1177/0734242X12470203.

[18] C. A. S. Coelho et al., "The 2014 southeast Brazil austral summer drought: regional scale mechanisms and teleconnections," Clim. Dyn., vol. 46, no. 11–12, pp. 3737–3752, 2016, doi: 10.1007/s00382-015-2800-1.

[19] S. K. M. Abujayyab, M. S. S. Ahamad, A. S. Yahya, M. J. K. Bashir, and H. A. Aziz, "GIS modelling for new landfill sites: Critical review of employed criteria and methods of selection criteria," IOP Conf. Ser. Earth Environ. Sci., vol. 37, no. 1, 2016, doi: 10.1088/1755-1315/37/1/012053.

[20] S. Z. Ahmad, M. S. S. Ahamad, M. S. Yusoff, and S. K. M. Abujayyab, "Enhanced Fuzzy-OWA model for municipal solid waste landfill site selection," AIP Conf. Proc., vol. 1892, no. October, 2017, doi: 10.1063/1.5005684.

[21] N. Xu, B. Price, S. Cohen, and T. Huang, "Deep Image Matting - Supplementary Materials," Cvpr, pp. 2970–2979, 2017, [Online]. Available: http://arxiv.org/abs/1703.03872

[22] G. H. Mohammed et al., "NASA Public Access," 2021, doi: 10.1016/j.rse.2019.04.030.Remote.

Al-Kitab Journal for Pure Sciences (2025); 9(2):154-168.
https://doi.org/10.32441/kjps.09.02.p10

Al-Kitab Journal for Pure Sciences
ISSN: 2617-1260 (print), 2617-8141(online)
https://isnra.net/index.php/kjps

Assessing The Environmental Quality of Kirkuk City and Taza District Based on Pressure-State-Response Framework for Winter 2023 Using Remote Sensing and GIS

Sundus Mohammed Azeez*, Muntadher Aidi Shareef, Fawzi Mardan Omer

Surveying/ Engineering Technical College- Kirkuk/ Northern Technical University, Mosul, Iraq

*Corresponding Author: Sundus.mohammedgs@ntu.edu.iq

Citation: Azeez SM, Shareef MA, Omer FM. Assessing The Environmental Quality of Kirkuk City and Taza District Based on Pressure-State-Response Framework for Winter 2023 Using Remote Sensing and GIS. Al-Kitab J. Pure Sci. [Internet]. 2025 Sep. 06;9(2):154-168. DOI: https://doi.org/10.32441/kjps.09.02.p10.

KeywordsEco-Environment, Ecologic Index, PSR Framework, Response Indicator, Sentinel-2.

Article History

Received	03 Aug.	2024
Accepted	26 Nov.	2024
Available online	06 Sep.	2025

Abstract:

Evaluating a region's Ecological Environment Quality (EEQ) is an essential factor in deciding its urbanization and sustainable development rate. This study aims to find the Ecological Index (EI). It evaluates it using the widely used Pressure-State-Response (PSR) framework based on a set of statistical and remote sensing indices in Kirkuk City and Taza district. Sentinel-2 satellite images were used to obtain 12 indicators that offer a foundation for sustainable development decision-making for Kirkuk City and Taza District during the winter of 2023. The finding reveals that the ecological condition is healthy in winter due to the atmospheric conditions and the social and economic activities. It presents the main relation between environmental health and human activities.

Keywords: Eco-Environment, Ecological Index, PSR Framework, Response Indicator, Sentinel-2.

تقييم جودة النظام البيئي في محافظة كركوك و مقاطعة تازة بالاعتماد على طريقة *framework Pressure-State-Response* لشتاء ٢٠٢٣ باستخدام التحسس النائي و نظم المعلومات الجغرافية

سندس محمد عزيز ومنتظر عيدي شريف وفوزي مردان عمر

قسم تقنيات هندسة المساحة\الكلية التقنية الهندسية-كركوك\ الجامعة التقنية الشمالية/ العراق

Sundus.mohammedgs@ntu.edu.iq; Muntadher.a.shareef@ntu.edu.iq; fawzialbeyati@ntu.edu.iq

الخلاصة:

تقييم النظام البيئي لمنطقة ما، هو عامل مهم في تحديد معدل التطور العمراني والتنمية المستدامة. تهدف هذه الدراسة لإيجاد المؤشر البيئي *(EI)* وتقييمه بواسطة الطريقة الشائعة *pressure-state-response (PSR) framework* بالاعتماد على مجموعة من المؤشرات الإحصائية والخاصة بالتحسس النائي في مدينة كركوك ومقاطعة تازة. تم استخدام الصور الفضائية *sentinel-2* للحصول على ١٢ من المؤشرات التي تم صنعها من التحسس النائي لتقييم جودة النظام البيئي. هذه المؤشرات توفر اساساً لصناعة القرار في التنمية المستدامة كتقنية حديثة تدعم التغير الذي يحدث على المدى البعيد من خلال انشاء الخرائط وعرضها تقوم هذه الدراسة بعرض المؤشر البيئي لفصل الشتاء لسنة ٢٠٢٣ في محافظة كركوك ومقاطعة تازة. يشير البحث الى ان الحالة البيئية تبدو أكثر صحة في فصل الشتاء وذلك تبعاً للظروف الجوية والنشاط الاجتماعي والاقتصادي للإنسان بالإضافة الى ان البحث يظهر العلاقة الرئيسية بين الصحة البيئية والنشاط البشري في مختلف الظروف الجوية.

الكلمات المفتاحية: البيئة، المؤشر البيئي، طريقة *PSR*، مؤشر الاستجابة، صور سينتنال-٢.

1. Introduction:

Over the past fifty years, the Ecological Index has become a crucial policy tool for efficient environmental management and pollution control [1]. The region's eco-environmental quality is crucial for sustainable socioeconomic development, ensuring harmony between social production and living environment, and assessing its ability to sustain long-term growth [2]. The natural environment is crucial for the survival and progress of humanity, as it provides vital resources such as water, land, biological resources, and climate [3]. Remote sensing technology is crucial for ecological monitoring in developing countries due to its comprehensive and dynamic compliance with environmental changes [4]. On the other hand, The PSR model highlights the impact of human activities on ecosystem health, including social pressures and resource depletion, highlighting the significant role of human activities [5]. An ecosystem's health status is determined by its vitality, structure, and resilience, while response indicators show how it reacts to changes caused by human activities and the ecosystem itself [6]. Factors like soil temperature, land use, vegetation, heat, soil texture, and aridity influence plant growth, impacting the entire ecosystem if disturbances occur [7]. Changes in land use, such as residential

expansion, can lead to increased environmental conditions. However, manmade and natural factors, such as population growth and economic development, also influence these variations [8]. Land use and cover maps are vital for improving our comprehension of environmental modeling and water management [9]. Theories on health, safety, well-being, residential contentment, and urban environment are derived from historical similar researches and decision-making in urban areas [10]. This study evaluates the eco-environmental system in Kirkuk City and Taza District, focusing on its impact on the impact of human activities and weather condition on the ecological health. It compares five ecological responses in winter 2023, preparing for serious measures.

2. Materials and methods:

2.1. Study area: Figure 1 shows Kirkuk city and Taza District which are situated in the northwestern region of Iraq. It is bordered by the Zagros Mountains to the north, the Hamrin Mountains to the south, the Lower Zab Mountains to the west, and Al-Sulaymaniyah City to the east. Kirkuk City is located at a latitude between 35°13' and 36°29' N and a longitude between 44°00' and 44°50' E. The city has a total size of around 9,679 km2 [11] . The research area experiences a semiarid and Mediterranean climate with hot summers and cold winters, with a heavy precipitation peak from December to March [9]. Temperature plays a significant role in the climate which drops to a low of -1 °C in the winter. The city of Kirkuk is situated in the hilly northern part of the Kirkuk plain, approximately 340-360 meters above sea level.

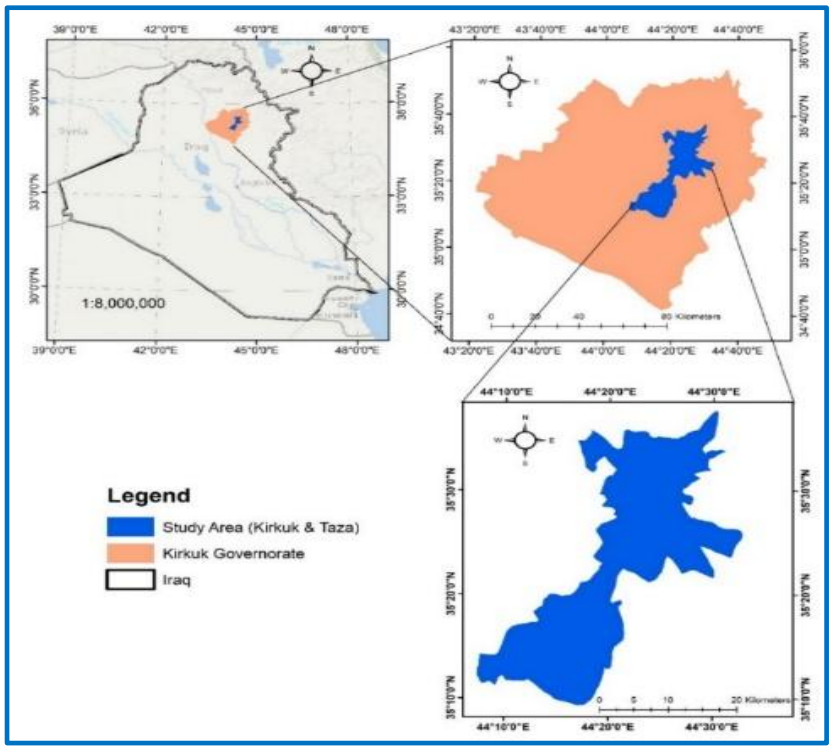

Figure 1: The Study Area of Kirkuk City and Taza District.

2.2. Data and pre-processing

2.2.1. Data used: The study utilized Sentinel-2 data, specifically level-2A images, from a multispectral sensor with 13 channels, ranging from 10 to 60 meters (image details in Table 1). All images were downloaded for free from the Copernicus website (a part of the European Union's space program) with a cloud coverage of less than 2%.

Table 1: Band details of sentinel two satellite image

Bands (wavelength region)	*Central wavelength (nm)*	*Resolution (m)*
Band-1 (coastal aerosol)	443	60
Band-2 (blue)	490	10
Band-3 (green)	560	10
Band-4 (red)	665	10
Band-5 (vegetation red edge)	705	20
Band-6 (vegetation red edge)	740	20
Band-7 (vegetation red edge)	783	20
Band-8 (NIR)	842	10
Band-8A (vegetation red edge)	865	20
Band-9 (water vapour)	945	60
Band-10 (SWIR-Cirrus)	1375	60
Band-11 (SWIR)	1610	60
Band-12 (SWIR)	2190	20

2.2.2. Data Pre-processing: The Bilinear interpolation method was used to resample photos, enhancing their quality and visual appeal. Geometric and atmospheric corrections were not made, as the images are already corrected for surface reflectance. The ortho-images, or granules, have dimensions of 110x110 square kilometers and are projected using the UTM/WGS84 coordinate system as well as registered.

2.3.Methods: The method adopted in this study to obtain the ecological index uses the pressure-state-response (PSR) framework, which utilizes nine indicators to determine the Pressure indicator and three to assess the State indicator. All indicators were obtained using SNAP 9.0.0 software and were output using ArcGIS 10.7 software. The equations were applied using GIS 10.7 software. On the other hand, the Pressure Indicators were including of Digital Elevation Model (DEM), Global Environmental Monitoring Index (GEMI), Land Use/Cover (LULC), Normalized Difference Moisture Index (NDMI), Normalized Difference Water Index (NDWI), Soil Adjusted Vegetation Index (SAVI), Road network and Railway network, Land Surface Temperature (LST). The state indicators were included from Fractional Vegetation Cover (FVC), Normalized Leaf Area Index (LAI), and Normalized Difference Vegetation Index (NDVI). To ensure that each indication has a comparable weight and significance in the outcome, all indicators were rescaled and normalized from 0 to 1. The overall methodology is explained in Figure 2.

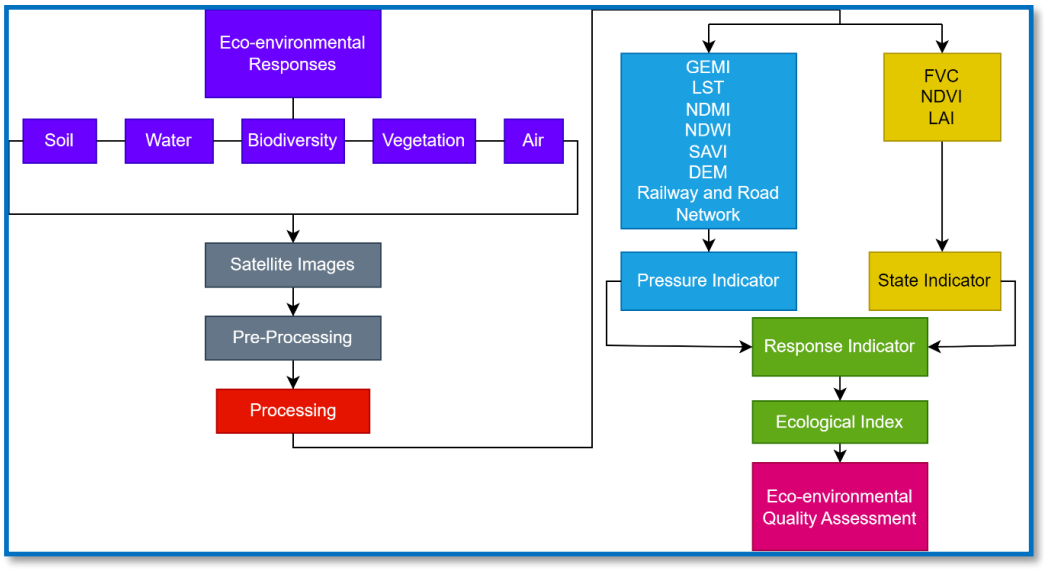

Figure 2: The Overall Methodology

2.3.1. Indicators used:

1. Global Environmental Monitoring Index (GEMI): GEMI is a nonlinear vegetation index derived from satellite data used for global environmental monitoring, more resistant to atmospheric influences than NDVI, ranging from 0 to 1, where 0 indicates the absence of plant cover and 1 indicates complete vegetation c(2.3over on the ground [12]. **Figure 3** shows the GEMI.
2. Fractional vegetation cover (FVC): is a crucial measure for understanding soil erosion, climate change, and ecosystem balance. It measures plant arrangement on Earth's surface, ranging from 0 to 1, with 0 indicating no vegetation and 1 indicating complete cover [13]. **Figure 4** shows the obtained FVC.
3. Leaf Area Index (LAI): is a dimensionless number used to characterize plant canopies, ranging from 0 to 10, indicating the presence of dense conifer forests [14]. **Figure 5** shows the LAI.
4. Normalized Difference Moisture Index (NDMI): This index is not standardized. The index, ranging from -1 to 1, is easily comprehensible and indicates a higher level of vegetation health and density [15]. The dry matter content of leaves is highly correlated with the NDMI indices [16]. **Figure 6** shows the NDMI.
5. Normalized Difference Vegetation Index (NDVI): Sensor data is used to measure plant density and health, with values ranging from -1 to 1, indicating greater vegetation abundance and density [15]. The index reduces or deletes characteristics with low red light and near-infrared reflectance, like water, while amplifying those with high NIR reflectance and lower red light reflectance, like terrestrial vegetation [17]. **Figure 7** shows the NDVI.

6.Normalized Difference Water Index (NDWI): Sensor data quantifies vegetation density and health using near-infrared and red wavelengths. Higher values indicate healthier vegetation. NDWI can provide information on liquid water content, although spectrum-matching techniques aren't suitable for determining vegetation water content [18]. **Figure 8** shows the NDWI.

7. Railway and road network: Human activity impacts ecosystems by examining road and rail networks, infrastructure, and utility systems. Increased modifications indicate higher frequency of activity. Population density correlates with larger roads, facilitating more frequent transportation. Road data in the research region includes primary, secondary, residential, and local roadways [7]. The increase in traffic brought on by projects could be offset by further highway funding [19]. The estimated railway and road networks are shown in **Figure 9**, where (A) is the road network map and (B) is the railway network map.

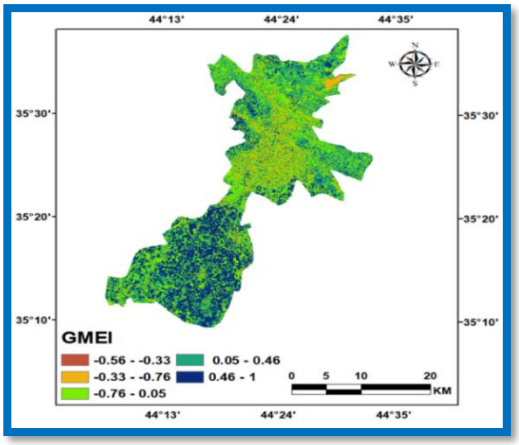

Figure 3: GEMI of Winter 2023.

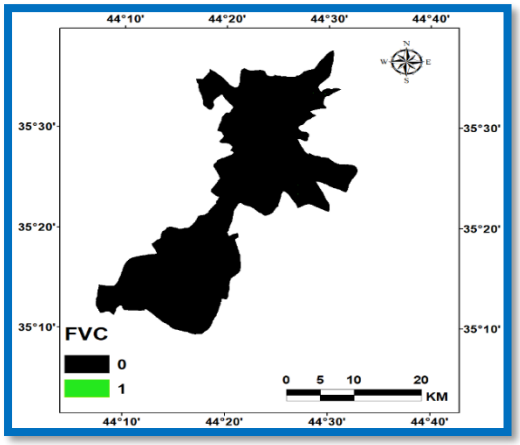

Figure 4: FVC of Winter 2023.

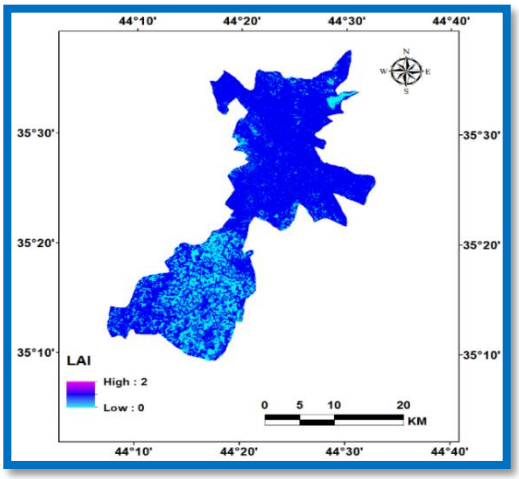

Figure 5: LAI of Winter 2023.

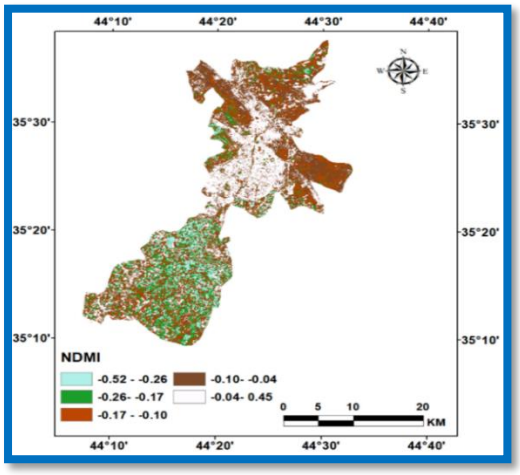

Figure 6: NDMI of Winter 2023.

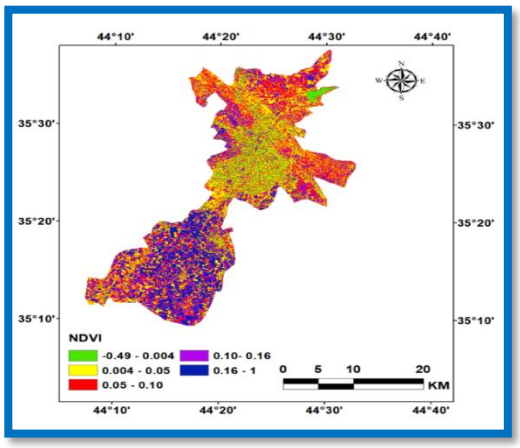

Figure 7: NDVI of Winter 2023.

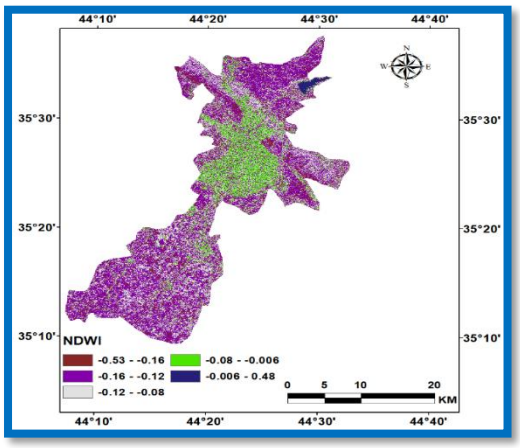

Figure 8: NDWI of Winter 2023.

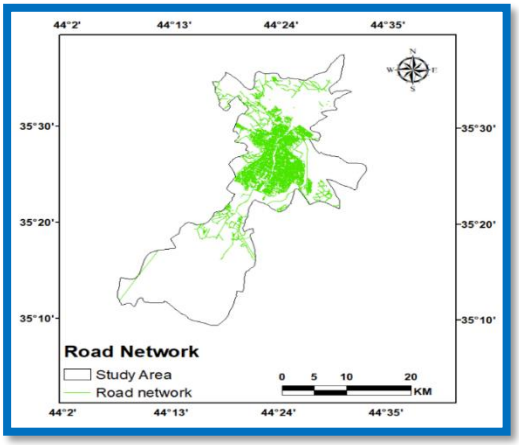

(A) Road network

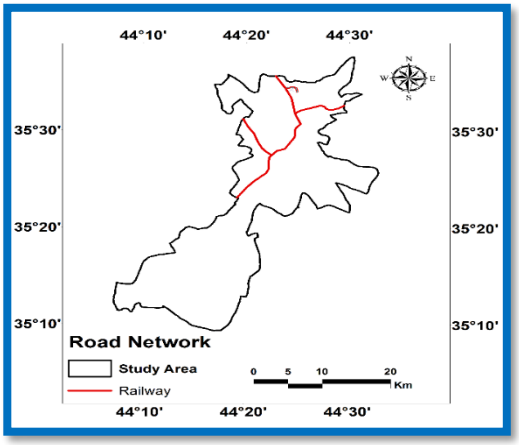

(B) railway network

Figure 9: Road Network and Railway Network

8.Land Use/Land Cover: Accurate land use and land cover data is crucial for urban planning, decision-making, population dynamics, and public health assessment [20]. Assessing land use and vegetation cover is crucial for urban planning and policy formulation due to growing structures and population spread in metropolitan areas [21]. Land inventories involve land use and land cover, crucial in climate models. Land use describes ecosystem function, social, economic, and cultural utility, requiring analysis of socioeconomic activities in the location [22]. The Support Vector Machine (SVM) classification method was used to obtain classes represented by urban areas, water bodies, barren areas, agricultural areas, and vegetation. The classification is shown in **Figure 10**.

9.Soil-Adjusted Vegetation Index (SAVI): Land inventories involve land use and land cover, crucial in climate models. Land use describes ecosystem function, social, economic, and cultural utility, requiring analysis of socioeconomic activities in the location [23]. It has significantly improved the development of global models that accurately describe dynamic soil-vegetation systems using remotely sensed data [24]. **Figure 11** shows the SAVI.

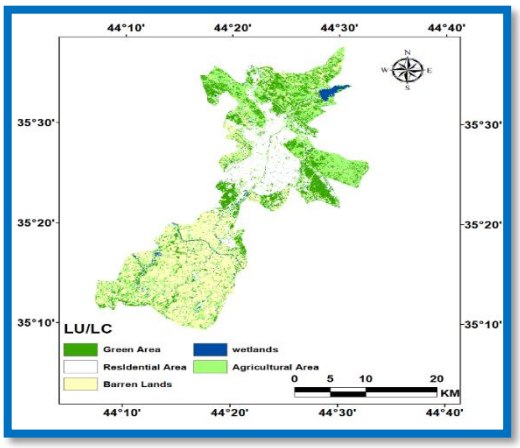

Figure 10: LULC of Winter 2023.

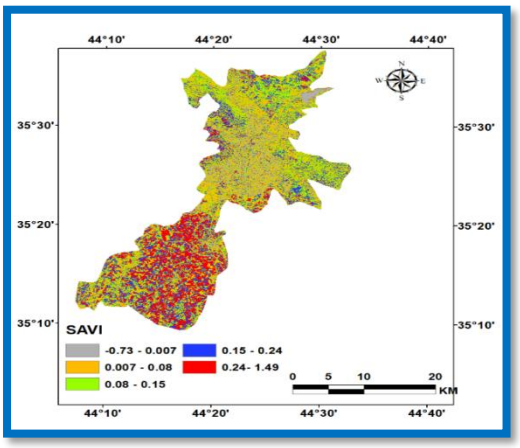

Figure 11: SAVI of Winter 2023.

10 . Digital Elevation Model (DEM): A digital elevation model (DEM) is a crucial spatial resource in GIS, representing terrain through a collection of digital data indicating ground elevation (spot height) [25]. Topography significantly impacts water balance in catchments, affecting surface and subsurface runoff, water movement, and routes. Fully distributed hydraulic and hydrological models use topography, represented by the Digital Elevation Model, to establish bathymetry [26]. The DEM that was used in this study is represented in Figure 12.

11. Land Surface Temperature (LST): Remotely sensed land surface temperature (LST) is intriguing for biological and environmental purposes due to challenges in weather observatories, field surveys, and data interpolation [27]. Land surface temperature (LST) is a crucial parameter in land-surface models, influencing turbulent heat exchanges and long-wavelength radiation at the ground-atmosphere interface, affecting aridity, soil moisture, and evapotranspiration [28]. It is directly correlated with the development and distribution of vegetation and the cycle of evaporation of surface water resources [29]. Figure 13 shows the obtained LST.

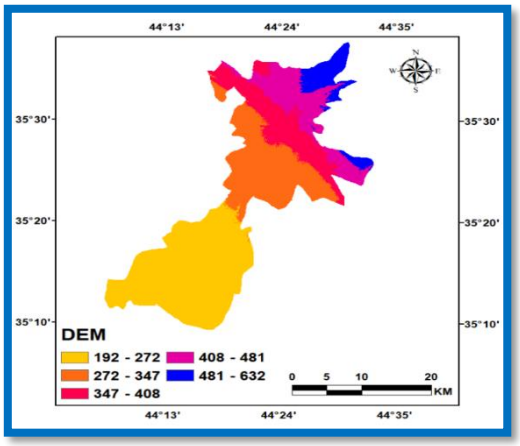

Figure 12: Digital Elevation Model (in meters) of Kirkuk City and Taza District

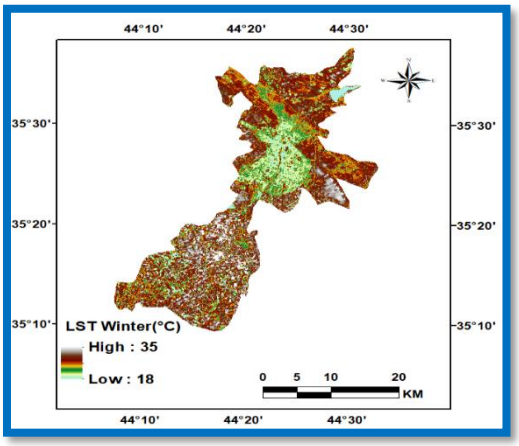

Figure 13: LST of Winter 2023.

2.3.2. PSR framework: The Pressure-State-Response concept explains how human activities impact the environment, providing more comprehensive information than two-dimensional indicator sets, using three categories: Pressure Indicator, State Indicator, and Response Indicator [30]. The dynamic and systematic interactions between the economic, social, and ecological environments can be reflected in the three dimensions of the PSR framework [31]. Depending on the concerns or progress that need to be looked at, a PSR framework's indicators can be chosen accordingly. There wouldn't be a standard set of indicators, and the choices might differ depending on the nation or the location. Data accessibility is still another crucial factor [32].

2.3.2.1. Pressure indicator (PI): Human activity's impact on ecosystem health is described using pressure indicators like social and resource demands [33]. the PI value from standardized data ranges from 0 to 1, giving each indicator in the research region equal weight, as shown in Eq. (1) [7].

$$PI = \frac{GEMI + SAVI + NDMI + LULC + Road + Rail + LI + NDWI + DEM}{9} \quad (1)$$

2.3.2.2. State indicator (SI): State indicators accurately represent an ecosystem's current health status by assessing its robustness, structure, and adaptability [33]. Healthy natural phenomena, such as NDVI, LAI, FVC, forests, mangroves, wetland wetlands, and waterbodies, are generally indicative of healthy ecosystems. All parameters were first standardized from a range of 0 to 1 and then given equal weight as per Eq. (2) to generate the state indicator. Higher SI values suggest improved ecological circumstances, while lower values indicate deteriorating ecological conditions [7].

$$SI = \frac{(NDVI + LAI + FVC)}{3} \quad (2)$$

2.3.2.3. Response indicator (RI): Response indicators depict an ecosystem's response to changes in its overall well-being, encompassing human activities and internal processes [33]. Response indicators indicate high-pressure conditions, indicating ecological disruption, while low reaction indicators suggest stable conditions with minimal changes due to lower demand, indicating sustainable development and controlled ecology, contrasting with elevated reactions suggesting significant environmental changes. RI can be calculated from the Eq. (3) [7].

$$RI = PI - SI \quad (3)$$

2.3.2.4. Calculation of EI: The ecological index significantly influences ecological quality assessment due to its consistency with average values within intervals, and normalizing it during calculation is crucial due to inconsistent dimensions [34]. EI can be calculated from Eq.

(4), where EI is an ecological indicator, and w and c represent the weight and standardized data [7].

$$EI = \sum_{i=1}^{n} W * C \quad (4)$$

By using all the ecological response parameters, the ecological indicator was calculated in this paper from Eq. (5).

$$EI = w(environment) + w(climate) + w(soil\ moisture) + w(greenness) + w(LCLU) + w(artificial\ features\ \&\ energy) + w(water\ content) + w(landscape) \quad (5)$$

Where the Environmental parameter refers to the global environmental monitoring index (GEMI); Climate parameter: Soil moisture: soil adjusted vegetation index (SAVI) and normalized difference moisture index (NDMI); Greenness: normalized difference vegetation index (NDVI), leaf area index (LAI), fractional vegetation cover (FVC); Land use/land cover: LULC change; Artificial features and energy: Road network, Railway network; Water content: normalized difference water index (NDWI); Landscape: digital elevation model (DEM).

The study analyzes the Eco-environmental quality assessment (EEQ) using the pressure-state-response (PSR) approach and describes the Ecological Index (EI) of winter 2023.

3. Results:

3.1.General assessment of PSR

3.1.1. Pressure indicator: The PI is a measure of atmospheric pressure in urbanized areas, with high levels observed in developed areas. The central region of Kirkuk city experiences high pressure, while surrounding villages experience mild pressure due to lower socio-economic activities. The PI is positively correlated with population size and negatively correlated when population decreases as shown in Figure 14.

3.1.2. State indicator: The SI is mostly derived from the measurements of FVC, NDVI, and LAI. As a result of the humid winters in Kirkuk City, the vegetation was in excellent condition. The southwestern portion of the research region has dense vegetation, resulting in comparatively higher NDVI values towards the south. Given that both FVC and LAI serve as indicators of robust vegetation, they exhibited a similar NDVI pattern. The ultimate SI map, depicted in Figure 15, exhibits the combined influence of all vegetative indices. The SI exhibits consistently high values in both seasons.

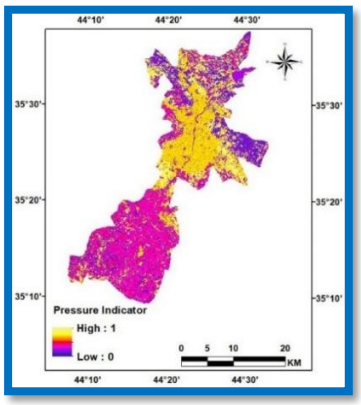

Figure 14: PI of Winter 2023.

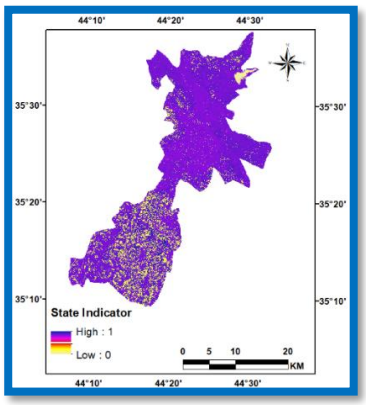

Figure 15: SI of Winter 2023.

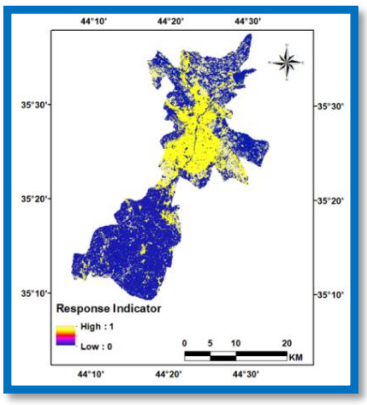

Figure 16: RI of Winter 2023.

3.1.3. Response indicator: Under significant anthropogenic strain, ecological conditions that are weaker, unhealthy, and unstable are indicated by strong reaction indicators, and conversely. Elevated RI values are symptomatic of heightened natural/human pressure and socioeconomic activity, such as industrial expansion, farming, and urban growth, which can lead to ecological disruption. Low RI values indicate less human involvement in ecosystems, including green fields, aquatic bodies, and remote areas far from metropolitan centers. According to the RI maps, the ecological status is consistently progressing, as seen in **Figure 16**. The study suggests that the southern part of the area possesses more favorable ecological traits in comparison to its central section. The data suggests that the resilience index (RI) for the agriculture and cultivation sectors was lower compared to the RI for socioeconomic activity locations.

3.2. Ecological Index: Elevated EI levels imply an ecological ecosystem that is strong and expanding, while lower values indicate the opposite. **Figure 17** shows a study region with a moderate to high EI value. The northeastern and eastern areas of the research region exhibit slightly superior conditions compared to other sections, as they display the greatest values concentrated around Khasa and in close proximity to Sulaymaniyah city towards the east. Human activity intensifies in the center region of the study area. Consequently, the central area of Kirkuk City has the lowest values spread out over a significant distance. The southern and southwestern regions of the research area, where Taza is situated, exhibit a moderate EI value, as depicted in Figure 17. The spatial distribution of EI maps indicates that the regions in close proximity to water bodies had exceptional EI conditions, while the adjacent area displayed a range of EI conditions from excellent to moderate. There were several industrial and residential regions characterized by suboptimal ecological conditions. The northern part of the research area has a high level of ecological condition, ranging from good to exceptional. In contrast, the southern part of the area shows a moderate level of ecological condition, ranging from good to

acceptable. Table 2 displays assessments and their respective regions derived from Figure 17. In contrast to the Taza district, the central area of the research region and Kirkuk City exhibit ecological conditions ranging from fair to bad. This highlights the urgent need for an intervention by a responsible and responsive ethics commission to address this significant problem.

Table 2: Evaluations and their Corresponding Areas.

Evaluation	*Corresponding area (km^2)*
Extreme excellent – excellent	229.3
Excellent – good	142.5
Good – fair	165.93
Fair – poor	97.36
Poor – bad	44.65

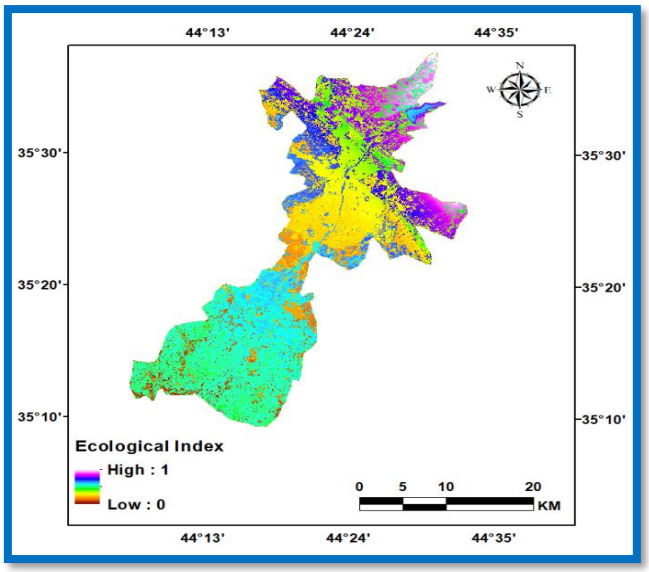

Figure 17: EI of Winter 2023.

4. Discussion

This research aims to identify and measure the ecological index to support the Environmental Quality Evaluation (EEQ) in Kirkuk City, Iraq. The Environmental Index (EI) is considered the most precise measure for evaluating the environmental state. GIS and remote sensing technologies are used to monitor environmental quality in areas like Kirkuk City, Iraq. The study uses time series remote sensing satellite data and the PSR framework to develop 12 indicators related to environmental concerns. The assessment considers land use/cover change, human and natural pressure, the environment's condition, and ecosystem health. The study also examines the role of the vegetative ecosystem in reducing pressure indicators and protecting the environment. The study identifies areas that have been safeguarded by the government to conserve the environment and minimize human activities. The findings are significant for

NGOs, government policymakers, and individuals interested in sustainable development due to their wide-ranging applications.

5. Conclusions

This research utilizes GIS and remote sensing data to assess the eco-environmental status. It achieves this by calculating the primary ecological indicators within the PSR framework in order to control the EEQ. The EI effectively evaluates the condition of the study region by employing a range of indicators that measure different influences on the environmental system. The study identifies that dryness and high temperatures have detrimental effects on the environment, while indicators of greenness and wetness have a positive impact. The improvement in EEQ (Environmental Quality Index) is dependent on the positive values observed in natural responses. Human activity, especially social and economic activities, significantly impacts the ecological health by causing harm to the system.

6. References

[1] X. Wang, Y. Cao, X. Zhong, and P. Gao, "A New Method of Regional Eco-environmental Quality Assessment and Its Application," *J. Environ. Qual.*, vol. 41, no. 5, pp. 1393–1401, 2012, doi: 10.2134/jeq2011.0390.

[2] H. Ma and L. Shi, "Assessment of eco-environmental quality of Western Taiwan Straits Economic Zone," *Environ. Monit. Assess.*, vol. 188, no. 5, 2016, doi: 10.1007/s10661-016-5312-5.

[3] A. M. Duda and M. T. El-Ashry, "Addressing the global water and environment crises through integrated approaches to the management of land, water and ecological resources," *Water Int.*, vol. 25, no. 1, pp. 115–126, 2000, doi: 10.1080/02508060008686803.

[4] J. Li, Y. Pei, S. Zhao, R. Xiao, X. Sang, and C. Zhang, "A review of remote sensing for environmental monitoring in China," *Remote Sens.*, vol. 12, no. 7, pp. 1–25, 2020, doi: 10.3390/rs12071130.

[5] S. Das, B. Pradhan, P. K. Shit, and A. M. Alamri, "Assessment of wetland ecosystem health using the pressure-state-response (PSR) model: A case study of Mursidabad District of West Bengal (India)," *Sustain.*, vol. 12, no. 15, 2020, doi: 10.3390/SU12155932.

[6] J. Xiong, W. Li, H. Zhang, W. Cheng, C. Ye, and Y. Zhao, "Selected environmental assessment model and spatial analysis method to explain correlations in environmental and socio-economic data with possible application for explaining the state of the ecosystem," *Sustain.*, vol. 11, no. 17, 2019, doi: 10.3390/su11174781.

[7] M. S. Boori, K. Choudhary, R. Paringer, and A. Kupriyanov, "Eco-environmental quality assessment based on pressure-state-response framework by remote sensing and GIS," *Remote Sens. Appl. Soc. Environ.*, vol. 23, no. April, p. 100530, 2021, doi: 10.1016/j.rsase.2021.100530.

[8] R. Sun *et al.*, "Effects of land-use change on eco-environmental quality in Hainan Island, China," *Ecol. Indic.*, vol. 109, no. 4, p. 105777, 2020, doi: 10.1016/j.ecolind.2019.105777.

[9] M. A. Shareef, N. D. Hassan, S. F. Hasan, and A. Khenchaf, "Integration of sentinel-1A and sentinel-2B data for land use and land cover mapping of the Kirkuk governorate, Iraq," *Int. J. Geoinformatics*, vol. 16, no. 3, pp. 87–96, 2020.

[10] M. Pacione, "Urban environmental quality and human wellbeing - A social geographical perspective," *Landsc. Urban Plan.*, vol. 65, no. 1–2, pp. 19–30, 2003, doi: 10.1016/S0169-2046(02)00234-7.

[11] V. F. Salahalden, M. A. Shareef, and Q. A. A. Nuaimy, "Red Clay Soil Physical and Chemical Properties Distribution Using Remote Sensing and GIS Techniques in Kirkuk City, Iraq," *Iraqi Geol. J.*, vol. 57, no. 1, pp. 194–220, 2024, doi: 10.46717/igj.57.1A.16ms-2024-1-27.

[12] A. B. Pinty, M. M. Verstraete, S. Vegetatio, N. Jul, and B. Pinty, "GEMI : A Non-Linear Index to Monitor Global Vegetation from Satellites GEMI : a non-linear index to monitor global vegetation from satellites," *Vegetatio*, vol. 101, no. 1, pp. 15–20, 2011.

[13] D. Chu, *Fractional vegetation cover, or FVC, is a crucial metric in the study of soil erosion, climate change, and ecosystem balance. It is frequently employed in the assessment and tracking of vegetation degradation and desertification. The only practical method*. 2019. doi: 10.1007/978-981-13-7580-4.

[14] H. Fang, F. Baret, S. Plummer, and G. Schaepman-Strub, "An Overview of Global Leaf Area Index (LAI): Methods, Products, Validation, and Applications," *Rev. Geophys.*, vol. 57, no. 3, pp. 739–799, 2019, doi: 10.1029/2018RG000608.

[15] S. Rahman and V. Mesev, "Change vector analysis, tasseled cap, and NDVI-NDMI for measuring land use/cover changes caused by a sudden short-term severe drought: 2011 Texas event," *Remote Sens.*, vol. 11, no. 19, 2019, doi: 10.3390/rs11192217.

[16] O. Strashok, M. Ziemiańska, and V. Strashok, "Evaluation and Correlation of Sentinel-2 NDVI and NDMI in Kyiv (2017-2021)," *J. Ecol. Eng.*, vol. 23, no. 9, pp. 212–218, 2022, doi: 10.12911/22998993/151884.

[17] S. K. McFeeters, "NDWI BY McFEETERS," *Remote Sens. Environ.*, vol. 25, no. 3, pp. 687–711, 1996.

[18] X. Wang, Y. Yan, and Y. Cao, "Impact of historic grazing on steppe soils on the northern Tibetan Plateau," *Plant Soil*, vol. 354, no. 1–2, pp. 173–183, 2012, doi: 10.1007/s11104-011-1053-y.

[19] A. C. Neri, P. Dupin, and L. E. Sánchez, "A pressure-state-response approach to cumulative impact assessment," *J. Clean. Prod.*, vol. 126, no. April, pp. 288–298, 2016, doi: 10.1016/j.jclepro.2016.02.134.

[20] S. F. Hasan, M. A. Shareef, and N. D. Hassan, "Speckle filtering impact on land use/land cover classification area using the combination of Sentinel-1A and Sentinel-2B (a case study of Kirkuk city, Iraq)," *Arab. J. Geosci.*, vol. 14, no. 4, 2021, doi: 10.1007/s12517-021-06494-9.

[21] M. A. Shareef, M. H. Ameen, and Q. M. Ajaj, "Change detection and gis-based fuzzy ahp to evaluate the degradation and reclamation land of tikrit city, Iraq," *Geod. Cartogr.*, vol. 46, no. 4, pp. 194–203, 2020, doi: 10.3846/gac.2020.11616.

[22] A. Comber and M. Wulder, "Considering spatiotemporal processes in big data analysis: Insights from remote sensing of land cover and land use," *Trans. GIS*, vol. 23, no. 5, pp. 879–891, 2019, doi: 10.1111/tgis.12559.

[23] P. P. Rhyma, K. Norizah, O. Hamdan, I. Faridah-Hanum, and A. W. Zulfa, "Integration of normalised different vegetation index and Soil-Adjusted Vegetation Index for mangrove vegetation delineation," *Remote Sens. Appl. Soc. Environ.*, vol. 17, no. December 2019, p. 100280, 2020, doi: 10.1016/j.rsase.2019.100280.

[24] A. R. Huete, "A soil-adjusted vegetation index (SAVI)," *Remote Sens. Environ.*, vol. 25, no. 3, pp. 295–309, 1988, doi: 10.1016/0034-4257(88)90106-X.

[25] Q. Zhou, "Digital Elevation Model and Digital Surface Model," *Int. Encycl. Geogr.*, no. March, pp. 1–17, 2017, doi: 10.1002/9781118786352.wbieg0768.

[26] J. Vaze, J. Teng, and G. Spencer, "Impact of DEM accuracy and resolution on topographic indices," *Environ. Model. Softw.*, vol. 25, no. 10, pp. 1086–1098, 2010, doi: 10.1016/j.envsoft.2010.03.014.

[27] M. Neteler, "Estimating daily land surface temperatures in mountainous environments by reconstructed MODIS LST data," *Remote Sens.*, vol. 2, no. 1, pp. 333–351, 2010, doi: 10.3390/rs1020333.

[28] G. C. Hulley, D. Ghent, F. M. Göttsche, P. C. Guillevic, D. J. Mildrexler, and C. Coll, *Land Surface Temperature*. 2019. doi: 10.1016/B978-0-12-814458-9.00003-4.

[29] W. Ren, X. Zhang, and H. Peng, "Evaluation of Temporal and Spatial Changes in Ecological Environmental Quality on Jianghan Plain From 1990 to 2021," *Front. Environ. Sci.*, vol. 10, no. May, pp. 1–14, 2022, doi: 10.3389/fenvs.2022.884440.

[30] B. Wolfslehner and H. Vacik, "Evaluating sustainable forest management strategies with the Analytic Network Process in a Pressure-State-Response framework," *J. Environ. Manage.*, vol. 88, no. 1, pp. 1–10, 2008, doi: 10.1016/j.jenvman.2007.01.027.

[31] J. Ji and J. Chen, "Urban flood resilience assessment using RAGA-PP and KL-TOPSIS model based on PSR framework: A case study of Jiangsu province, China," *Water Sci. Technol.*, vol. 86, no. 12, pp. 3264–3280, 2022, doi: 10.2166/wst.2022.404.

[32] H. F. Huang, J. Kuo, and S. L. Lo, "Review of PSR framework and development of a DPSIR model to assess greenhouse effect in Taiwan," *Environ. Monit. Assess.*, vol. 177, no. 1–4, pp. 623–635, 2011, doi: 10.1007/s10661-010-1661-7.

[33] D. Liu and S. Hao, "Ecosystem health assessment at county-scale using the pressure-state-response framework on the loess plateau, China," *Int. J. Environ. Res. Public Health*, vol. 14, no. 1, 2017, doi: 10.3390/ijerph14010002.

[34] R. Sensing and E. Index, "Evaluation of the Spatiotemporal Variations in the Eco-environmental Quality in China Based on the Remote Sensing Ecological Index," *Remote Sens.*, 2020.

Al-Kitab Journal for Pure Sciences (2025); 9(2):169-180.
https://doi.org/10.32441/kjps.09.02.p11

Al-Kitab Journal for Pure Sciences
ISSN: 2617-1260 (print), 2617-8141(online)

https://isnra.net/index.php/kjps

Synthesis, Characterization, and CO2 Capture Application of Cu(II)-paracetamol complex

Mohanad Ali Sultan

Department of Chemical Engineering, College of Engineering, University of Diyala, Baqubah, Iraq

*Corresponding Author: maalazzawi85@uodiyala.edu.iq

Citation: Sultan MA. Synthesis, Characterization, and CO2 Capture Application of Cu(II)-paracetamol complex. Al-Kitab J. Pure Sci. [Internet]. 2025 Sep. 07;9(2):169-180. DOI: https://doi.org/10.32441/kjps.09.02.p11

Keywords: Cu(II), Paracetamol, CO_2 Capture, Metal Complexes , Tridentate Ligand.

Article History

Received	26 Jun.	2025
Accepted	31 Jul.	2025
Available online	08 Sep.	2025

Abstract:

A cu(II)-paracetamol complex was synthesized and characterized using UV-Vis and FTIR spectroscopy and melting point analysis. The ligand paracetamol acted as a tridentate chelating agent, coordinating through the hydroxyl, carbonyl, and amine groups. The complex was found to be more soluble in DMSO. Job's method of continuous variation suggested a 1:2 metal-to-ligand stoichiometry. The synthesized Cu(II) complex was evaluated for CO_2 adsorption performance, demonstrating promising uptake capacity due to the strong affinity of the metal center for CO_2 molecules.

Keywords: Cu(II), Paracetamol, CO_2 Capture, Metal Complexes, Tridentate Ligand.

تحضير، توصيف، وتطبيق احتجاز ثاني أكسيد الكربون لمعقد النحاس-باراسيتمول

الخلاصة:

تم تحضير وتوصيف معقد-Cu(II) باراسيتامول باستخدام أطياف الأشعة فوق البنفسجية-المرئية (UV-Vis) وتقنية الأشعة تحت الحمراء (FTIR) بالإضافة إلى تحليل نقطة الانصهار. عمل الباراسيتامول كـ ليغند ثلاثي السن، منسقاً من خلال مجموعات الهيدروكسيل والكربونيل والأمين. وُجد أن المعقد أكثر ذوبانية في DMSO. أظهرت طريقة جوب للتغير المستمر أن نسبة المعدن إلى الليغند هي ١:٢. تم تقييم المعقد المحضر من Cu(II) من حيث أدائه في امتصاص غاز ثاني أكسيد الكربون، حيث أظهر قدرة امتصاص واعدة بسبب قوة التآلف العالية بين مركز المعدن وجزيئات CO_2.

الكلمات المفتاحية: Cu(II)، باراسيتامول، احتجاز ثاني أكسيد الكربون، المعقدات الفلزية، ليغند ثلاثي السن.

1. Introduction:

Paracetamol (acetaminophen) is a commonly used analgesic and antipyretic drug that has also gained attention in coordination chemistry [1] [2]. Paracetamol exhibits important ligand properties due to the presence of hydroxyl (-OH), amine (-NH_2), and carbonyl (C=O) groups, making it suitable for coordination with transition metals [3] [4]. These groups act as donor sites in chelation, forming stable complexes with various metal ions.

Copper(II) ions are particularly valuable in coordination chemistry due to their flexible geometry, strong Lewis acidity, and redox activity. Cu(II) complexes have shown monumental applications in catalysis, antibacterial agents, and environmental treatment [5]. When coordinated with multidentate ligands such as paracetamol, copper ions often adopt square planar or distorted octahedral geometries, depending on ligand field strength [6].

Copper(II) complexes of various ligands have demonstrated wide biology and catalytic applications due to the favorable redox behavior of cu(II) ions. Despite studies on Cu(II)-paracetamol complexes in biomedical and catalytic areas, their potential role in environmental applications- especially CO_2 capture- remains largely unexplored. This represents a critical research gap, especially given the global need for sustainable and cost-effective carbon dioxide sequestration technology [7].

Traditional adsorbents such as zeolites, activated carbon, and metal-organic frameworks (MOFs) are widely studied for CO_2 capture. However, challenges such as high cost, synthetic complexity, or recovery difficulty limit their broader usages [8] [9] [10]. Recent literature has shown the importance of exploring novel coordination complexes as functional CO_2 adsorbents. The strong Lewis acidity of Cu(II) and the formation of a polar surface upon complexation

make such materials promising for binding CO_2 through physisorption or chemisorption mechanisms [11] [12][13].

The objective of this study is to synthesize and characterize a Cu(II)-paracetamol complex, investigate its coordination manner, and evaluate its performance in CO_2 capture. A schematic representation of the expected coordination structure will later be provided in the Discussion section to clarify the binding mode between copper and paracetamol. The importance of this work demonstrates a simple, accessible, and functional coordination complex stemming from a pharmaceutical ligand for environmental CO_2 capture under mild conditions.

2. Material and methods:

Pure paracetamol ($C_8H_9NO_2$, 99% purity), melting point:(169°C) was obtained from Kendy Pharmaceuticals, $Cu(NO_3)_2.6H_2O$ analytical grade, methanol, and distilled water were used as solvents. The copper complex was synthesized by mixing 0.01 mol of $Cu(NO_3)_2.6H_2O$ dissolved in 100 ml of distilled water and 0.02 of paracetamol dissolved in 100 ml of methanol. The reaction mixture was mixed and stirred for 1 hour at room temperature (~25°C) and subsequently heated at 60 °C for 2 hours on a hot plate until all the solution was evaporated. A greenish-dark precipitate was formed, filtered using a Bucher funnel, and dried at ambient temperature. The obtained complex was characterized for thermal stability, color, and spectroscopic signatures [14].

FTIR spectra were recorded in the range of 400 -4000 cm^{-1} using KBr pellets (1:100 sample-to-KBr ratio). Spectra were collected for both the free ligand and the synthesized complex to identify shifts in functional group frequencies due to metal coordination. Additionally, UV-Visible spectra were obtained in the range of 200 -800 nm using methanol as solvent. Absorbance changes between free ligand and complex solutions were evaluated to confirm electronic transitions and coordination [15] [16]. Moreover, the Job's method of continuous variation was used to determine metal-to-ligand stoichiometry, where absorbance values at a fixed wavelength were plotted against mole fractions of paracetamol [17]. Gravimetric CO_2 adsorption experiments were conducted within a temperature range from 25 to 60 °C under 1 atm pressure, in which adsorbent mass and exposure time were kept constant, and uptake values were calculated in mmol/g. Additionally, as the entire process was done in the solid phase, PH control was not necessary.

3. Results:

The coordination of paracetamol with the Cu(II) ion was elucidated through Fourier Transform Infrared Spectroscopy (FTIR) and Ultraviolet-Visible (UV-Vis) Spectroscopy,

which are key techniques for confirming metal-ligand interactions and electronic transitions in coordination compounds [18]. Moreover, the Cu(II)-paracetamol complex showed observable CO_2 adsorption performance under room and increased temperatures. At 25 ^{0}C and 1 atm, the complex demonstrated a CO_2 uptake of 1.22 mmol/g, indicating moderate affinity toward CO_2. As the temperature increased, the adsorption capacity decreased to 0.95 mmol/g at 40 ^{0}C and 0.59 mmol/g at 60 ^{0}C, compatible with the exothermic nature of physisorption. The adsorption manner followed the Langmuir isotherm model, indicating monolayer surface coverage and confirming physical adsorption as the main mechanism [19] [20] [21]. The trend shows that the CO_2 capture is favorably achieved at lower temperatures. Compared to the standard adsorbents such as activated carbon and zeolites, the Cu(II)-paracetamol performs within a suitable range, highlighting its importance as an easy synthesis and a cost-effective material for CO_2 capture applications.

4. Discussion

The FTIR spectrum of free paracetamol revealed characteristic vibrational modes assigned to its functional groups for its structural identity and purity. The broad band around 3325 cm^{-1} is assigned to O-H stretching, which is typically appears in this region due to hydrogen bonding Additionally , a distinct sharp band at 3163 cm^{-1} corresponds to N-H stretching of the amine group, confirming the presence of an acetamide moiety in the molecule.

Another prominent peak observed at 1650 cm^{-1} is attributed to C=O (carbonyl) stretching of the amide functionality. This band is generally strong and sharp, supporting the presence of a conjugated amide system. The C-N bending and N-H bending vibrations typically appear between 1500-1580 cm^{-1} and indeed several medium-intensity bands are seen in that region, reinforcing the assignment of an acetamide structure.

Furthermore, peaks observed in the region of 1240-1020 cm^{-1} are consistence with C-O stretching vibrations from the phenolic group, and the out-of-plane C-H bending of the armoctic ring appears in the 750-840 cm^{-1} range.

These spectral features collectively confirm the presence of hydroxyl , amide, and aromatic functionalities in the paracetamol molecule. **Figure 1** shows the FITR spectrum of free paracetamol , clearly indicating all characteristic absorption bands discussed.

Upon complexation with Cu(II), significant shifts and changes in these absorption bands were observed in the FTIR spectrum of paracetamol, indicating coordination through multiple donor sites. Specifically, the O-H stretching band was shifted from 3325 cm^{-1} to approximately 3562 cm^{-1} in the complex, indicating involvement of the phenolic –OH group in direct

coordination to the metal center, albeit without full deprotonation. Furthermore, the N-H stretching band at 3163 cm^{-1} , which was clearly visible in the free paracetamol spectrum, completely disappeared from the spectrum of the Cu(II) complex. This disappearance supports the coordination of the amide nitrogen to the metal center via the lone pair donation, suggesting chelation through the nitrogen atom.

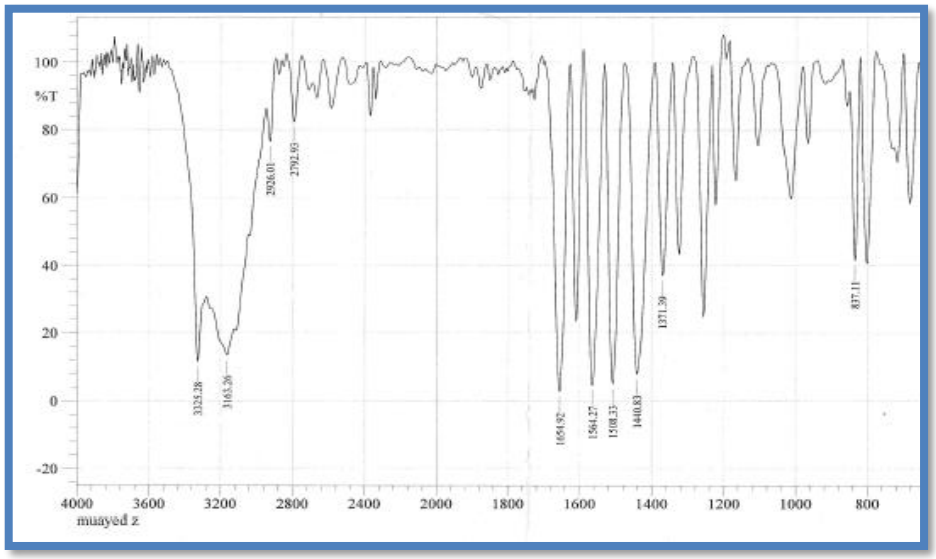

Figure 1: FTIR spectrum of pure paracetamol, showing characteristic absorption bands of functional groups present in the molecule

The C=O band, typically observed at 1650 cm^{-1}, was significantly shifted to a broader, less intensity region between 1614-1548 cm^{-1}. This red shift in the carbonyl vibration is characteristic of coordination via the carbonyl oxygen, which weakens the C=O bond due to electron delocalization toward the metal ion. Such behavior is well-known in the metal-amide complexes binding modes. Additional spectral changes were observed in the low-frequency region (<600 cm^{-1}) where new bands emerged that were absence in the spectrum of free paracetamol. These are assigned to M-O and M-N stretching vibrations, further confirming the formation of a metal-ligand coordination network.

Altogether, these spectral changes- namely the shift or disappearance of O-H, N-H, and C=O bands,and the appearance of metal-ligand vibrational modes - strongly confirm that paracetamol behaves as a tridentate ligand, binding through its hydroxyl oxygen, amide nitrogen, and carbonyl oxygen atoms. This coordination configuration forms a stable chelate with Cu(II), likely resulting in a six-membered chelate ring. **Figure 2** presents the FTIR spectrum of the Cu(II)-paracetamol complex, clearly showing the discussed changes and confirming successful complex formation.

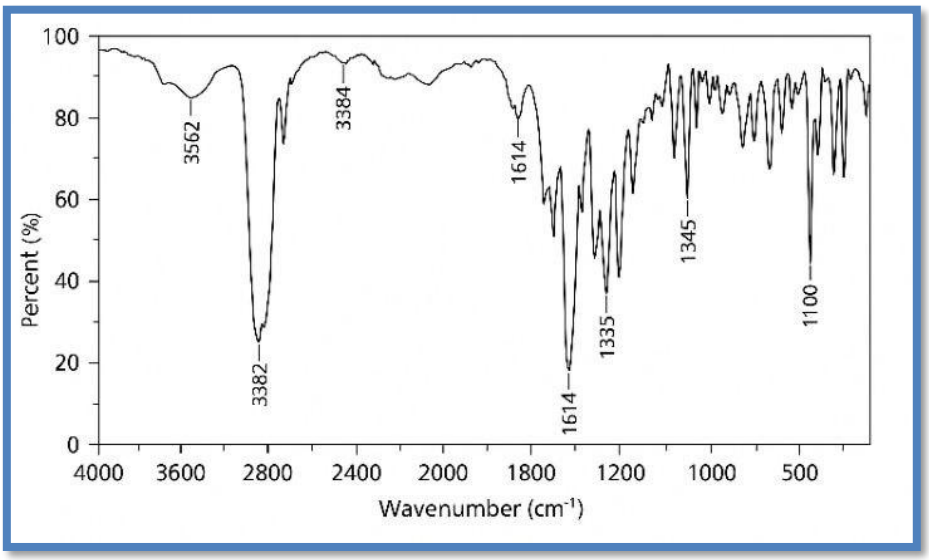

Figure 2:FTIR spectrum of pure Cu(II)-paracetamol complex, showing characteristic absorption bands. Key peaks indicate the presence of functional groups involved in complexation.

UV-Vis absorption spectrum of the free paracetamol ligand exhibited a prominent peak around ~243 nm, shown in **Figure 3**, which is associated with π → π* transitions of the aromatic ring system. These transition are characteristic of conjugated systems and provide evidence of the electronic configuration and aromatic character of the ligand. The band reflects the presence of delocalized π electrons in the phenyl ring of paracetamol and is often used as a fingerprint region for aromatic compounds.

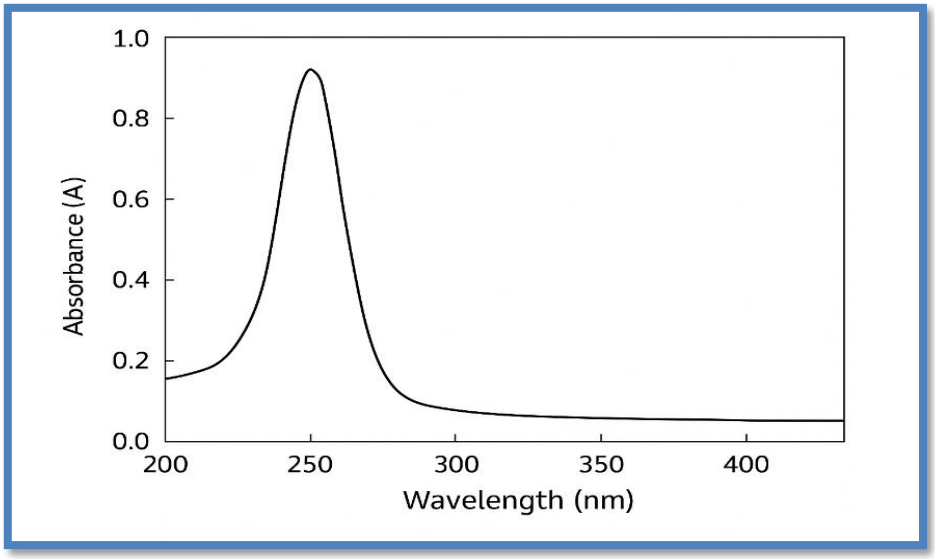

Figure 3: UV-Visible absorption spectrum of free paracetamol.

However, upon complexation with Cu(II), the absorption maximum (λ max) was red-shifted to approximately 340 nm, indicating a change in the electronic environment of the ligand due to metal coordination as depicted in **Figure 4**. This bathochromic shift is characteristic of n → π* transitions and ligand-to-metal charge transfer (LMCT) interactions, suggesting a strong

interaction between the lone pair electrons (particularly on oxygen and nitrogen atoms) and the Cu(II) metal center. Such transitions are indicative of delocalization of electron density across the metal-ligand framework, which is common in chelated systems involving transition metals. The presence of a d-d transition band observed near 580 nm was also observed in the visible region, often contributing to the distinctive greenish coloration of the complex. These electronic transitions are consistent with a distorted octahedral or square planar geometry, commonly adopted by Cu(II) complexes, depending on the ligand field strength and donor set.

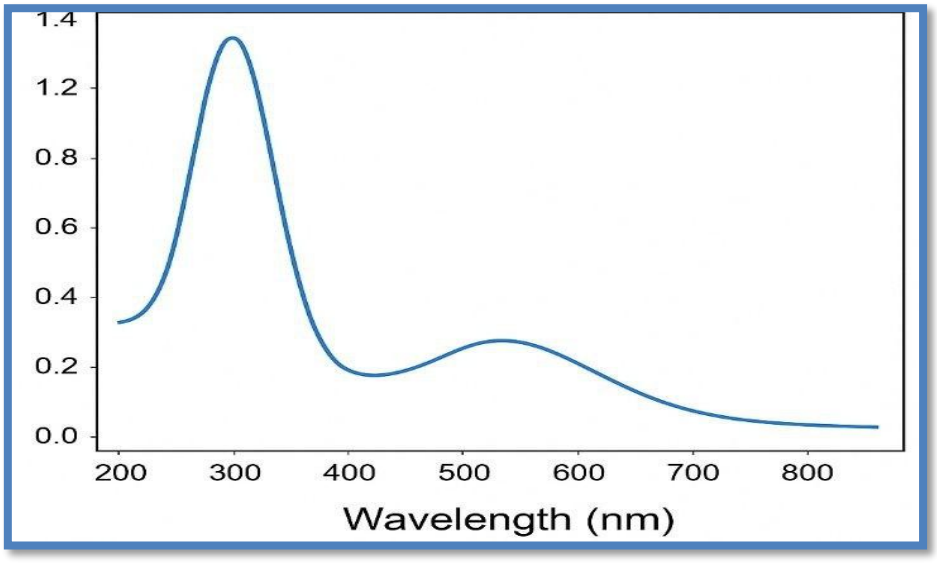

Figure 4: UV-Visible absorption spectrum of the copper-paracetamol complex recorded in the range of 200-800 nm

The plot of continuous variations (Job's method) provides important insights into the stoichiometry and complexation behavior between copper (II) and paracetamol in solution. The absorbance is plotted against the mole fraction of paracetamol to determine the binding ratio between the central ion and the ligand shown in **Figure 5**.

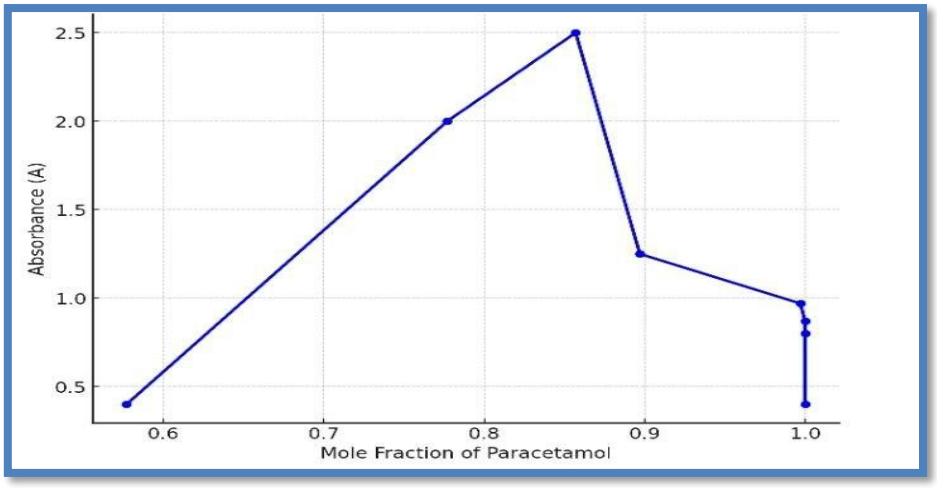

Figure 5: Jon's method plot showing the variation in absorbance of the Cu(II)-paracetamol complex with mole fraction of paracetamol, indicating a 1:2 metal-to-ligand stoichiometry at maximum absorbance (0.857 mole fraction)

The curve in **Figure 5** shows a distinct profile characterized by a gradual increase in absorbance as the mole fraction of paracetamol increases, reaching a maximum at about 0.857 mole fraction, followed by a successive decrease. The maximum absorbance peak is associated with the composition at which the molar ratio of approximately 1:2 metal-to-ligand ratio, suggesting that each copper ion binds with two molecular units of the ligand. Such stoichiometric data are consistent with prior works on Cu(II)-paracetamol complex **[22] [23],** and the proposed coordination environment is further supported by FTIR and UV-Visible. Spectroscopic findings. The ligand-to-metal ratio indicates a strong interaction between the phenolic, amide, and carboxylate groups of paracetamol, possibly forming an octahedral coordination environment. To support the Job's plot data, **Figure 6** illustrates a schematic bonding diagram of the proposed Cu-paracetamol complex, confirming the tridentate configuration. This structural presentation is crucial for correlating spectroscopic changes with the complex geometry.

The decline in absorbance beyond the 0.857 mole fraction indicates that excess paracetamol does not contribute to further complex formation. Instead, it may give rise to ligand saturation. This means that free paracetamol stays unbound in solution and does not produce the UV-Visible absorbing complex. Therefore, the overall absorbance is decreased due to the dilution of the complex concentration.

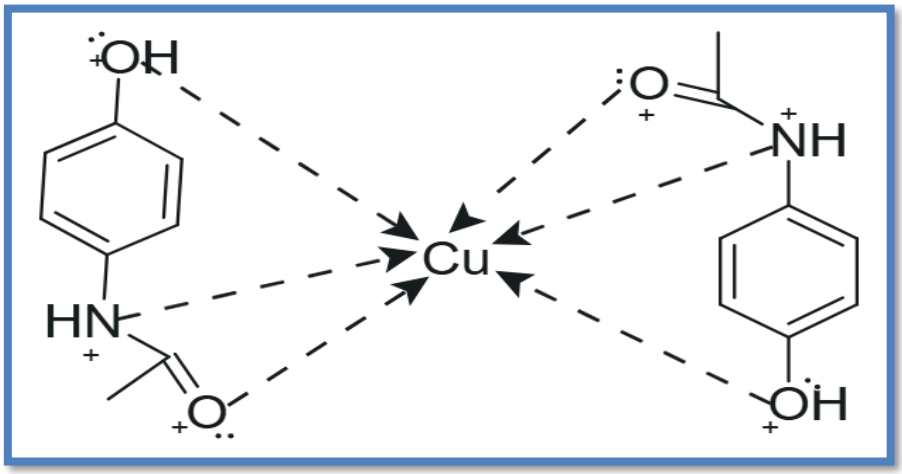

Figure 6: Proposed structure of the Cu(II)-paracetamol complex showing tridentate coordination by each paracetamol ligand through the phenolic-OH, amide nitrogen, and carbonyl oxygen, resulting in an octahedral geometry around the central Cu^{2+} ion

The adsorption measurements were done under 1 atm pressure for 60 minutes using 100 mg of the complex in a sealed chamber. The complex exhibited CO_2 uptake of 1.22 mmol/g 25ºC and at 60 ºC, the uptake values decreased to 0.59 mmol/g as shown in **Table 1**. The manner is consistent with the Langmuir model, which is expressed as $qe = \frac{qmax\ KL\ Ce}{1+KL\ Ce}$ **[24] [25].**

Where:

q_e is the amount of adsorbate at equilibrium (mmol/g)

q_{max} is the maximum adsorption capacity (mg/g)

Ce is the equilibrium concentration of adsorbate (mg/L)

and

KL is the Langmuir constant related to the affinity of binding sites (L/mg)

Table 1: CO_2 adsorption capacity of the Cu(II)-paracetamol complex at different temperatures under 1 atm pressure.

Temperature	Pressure	CO_2 Uptake (mmol/g)
25 ^{0}C	1 atm	1.22
30 ^{0}C	1 atm	1.13
35 ^{0}C	1 atm	1.04
40 ^{0}C	1 atm	0.95
45 ^{0}C	1 atm	0.86
50 ^{0}C	1 atm	0.77
55 ^{0}C	1 atm	0.68
60 ^{0}C	1 atm	0.59

To demonstrate the thermal behavior of CO_2 adsorption on the complex surface, an Arrhenius-type plot of ln(qe) versus 1/T (K^{-1}) was constructed using the experimental uptake values at different temperatures. A good linear relationship was noticed, suggesting the temperature dependence of adsorption follows the Arrhenius equation. The slope of the line was used to determine the adsorption energy, which was found to be **-16.89kJ/mol**. This negative value confirms the exothermic nature of the adsorption process and is unique to physisorption, where a relatively weak van der Waals interaction is the main force between the adsorbate CO_2 and the adsorbent surface, as shown in **Figure 7**.

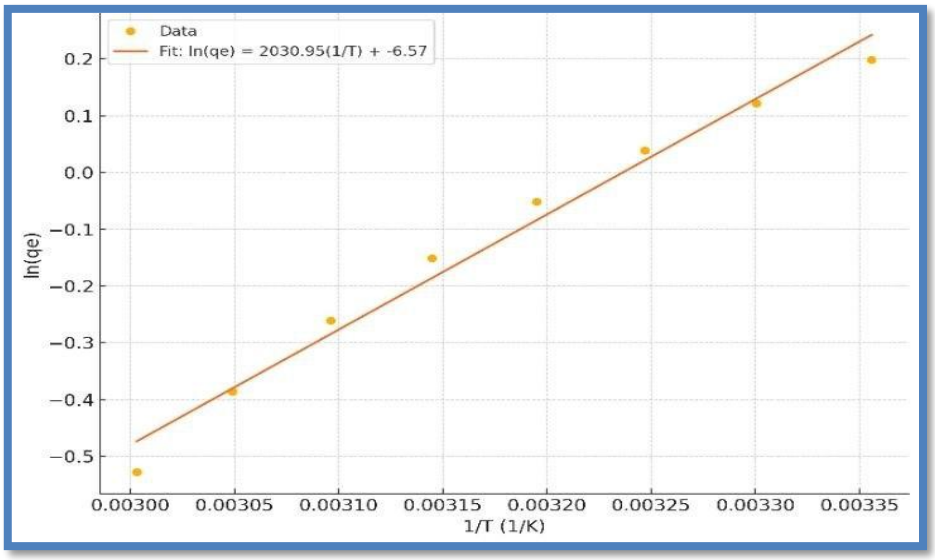

Figure 7: Arrhenius plot of ln(q_e) vs. 1/T for CO_2 Adsorption onto the complex

The Cu(II)-paracetamol complex demonstrated a CO_2 adsorption capacity of 1.22 mmol/g at 25 ^oC and 1 atmosphere, which is a significant result when compared with the class of molecular coordination complexes. This uptake indicates that the synthesized material possesses a moderately high affinity for CO_2 under ambient conditions, suggesting favorable thermodynamic and kinetic interaction between the gas molecules and the adsorbent. From a coordination chemistry perspective, the Cu(II) center acts as a Lewis acid with an open coordination site or labile positions in the ligand field. The adsorption mechanism is dominated by physisorption, likely driven by dipole-quadruple interaction between the polar Cu(II) center and linear CO_2 molecules. The presence of functional groups such as hydroxyl(-OH), carbonyl (C=O), and amine ($-NH_2$) in the paracetamol ligand contributes additional Lewis basic sites, facilitating localized CO_2 adsorption via hydrogen bonding or acid-base. Furthermore, the relatively high uptake at 25 ^oC- where adsorption is typically thermodynamic favored- is consistent with physisorption behavior. The result also indicates that no significant steric hindrance occurs with the complex structure that would otherwise inhibit CO_2 accessibility to active sites. It is likely that the complex forms a supramolecular network or aggregates that retain free volume or interstitial voids, providing an accessible microenvironment for gas diffusion and retention [26]. In terms of performance benchmarking, the value of 1.22 mmol/g places this material in the same operational range as many non-porous adsorbents and functionalized organic compounds seen in **Table 2**. While it is not as high as metal-organic frameworks (MOFs), which often exceed 4.4 mmol/ g under similar conditions, it offers distinct advantages in terms of synthesis simplicity, stability in ambient environments, and potential biodegradability, which are crucial for low-cost and CO_2 management systems.

Table 2: Comparison of CO_2 uptake capacities at 25 ^0C for various adsorbent materials

Materials type	Uptake at 25 ^oC mmol/g
Amine-functionalized silica	1.0-3.5
Zeolites	2.5-3.0
MOFs (e.g, HKUST-1)	4.5-6.0
Activate carbon	0.8-2.0
Cu(II)-paracetamol complex	**~1.22**

5. Conclusions

This study successfully synthesized a cu(II)-paracetamol complex, characterized by FTIR, UV-Vis spectroscopy, and stoichiometry analysis. The spectral data confirmed coordination through the hydroxyl , amine, and carbonyl groups of paracetmol, forming a tridentate ligand. UV.Vis analysis showed red-shifted absorption, indicating metal-ligand interactions. The

complex exhibited a CO_2 uptake capacity of ~1.22 mmol/g under ambient conditions, suggesting potential as a cost-effective and environmental friendly CO_2 capture material. These results demonstrate the dual utility of the complex in both pharmaceutical coordination chemistry and environmental applications.

6. References

[1] Lawal A, Obaleye JA. Synthesis, characterization and antibacterial activity of aspirin and paracetamol metal complexes. Biokemistri. 2007;19(1):17–23.

[2] Adadey SM, Sarfo JK. Copper-paracetamol complexes: promising lead antibacterial drug candidates. Afr J Pure Appl Chem. 2016;10(5):56–62.

[3] Osowole AA, Ojo BO. Synthesis and characterization of mixed ligand transition metal complexes of paracetamol and vanillin. Asian J Pharm Clin Res. 2014;7(3):145–9.

[4] Chui SSY, Lo SMF, Charmant JPH, Orpen AG, Williams ID. A chemically functionalizable nanoporous material $[Cu_3(TMA)_2(H_2O)_3]n$. Science. 1999;283(5405):1148–50.

[5] Kulkarni PP, Jadhav PD, Patil VS, Deshmukh CD. Synthesis, characterization and antimicrobial studies of Cu(II) complexes with biologically active ligands. J Chem Pharm Res. 2012;4(1):726–31.

[6] El-Sherif AA, Ali H, Ahmed SM. Spectroscopic studies and biological activity of novel metal complexes of paracetamol. Spectrochim Acta A Mol Biomol Spectrosc. 2009;72(4):897–902.

[7] Mohapatra S, Parida KM. A review on CuO-based composite materials for CO_2 capture and catalytic conversion. RSC Adv. 2016;6(84):80047–68.

[8] Sumida K, Rogow DL, Mason JA, McDonald TM, Bloch ED, Herm ZR, et al. Carbon dioxide capture in metal-organic frameworks. Chem Rev. 2012;112(2):724–81.

[9] Wang Q, Luo J, Zhong Z, Borgna A. CO_2 capture by solid adsorbents and their applications: current status and new trends. Energy Environ Sci. 2011;4(1):42–55.

[10] Nakamoto K. Infrared and Raman Spectra of Inorganic and Coordination Compounds. 6th ed. Hoboken (NJ): Wiley; 2009.

[11] Lever ABP. Inorganic Electronic Spectroscopy. 2nd ed. Amsterdam: Elsevier; 1984.

[12] Raganati F, Liguori B, Ammendola P. Adsorption of carbon dioxide on solid sorbents: a review. Energy Fuels. 2021;35(1):1287–1314.

[13] Wang J, Luo J, Zheng Y, Wang S. Recent advances in solid sorbents for CO_2 capture: a review. J Clean Prod. 2017;161:821–839.

[14] Sultan MA, Karim AE, Kandory A, Al-Metwali A. Synthesis and characterization of Al(III) complex with paracetamol. Int J Pharm Qual Assur. 2020;10(1):156–9.

[15] Structure-Properties Relationship of Cu(II)–Paracetamol Based Complex: a theoretical and spectroscopic study. Napdd Intl J Pharm Drug Deliv Tech. c2021.

[16] Synthesis and characterization of metal complexes of Mg(II) and Cu(II) ions with N-(4-hydroxyphenyl)acetamide. J SSRR. 2025;22 Jan.

[17] Rose NJ, Drago RS. Generalization of the Job method of continuous variation for complex stoichiometry. J Am Chem Soc. 1959;81(24):6138–41.

[18] El-Shahawy MA, et al. Synthesis and characterization of Fe(II), Cu(II), Zn(II) complexes with paracetamol. Korea Scie. c2022.

[19] Adsorption of paracetamol onto activated carbon derived from sawdust. Sustainability. 2023;15(3):2516.

[20] Removal and adsorption characteristics of paracetamol using hemp-derived activated carbon: Langmuir & Freundlich modelling. Environ Eng Res. 2022;37(4):357–368.

[21] Adsorption mechanisms of paracetamol on graphene-based nanomaterials: experimental and DFT insights. Front Carbon Res. 2024.

[22] Kulkarni PP, Jadhav PD, Patil VS, Deshmukh CD. Synthesis, characterization and antimicrobial studies of Cu(II) complexes with biologically active ligands. J Chem Pharm Res. 2012;4(1):726–731.

[23] Sarkar S, Das A, Dutta C. Cu(II) complex of paracetamol: Structure and spectroscopic characterization. Polyhedron. 2020;175:114159.

[24] STM and DFT studies of CO_2 adsorption on Cu surfaces indicate weak, physisorptive interactions (~15-20 kJ/mol). arXiv. 2018.

[25] Ion-imprinted strategy for Cu-based adsorbents: application for CO_2 capture and catalytic compatibility. J Hazard Mater. 2025.

[26] A new tridentate Schiff base Cu(II) complex: synthesis, FTIR, UV-Vis and single-crystal analysis. J Inorg Organomet Polym. 2013;23:1015-1025.

Al-Kitab Journal for Pure Sciences (2025); 9(2):181-190.
https://doi.org/10.32441/kjps.09.02.p12

Al-Kitab Journal for Pure Sciences
ISSN: 2617-1260 (print), 2617-8141(online)

https://isnra.net/index.php/kjps

Effect of the Structural and Electrical Properties of Bi2-xPbxBa2Ca2Cu3O10+δ Superconductors with Partial Substitution of Lead by Bismuth

Alyaa H. Ail Jassim

Department of Physics, College of Education for Pure Sciences, University of Kirkuk, Iraq.

*Corresponding Author: alyaahamid@uokirkuk.edu.iq

Citation: Jassim AHA. Effect of the Structural and Electrical Properties of Bi2-xPbxBa2Ca2Cu3O10+δ Superconductors with Partial Substitution of Lead by Bismuth. Al-Kitab J. Pure Sci. [Internet]. 2025 Sep. 10;9(2):181-190. DOI: https://doi.org/10.32441/kjps.09.02.p12

Keywords: Bismuth, Lead, Superconducting Properties, Solid State Reaction Method, Electrica1 Conductivity, Tetragonal Structure.

Article History

Received	12 Jan.	2025
Accepted	25 Feb.	2025
Available online	10 Sep.	2025

Abstract:

This manuscript discusses the preparation of $Bi_{2-x}Pb_xBa_2Ca_2Cu_3O_{10+\delta}$ compounds by the method of solid-state reaction at the annealing temperature 850 C˚. Under pressure of 8ton/cm^2 with a presence of enough oxygen and these are considered as ideal conditions according to the previous researches in the preparation of electric superconductors of high degree temperatures the effect of partial substitution was on Lead (Pb) e1ement in the Bismuth (Bi) e1ement was studied to produce a compound with formula of $Bi_{2-x}Pb_xBa_2Ca_2Cu_3O_{10+\delta}$ and for different ratios of x to know the effect of partial substitution to form Bi2223 phase at the annealing time 72 hrs and we concluded from study of diffraction of x-ray that the compound kept its tetragonal structure , and critical temperature(Tc) degrees were obtained Tc= 128K,130K, 135K, 132K, and that's at substitution ratios x=0,0.15,0.25,0.3, respectively it was clear the best substitution ratios of pb in Bi was when x=0.25.

Keywords: Bismuth, Lead, Superconducting Properties, Solid State Reaction Method, Tetragonal Structure.

تأثير الخواص التركيبية والكهربائية لموصلات $Bi_{2-x}Pb_xBa_2Ca_2Cu_3O_{10+\delta}$ الفائقة عند الاستبدال الجزئي للرصاص بالبزموث

عليا حامد علي جاسم

قسم الفيزياء، كلية التربية للعلوم الصرفة، جامعة كركوك، العراق

alyaahamid@uokirkuk.edu.iq

الخلاصة:

يدرس هذا البحث إعداد مركبات Bi2-xPbxBa2Ca2Cu3O10+δ باستخدام طريقة التفاعل في الحالة الصلبة عند درجة حرارة تلبيد تبلغ 850 درجة مئوية، وتحت ضغط 8 طن/سم²، مع وجود كمية كافية من الأوكسجين، وتُعتبر هذه الظروف مثالية بناءً على الأبحاث السابقة في تحضير الموصلات الفائقة الكهربائية ذات درجات الحرارة العالية.تمت دراسة تأثير الاستبدال الجزئي لعنصر Pb بعنصر Bi لإنتاج مركب بصيغة Bi2-xPbxBa2Ca2Cu3O10+δ و لتراكيز مختلفة لـ x، وذلك لمعرفة تأثير الاستبدال الجزئي على تكوين الطور Bi2223 عند زمن تلبيد بلغ 72 ساعة. ومن خلال دراسة حيود الأشعة السينية(XRD) ، تبين أن المركب يحافظ على صفته الرباعية (tetragonal)، وتم قياس درجات الحرارة الحرجة حيث كانت القيم 128K، K١٣٠، K١٣٥، ١٣٢ K عند نسب استبدال x = 0, 0.15, 0.25, 0.3على التوالي. وقد كان واضحًا أن أفضل نسبة استبدال لعنصر Pb ب عنصر Bi هي عند x = 0.25.

الكلمات المفتاحية: البزموث، الرصاص، خصائص الموصلية الفائقة، طريقة التفاعل في الحالة الصلبة، التركيب الرباعي.

1. Introduction:

When materials are cooled to a specific temperature, known as the Tc, they become superconducting, allowing electric current to flow without resistance and with no magnetic flux at all. This property is crucial for many applications in electronics, connectivity, and medical equipment. [1,2]. After the discovery of some ceramic materials with a temperature of more than 90 K, which were referred to as high-temperature superconductors, superconductors entered a new stage. The ability to use liquid nitrogen for cooling [3] and liquid nitrogen at a temperature of (77 K), which can be obtained readily and at an affordable price [4,5], and the discovery of these materials have mad.

High temperature superconducting materials, including the BBCCO system, have been identified and synthesize [6] is an abbreviation for HTSC, composed of e1ement oxides (bismuth, barium, calcium, copper) with the typical chemica1 formula ($Bi_{2-x}Pb_xBa_2Ca_{n-1}CunO_{6+\delta}$), where (n = 1, 2, 3). It is of significant significance because of its high frequency, elevated temperature tolerance, and excellent chemica1 resistance to moisture. Consequently, significant efforts have been devoted to examining the preparation methods, treatments, and

properties of this system [7,8]. The superconducting system (BBCCO) exhibits a 1ayered structure including copper oxide 1ayers (CuO) with Critical temperatures (Tc) of 110, 80 and 10 K, respectively, at which the electrica1 resistance reaches zero (R=0) [9,10].The superconducting and transition properties of high-temperature CuO compounds are very different [11,12]. The unsupported alternating conductivity at frequency, coupled with a low insulation constant at high frequencies (60 GHz) at room temperature, and the material's polarization may necessitate the use of frequency-dependent conductivity [12].

The discovery of high temperature superconducting material initiated a revolutionary advancement in industrial applications and materials science [13,14]. High temperature superconducting systems include Bi-2201, Bi-2212, and Bi-2223 [15], which are distinguished by their two-dimensional basis and 1-ayered structure, comprising three phases: Bi-2201, Bi-2212, and Bi-2223. A final numeral for each phase denotes the quantity of CuO layers, which corresponds to the Tc (10K, 80K, and 110K); the latter signifies the temperature at which electrica1 resistance is zero (R = 0) [16] . The Bi-2223 phase is challenging to synthesize, although it possesses the advantage of being a single phase with the highest Tc (110 K) among 204 effects of partial substitution of silver and copper on the structural and electrica1 characteristics of Bi2Ba2Ca2Cu3O10+δ superconductors across three phases [17]. The characteristics of superconductors can be adjusted by incorporating or eliminating an element with varying ionic radius and bonding properties, and the enhancement or decline in superconducting properties is contingent upon the attributes of the added or substituted e1ements that differ in radius and bonding. The majority of the research concentrates on enhancing the morphology and characteristics of (Bi-2223) through substitution studies [18-20]. This current work discusses the temperature-dependent electrical characteristics and structural properties of the Bi2-xPbxBa2Ca2Cu3O10+δ samples and at concentrations x=0,0.15,0.25 and 0.3.

2. Material and methods:

The molecular weights of these materials relative to the weight of the element in each of the base material and the compound (sample) to be generated were used to calculate the weight ratios of the materials that contribute to the creation of the $Bi_{2-x}Pb_xBa_2Ca_2Cu_3O_{10+\delta}$ compound.

The oxides and carbonates are weighed out, combined, and then put into granules. These materials are then ground finely for 30 minutes using an agate grinder so that the mixture becomes homogeneous. An isopropanol solution is added during the grinding process to prevent falling or losing powder during the grinding process. The isopropanol alcohol is then removed from the grinder by placing it in an electric oven set between (50°C, 60°C).

These powders are put in a convection oven, which is heated to 850°C and heated at a pace of 120°C per hour in an air-saturated environment. This form is kept at (850 C) for (12) hours before being lowered to allow it to cool to a specific temperature. The model is taken out of the furnace at room temperature with a cooling rate of 30°C/hr and temperature control using a thermocouple. To prevent vaporization and loss, the powder is then combined and continuously processed for another 30 minutes. The ester of is solution is then added. 50˚C, 60˚C).

The powder is then manufactured under pressure (8 Ton/cm) in the form of tablets. These tablets had (12 mm) diameters and ranged in thickness from (0.8 mm) to (1.2 mm). These discs are put in an electric oven, where the temperature is progressively increased to (850 C˚) at a pace of (120 C˚ /hr) and held there for 12 hours before being gradually lowered at a rate of (30 C˚). After acquiring the samples that were made in the shape of tablets from the previous sentence, the process of heating and cooling takes place in an atmosphere that is saturated with oxygen until it reaches room temperature. This process is known as sintering. The prepared samples are obtained as tablets, which are then placed in an electric oven and heated to (600 C˚) at a rate of (120 C˚ /hr) from room temperature. The sample is then kept at this temperature for (12) hours before the temperature is raised. The oven heats up to 850 degrees Celsius at a rate of 120 degrees Celsius per hour, where it stays for 24 hours in an oxygen-rich environment. The model then cools to 600 degrees Celsius at a rate of 30 degrees Celsius per hour, where it stays for another 12 hours before being cooled to room temperature at a rate of 60 degrees Celsius per hour to room temperature. Tablet-shaped samples are obtained, and after being processed, they will be examined using an X-ray diffraction instrument to determine their structural characteristics and to look at their electrica1 properties with the four probes method.

3. Results:

When the element pb is partially substituted for the element Bi in the compound $Bi_{2-x}Pb_xBa_2Ca_2Cu_3O_{10+\delta}$ compound, with x=0,0.15,0.25,٠،٣ the structural properties of the compound have been studied. However, the structural properties of the compound $Bi_{2-x}Pb_xBa_2Ca_2Cu_3O_{10+\delta}$, which was prepared at an annealing temperature of 850 and under a hydrostatic pressure of 8 tons/cm^2 are different. When creating the models with the X-ray device and putting the value of x into the compound, the X-ray diffraction investigation of these samples revealed. The regularity of the crystalline structure and the appearance of distinct peaks are noticed as shown in **Figure 1**.

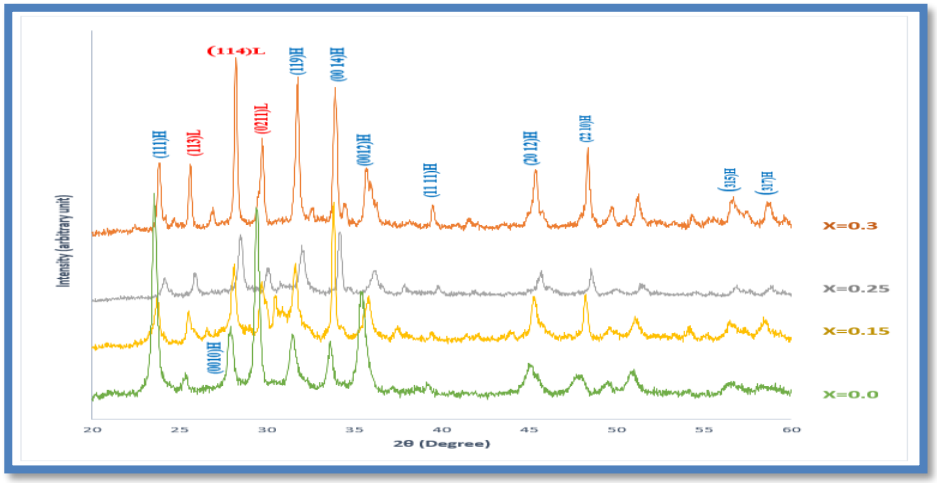

Figure 1. X-ray diffraction of $Bi_{2-x}Pb_xBa_2Ca_2Cu_3O_{10+\delta}$ compound as function of 2Θ, with indicated values of x=0,0.15,0.25, x=0.3

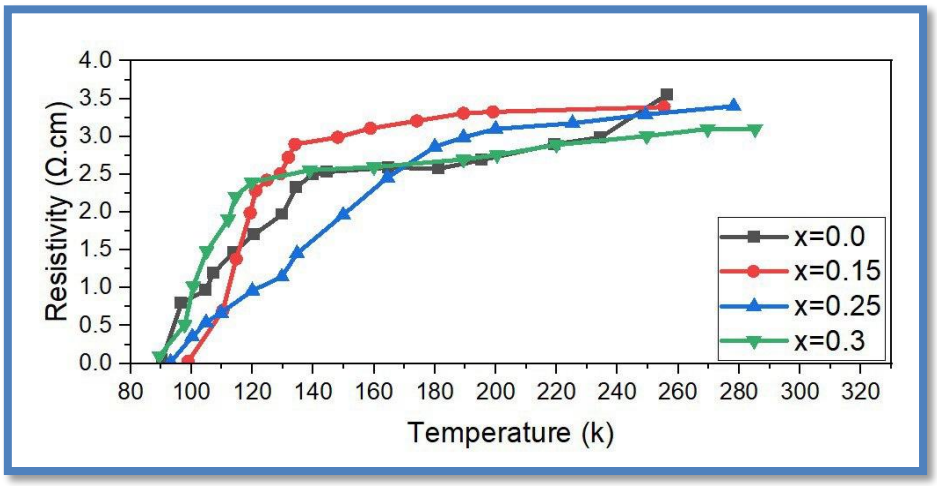

Figure 2: Resistivity of $Bi_{2-x}Pb_xBa_2Ca_2Cu_3O_{10+\delta}$ compound as function of pb, with indicated values of x=0,0.15,0.25, x=0.3

Figure 2 presents the electrical resistance behavior as a function of temperature for the four samples, both before and during the partial replacement. The maximum zero-resistivity (Tc) of 135 K was achieved at x = 0.25; however, at other concentrations, Tc increased with x concentration, as shown in **Table 1**.

Table (1): Values axes a, c, Tc(onset), ΔT and Tc(offset) of $Bi_{2-x}Pb_xBa_2Ca_2Cu_3O_{10+\delta}$ compound as function of pb, with indicated values of x=0,0.15,0.25,0.3

X	a (°A)	c (°A)	c/a	Tc (OFF)(K)	Tc (ON) (K)	Tc(K)
0	5.0923	35.017	6.97	95	150	123
0.15	5.339	36. 895	6.91	198	160	129
0.25	5.432	37.028	6.81	100	170	135
0.3	4.973	36.962	7.64	99	122	110

4. Discussion

The regularity of the crystalline structure and the appearance of distinct peaks are noticed as shown in **Figure 1**.

Miller coefficients hkl are then discovered, and using a particular BASIC software, the values of the unit cell's dimensions are discovered. a = b = 5.09A0 and, c = 35.01A0 for x= 0, where: a = b = 5.33 A0, c = 36. 89 A0 for x= 0.15, a = b = 5.43A0 and, c = 37.02 A0 for x= 0.25, as shown in **Table 1**. The table indicates that elevating the concentration of partially transcendent elements results in a significant alteration of both the network constants and their size. An increase in the value of c resulted in variations in the concentrations x = 0.0, 0.15, 0.25, 0.3, attributed to disturbances in the number of CuO chains and CuO2 levels that govern the various isotropic materials and the Tc of superconducting materials. A decrease in the coefficient c diminishes the intensity of the fermi energy levels, thereby lowering the Tc, causing imbalance and variability, and affecting the unit cell volume in a compound **[21]**. The change in 1attice constants arises from the variation in ionic radii of the substituted e1ements resulting from an increase in substitution concentration. X-ray diffraction measurements indicated that the crystalline structure remained tetragonal **[22]**, with a noticeable reduction in the c-axis length when the compensation ratio increased to x = 0.3, attributed to the relocation of atomic defects or oxygen deficiency. The vacuoles or abnormalities of the positive ions result in the accumulation of stacking faults. The distortion of the crystal structure eventually results from the influence along the (c) axis **[23]**.

As shown in **Figure 2** the results indicate that all samples exhibited metallic behavior, with the Tc rising in accordance with the increasing x concentration. The electrica1 resistance decreases as the temperature decreases in the region preceding (Tc(onset)), as the material transitions from its natural state. The change to the superconducting state occurred in several stages, influenced by several transitions arising from the various phases present in the sample, as well as the presence of certain crystals and impurities. The findings indicated that the Tc varies with increasing x concentration **[22]**. The maximum zero-resistivity (Tc) of 135 K was achieved at x = 0.25; however, at other concentrations, Tc increased with x concentration, as shown in **Table 1**.

This result can be explained by the compound playing the perfect role in the crystal structure **[20]**, and this percentage of compensation caused the Tc to rise as a result of an increase in the high phase 2223 with an increase in the lead concentration in the samples.

Using the four-probe approach, the electrica1 characteristics of the compound were investigated in order to determine Tc(onset) and Tc(offset) for calculating the electrica1 resistivity as a function of temperature after the e1ement pb was partially substituted in the Bi e1ement of the $Bi_{2-x}Pb_xBa_2Ca_2Cu_3O_{10+\delta}$ compound.

5. Conclusions

The effect of partial bismuth replacement with lead on the superconducting characteristics of $Bi_{2-x}Pb_xBa_2Ca_2Cu_3O_{10+\delta}$ is examined in this publication with x = 0, 0.15, 0.25and 0.3. The solid-state reaction approach was used to prepare the samples. The four-probe method was used to evaluate the electrica1 conductivity in order to calculate the Tc. The Tc was observed to rise as the quantities of silver in all produced samples increased. The optimal compensation ratio for x was also discovered to be 0.25, which results in the highest Tc. X-ray diffraction was used to examine the samples' ultrastructural characteristics. All of the prepared samples had a tetragonal structure, with a distinct change in the 1attice constants, according to an X-ray diffraction investigation. The ideal role that the compound played in the crystal structure can be utilized to explain this result. This percentage of compensation led to an increase in the Tc and an increase in the high phase 2223 with an increase in the lead concentration in the samples.

References

[1] Jassim AHA, Saleh CAZ, Jasim KA. Improving the electrical and thermal conductivity of Pb1-xHgxBa2Ca2Cu3O8+ d superconducting compound by partial replacement of lead with mercury. In: AIP Conference Proceedings. AIP Publishing; 2023. https://doi.org/10.1063/5.0129549

[2] Saleh CAZ, Jassim AHA, Jasim KA. Partial substitution of lead with nickel on the structural and electrical properties of Pb1-xNix Ba2Ca2Cu3O8+ δ superconducting compound. In: AIP Conference Proceedings. AIP Publishing; 2023. https://doi.org/10.1063/5.0171582

[3] Jasim KA, Saleh CAZ, Jassim AHA. Synthesis and Analysis of the Impact of Partial Mercury Replacement with Lead on the Structural and Electrical Properties of the Hg1-xPbxBa2Ca2Cu3O8 Superconductor. Korean Journal of Materials Research. 2024;34(1):21–6. https://doi.org/10.3740/MRSK.2024.34.1.21

[4] Jassim, K. A., Jassim, W. H., & Mahdi, S. H. (2017, The effect of sunlight on medium density polyethylene water pipes. Energy Procedia, 2017, 119, pp. 650–655) https://doi.org/10.1016/j.egypro.2017.07.091

[5] Woch WM, Zalecki R, Kołodziejczyk A, Deinhofer C, Gritzner G. The Irreversibility Fields of ($Tl_{0.5}Pb_{0.5}$)($Sr_{0.85}Ba_{0.15}$)$_2Ca_2Cu_3O$ Film on Polished Silver Substrate. Acta Phys Pol A. 2007;111(5):737–43. http://przyrbwn.icm.edu.pl/APP/ABSTR/111/a111-5-9.html

[6] Haider HMJ, Wadi KM, Mahdi HA, Jasim KA, Shaban AH. Studying the partial substitution of barium with cadmium oxide and its effect on the electrical and structural properties of HgBa2Ca2Cu3O8+ δ superconducting compound. In: AIP Conference Proceedings. AIP Publishing; 2019. https://doi.org/10.1063/1.5116960

[7] Maeda H, Tanaka Y, Fukutomi M, Asano T. A new high-Tc oxide superconductor without a rare earth element. Jpn J Appl Phys. 1988;27(2A):L209. https://doi.org/10.1143/JJAP.27.L209

[8] Bhardwaj JK, Harkrishan, Tyor AK. Sublethal effects of imidacloprid on Haematological and biochemical profile of Freshwater fish, Cyprinus carpio. JOURNAL OF ADVANCED ZOOLOGY. 2020;41(1):75–88. https://doi.org/10.17762/jaz.v41i01-02.59

[9] Xiao TD, Gonsalves KE, Strutt PR. Synthesis of aluminum nitride/boron nitride composite materials. Journal of the American Ceramic Society. 1993;76(4):987–92. https://doi.org/10.1111/j.1151-2916.1993.tb05323.x

[10] Kareem Ali Jassim, Structure and electrical properties of lanthanum doped Bi2Sr2Ca2-xLaxCu3O10+δ superconductor, Turk J. Phys. 36, 245 – 251). (2012). https://journals.tubitak.gov.tr/physics/vol36/iss2/10/

[11] Choudhary NL, Chishty N. Copulation Behaviors of Indian Vulture (Gyps Indicus) in Udaipur District, Rajasthan, India. J Adv Zool. 2021;42(1):7–19. https://www.academia.edu/76012911/Copulation_Behaviors_of_Indian_Vulture_Gyps_Indicus_in_Udaipur_District_Rajasthan_India

[12] Gul IH, Rehman MA, Ali M, Maqsood A. Effect of vanadium and barium on the Bi-based (2223) superconductors. Physica C: Superconductivity and its applications. 2005;432(1–2):71–80. https://doi.org/10.1016/j.physc.2005.07.013

[13] Cantoni, M., Schilling, A., Nissen, H., & Ott, H., Physica C: Superconductivity, Volume 215, Issues 1–2, 20 September 1993, Pages 11-18. https://www.sciencedirect.com/journal/physica-c-superconductivity-and-its-applications/vol/215/issue/1?utm_source=chatgpt.com

[14] Xu Q, Chen Z, Meng G, Peng D. Microstructure and Superconductivity in Bi–Sr–Ca–Cu–O System Doped with Pb and Sb. Jpn J Appl Phys. 1990;29(10R):1918. https://link.springer.com/article/10.1007/BF00624506

[15] Jasim KA, Alwan TJ. Effect of Oxygen Treatment on the Structural and Electrical Properties of Tl 0.85 Cd 0.15 Sr 2 CuO 5− δ, Tl 0.85 Cd 0.15 Sr 2 Ca 2 Cu 2 O 7− δ and Tl 0.85 Cd 0.15 Sr 3 Ca 2 Cu 3 O 9− δ Superconductors. J Supercond Nov Magn. 2017;30:3451–7. https://doi.org/10.1007/s10948-017-4147-9

[16] Jassim KA, Hussein HS. Effect of Partial Substitution of Lanthanum (La) on the Structural and Electric Properties of Bi2Sr2Ca2Cu3xLaxO10+ Î´. Ibn AL-Haitham Journal For Pure and Applied Sciences. 2017;30(3):35–43. https://jih.uobaghdad.edu.iq/?utm_source=chatgpt.com

[17] De Biasi RS, Araujo SM V. Influence of the annealing parameters on the volume fraction of the high-Tc phase in the Bi-Sr-Ca-Cu-O system. J Magn Magn Mater. 1992;104:471–2. https://www.sciencedirect.com/science/article/pii/030488539290881N?utm_source=chatgpt.com

[18] Nkum RK, Datars WR. Weak link in ceramic In-doped Bi-Pb-Sr-Ca-Cu-O. Supercond Sci Technol.1995;8(11):822. https://scholar.google.com/citations?hl=en&user=n4mN6lcAAAAJ&utm_source=chatgpt.com

[19] Gul IH, Amin F, Abbasi AZ, Anis-ur-Rehman M, Maqsood A. Effect of Ag2CO3 addition on the morphology and physical properties of Bi-based (2223) high-Tc superconductors. Physica C: Superconductivity and its applications. 2006;449(2):139–47. http://dx.doi.org/10.1016/j.physc.2006.08.004

[20] Zhigadlo ND, Petrashko V V, Semenenko YA, Panagopoulos C, Cooper JR, Salje EKH. The effects of Cs doping, heat treatments on the phase formation and superconducting properties of (Bi, Pb)–Sr–Ca–Cu–O ceramics. Physica C Supercond. 1998;299(3–4):327–37. https://www.sciencedirect.com/science/article/abs/pii/S0921453497018662?utm_source=chatgpt.com

[21] Jasim KA, Mohammed LA. The partial substitution of copper with nickel oxide on the Structural and electrical properties of HgBa2 Ca2 Cu3xNix O8+ δ superconducting

compound. In: Journal of Physics: Conference Series. IOP Publishing; 2018. p. 012071. https://www.researchgate.net/publication/325354696_The_partial_substitution_of_copper_with_nickel_oxide_on_the_Structural_and_electrical_properties_of_HgBa_2_Ca_2_Cu_3x_Ni_x_O_8d_superconducting_compound?utm_source=chatgpt.com

[22] Jasim KA. Superconducting Properties of Hg 0.8 Cu 0.15 Sb 0.05 Ba 2 Ca 2 Cu 3 O 8+ δ Ceramic with Controlling Sintering Conditions. J Supercond Nov Magn. 2012;25:1713–7. https://jih.uobaghdad.edu.iq/index.php/j/article/view/3309?utm_source=chatgpt.com

[23] Azzouz F Ben, M'chirgui A, Yangui B, Boulesteix C, Salem M Ben. Synthesis, microstructural evolution and the role of substantial addition of PbO during the final processing of (Bi, Pb)-2223 superconductors. Physica C Supercond. 2001;356(1–2):83–96. https://www.researchgate.net/publication/276489457_Optimizing_the_Preparation_Conditions_of_Bi-2223_Superconducting_Phase_Using_PbO_and_PbO2?utm_source=chatgpt.com

Al-Kitab Journal for Pure Sciences (2025); 9(2):191-205.
https://doi.org/10.32441/kjps.09.02.p13

Al-Kitab Journal for Pure Sciences
ISSN: 2617-1260 (print), 2617-8141(online)

https://isnra.net/index.php/kjps

Determination of Heavy Metals in Selected Types of Local and Imported Tea from Iraqi Markets

Wedad H. Al-Dahhan[1], Rafeef Dawood[2], Hassan N. Hashim[3], Mohammed Kadhom[4], Emad Yousif[2,*], Rahimi Yusop[5], Amra Bratovcic[6], Salam Mohammed[7]

[1] Department of Biochemistry, College of Health and Medical Technology, Alshaab University, Baghdad, Iraq.
[2] Department of Chemistry, College of Science, Al-Nahrain University, Baghdad, 10071, Iraq.
[3] Department of Physics, College of Science, Al-Nahrain University, Baghdad, 10071, Iraq.
[4] Department of Environmental Science, College of Energy and Environmental Sciences, Alkarkh University of Science, Baghdad, 10081, Iraq.
[5] School of Chemical Science and Food Technology, Faculty of Science and Technology, University Kebangsaan, Malaysia, 43600 Bangi, Selangor, Malaysia.
[6] Department of Physical Chemistry and Electrochemistry, Faculty of Technology, University of Tuzla, Tuzla, Bosnia and Herzegovina.
[7] Department of Chemical and Petrochemical Engineering, College of Engineering and Architecture, University of Nizwa, Oman.

*Corresponding Author: emad.yousif@nahrainuniv.edu.iq

Citation: Al-Dahhan WH, Dawood R, Hashim HN, Kadhom M, Yousif E, Yusop R, Bratovcic A, Mohammed S. Determination of Heavy Metals in Selected Types of Local and Imported Tea from Iraqi Markets. Al-Kitab J. Pure Sci. [Internet]. 2025 Sep. 15;9(2):191-205. DOI: https://doi.org/10.32441/kjps.09.02.p13

Keywords: Heavy Metals; Toxicity; Black Tea; Green Tea; EDX; Atomic Absorption.

Article History
Received 21 Aug. 2024
Accepted 09 Dec. 2024
Available online 15 Sep. 2025

Abstract:

The presence of heavy metals in plants, including tea plants, is influenced by factors such as the plant's origin, geographic location, soil geochemistry, and environmental contaminants in soil, water, and air. Elevated concentrations of heavy metals pose serious health risks to humans, including the potential for various cancers and damage to vital organs such as the liver, kidneys, and brain. In this study, seven tea samples were collected from the Iraqi market to examine their safety for consumption, indicated as T1-T7. The selection of the samples is based on a questionnaire answered by 140 individuals; T1-T6 samples are black tea, and T7 is green tea. Although the primary objective of this research is to determine the heavy metal content and toxicity of all the tea samples, the secondary one is to assess whether the drying process affects the levels of heavy metals by comparing green and black tea. The analysis is conducted on the samples via the Energy-Dispersive X-ray (EDX) and atomic absorption spectroscopy (AAS). The EDX results showed the presence of S, K, Al, and P in the T1 sample, while K, Al, and Mg

were identified in the T2 sample, S, K, Al, and P in T3, only K in T4, K and Fe in T5, K, P, and S in T6, and Only K in T7. The results obtained from the AAS showed that all samples have normal concentrations of Fe and Zn but not for Ni (in samples T1, T2, and T3) and manganese (in samples T1, T2, T4, T5, T6, and T7). Those detected concentrations are higher than the permissible levels, and their levels are within the toxic limits according to the standard limits set by the World Health Organization (WHO) and the Food and Agriculture Organization (FAO). However, the other heavy metals (Cd, Cu, Pb, Cr, and Co) were either not detected or were below the detection limits of AAS, indicating that these samples are free from the mentioned toxic heavy metals.

Keywords: Heavy Metals; Toxicity; Black Tea; Green Tea; EDX; Atomic Absorption

(Immediately after the abstract, provide 5-7 keywords and arrange them alphabetically, using American spelling and avoiding general and plural terms and multiple concepts (avoid, for example, 'and', 'of'). Be sparing with abbreviations: only abbreviations firmly established in the field may be eligible. These keywords will be used for indexing purposes).

تحديد العناصر الثقيلة في أنواع مختارة من الشاي المحلي والمستورد من الأسواق العراقية

وداد الدهان [١]، رفيف داود[٢]، حسن هاشم [٣]، محمد كاظم [٤]، عماد يوسف [٢،*]، رحيمي يعسوب [٥]، أمرة براتوفتشيتش [٦]، سلام محمد [٧]

[١]قسم الكيمياء الحياتية، كلية التقنيات الصحية والطبية، جامعة الشعب، بغداد ، العراق.

[٢] قسم الكيمياء، كلية العلوم، جامعة النهرين، بغداد، ١٠٠٧١، العراق.

[٣] قسم الفيزياء، كلية العلوم، جامعة النهرين، بغداد، ١٠٠٧١، العراق.

[٤] قسم علوم البيئة، كلية علوم الطاقة والبيئة، جامعة الكرخ للعلوم، بغداد، ١٠٠٨١، العراق.

[٥] كلية علوم الكيمياء وتكنولوجيا الأغذية، كلية العلوم والتكنولوجيا، جامعة كبانغسان، ماليزيا، ٤٣٦٠٠ بانجي، سيلانغور، ماليزيا.

[٦] قسم الكيمياء الفيزيائية والكيمياء الكهربائية، كلية التكنولوجيا، جامعة توزلا، توزلا، البوسنة والهرسك.

[٧] قسم الهندسة الكيميائية والبتروكيماوية، كلية الهندسة والعمارة، جامعة نزوى، عمان.

wedad.hamad@alshaab.edu.iq, rafeefdjamila@gmail.com, hassan.hashim@nahrainuniv.edu.iq, kadhom@kus.edu.iq, emad.yousif@nahrainuniv.edu.iq, rahimi@ukm.edu.my, amra.bratovcic@untz.ba, salam.mohammed@unizwa.edu.om.

الخلاصة:

يتأثر وجود المعادن الثقيلة في النباتات، بما في ذلك نباتات الشاي، بعوامل عدة مثل أصل النبات، والموقع الجغرافي، والكيمياء الجيولوجية للتربة، والملوثات البيئية في التربة والمياه والهواء. وتشكل التراكيز المرتفعة من هذه المعادن مخاطر صحية جسيمة على الإنسان، بما في ذلك احتمال الإصابة بأنواع مختلفة من السرطان وتلف الأعضاء الحيوية مثل الكبد والكلى والدماغ. في هذه الدراسة، تم جمع سبع عينات من الشاي من السوق العراقية لفحص مدى سلامتها للاستهلاك، أُشير إليها بالرموز T1إلى T7، وتم اختيار العينات بناءً على استبيان شمل ١٤٠ فردًا، حيث كانت العينات T1–T6من الشاي الأسود، بينما كانت العينة T7من الشاي الأخضر. يهدف البحث إلى تحديد محتوى المعادن الثقيلة وسمية جميع العينات،

مع تقييم تأثير عملية التجفيف على مستويات المعادن الثقيلة من خلال مقارنة الشاي الأسود بالشاي الأخضر. تم تحليل العينات باستخدام تقنية الأشعة السينية للطاقة المشتتة (EDX) وتقنية مطيافية الامتصاص الذري (AAS)، حيث أظهرت نتائج تحليل EDX وجود عناصر مثل الكبريت والبوتاسيوم والألمنيوم والفوسفور في العينة T1، وعناصر البوتاسيوم والألمنيوم والمغنيسيوم في العينة T2، وعناصر الكبريت والبوتاسيوم والألمنيوم والفوسفور في العينة T3، والبوتاسيوم فقط في العينة T4، وعناصر البوتاسيوم والحديد في العينة T5، وعناصر البوتاسيوم والفوسفور والكبريت في العينة T6، والبوتاسيوم فقط في العينة T7. أما نتائج تحليل AAS، فقد أظهرت أن جميع العينات تحتوي على تراكيز طبيعية من الحديد والزنك، بينما تجاوزت تراكيز النيكل في العينات T1و T2وT3، وتراكيز المنغنيز في العينات T1و T2و T4و T5و T6و T7 الحدود المسموح بها وفقًا للمعايير التي وضعتها منظمة الصحة العالمية (WHO) ومنظمة الأغذية والزراعة (FAO)، مما يشير إلى وجود مستويات سامة من هذه المعادن. ومع ذلك، لم تُكشف المعادن الثقيلة الأخرى (الكادميوم، النحاس، الرصاص، الكروم، الكوبالت) أو كانت تراكيزها أقل من حدود الكشف باستخدام تقنية AAS، مما يدل على أن هذه العينات خالية من المعادن الثقيلة السامة المذكورة.

الكلمات المفتاحية: المعادن الثقيلة، السمية، الشاي الأسود، الشاي الأخضر، EDX، الامتصاص الذري.

1. Introduction:

Camellia Sinensis, globally renowned as the most popular botanical source of tea, is cherished for both its flavor and reputed therapeutic benefits [1]. Tea drinking has deep historical roots, dating back approximately five millennia, as evidenced by ancient tales from China and India [2]. In Iraq, tea holds significant cultural significance, being enthusiastically embraced and routinely savored across various occasions and gatherings. Particularly, Iraqi Kurds exhibit a remarkable fondness for tea; the annual consumption rate is around 1.5 kg per person, positioning the Kurdistan region among the world's top four areas, alongside Turkey, Ireland, and the United Kingdom [3, 4]. Traditionally, tea has been imbibed for its purported abilities to enhance circulation, detoxify the body, and bolster resistance against illnesses [5].

Tea originates from the leaves of the Camellia Sinensis shrub [6], which thrive in regions characterized by high humidity, moderate temperatures, acidic soils, and spanning from sea level to high-altitude mountains [7,8]. While both black and green teas are derived from the same plant, their distinct appearance, flavor, and aroma are remarkably different. This is attributed to the variations in the dryness process during tea production. This process imbues teas with floral, spicy, or fruity notes, resulting in discernible differences between black and green teas based on their processing methods and oxidation levels [9]. Nonetheless, it's important to note that tea leaves are prone to absorbing heavy metals (HMs) throughout their lifecycle, from cultivation to packaging and transportation, potentially leading to increased metal exposure in consumers [10]. Among the common heavy metals that tea leaves may

accumulate are Cadmium (Cd), Copper (Cu), Lead (Pb), Chromium (Cr), Nickel (Ni), Iron (Fe), Manganese (Mn), mercury (Hg), Zinc (Zn), and Cobalt (Co). [11].

Heavy metals are natural elements characterized by their relatively high atomic mass and density; they play integral roles in the food chain, various human activities, and consumption patterns. Heavy metals are characterized by their relatively high atomic mass and density, occurring naturally in varying concentrations across the Earth's crust. Typically defined by a density of at least 5 g/cm³, HMs can also be distinguished by an atomic mass greater than 23 or an atomic number surpassing 20 [12]. In biological systems, heavy metals are classified as essential or nonessential. In contrast, essential heavy metals, such as Mn, Fe, Cu, and Zn, are vital for living organisms and are required in trace amounts. Contrarily, nonessential heavy metals, like Cd, Pb, and Hg, are toxic and lack biological significance [13-15]. The accumulation of HMs in tea plants is influenced by various factors, including the plant's origin, geographic location, soil geochemistry, and environmental contaminants present in soil, water, and air [16, 17]. Soil contamination sources, such as industrial activities, pesticide and fertilizer usage, and untreated wastewater, also contribute to elevated levels of HMs. Consequently, tea plants absorb these metals from the soil, potentially leading to high concentrations in edible parts, such as leaves [18-20]. While naturally occurring in soil, mining and smelting activities can exacerbate contamination levels. Here, tea plants, with their ability to uptake HMs from the soil, may transfer certain amounts to the leaves that are ultimately used in tea production [21-23].

2. Material and methods:

2-1 Sample Selection:

The sample selection method was based on the availability of products in the Iraqi market. However, three critical factors were considered while selecting the samples. Firstly, the product's popularity was considered, which ensured that only commonly used products were included in the study. Thus, a questionnaire was created and distributed online to individuals from varying economic backgrounds, and over 140 responses were obtained. This approach helped to establish a clear understanding of the popularity of the products within the target population and aided in the selection of products for the study. **Figure 1** shows the results of the public questionnaire.

The second factor was the geographical location, which played a crucial role in ensuring a diverse range of products was collected. Finally, the price of the product was also considered to ensure that a range of products, from low to high prices, were included in the study. The combination of these three factors helped to provide a diverse range of samples that were

representative of the Iraqi market. Furthermore, one of the samples was green tea instead of black tea for broader exploration.

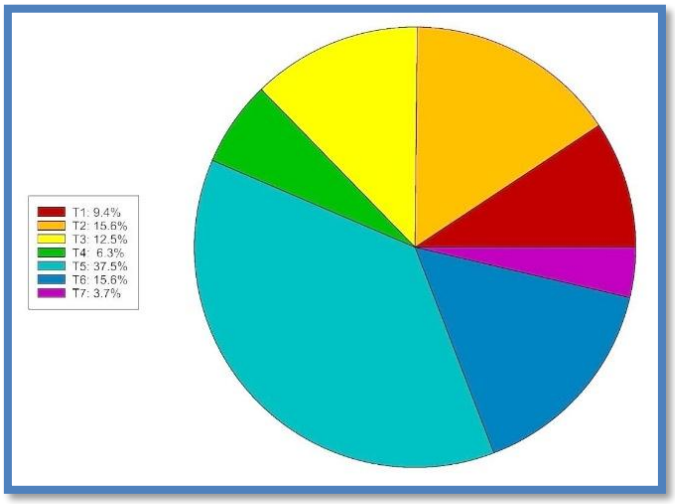

Figure 1: The public questionnaire results of selected samples.

2-2 Reagents and Chemicals

2-2-1 Reagents Used in Acid Digestion: Sample preparation involved analytical-grade nitric acid (65%, Sigma Aldrich) and hydrochloric acid (37%, Sigma Aldrich) [24, 25].

2-2-2 Reagents Used in Atomic Absorption: All the solutions were prepared using deionized water [26, 27]. Standard solutions for calibration of Mg, Zn, K, Cu, Cr, Ni, Co, Cd, Pb, and Fe were prepared from 1000 mg/L (ppm) Standard Stock Solution of GFS Fishers' AAS Reference Standard. Dilution correction was applied for samples diluted or concentrated during analysis.

2-3 Samples Drying

The tea samples, each weighing 1 g, were individually placed in watch glasses. Subsequently, they were dried in an electrical oven at 100°C overnight. Hence, they were ensured to be completely dry and ready for use in acid digestion and for Energy-Dispersive X-ray (EDX) spectroscopy analysis.

2-4 EDX Analysis

An EDX of Bruker model XFlash6I10 was used to analyze the chemical characterization/elemental analysis of materials.

2-5 Acid Digestion Method

A 0.5 g of the selected dry sample was placed separately into 200 ml beakers, then 15 ml of 65% HNO_3 and 10 mL of 37% HCl were added **[24, 25, 28]**. The contents were mixed by stirring thoroughly and heated on a hot plate. The heating continued until the dissolution of the content, and the digested sample was then filtered using Whatman filter paper No.41. The

filtration solution was diluted with deionized water to 100 ml. The resulting solution was used for the spectrophotometric determination of various metals using atomic absorption spectroscopy (AAS). In accordance with chemical laboratory safety rules, this procedure was conducted in a fume hood.

2-6 Atomic absorption Spectroscopy (AAS) Analysis

An Agilent AAS of the FS240 model was used to determine the content of heavy metals and their concentrations in the previously acid-digested prepared samples. To determine the concentration of heavy metals (HMs) in the samples, the results were multiplied by a calculation factor obtained by dividing 100 mL (the volume used for sample dilution following digestion) by 0.5 g (the quantity of tea sample used for the analysis).

3. Results and Discussion:

3-1 Energy-Dispersive X-ray (EDX) Analysis

The six black tea samples (T1-T6) and the green tea sample (T7) selected from Iraqi markets were tested via EDX spectroscopy for elemental determination. The normal scan results obtained for this test were illustrated in **Figures 2**, a-g, respectively. The elements shown in the figures were in concentrations higher than 0.003 cps/ev.

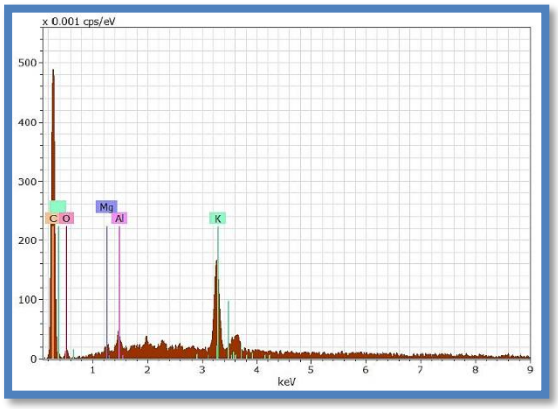

(a)

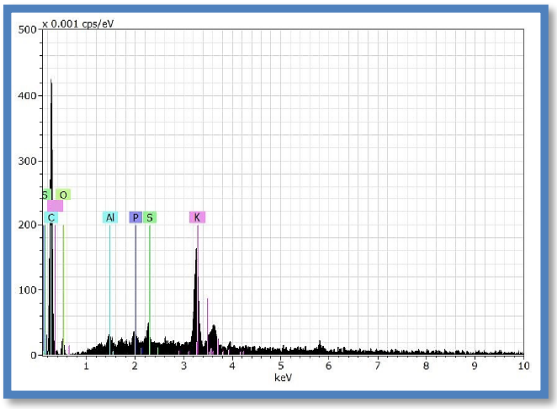

(b)

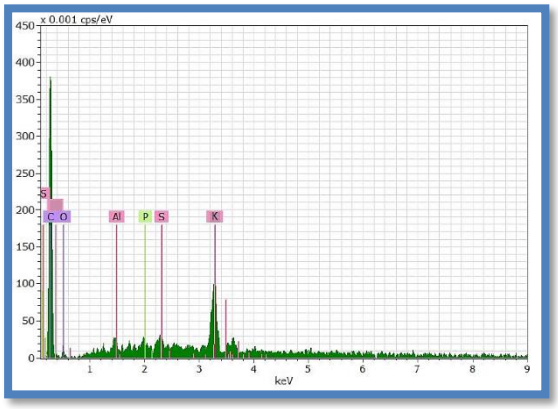

(c)

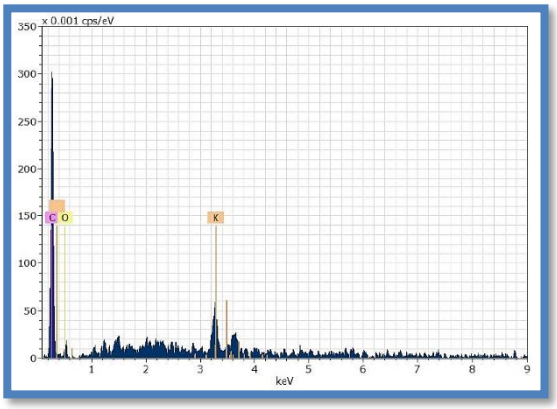

(d)

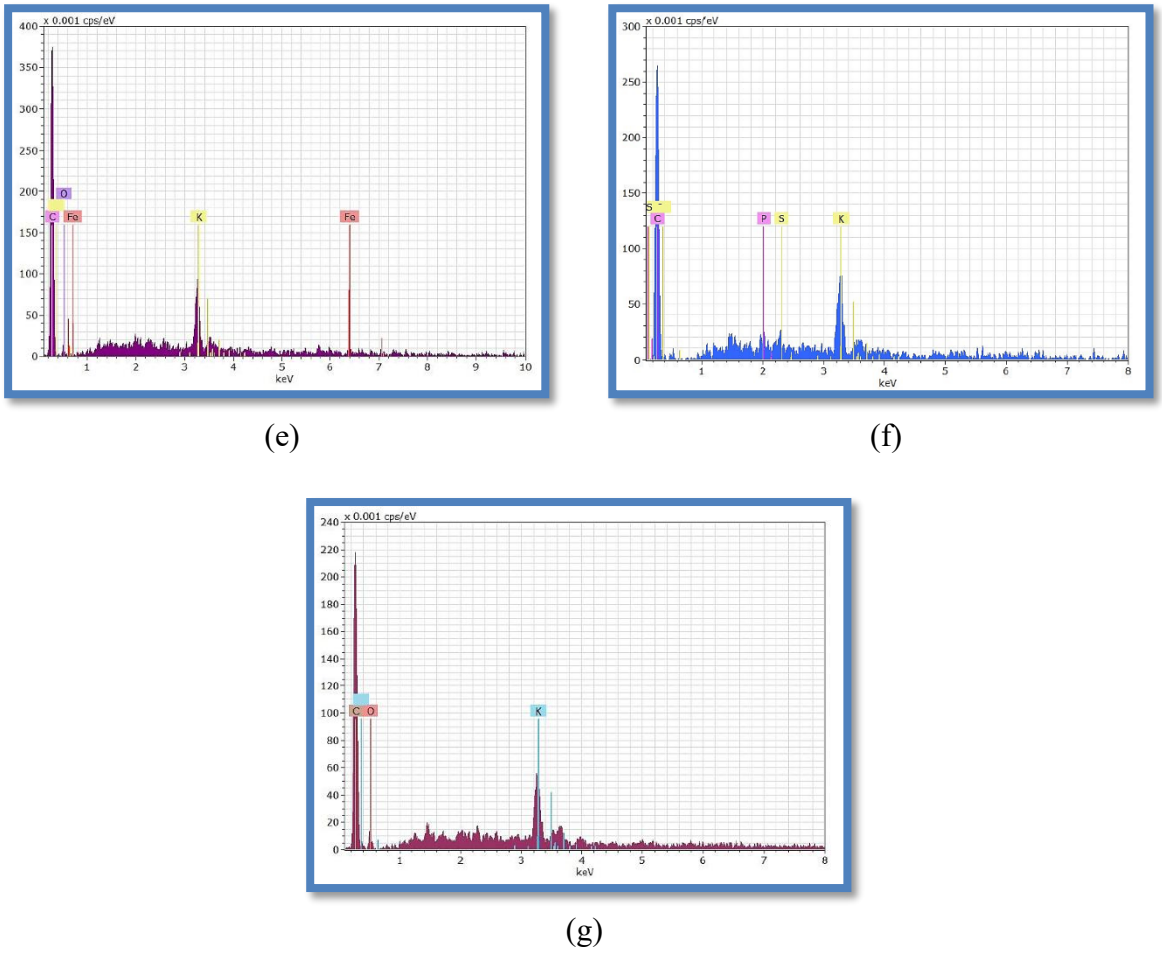

Figure 2: EDX Analysis for Samples (a) T1, (b) T2, (c) T3, (d) T4, (e) T5, (f) T6, and (g) T7.

A normal scan of EDX analysis shows the presence of S, K, Al, and P in T1, while K, Al, and Mg were found in T2. Furthermore, S, K, Al, and P were found in T3, but only K was detected in T4. K and Fe were detected in T5, K, and P, and only S was identified in T6, and only K was found in T7. All of the elements that were diagnosed above and detected are considered essential elements, which are necessary for living organisms and may be required in the body in low concentrations. However, the other elements were detected to be within the acceptable range (concentrations lower than 0.003 cps/ev) as shown in **Figure 3** a and b for T1, c and d for T2, e and f for T3, g and h for T4, i and j for T5, k and l for T6, and m and n for T7. To determine the exact concentrations of elements identified by the EDX device, along with those indicated by other research studies but possibly present in a concentration too low to be detected by the EDX due to its sensitivity limits, a digestion process was conducted on the selected samples. Acid digestion using a mixture of 65% HNO_3 and 37% HCl was performed to release HMs from the organic components in tea samples. The resulting solutions were then tested using an atomic absorption instrument to detect and determine the concentrations of the metals.

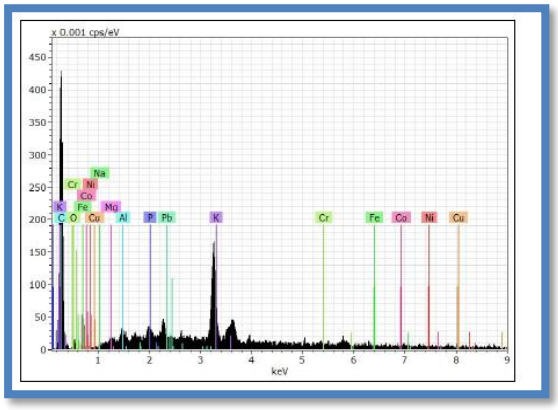

(a): Accurate EDX Analysis for T1.

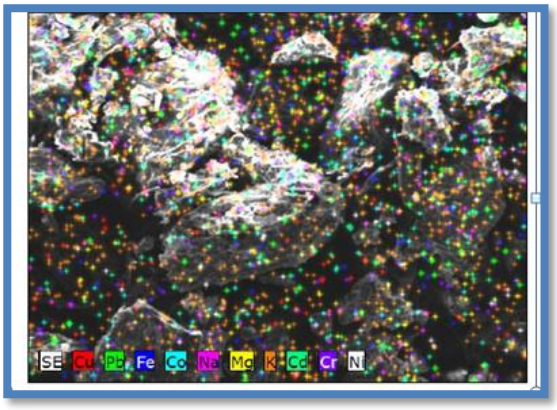

(b): Accurate EDX Analysis for T1.

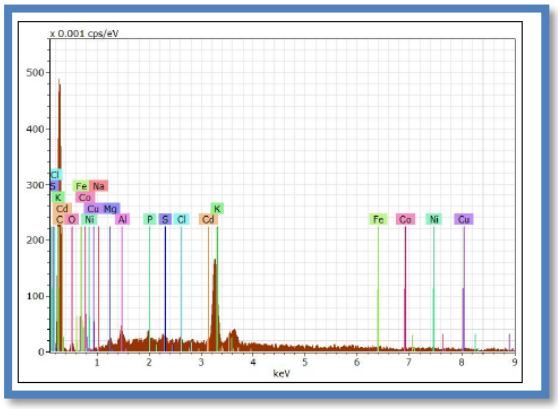

(c): Accurate EDX Analysis for T2.

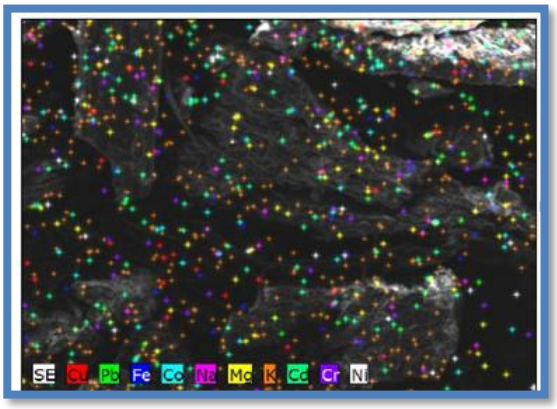

(d): Elements distribution in T2.

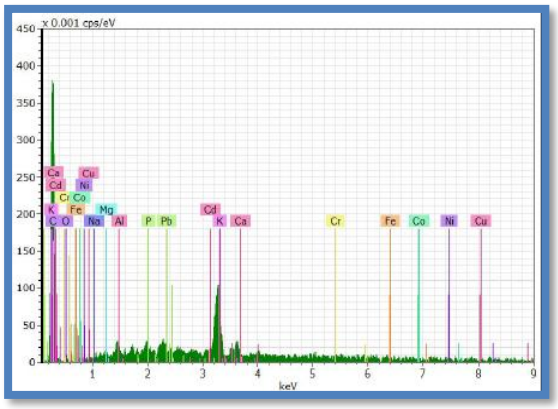

(e): Accurate EDX Analysis for T3.

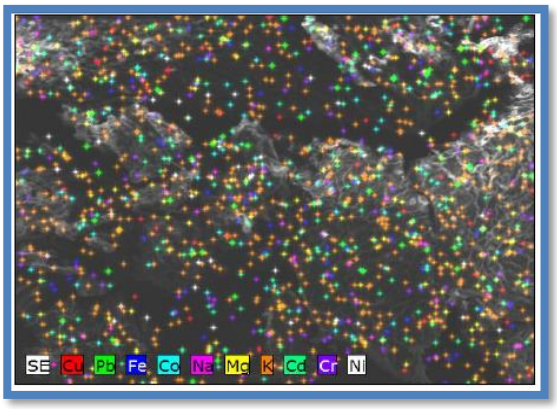

(f): Accurate EDX Analysis for T3.

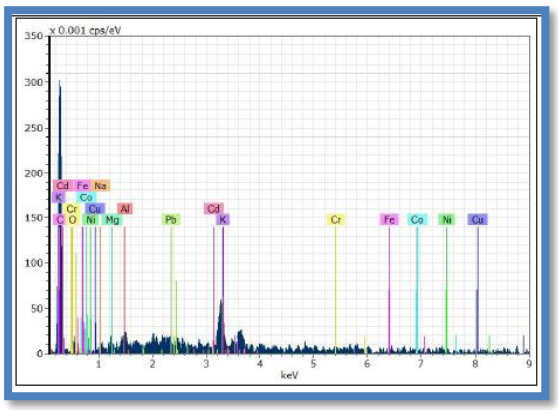

(g): Accurate EDX Analysis for T4.

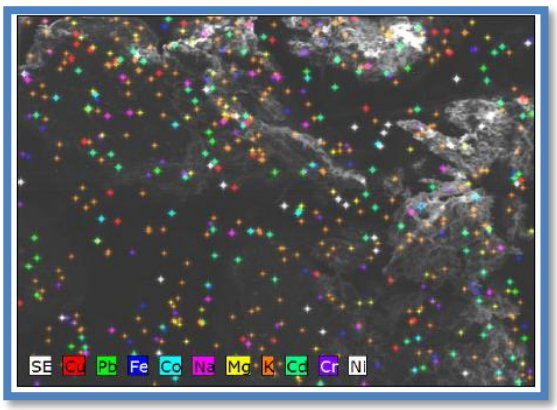

(h): Accurate EDX Analysis for T4.

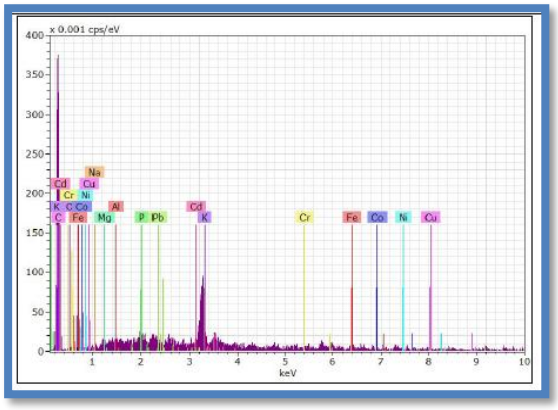

(i): Accurate EDX Analysis for T5.

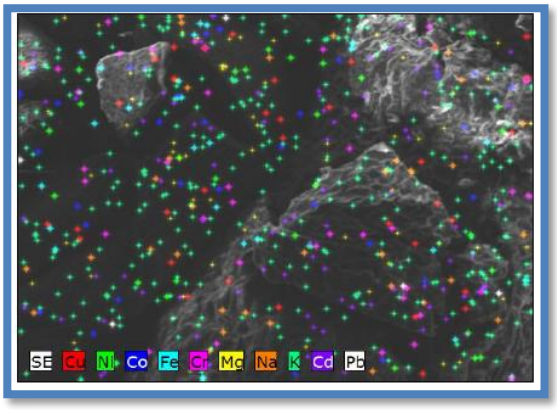

(j): Accurate EDX Analysis for T5.

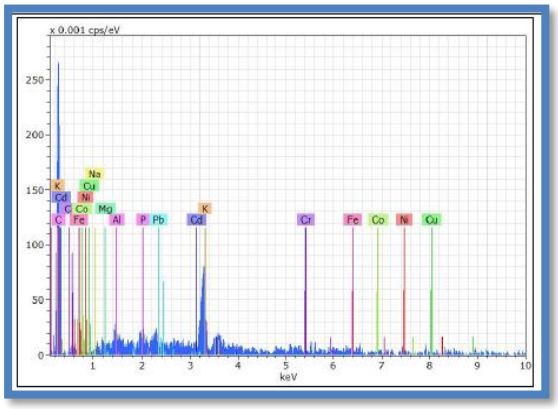

(k): Accurate EDX Analysis for T6.

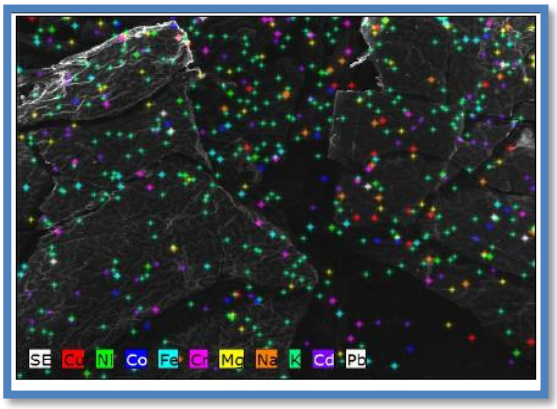

(l): Accurate EDX Analysis for T6.

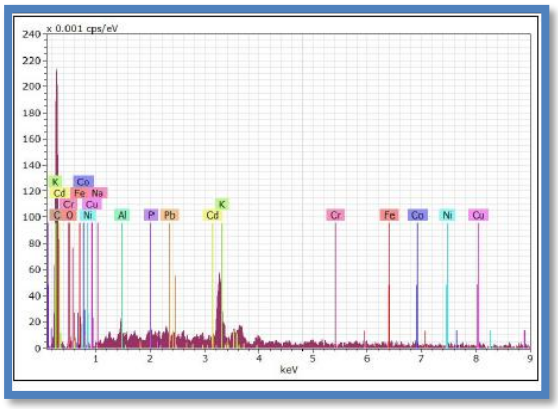

(m): Accurate EDX Analysis for T7.

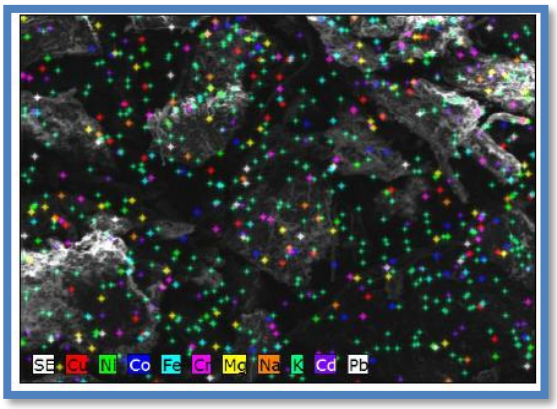

(n): Accurate EDX Analysis for T7.

Figure 3: Accurate EDX Analysis for Samples a and b for T1, c and d for T2, e and f for T3, g and h for T4, i and j for T5, k and l for T6, and m and n for T7.

3-2 AAS Analysis

In order to establish a calibration curve for a specific metal within the detection limits of a device, four standard solutions with low concentrations (in ppm) of nine HMs and one essential element were prepared. Subsequently, solutions derived from the digestion of seven tea samples were compared with these standards. **Table 1** shows the final results for the selected elements in tea samples, while the ratios of metal are illustrated in **Table 2**.

Table 1: AAS Analysis results in ppm

Sample / Element	T1	T2	T3	T4	T5	T6	T7
K	14000	14630	10178	6602	14000	12460	8260
Cd	ND	ND	ND	ND	ND	ND	ND
Cu	ND	ND	ND	ND	ND	ND	ND
Pb	ND	ND	ND	ND	ND	ND	ND
Cr	ND	ND	ND	ND	ND	ND	ND
Ni	46	46	66	ND	ND	ND	ND
Fe	500	500	376	376	376	ND	300
Mn	1866	666	332	932	566	466	1000
Zn	54	10	22	66	4	10	ND
Co	ND	ND	ND	ND	ND	ND	ND

ND= Not detected

Table 2: The percentages (%) of HMs and potassium in tea samples

Sample / Element	T1	T2	T3	T4	T5	T6	T7
K	1.4	1.46	1.01	0.66	1.4	1.24	0.82
Ni	0.0046	0.0046	0.0066	ND	ND	ND	ND
Fe	0.05	0.05	0.037	0.037	0.037	ND	0.03
Mn	0.18	0.06	0.03	0.09	0.06	0.05	0.1
Zn	0.005	0.001	0.002	0.007	0.0004	0.001	ND

According to the standard limits given by the World Health Organization (WHO) and Food and Agriculture Organization (FAO) (as presented in **Table 3**) and the results obtained from the AAS, all samples (6 black tea and the seventh green tea) had normal concentrations of Iron (it exceeded the permissible limit but did not exceed the toxic level). Also, Zinc and nickel (in samples T1, T2, and T3) and manganese (in samples T1, T2, T4, T5, T6, and T7) were higher than the permissible levels, and their concentrations were within the limits of toxic concentrations. The other HMs (Cd, Cu, Pb, Cr, and Co) were either not detected or were less than the detection limits of these metals in atomic absorption, which makes these samples free from highly toxic HMs. Metal concentrations for samples (T1-T7) compared with permissible and toxic concentrations are illustrated in **Figure 4** (a-g).

Table 3: Normal and Toxic concentrations of heavy metals given by WHO and FAO [29, 30].

Element	Normal concentrations (mg kg^{-1})	Toxic concentration (mg kg^{-1})
Cu	3–15	20
Ni	0.1–5	30
Pb	1–5	20
Hg	<0.1–0.5	5
Cr	<0.1–1	2
Mn	15–100	400
Zn	15–150	200
Mo	0.1–0.5	10–50
Co	0.05–0.5	30–40
Fe	50–250	(>500)
As	10–60	<2
Sb	<2–29	5–10 g

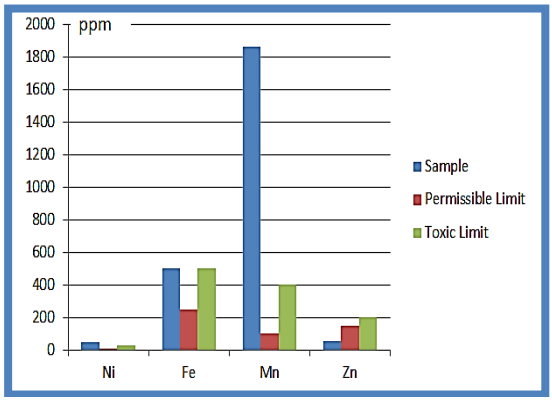

(a): Metal concentration of the sample(T1)

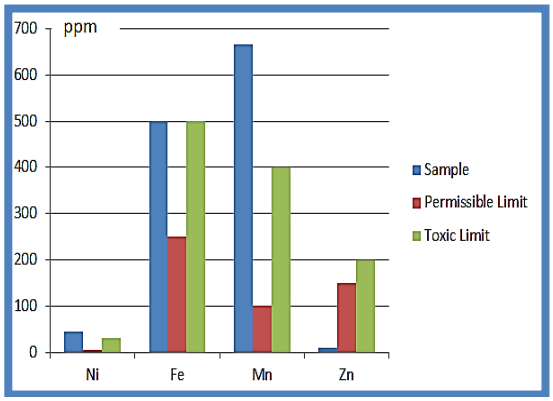

(b): Metal concentration of the sample(T2)

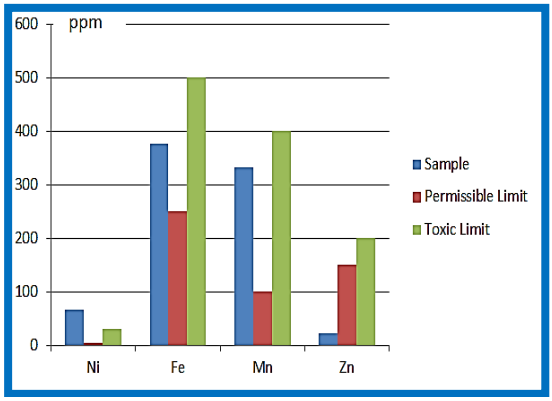

(c): Metal concentration of the sample(T3)

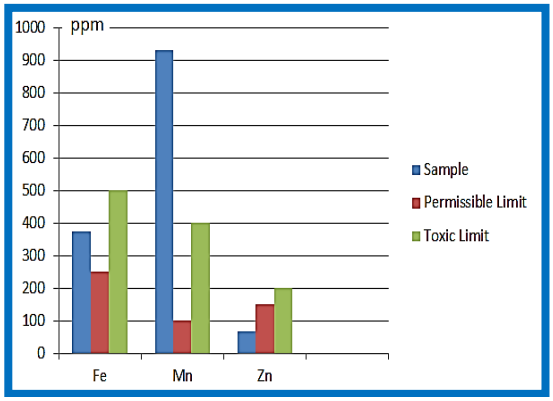

(d): Metal concentration of the sample(T4)

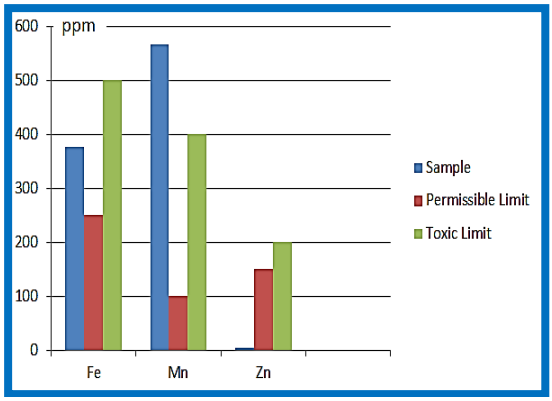

(e): Metal concentration of the sample(T5)

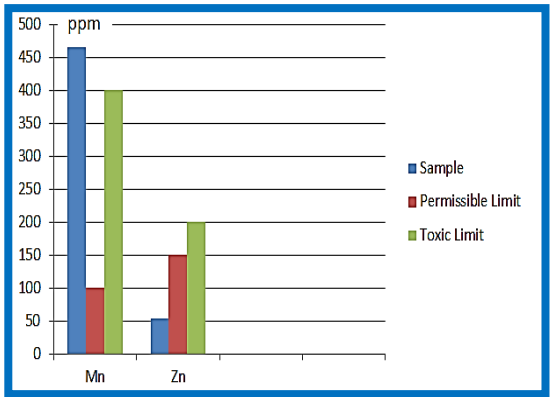

(f): Metal concentration of the sample(T6)

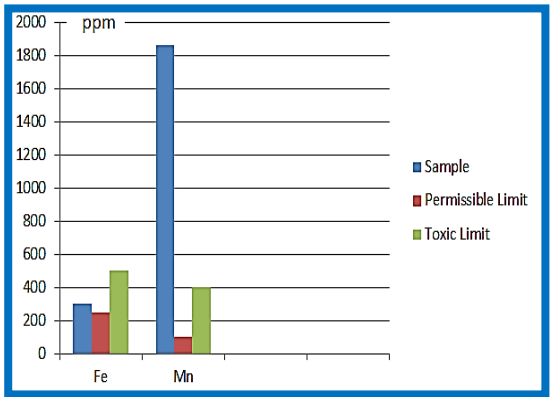

(g): Metal concentration of the sample(T7)

Figure 4: Metal concentrations for samples (a) T1, (b) T2, (c) T3, (d) T4, (e) T5, (f) T6, and (g) T7compared with permissible and toxic concentrations.

Potassium is the third most important plant nutrient, and it's the second most important nutrient after nitrogen for tea. Tea requires a comparatively higher quantity of K for better production and quality of the product. Here, K plays a vital role in enzyme activation, water relation, translocation, energy relations, and translocation of assimilated photosynthesis and protein and starch synthesis. Potassium's concentrations are clearly higher than the other elements, but potassium is considered an electrolyte mineral that helps regulate heartbeat and balance the body's fluid levels. It can help offset the adverse effects of consuming too much sodium [31].

According to research published by the University of Maryland Medical Center, a cup of green tea supplies lower potassium concentrations than black tea [32]. In our work, the results proved that the potassium concentration of sample 7 (the green tea) had a lower potassium level than 83.3% of the black tea samples. From the EDX Analysis, sulfur, phosphorus, aluminum, and magnesium were detected in too-low concentrations that were placed within the safe range. Additionally, it is essential to mention that the selected samples did not contain HMs like Cd, Pb, and Hg, which are toxic and are regarded as biologically non-essential in remarkable quantities.

4. Conclusions

Tea is considered one of the foodstuffs commonly used globally and locally in Iraq, and the high consumption rates make it at the forefront of foodstuffs that require knowledge of its suitability for human consumption. Some consumer concerns are generated about the potential risks of consuming tea, especially with poor control over imported food. To dispel doubts or prove them, data were obtained in this work to determine the validity of the food product concerning its containment of HMs within the permissible limits according to international health and safety standards. Here, seven samples of tea types commonly used in the Iraqi market were selected. Processes of preparing the samples for specialized examinations of HMs (EDX and AAS) were conducted according to the scientific protocols related to them. Results of these tests show that all the selected samples had high concentrations of nickel (in samples T1, T2, and T3) and manganese (in samples T1, T2, T4, T5, T6, and T7). The other HMs (Cd, Cu, Pb, Cr, and Co) were not detected or found in levels less than the detection limits of the used AAS, which makes these samples free from highly toxic HMs. Researchers recommend studying the chemicals in tea and discussing their toxicity. We also recommend the necessity of examining imported materials to ensure that they are free of toxic materials or materials that affect human health.

Acknowledgment

The authors would like to thank the Department of Chemistry, College of Science, Al-Nahrain University for their support.

5. References

[1] Harvard Health Publishing. The Health Benefits of Tea, 2023; Available online: https://www.hsph.harvard.edu/nutritionsource/food-features/tea/ (accessed on 1 June 2024).

[2] Dufresne, C.; Farnworth, E. A review of latest research findings on the health promotion properties of tea. J. Nutr. Biochem. 2001; 12, 404–421.

[3] Levkowitz, J. Middle East Institute, In Iraqi Kurdistan, there's more than just tea brewing in the teahouse, 2018. https://mei.edu/publications/iraqi-kurdistan-theres-more-just-tea-brewing-teahouse

[4] Ferdman, R. The Atlantic, The Countries That Drink the Most Tea, 2014. https://www.theatlantic.com/international/archive/2014/01/map-the-countries-that-drink-the-most-tea/283231/

[5] Balentine, D.; Wiseman, S.; Bouwens, L. The chemistry of tea flavonoids. Food Sci. Nutr. 1997; 37, 693–704.

[6] Soliman, N. Metals Contents in Black Tea and Evaluation of Potential Human Health Risks to Consumers. Health Econ. Outcome Res. 2016; 2, 1-4.

[7] Kong et al. Global research trends on herbal tea: a bibliometric and visualized analysis, Beverage Plant Research 2023; 4: e007.

[8] Chebet, J.; Kinyanjui, T.; Wanyoko, J.; Wachira, F. Effect of Sunlight Exposure and Different Withering Durations on Theanine Levels in Tea (Camellia sinensis). Food Nutr. Sci. 2015; 6, 11.

[9] Laumiere. 10-evidence-based-benefits-of-green-tea. Available online: https://laumieregourmet.com/blogs/news/10-evidence-based-benefits-of-green-tea (accessed on 1 June 2024).

[10] Karimi, G.; Hasanzadeh, M.K.; Nili, A.; Khashayarmanesh, Z.; Samiei, Z.; Nazari, F.; Teimuri, M. Concentrations and Health Risk of Heavy Metals in Tea Samples Marketed in IRAN. Pharmacologyonline 2008; 3, 164-174.

[11] Rashid, M.H.; Fardous, Z.; Chowdhury, M.; Alam, Md.; Bari, Md.; Moniruzzaman, M.; Gan, S. Determination of heavy metals in the soils of tea plantations and in fresh and processed tea leaves: an evaluation of six digestion methods. Chem Cent J 2016.

[12] Duffus, J. Heavy metals – A meaningless term. Pure Appl. Chem. 2002; 74, 5, 793–807.

[13] Soni, S.; Pandey, R. Interaction of Hazardous Heavy Metals with Humans and Environment and their Toxicological Impacts. Int. J. Sci. Res. Biol. Sci. 2021; 8, 5, 39-45.

[14] Ullah, I.; Khan, A.; Rahim, M.; Haris, M. R. H. M. Health Risk from Heavy Metals via Consumption of Food Crops in the Vicinity of District Shangla. J. Chem. Soc. Pak. 2016; 38.

[15] Al-Dahhan, W.; Ahmad, S.; Mansour, O.; Jebali, J.; Yousif, E. Determination of Heavy Metals in Some Types of Imported Fish from Local Markets. Al-Nahrain J. Sci. 2022; 25, 2, 14-19.

[16] Ansari, R.; Karami, M.; Fathabad, A.E.; Sadeghi, A. Study and measurement of Pb, Cd, Cr and Zn in green leaf of tea cultivated in Gillan Province of Iran. Pak. J. Nutr. 2005; 4, 4, 270-272.

[17] Saad, B.; Azaizeh, H.; Abu-Hijleh, G.; Said, O. Safety of traditional Arab herbal medicine. Evid. Based Complement. Alternat. Med. 2006; 3, 4, 433-439.

[18] Cheng, S. Heavy metals in plants and phytoremediation. Environ. Sci. Pollut. Res. 2003; 10, 5, 342-353.

[19] Annan, K.; Dickson, R.A.; Amponsah, I.K.; Nooni, I.K. The heavy metal contents of some selected medicinal plants sampled from different geographical locations. Pharmacogn. Res. 2013; 5, 2, 103-8.

[20] Khan, M.A.; Ahmad, I.; Rahman, I. Effect of Environmental Pollution on Heavy Metals Content of Withania Somnifera. Chinese Chem. Soc. Taipei 2007; 54, 2.

[21] Chayamiti, T. Heavy Metal Content of Selected Raw Medicinal Plant Materials: Implication for Patient Health. Bull. Environ. Pharmacol. Life Sci. 2012.

[22] Yang, F.; Li, Y.P. The effects of different marinating methods on solubility of lead in tea leaves. Chin. J. Health Lab. Technol. 2001; 11, 6, 349.

[23] Adnan, M.; Xiao, B.; Xiao, P.; Zhao, P.; Li, R.; Bibi, S. Research Progress on Heavy Metals Pollution in the Soil of Smelting Sites in China. Toxics 2022; 10, 231, 1-30.

[24] Al-Dahhan, W.; Husain, A.; Kadhom, M.; Yousif, E. Determination of Heavy Metals Levels in Imported Red Meat from Iraqi Markets. In Proceedings of the 5th Samarra International Scientific Conference, Samarra, Iraq, 23–24 February 2022; Samarra J. Pure Appl. Sci.

[25] Hseu, Z.-Y. Evaluating heavy metal contents in nine composts using four digestion methods. Waste Manag. 2004; 24, 1, 53-59.

[26] Al-Dahhan, W.; Yousif, E.; Hashim, H. Determination of Toxic Metals in Tobacco from Selected Imported Cigarette Brands and Local Tobacco in Iraqi Markets. SQU J. Sci. 2020; 25, 2, 78-84.

[27] Kara, H.T. Atomic Absorption Spectroscopic Determination of Heavy Metal Concentrations in Kulufo River, Arbaminch, Gamo Gofa, Ethiopia. Int. J. Environ. Anal. Chem. 2016; 3, 1.

[28] Rodushkin, I.; Ruth, T.; Huhtasaari, A. Comparison of two digestion methods for elemental determinations in plant material by ICP techniques. Anal. Chim. Acta 1999; 378, 1-3, 191-201.

[29] Osmani, R.; Bani, A.; Hoxha, B. Heavy Metals and Ni Phytoextraction in the Metallurgical Area Soils in Elbasan. J. Environ. Prot. Ecol. 2016; 17, 3, 935-944.

[30] Vijayalakshmi, S.; Kripa, K.G. Heavy metal analysis of Blepharis maderaspatensis (L.) heyne ex Roth. Asian J. Pharm. Clin. Res. 2018; 11, 10, 251.

[31] Bellows, L.; Moore, R. Potassium in the Diet. Colorado State University Extension, n.d.

[32] Sen Ray, K.; Singhania, P.R. Effect of green tea consumption on selected metabolic biomarkers in Asian Indian women with metabolic syndrome. Food Nutr. Res. 2014; 58, 1, 1-10.